

Copper and Silicon: Implications for the Long-term Stability of Plated Contacts for Silicon Solar Cells

Jack Killian Colwell

A thesis in fulfilment of the requirements for the degree of
Doctor of Philosophy



School of Photovoltaic and Renewable Energy Engineering
Faculty of Engineering

August 2018

THE UNIVERSITY OF NEW SOUTH WALES
Thesis/Dissertation Sheet

Surname or Family name: **COLWELL**

First name: **Jack**

Other name/s: **Killian**

Abbreviation for degree as given in the University calendar: **PhD**

School: **Photovoltaic and Renewable Energy Engineering**

Faculty: **FACULTY OF ENGINEERING**

Title: **Copper and Silicon: Implications for the Long-term Stability of Plated Contacts for Silicon Solar Cells**

Abstract 350 words maximum: (PLEASE TYPE)

Employing copper (Cu) plating as an alternative to screen-printed silver (Ag) for silicon (Si) solar cells can offer significant cost benefits. However, concerns that Cu may penetrate through nickel (Ni) barrier layers into Si where it impacts cell performance and module durability have contributed to the limited adoption of plated metallisation in manufacturing. This thesis aimed to investigate the thermal stability of Cu-plated Si solar cells with a particular focus on cells with Ni/Cu grids plated on openings formed by selective-ablation of the antireflection coating using a UV ps laser.

The formation of Cu precipitates in float-zone-Si was investigated using advanced lifetime spectroscopy of temperature and injection-dependent lifetime curves, with two defect levels identified at $E_T-E_i = -(0.14-0.16)$ eV and $E_T-E_i = (0.08-0.11)$ eV. Different capture cross-section ratios were obtained for Cu precipitates formed under illumination ($k = 1.4 \pm 0.2$) and ingot-grown precipitates ($k = 5.6 \pm 1.4$). A power-law dependence of the capture cross section was identified (with $\alpha=1.35-2.54$) and α was observed to increase with increasing precipitate size/density, the latter being theorised to be related to the faster precipitation rate under illumination generating smaller precipitates.

A physics of failure methodology was used to characterise Cu diffusion from plated contacts and degradation in Cu-plated p-type PERC and n-type PERT solar cells during thermal testing. Significant Cu diffusion through Ag capping layers was observed during treatments at 200 °C, the extent of the diffusion depending on the capping layer microstructure. Voids which formed as a result of Cu diffusion distorted Suns- V_{OC} measurements, leading to 5-10% errors in the measured pseudo fill factor of the cells. Cross-sectional imaging (FIB/TEM/EDS) and LA-ICP-MS were used to identify that Ni and Cu can penetrate into Si on heating, with increased Ni/Cu detection correlated with increased electrical degradation. Finally, thermal treatments both in the dark and under illumination revealed increased degradation of p-type PERC cells under illumination due to Cu-LID, whilst non-uniformities in the laser-ablation and Ni barrier formation were proposed as the most probable reasons for the observed variable thermal stability of Cu-plated contacts to the p-type PERC and n-type PERT cells.

Declaration relating to disposition of project thesis/dissertation

I hereby grant to the University of New South Wales or its agents the right to archive and to make available my thesis or dissertation in whole or in part in the University libraries in all forms of media, now or here after known, subject to the provisions of the Copyright Act 1968. I retain all property rights, such as patent rights. I also retain the right to use in future works (such as articles or books) all or part of this thesis or dissertation.

I also authorise University Microfilms to use the 350 word abstract of my thesis in Dissertation Abstracts International (this is applicable to doctoral theses only).

.....
Signature

.....
Witness Signature

.....
Date

The University recognises that there may be exceptional circumstances requiring restrictions on copying or conditions on use. Requests for restriction for a period of up to 2 years must be made in writing. Requests for a longer period of restriction may be considered in exceptional circumstances and require the approval of the Dean of Graduate Research.

FOR OFFICE USE ONLY

Date of completion of requirements for Award:

INCLUSION OF PUBLICATIONS STATEMENT

UNSW is supportive of candidates publishing their research results during their candidature as detailed in the UNSW Thesis Examination Procedure.

Publications can be used in their thesis in lieu of a Chapter if:

- The student contributed greater than 50% of the content in the publication and is the “primary author”, ie. the student was responsible primarily for the planning, execution and preparation of the work for publication
- The student has approval to include the publication in their thesis in lieu of a Chapter from their supervisor and Postgraduate Coordinator.
- The publication is not subject to any obligations or contractual agreements with a third party that would constrain its inclusion in the thesis

Please indicate whether this thesis contains published material or not.



This thesis contains no publications, either published or submitted for publication (if this box is checked, you may delete all the material on page 2)



Some of the work described in this thesis has been published and it has been documented in the relevant Chapters with acknowledgement (if this box is checked, you may delete all the material on page 2)



This thesis has publications (either published or submitted for publication) incorporated into it in lieu of a chapter and the details are presented below

CANDIDATE'S DECLARATION

I declare that:

- I have complied with the Thesis Examination Procedure
- where I have used a publication in lieu of a Chapter, the listed publication(s) below meet(s) the requirements to be included in the thesis.

| Name | Signature | Date (dd/mm/yy) |
|--------------|-----------|-----------------|
| Jack COLWELL | | |

Postgraduate Coordinator's Declaration (to be filled in where publications are used in lieu of Chapters)

I declare that:

- the information below is accurate
- where listed publication(s) have been used in lieu of Chapter(s), their use complies with the Thesis Examination Procedure
- the minimum requirements for the format of the thesis have been met.

| PGC's Name | PGC's Signature | Date (dd/mm/yy) |
|------------|-----------------|-----------------|
| | | |

Originality Statement

‘I hereby declare that this submission is my own work and to the best of my knowledge it contains no materials previously published or written by another person, or substantial proportions of material which have been accepted for the award of any other degree or diploma at UNSW or any other educational institution, except where due acknowledgement is made in the thesis. Any contribution made to the research by others, with whom I have worked at UNSW or elsewhere, is explicitly acknowledged in the thesis. I also declare that the intellectual content of this thesis is the product of my own work, except to the extent that assistance from others in the project's design and conception or in style, presentation and linguistic expression is acknowledged.’

Signed

Date

Copyright Statement

'I hereby grant the University of New South Wales or its agents the right to archive and to make available my thesis or dissertation in whole or part in the University libraries in all forms of media, now or here after known, subject to the provisions of the Copyright Act 1968. I retain all proprietary rights, such as patent rights. I also retain the right to use in future works (such as articles or books) all or part of this thesis or dissertation. I also authorise University Microfilms to use the 350 word abstract of my thesis in Dissertation Abstract International (this is applicable to doctoral theses only). I have either used no substantial portions of copyright material in my thesis or I have obtained permission to use copyright material; where permission has not been granted I have applied/will apply for a partial restriction of the digital copy of my thesis or dissertation.'

Signed

Date

Authenticity Statement

'I certify that the Library deposit digital copy is a direct equivalent of the final officially approved version of my thesis. No emendation of content has occurred and if there are any minor variations in formatting, they are the result of the conversion to digital format.'

Signed

Date

Abstract

Employing copper (Cu) plating as an alternative to screen-printed silver (Ag) for silicon (Si) solar cells can offer significant cost benefits. However, concerns that Cu may penetrate through nickel (Ni) barrier layers into Si where it impacts cell performance and module durability have contributed to the limited adoption of plated metallisation in manufacturing. This thesis aimed to investigate the thermal stability of Cu-plated Si solar cells with a particular focus on cells with Ni/Cu grids plated on openings formed by selective-ablation of the antireflection coating using a UV ps laser.

The formation of Cu precipitates in float-zone-Si was investigated using advanced lifetime spectroscopy of temperature and injection-dependent lifetime curves, with two defect levels identified at $E_t-E_i = -(0.14-0.16)$ eV and $E_t-E_i = (0.08-0.11)$ eV. Different capture cross-section ratios were obtained for Cu precipitates formed under illumination ($k = 1.4 \pm 0.2$) and ingot-grown precipitates ($k = 5.6 \pm 1.4$). A power-law dependence of the capture cross section was identified (with $\alpha=1.35-2.54$) and α was observed to increase with increasing precipitate size/density, the latter being theorised to be related to the faster precipitation rate under illumination generating smaller precipitates.

A physics of failure methodology was used to characterise Cu diffusion from plated contacts and degradation in Cu-plated p-type PERC and n-type PERT solar cells during thermal testing. Significant Cu diffusion through Ag capping layers was observed during treatments at 200 °C, the extent of the diffusion depending on the capping layer microstructure. Voids which formed as a result of Cu diffusion distorted Suns- V_{OC} measurements, leading to 5-10% errors in the measured pseudo fill factor of the cells. Cross-sectional imaging (FIB/TEM/EDS) and LA-ICP-MS were used to identify that Ni and Cu can penetrate into Si on heating, with increased Ni/Cu detection correlated with increased electrical degradation. Finally, thermal treatments both in the dark and under illumination revealed increased degradation of p-type PERC cells under illumination due to Cu-LID, whilst non-uniformities in the laser-ablation and Ni barrier formation were proposed as the most probable reasons for the observed variable thermal stability of Cu-plated contacts to the p-type PERC and n-type PERT cells.

Acknowledgements

If you love what you do, you will never have to work a day in your life...if only that were true. No matter how much you love what you do, you're still going to have to work, and you're going to have to work hard. Sometimes, those all-nighters seem a lot more like work than love, but it's the people in your life that help you through those long days and it's about time I acknowledge those wonderful people.

First and foremost, I'd like to thank my supervisors Alison Lennon and Ziv Hameiri, who have guided and supported me through the past four years. Alison, I began this journey because of an enthusiasm for research that you helped develop in me through the final years of my undergraduate degree. Ziv, if not the hardest-working man in SPREE then definitely in the top three, you have taught me so much in a short time. Both of you have made me a better researcher and your dedication to research and your students is a true inspiration and I could not have hoped for better or more attentive supervision to aid me throughout this project.

The added benefit of having two supervisors is that I also ended up being a part of two great research groups full of many talented people who helped me throughout the years. In particular, I'd like to thank Paget, Xi Wang, Xiaowei, Ben and Dylan for all the help with plating the cells that I then destroyed in various ways. In the defects group, Yan, Rob Dumbrell and Carlos helped accelerate my understanding of lifetime spectroscopy and were exceptionally generous with their time and patience. Outside of those directly involved in my research, there are the rest of those research groups – Taffy, Ning, Charles, Elaine, Daniel, Udo, Derwin, μ Rob, Kyung and Shuai, just to name a few (I've got the memory of a goldfish, so apologies to anyone I forgot). There are also those who suffered me without needing to – Anastasia, Arman, Danny Chen, Moonyong, Kean, Ran, Josh, and many others. Thank you all for discussions, advice or simply a conversation when I really needed one.

Outside of the research groups, there are those that keep everything running from day to day. The LDOT team – in particular Mark (both Griffin and Silver), Kian, Alan,

Nick, Tom and Bernhard, have suffered both beside me with temperamental tools and even at my inexperienced hand from time to time. But their helpfulness is unending and I'd be finishing these experiments with less efficiency than the Sydney Light Rail network without them. Outside of the labs, there are so many people that keep this building running that I can't name them all for fear of leaving anyone out, so thanks to all who keep this SPREE ship afloat.

Before I talk about my biological family, my other family should be recognised. Weird, dysfunctional and wonderful – I would not have survived without them. Catherine Chan, Ned Western, The Cieslas (Ali and Mike), The Juhls (Mattias and Rosie), David Payne, Michael Pollard, John Rodriguez, James Hazelton, Nitin “No BO” Nampalli, Alex “AlOx” To, Iskra Zafirovska, Dee Smith, Terry Yang, Karthik Mukkavilli, Maryam Hasheminamin. I am sure I've told you all on numerous occasions how much you all have meant to me over the years - thanks for everything. I reserve a special spot at the end here for Natasha Hjerrild, a real-life unicorn who endured not only her own thesis stress, but mine as well and somehow survived with a full thesis, a smile on her face and her sanity intact (peer review required).

Now, no hobbit's journey is complete without thinking back to the Shire in which he was raised. There are friends that I've had longer than my memory cares to recollect, and although I don't see them as much these days, they still earn a spot in this little tribute. There are friends from school, soccer and water polo that I always enjoy seeing when I'm back down there, and I look forward to catching up with you all at the end of all this. In particular, there's a certain fool named Daniel Fynn, who has matched my level of oddity at every turn – a powerful simpatico relationship for which I am forever grateful.

If you read this and I haven't mentioned you, do not hesitate to contact me to let me know of your disappointment. I will apologise on the spot, beg forgiveness and update you personally on your importance in my life leading up to this point.

Last, but most certainly not least, I want to thank my family. It's been a more tumultuous writing period than any of us probably anticipated, but I will be forever thankful for the unwavering support, humour and love they provide, which shapes the person I am whilst guiding the way to the person I want to be.

Table of Contents

| | |
|--|-------------|
| Abstract | ix |
| Acknowledgements | xi |
| Table of Contents | xiii |
| List of Abbreviations | xvi |
| List of Symbols | xvii |
| Chapter 1 Introduction | 1 |
| 1.1 Trends in Solar Cell Metallisation | 1 |
| 1.2 Copper: The Double-edged Sword | 3 |
| 1.3 Thesis Objectives..... | 5 |
| 1.4 Thesis Outline..... | 6 |
| Chapter 2 Copper in Silicon: A Historical Perspective | 9 |
| 2.1 Diffusivity, solubility and gettering of copper in silicon | 9 |
| 2.2 Defect states of copper in silicon | 12 |
| 2.2.1 Substitutional copper..... | 12 |
| 2.2.2 Point defects and complexes..... | 12 |
| 2.2.3 Copper precipitates | 13 |
| 2.3 Light-induced degradation in silicon..... | 15 |
| 2.3.1 Boron-oxygen light-induced degradation..... | 15 |
| 2.3.2 Copper-related light-induced degradation..... | 18 |
| 2.3.3 Light and elevated temperature induced degradation | 20 |
| 2.4 Copper precipitate formation kinetics..... | 22 |
| 2.4.1 Precipitate nucleation..... | 22 |
| 2.4.2 Precipitate growth | 23 |
| 2.5 Chapter Summary | 27 |
| Chapter 3 Lifetime Spectroscopy Analysis of Copper in Silicon | 29 |
| 3.1 Defect Parameterisation using Lifetime Spectroscopy | 29 |

| | | |
|--|--|-----------|
| 3.1.1 | Recombination mechanisms in silicon | 29 |
| 3.1.2 | SRH fitting and defect parameter extraction | 36 |
| 3.2 | Characterisation of Cu precipitates using TIDLs..... | 38 |
| 3.2.1 | Introduction..... | 38 |
| 3.2.2 | Experimental | 39 |
| 3.2.3 | Results and discussion..... | 43 |
| 3.3 | Chapter Summary..... | 61 |
| Chapter 4 Copper Diffusion through Plated Metals in Solar Cell Contacts | | 65 |
| 4.1 | Diffusion barriers for plated solar cells | 65 |
| 4.1.1 | Categorisation of diffusion barriers..... | 65 |
| 4.1.2 | Ni as a diffusion barrier for solar cells..... | 68 |
| 4.2 | Cu diffusion through plated Ag layers | 72 |
| 4.2.1 | Introduction..... | 72 |
| 4.2.2 | Experimental | 72 |
| 4.2.3 | Results and discussion..... | 76 |
| 4.3 | Evidence of Cu diffusion through plated Ni barriers | 91 |
| 4.3.1 | Introduction..... | 91 |
| 4.3.2 | Experimental | 92 |
| 4.3.3 | Results and discussion..... | 92 |
| 4.4 | Chapter Summary..... | 97 |
| Chapter 5 Elemental Analysis of Plated Ni Barrier Performance | | 99 |
| 5.1 | Elemental analysis techniques for bulk impurities in silicon..... | 99 |
| 5.2 | Minimising surface interference during LA-ICP-MS | 104 |
| 5.2.1 | Introduction..... | 104 |
| 5.2.2 | Experimental | 104 |
| 5.2.3 | Results and discussion..... | 107 |
| 5.3 | Ablation characteristics for Si substrate analysis | 109 |
| 5.3.1 | Introduction..... | 109 |
| 5.3.2 | Experimental | 109 |
| 5.3.3 | Results and discussion..... | 110 |
| 5.4 | Characterisation of diffusion barrier quality using LA-ICP-MS..... | 114 |
| 5.4.1 | Introduction..... | 114 |

| | | |
|-----------------------------|---|------------|
| 5.4.2 | Experimental..... | 114 |
| 5.4.3 | Results and discussion | 117 |
| 5.5 | Chapter summary..... | 125 |
| Chapter 6 | Thermal Stability Testing for Plated Solar Cells | 127 |
| 6.1 | Arrhenius analysis of solar cell degradation | 127 |
| 6.2 | Comparison of n-type and p-type cell degradation | 130 |
| 6.2.1 | Introduction..... | 130 |
| 6.2.2 | Experimental..... | 130 |
| 6.2.3 | Results and discussion | 132 |
| 6.3 | Influence of illumination on degradation | 143 |
| 6.3.1 | Introduction..... | 143 |
| 6.3.2 | Experimental..... | 143 |
| 6.3.3 | Results and discussion | 144 |
| 6.4 | Impact of process variability on long-term stability testing..... | 153 |
| 6.4.1 | Introduction..... | 153 |
| 6.4.2 | Results and Discussion..... | 153 |
| 6.5 | Chapter Summary | 162 |
| Chapter 7 | Conclusions and Outlook | 165 |
| 7.1 | Original Contributions | 167 |
| 7.2 | Future Work and Outlook..... | 168 |
| List of Publications | | 171 |
| Appendix A | Calibration Procedure for TIDLS Measurements | 173 |
| Appendix B | Calculation of Laser Fluence | 175 |
| Appendix C | Cell degradation results for different Ag capping layers | 176 |
| Appendix D | Complete thermal stability results for Cu-plated solar cells | 178 |
| References | | 181 |

List of Abbreviations

| | |
|-----------|---|
| Al-BSF | Aluminium back surface field |
| ARC | Antireflection coating |
| BO | Boron-oxygen |
| Cz | Czochralski |
| DLTS | Deep-level transient spectroscopy |
| DPSS | Defect parameter solution surface |
| EDS | Energy dispersive x-ray spectroscopy |
| EQE | External quantum efficiency |
| FIB | Focussed ion beam |
| FIP | Field-induced plating |
| FZ | Float zone |
| IC | Integrated circuits |
| LA-ICP-MS | Laser ablation inductively-coupled plasma mass spectrometry |
| LeTID | Light and elevated temperature-induced degradation |
| LID | Light-induced degradation |
| LIP | Light-induced plating |
| PCD | Photoconductance decay |
| PECVD | Plasma enhanced chemical vapour deposition |
| PERC | Passivated emitter and rear cell |
| PERT | Passivated emitter rear totally-diffused |
| PL | Photoluminescence |
| SCR | Space charge region |
| SEM | Scanning electron microscopy |
| SIMS | Secondary ion mass spectrometry |
| SRH | Shockley-Read-Hall |
| SRV | Surface recombination velocity |
| TEM | Transmission electron microscopy |
| TID | Transient ion drift |
| TIDLS | Temperature and injection-dependent lifetime spectroscopy |
| UV ps | Ultraviolet picosecond |

List of Symbols

| | | |
|------------------|---------------------------------|----------------------------|
| Si | Silicon | — |
| Ni | Nickel | — |
| Cu | Copper | — |
| Ag | Silver | — |
| B | Boron | — |
| P | Phosphorus | — |
| O | Oxygen | — |
| k_B | Boltzmann constant | eV/K |
| N_A | Doping concentration | cm ⁻³ |
| V_{OC} | Open-circuit voltage | mV |
| J_{sc} | Short-circuit current | mA/cm ² |
| pFF | Pseudo fill-factor | % |
| FF | Fill factor | % |
| η | Cell efficiency | % |
| R_s | Series Resistance | $\Omega \cdot \text{cm}^2$ |
| J_0 | Saturation current density | A/cm ² |
| k | Capture cross-section ratio | — |
| E_t | Defect energy level | eV |
| $\sigma_{n,p}$ | Capture cross-section | cm ² |
| S_{eff} | Surface recombination velocity | cm/s |
| τ | Carrier lifetime | μs |
| n_i | Intrinsic carrier concentration | cm ⁻³ |
| n/p | Electron/hole concentration | cm ⁻³ |
| Δn | Excess carrier concentration | cm ⁻³ |
| SiN _x | Silicon nitride | — |
| AlO _x | Aluminium oxide | — |
| SiO ₂ | Silicon oxide | — |
| N_{prec} | Precipitate density | cm ⁻³ |
| r_{prec} | Precipitate radius | nm |
| W | Si wafer thickness | μm |

Chapter 1 Introduction

Crystals are like people – it is the defects in them which tend to make them interesting.

- Professor Colin Humphreys

Introduction to Analytical Electron Microscopy

Earth has reached a critical stage of development over the past century. Since the onset of industrialisation, the planet has entered a new era defined by humanity's impact on the global ecosystem [1]. This period is primarily characterised by rapidly increasing levels of atmospheric carbon dioxide, CO₂ (~ 402 ppm in 2017 [2] compared to 260-270 ppm pre-industrial levels [3]), resulting in unparalleled shifts in weather patterns, record high temperatures and rising sea levels due to both glacial reduction and ocean warming [4]. Recent studies have shown that CO₂ emissions are now reaching levels such that even moderately strict mitigation strategies may not be adequate to prevent jumping over the "2 °C guardrail" often set as the limit in global temperature rise required to prevent significant and disastrous functional changes to the planetary ecosystem [5, 6]. A large-scale shift in the world's energy supply from fossil fuels to predominantly renewable energy sources, such as photovoltaics (PV), is required in the near future if any significant impact is to be made in mitigating anthropogenic climate change.

1.1 Trends in Solar Cell Metallisation

Solar cells require electrical contact to both p- and n-type regions of a silicon (Si) substrate for light-generated current collection. Screen-printing of silver (Ag) for front-side metallisation of Si solar cells has remained the dominant technology in the PV manufacturing industry since the 1970s, and currently accounts for more than 90% of commercially-produced solar cells [7]. The high resistance of Ag to corrosion, coupled with its high electrical conductivity, make it an ideal conductor for Si-based PV devices.

However, as the cost of PV modules decrease, the metallisation of solar cells is increasingly becoming the focus of furthering cost reductions as Ag represents the largest non-Si cost component for commercial solar cells (1 USD cent/Wp, or 13% of the non-Si cell price for a 20% mc-Si PERC cell [7]). Even with continuing efforts to reduce the use of Ag in cell contact grids, the high and sometimes volatile cost of Ag (533 USD/kg as of February 2018 [7]) indicates a necessity for alternative metallisation schemes if large-scale PV manufacturing costs are to be minimised.

Copper (Cu) is an attractive alternative to Ag for several reasons. Not only is Cu significantly more abundant in the Earth's crust [8], which contributes to its much lower cost compared to Ag, but its price has remained relatively stable at <10 USD/kg for at least the past 30 years [9]. Furthermore, it has an electrical conductivity comparative to that of Ag (5.85×10^7 S/m and 6.2×10^7 S/m for Cu and Ag, respectively [10]). The use of plated Cu as a potential replacement for Ag in solar cell metallisation can be traced back to the 1970s and 1980s, when early Si PV pioneers Motorola, Solarex and Siemens invested heavily in the development of electroless nickel (Ni) and Cu plating [11–14]. In the 1990s, Wenham and Green adopted Motorola's electroless plating processes in their development of the buried contact cell technology [15, 16]. This cell design, which used electroless plating of a Ni diffusion barrier and seed layer followed by Cu plating, was subsequently adapted for industrial-scale solar manufacturing as the laser-buried grid (LBG) Saturn PV cell (see Figure 1.1) which was successfully manufactured by BP Solar up until 2009 [17–20].

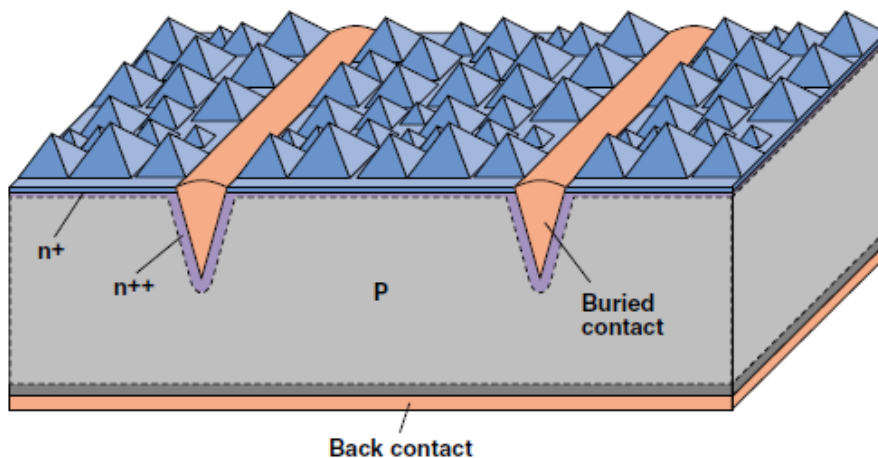


Figure 1.1: Schematic of BP Solar's LBG Saturn Solar cells with plated Cu fingers contained within heavily-doped laser trenches (adapted from [19]).

Suntech also incorporated plated metallisation into the production of their laser-doped selective emitter (LDSE) Pluto cell design [21, 22]. To improve the plating rate, electroless plating was replaced with light-induced plating (LIP) [23–25] which significantly increased the plating rate and resulted in a higher throughput process. The LIP process also significantly reduced the cost of the Ni/Cu plating process used by BP Solar, in that a corroding anode could be used to provide a source of Cu ions for deposition. This process, along with eliminating the need to use toxic cyanide-based electrolytes, also reduced bath maintenance costs [14]. However, issues with contact adhesion raised concerns over both interconnection and module lifetime [26]. Despite the problems raised by Suntech’s Pluto process, the International Technology Roadmap for Photovoltaics (ITRPV) continues to predict that plating-based metallisation technologies will hold increasing market share over the next decade, as shown in Figure 1.2 below [7, 27].

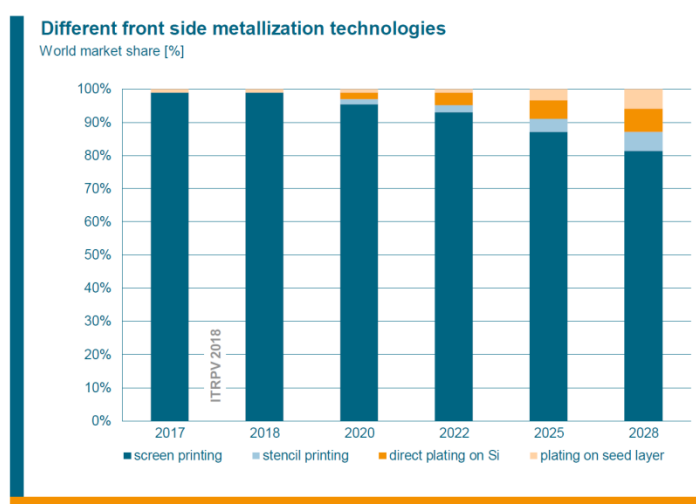


Figure 1.2: ITRPV 2018 predicted trends for different front-side metallisation technologies (from [7]).

1.2 Copper: The Double-edged Sword

Despite recent projections, the predicted market share of plated technologies has been consistently reduced across previous ITRPV reports, with the 2014 report predicting > 30% market share within the same timeframe [7]. Widespread adoption of Cu plating as a replacement for Ag screen-printing has failed to gain any significant traction due to concerns about the long-term stability of Cu-plated solar cells [7]. This is

not only related to the problem of plated contact adhesion, but also to the risk of Cu-related degradation from the plating process or the plated contacts themselves [26]. The deleterious effect of Cu in Si has been studied extensively over the years (as detailed in previous studies [28, 29]), with significant research motivated by the integrated circuits (IC) industry culminating in IBM's introduction of Cu electroplating for the fabrication of interconnects for ultra large-scale integration (ULSI) applications in 1997 [30–35].

Copper is a fast-diffusing impurity in Si, and can significantly reduce the minority carrier lifetime in both p-type and n-type Si through the formation of Cu defects (most likely platelet-like Cu_3Si precipitates) which introduce band-like defect states in the upper half of the bandgap [28, 36, 37]. Early studies also showed that the presence of Cu in Si can lead to an increase in p-n junction leakage current [38–41]. More recently, the impact of illumination has also become a topic of great interest, with Cu demonstrating similar light-induced degradation behaviour to boron-oxygen defects (BO) [42–45]. To mitigate these issues, an intervening metal layer is often employed as a diffusion barrier, with Ni most commonly used in plated solar cells [14]. However, variability in barrier quality can reduce its effectiveness [46–49] and thus some form of long-term stability testing is required to assess the durability of plated barrier layers on Si solar cells. To investigate the durability of plated solar cells, an accelerated aging test was reported by Bartsch *et al.*, whereby plated cells are exposed to elevated temperatures for extended periods to simulate long-term field operation, with a reduction in pseudo fill factor (pFF) being used as an indicator of Cu-related degradation, as demonstrated in Figure 1.3 [50].

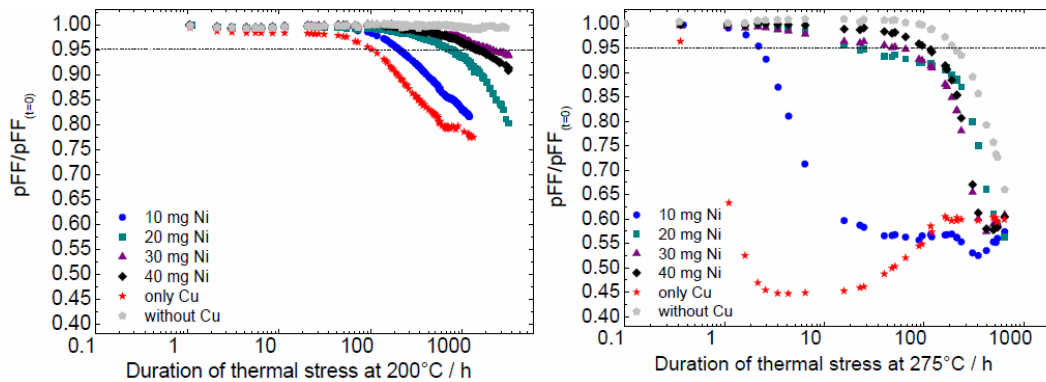


Figure 1.3: Degradation of pFF over time at a temperature of 200 °C (left) and 275 °C (right) for plated cells with different Ni diffusion barrier masses (from [51]).

Recent reports suggest that Cu-plated Si PV modules have sufficient long-term stability [51–57]. The previously-mentioned BP Solar Saturn modules have performed relatively well, with a power plant in Toledo (Spain) demonstrating performance ratios (PR) of over 70% after 20 years in the field, consistently higher than that of screen-printed modules manufactured at the same time [52, 53]. Also, long-term durability testing based on the method employed by Bartsch *et al.* suggests Ni is a sufficient diffusion barrier for Cu plated solar cells [51, 54, 55]. However, the manufacturing of p-type Si solar cells in China is rapidly moving towards the production of higher efficiency passivated emitter and rear cells (PERC) [58]. The reduced surface recombination achieved with these cell designs makes them more sensitive to impurities that may introduce additional recombination in other regions of the device. Thus, a higher requirement is placed on both the plating process and the long-term durability of PERC cells to not introduce additional recombination (contact and bulk) if Cu-plated metallisation is to be adopted as a viable alternative to screen-printed Ag.

1.3 Thesis Objectives

The aim of this thesis was to investigate the thermal stability of Cu-plated Si solar cells with a particular focus on cells with Ni/Cu grids plated on openings formed by selective-ablation of the antireflection coating using an ultraviolet (UV) picosecond (ps) laser. The impact of Cu diffusion into and within Si was investigated at both a wafer and cell level, with the following specific objectives:

- To use temperature and injection-dependent lifetime spectroscopy for the characterisation of defect properties, such as capture cross-section and defect energy levels, of Cu precipitates formed under different processing conditions.
- To investigate Cu diffusion mechanisms through plated metal layers using a combination of Suns- V_{OC} measurements and electron microscopy techniques to identify factors most critical in determining diffusion barrier performance.
- To quantify Cu penetration through plated Ni barrier layers using elemental characterisation techniques and correlate obtained measurements with observed electrical degradation due to Cu diffusion and defect formation.

- To perform thermal stability tests on plated p-type PERC and n-type passivated emitter rear totally-diffused (PERT) Si solar cells with laser ablation front grid patterning and perform a critical assessment of the processing factors that influence Cu-related cell degradation.

1.4 Thesis Outline

Chapter 2 begins with a historical perspective of the properties of Cu in Si. Several decades of extensive research on the diffusivity, solubility and defect states of Cu is discussed. Light-induced degradation of Cu-contaminated Si is examined in both Chapter 3 and Chapter 6 of this thesis, thus a review of current understanding of the impact of illumination on degradation of Si is provided. Since Cu precipitates are the most-likely candidate for the defect responsible for Cu-related degradation of Si, this chapter concludes with a breakdown of Cu precipitate formation and growth kinetics.

The first of four experimental chapters, Chapter 3 reports on the use of lifetime spectroscopy for the analysis of Cu defect properties in Si. Temperature and injection-dependent lifetime spectroscopy (TIDLS) has only recently been used to characterise the Cu-related defect in Si, so this chapter details experiments on TIDLS measurements of Cu-contaminated Si prepared using different techniques, demonstrating a significant difference in capture cross-section ratio between surface-contaminated Si experiencing Cu-LID and ingot-contaminated Si containing precipitates formed during ingot crystallisation. Two different curve fitting procedures were applied to the lifetime data obtained to extract information about the precipitate size/density and the associated recombination activity between the two differently-prepared Si samples.

Chapter 4 reports on an investigation of the limitations of thin polycrystalline metal layers as diffusion barriers for Cu-plated Si solar cells. Suns- V_{OC} measurements of plated solar cells during extended thermal stability testing were utilised to detect Cu diffusion through plated metal layers, both into the Si and through the Ag capping metal. High contact resistance effects evident in Suns- V_{OC} were the result of significant diffusion of Cu through plated Ag capping layers and the impact on the capping layer properties on extent of Cu diffusion was investigated in detail. Corresponding cross-sectional imaging techniques were used to assess the integrity of the contact structure after thermal stability testing and determine any diffusion of metals in the Si substrate.

Before a critical assessment of plated degradation analysis can be discussed, a material characterisation technique for confirming the penetration of plated metals into the Si substrate was developed, and this is presented in Chapter 5. The focus of this experimental work revolved around the implementation of laser ablation inductively-coupled plasma mass spectrometry (LA-ICP-MS) for the detection of diffused metals from plated contacts in Si solar cells. Optimisation of the technique for solar cell analysis is described, and a suitable chemical etching method is developed to improve accuracy of LA-ICP-MS in analysing Ni and Cu contamination of the Si under plated contacts. The chapter concludes with a discussion of results correlating Ni and Cu signals from LA-ICP-MS measurements with different electrical degradation indicators measured on plated cells following extended thermal stability testing.

Chapter 6 brings together the key findings of previous chapters to present a critical assessment of plated solar cell degradation analysis as it was performed in this research project. Degradation analysis is presented for both p-type PERC and n-type PERT cells with Ni/Cu plated contacts to illustrate the different responses to extended thermal stability testing. Due to the results of work presented in Chapter 3, the effect of illumination on the degradation rates observed in plated Si solar cells during thermal stability testing was also examined. Finally, concerns over process variability and reliability are examined in more detail, with particular focus on the issues of non-uniform laser ablation patterning and subsequent Ni barrier formation.

Finally, Chapter 7 summarises the key results of this research project as presented in this thesis, including a summary of the key findings and contributions of this thesis, as well as possible future directions for plated metallisation and Cu-related degradation analysis.

Chapter 2 Copper in Silicon: A Historical Perspective

A greater understanding of the experimental work presented in this thesis can be attained with an examination of current knowledge on the properties of Cu in Si. Significant work has been performed over the last half-century in characterising transition metals such as Cu, as well as more recently, the mechanisms that determine its role as such a detrimental impurity in Si. Istratov *et al.* provide extensive reviews on the behaviour of Cu in Si [28, 29, 59]. Thus, the purpose of this chapter is to present an overview of several decades of research on the critical properties of Cu, including its diffusivity and solubility which determines its movement within the substrate, to the various states in which Cu can occupy in the Si lattice. Diffusion of Cu through thin films and barrier metals between Cu and Si will be covered separately in Chapter 4. Also discussed are the mechanisms of light-induced degradation in Si [60] as well as the kinetics of Cu precipitate formation, which have been demonstrated to be highly influential in Cu defect formation and provides the theoretical basis for experiments detailed in Chapter 3 and Chapter 6 of this thesis.

2.1 Diffusivity, solubility and gettering of copper in silicon

Copper is a $3d$ transition metal, and in its interstitial state diffuses as a single donor species, Cu_i^+ [61]. Early work by Hall and Racette in 1964 [62] established a temperature-dependent diffusion coefficient in Si based on diffusion studies on low resistivity p-type wafers ($N_A = 5 \times 10^{20} \text{ cm}^{-3}$). However, this early work neglected the impact of donor-acceptor pairing between positively-charged Cu_i^+ and negatively charged substitutional Boron (B), B_s^- . In the presence of donor-acceptor pairing, the mobility of available Cu is limited by the doping concentration (N_A) and thus the effective diffusion coefficient in p-type Si is lower than expected [63]. It was later demonstrated that the dissociation energy of these Cu-acceptor pairs depended on the acceptor type (0.61 eV for Cu-B pairs [64]), indicating the presence of both Coulombic and covalent interactions [65]. Transient Ion Drift (TID) measurements of low B-doped

Si ($N_A = 1.5 \times 10^{14} \text{ cm}^{-3}$) performed by Istratov *et al.* in 1998 [66] minimised Cu-B interactions, providing a more accurate expression for the intrinsic diffusion coefficient:

$$D_{int} = (3.0 \pm 0.3) \times 10^{-4} \times \exp\left(-\frac{0.18 \pm 0.01 \text{ eV}}{k_B T}\right) \text{ (cm}^2/\text{s)} \quad (2.1)$$

where k_B is the Boltzmann constant and T is the temperature in Kelvin. The low activation energy of 0.18 eV is significantly closer to theoretical predictions than Hall and Racette's original estimation [67]. Equation 2.1 is valid in the case of intrinsic and n-type Si, but for B-doped wafers with a doping concentration of $N_A \leq 10^{17} \text{ cm}^{-3}$, the effective diffusion coefficient in the presence of Cu-B pairing is given by the expression [66]:

$$D_{eff} = \frac{3 \times 10^{-4} \times \exp(-2090/T)}{1 + 2.584 \times 10^{-20} \times \exp(4990/T) \times (N_A/T)} \text{ (cm}^2/\text{s)} \quad (2.2)$$

At room temperature, this corresponds to a value of $3.7 \times 10^{-8} \text{ cm}^2/\text{s}$ for a $3 \text{ } \Omega\cdot\text{cm}$ p-type Si wafer, indicating that Cu can diffuse $500 \text{ } \mu\text{m}$ without any thermal treatment within 12 hours. Figure 2.1 illustrates the impact of dopant concentration on D_{eff} for Cu in comparison to the intrinsic coefficient and highlights the large under-estimation of diffusion coefficient when not accounting for Cu-B interactions.

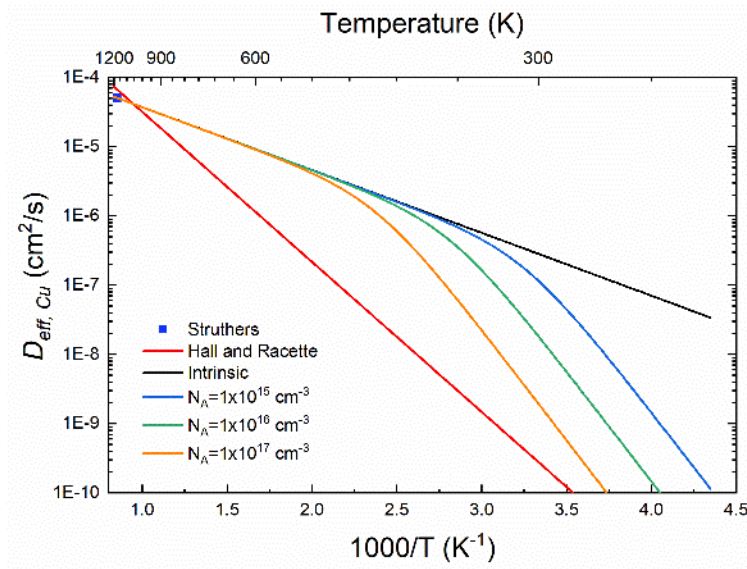


Figure 2.1: Effective diffusion coefficient for Cu in Si at various doping levels, compared to the original estimations by Struthers [68], Hall and Racette [62], as well as the intrinsic diffusion coefficient determined by Istratov *et al.* [66].

Copper has the lowest diffusion barrier of all the 3d transition metals, primarily due to the small ionic radius of Cu in Si and its weak covalent interactions with the Si lattice [28]. In terms of solubility, Cu concentration in Si can exceed 10^{18} cm^{-3} at high temperatures ($> 800 \text{ }^\circ\text{C}$), with solubility below the eutectic temperature ($T_{eu} = 1075 \text{ K}$) calculated using [61, 69]:

$$S_{Cu} = 5.512 \times 10^{23} \times \exp\left(-\frac{1.49 \text{ eV}}{k_B T}\right) \text{ (cm}^{-3}\text{)} \quad (2.3)$$

Despite this, the solubility of Cu is exceedingly low (less than 1 atom/cm^3) at room temperature and thus Cu_i^+ concentration in the Si bulk will decrease soon after any diffusion process. The rate at which Cu_i^+ is maintained at high concentration in the bulk has been shown to be dependent on both the doping concentration (as discussed earlier) and the cooling rate after Cu in-diffusion. Rapid cooling/quenching of Si after Cu in-diffusion can effectively “freeze” Cu_i^+ in the bulk, with concentrations of Cu_i^+ as high as the doping concentration quenched interstitially in p-type Si [70], but a significantly lower threshold for Cu_i^+ quenching in n-type Si ($\sim 10^{13} \text{ cm}^{-3}$ [71]). The instability of Cu_i^+ at room temperature means it will preferentially out-diffuse towards the Si surface or form stable complexes to reach a thermodynamically stable state [72, 73]. First reported by Shabani *et al.* [74, 75], out-diffusion has been observed to occur over several days in p-type Si, depending on the wafer thickness and doping according to Equation 2.2. The presence of a charged dielectric or surface has also been shown to delay or enhance the out-diffusion process depending on the stored charge in the surface layer, with silicon oxide, SiO_x (positive stored charge) used to prevent Cu out-diffusion [74] and aluminium oxide, AlO_x (negative stored charge) shown to accelerate the process [76, 77]. On the other hand, out-diffusion of Cu in n-type Si was only observed after heating the Si above at least $400 \text{ }^\circ\text{C}$ [74], which is most likely related to the dissociation of Cu precipitates, which will be discussed more in Section 2.2.3.

The high diffusivity of Cu_i^+ also allows it to be easily getterred to doped n+, p+ and polysilicon regions in Si [28]. Based on a difference in Cu solubility between the base and heavily-doped regions [78, 79], Cu segregation to these regions is generally achieved during high temperature diffusions and anneals [80–82]. Inglese *et al.* [83] and Nampalli *et al.* [84] have also shown that high temperature firing with controlled slow cooling rates can effectively getter Cu to lightly-doped industrial n-type emitters.

2.2 Defect states of copper in silicon

Whilst Cu_i^+ has no known recombination activity in Si [85–87], it can form several complexes and defects that can significantly impact minority carrier lifetime in Si. These include substitutional Cu (Cu_s), as well as various complexes of substitutional Cu (Cu_sCu_i , Cu_sH_i and $\text{Cu}_s\text{Cu}_{3i}$) and Cu-silicide precipitates ($\eta''\text{-Cu}_3\text{Si}$), which are the predominant defect for Cu in Si and the focus for the work presented in this thesis.

2.2.1 Substitutional copper

At high temperatures, a small amount of Cu ($\leq 0.1\%$ of Cu solubility) will occupy substitutional lattice sites in Si, reacting with vacancies or Si self-interstitials to form Cu_s . Deep level transient spectroscopy (DLTS) measurements in various studies have subsequently associated Cu_s with two energy levels at $E_V + (0.2\text{--}0.23)$ eV and $E_V + (0.41\text{--}0.46)$ eV, with hole capture cross-sections of $3 \times 10^{-14} \text{ cm}^2$ and $1.5 \times 10^{-14} \text{ cm}^2$, respectively [69]. More recently, density functional theory (DFT) calculations by Sharan *et al.* determined three energy levels for Cu_s – a donor level (+/0) at $E_V + 0.2$ eV, an acceptor level (0/–) at $E_V + 0.54$ eV and a double-acceptor level (–/–2) at $E_V + 0.97$ eV, indicating an amphoteric nature to Cu_s [87]. In p-type Si, Cu_s is most stable in the +1 charge state to compensate hole conductivity, whilst Cu_s is most stable in the -2 charge state for n-type Si, where the Fermi level (E_F) is near the edge of the conduction band (CB), behaving as a compensation centre for n-type conductivity. At intermediate Fermi levels, Cu_s is either electrically inactive (stable neutral state for E_F from $E_V + 0.2$ eV to $E_V + 0.54$ eV) or stable in the -1 acceptor state (for E_F from $E_V + 0.54$ eV to $E_V + 0.97$ eV). The energy levels associated with Cu_s can be seen in Figure 2.2.

2.2.2 Point defects and complexes

Several complexes with substitutional Cu can also exist in Si. Due to the amphoteric nature of Cu_s mentioned earlier, complexes between Cu_s^- and Cu_i^+ are likely to form with increasing stability as the Fermi level shifts closer to the CB edge [87]. Thus, three energy levels have been calculated for Cu_sCu_i using DFT analysis - $E_V + 0.18$ eV, $E_V + 0.63$ eV and $E_V + 1.00$ eV [87]. The negative charge state associated with Cu_sCu_i in n-type Si means it is likely to attract more Cu_i^+ , leading to the formation of Cu complexes containing two or more Cu atoms, including the $\text{Cu}_s\text{Cu}_{3i}$ complex often associated with

an intense zero-phonon photoluminescence (PL) emission at 1.014 eV and an associated donor level at $E_V + (0.07-0.1)$ eV, known as the Cu_{PL} signal [88]. This signal is higher in Float Zone (FZ) Si compared to Czochralski (Cz) Si which has been attributed to the higher vacancy concentration in FZ-Si which allows for Cu_5 formation [89]. However, recent DFT calculations have indicated that Cu_5Cu_{3i} is unlikely to be the source of this emission [87], with some other complex of Cu_5 and Cu_i the most probable source [29]. Complexes of Cu_5 and hydrogen (H) are also possible, with recent experimental results based on Laplace-transform DLTS [90] revealing two peaks at $E_V + 0.1$ eV and $E_V + 0.49$ eV, and a double-acceptor level detected at $E_V + 0.81$ eV matching results obtained through DFT calculations (0.04 eV, 0.44 eV and 0.85 eV above the valence band [87]). It has also been observed that Cu complexes will decrease in concentration at a temperature of ~ 150 °C, converting such point defects into extended defects such as Cu precipitates [91]. These complexes are also included in the band diagram presented in Figure 2.2.

2.2.3 Copper precipitates

The most commonly-observed Cu-related defect is a silicide-based precipitate of Cu, with the dominant phase being η'' - Cu_3Si (η'' is the low T silicide phase [92]). Unlike Cu_5 and associated complexes, Cu-silicide precipitates generate a band of defect energy levels (E_t) located in the upper half of the Si bandgap that has been determined to be between $E_C - (0.15-0.2)$ eV and $E_C - (0.4-0.62)$ eV [36, 93–95], with an estimated electron capture cross-section of $\sigma_n = 3 \times 10^{-16}$ cm² [96]. The band of defect energy states associated with Cu precipitates are also included in the band diagram summarising the defect levels associated with different Cu states in Figure 2.2. The precipitate size, shape and distribution have been shown to depend on a variety of factors, including the concentration of interstitial Cu, base doping concentration, bulk microdefect (BMD) concentration and cooling rate [28]. Illumination is also known to be highly influential in Cu precipitate nucleation and growth (discussed more in Section 2.4 and Chapter 3). In samples with a high initial Cu concentration (10^{17} cm⁻³), it has been observed that for slow cooling rates (1-25 K/s), precipitate colonies form primarily in the near surface region as a result of agglomeration during Cu out-diffusion (known as ‘haze’), where precipitate growth nucleates around dislocation loops and stacking faults created by existing precipitates [97, 98]. On the other hand, quenching (> 100 K/s) results in a

supersaturation of Cu_i that leads to a homogeneous distribution of Cu precipitates in the Si bulk, with platelet-like precipitates (30-200 nm diameter) observed in p-type Si mostly along {111} planes in concentrations of up to 10^{13} cm^{-3} after rapid cooling [36, 97]. The molecular volume of η'' -Cu₃Si is significantly larger than Si (46 Å compared to 20 Å [99]), and this large lattice mismatch has been observed to result in the formation of lattice strain and stacking faults, which then provide a low nucleation barrier for further precipitate formation and growth [96]. As a result, larger precipitate colonies (0.5-80 μm) consisting of platelet-like precipitates surrounded by smaller spherical precipitates decorating stacking faults are often observed [97, 100]. The kinetics of Cu precipitate nucleation and growth are discussed in more detail in Section 2.4.

Partial dissolution of Cu precipitates formed at stacking faults have been observed during low temperature anneals between 360-460 °C [73, 101]. Despite theoretical dissolutions calculations predicting that 45 min at 560 °C should be sufficient to completely dissolve precipitates up to a radius of 420 nm [102], only partial dissolution of such heterogeneous precipitates have been observed in Cz-Si at temperatures of 360-560 °C which is theorised to be related to the existence of large precipitate colonies formed around stacking faults [73, 101]. However, rapid thermal annealing at 800 °C has been demonstrated to remove Cu precipitates from the bulk of Cz-Si as long as the cooling rate was slow enough to allow out-diffusion ($\sim 4 \text{ °C/min}$) [84, 95]. This indicates that the dissolution efficiency of precipitates is dependent on various factors, including the time, temperature, cooling rate and size of the precipitates [102].

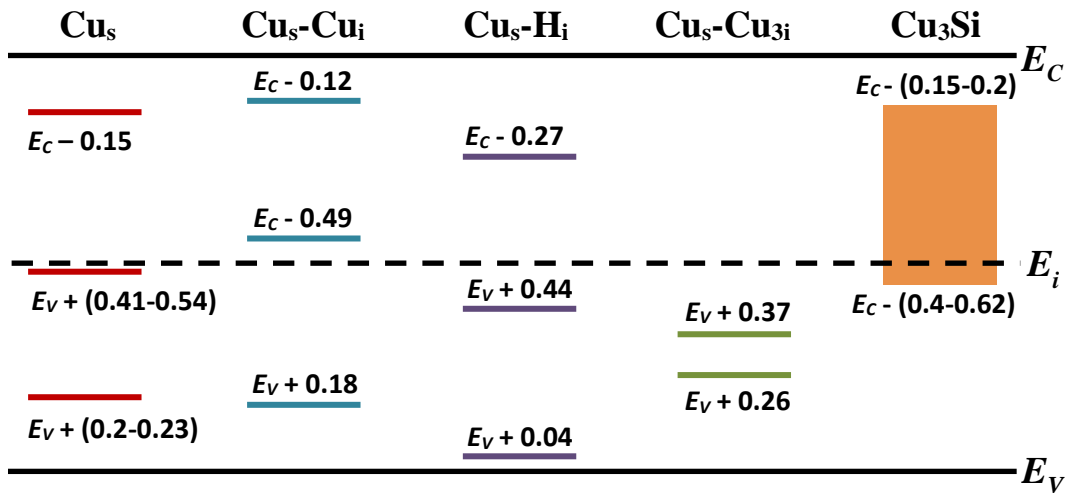


Figure 2.2: Summary of Cu defect energy levels in Si, including Cu_s and associated complexes, as well as the band of defect energy states identified for Cu₃Si precipitates.

2.3 Light-induced degradation in silicon

Light-induced degradation (LID) is the term given to the loss of minority carrier lifetime or cell efficiency in Si-based devices under excess carrier injection conditions during above bandgap illumination [60]. There are several different forms of LID that have been identified - boron-oxygen (BO-LID) [103], Cu-related (Cu-LID) [104, 105] and light and elevated-temperature induced degradation (LeTID) [106] – and all can potentially impact the efficiency of p-type Cz PERC cells in the field. This section briefly details the main features of each pertinent to the work presented in this thesis.

2.3.1 Boron-oxygen light-induced degradation

Observations of LID were first reported by Fischer and Pschunder in 1973, in which a 3-5% relative loss in cell efficiency was measured after 12 hours of illumination [107]. Subsequently, the occurrence of degradation was determined to be limited to Cz-Si with sufficiently high B and oxygen (O) concentrations, characterised by a rapid initial exponential decay (timescale of seconds to minutes) followed by a slower asymptotic decay, as seen in Figure 2.3 below. This two-stage decay is either attributed to two separate recombination centres – fast (FRC) and slow (SRC) [60, 103], or to a single defect with a multi-stage formation process [108–110].

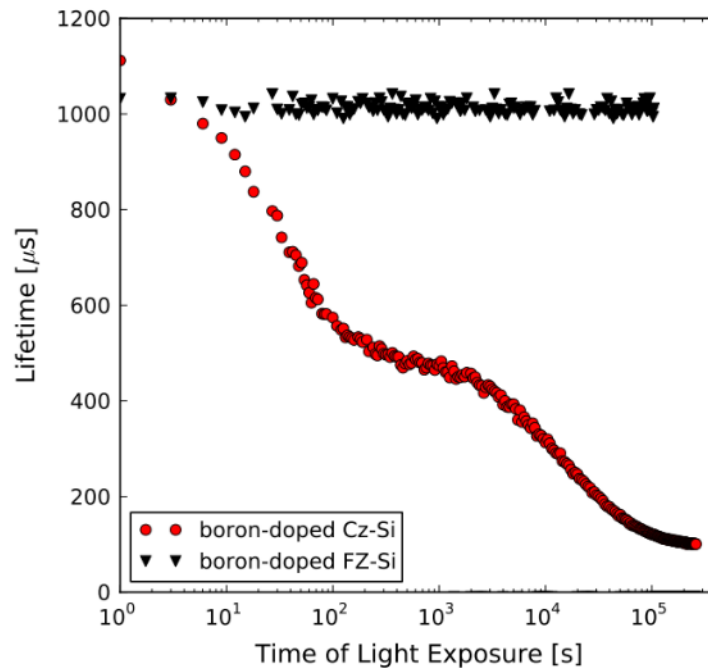


Figure 2.3: Effective minority carrier lifetime as a function of illumination duration for a B-doped Cz-Si and FZ-Si wafer with the same a-Si:H passivation layer (from [111]).

Although called LID, the only requirement for BO-LID is an injection of excess minority carriers [112], thus BO-LID can occur both under illumination (regardless of wavelength or penetration depth, so long as the photon energy exceeds the Si bandgap energy [113]), as well as in the dark during forward biasing. In fact, demonstration of BO-LID behaviour at temperatures above 300 K in the dark at zero bias by Bothe *et al.* indicated that the formation of BO-LID was dependent on the total minority carrier concentration, which is dependent on both the temperature and injection conditions [114], although a dependence on total hole concentration has also been suggested [115].

The density of light-induced defects during BO-LID is often presented as a normalised defect density (NDD), $N^*(t)$, which assumes the only light-activated defect impacting the effective lifetime of Si is the BO-LID defect (surface and other bulk recombination remains unaffected by illumination). By tracking the inverse effective lifetime under low injection conditions ($\Delta n/p_0 = 0.1$), $N^*(t)$ can be fitted by [116]:

$$N^*(t) = N_{sat}^* [1 - \exp(-R_{def}t)] = \left(\frac{1}{\tau_\infty} - \frac{1}{\tau_0} \right) \left[1 - \exp\left(-\frac{t}{\tau_{def}}\right) \right] \quad (2.4)$$

where N_{sat}^* is the saturated NDD after long periods of illumination (determined by the difference between the saturated inverse lifetime, $1/\tau_\infty$, and initial inverse lifetime, $1/\tau_0$), R_{def} is the degradation rate and τ_{def} is the corresponding degradation time constant. Equation 2.4 can be applied separately to both the fast and slow decays observed during BO-LID. Although the degradation rate of the SRC (R_{SRC}) was thought to be illumination wavelength and intensity independent above 1 mW.cm^{-2} [113], Hamer *et al.* recently observed an increase in R_{SRC} as a function of increasing illumination intensity in the range $44\text{-}3550 \text{ mW.cm}^{-2}$ [115]. Additionally, R_{SRC} was previously thought to also be proportional to B concentration $[B_s]^2$ [117], yet studies on both B-doped and phosphorus (P)-doped compensated p-type Si have indicated that R_{SRC} may instead be dependent on either the equilibrium hole concentration, p_0^2 [118], or the total hole concentration, based on the illumination intensity-dependence observed by Hamer *et al.* [115]. The activation energy for BO-LID can be determined from the following Arrhenius relationship [60]:

$$R_{def}(T) = \kappa_0 \exp\left(-\frac{E_{def}}{k_B T}\right) \quad (2.5)$$

In clean Cz-Si, the activation energy for the FRC of 0.17-0.25 eV was obtained, along with the activation energy of 0.3-0.5 eV for the SRC [119–121]. Whilst no dependency on B or O concentration was observed, the pre-exponential term κ_0 was found to increase as a function of B concentration [103]. However, full dissociation of both the FRC and SRC can be achieved after annealing at 200 °C both in the dark [107] and under illumination [122], although subsequent illumination results in reformation of the defect, classing the BO defect as a metastable defect [60].

In terms of recombination activity, lifetime spectroscopy techniques (described in more detail in Chapter 3 and by Rein [123]) have been used to estimate a deep defect level (SRC) at $E_C - 0.41$ eV with an associated capture cross-section ratio, k , of 10 ± 1 [124], corresponding with DLTS measurements which indicate a minority carrier trap at the same energy level [125]. Also, defect levels associated with the FRC have been identified in the range $E_V + (0.27-0.77)$ eV with significantly higher but varying k values in the range 50-100 [103, 126]. However, the wide range of sample and measurement conditions, as well as a lack of consensus on the number of defects responsible for the BO-LID decay behaviour (single vs two defect models), have resulted in vastly different results between studies (see reviews by Nampalli [127] and Lindroos [60] for a more comprehensive overview of previous studies characterising the recombination activity of the BO defect).

The impact of BO-LID can be eliminated in several ways. Minimising B and O concentration in the Si bulk has proven effective, with no LID measured on clean B-doped FZ-Si or Cz-Si with an O concentration below 1 ppm [116, 128]. Replacing B with gallium (Ga) as a p-type substrate or switching to a P-doped n-type Si substrate also offer potential alternatives to B-doped Cz-Si [128, 129]. Alternatively, simultaneous illumination and annealing at temperatures of 65-210 °C (known as regeneration) can permanently deactivate the BO defect [122, 130, 131]. The regeneration time can vary from 10 s to several hours depending on a variety of factors, including illumination intensity, temperature and H content in the Si [131, 132]. Hydrogen is suspected to be the species responsible for deactivating BO defects (the H being introduced during high temperature firing of plasma enhanced chemical vapour deposition (PECVD) silicon nitride, SiN_x , dielectrics on Si solar cells). In the work presented in this thesis, BO-LID is accounted for either with the use of FZ-Si or with

annealing conditions that minimise BO-LID without severely impacting analysis of Cu-related degradation.

2.3.2 Copper-related light-induced degradation

Light-induced degradation of Cu-contaminated Si was observed in early experiments performed by Henley *et al.* [104] and Tarasov *et al.* in 1998 [133], who observed a degradation of minority carrier diffusion length in 9-20 $\Omega\cdot\text{cm}$ p-type Cz-Si. Similar observations in B-doped FZ-Si [42, 105], n-type Si [42] and Ga-doped Si [43] confirmed the occurrence of such degradation regardless of B or O concentration. The existence of LID in intentionally Cu-contaminated Ga-doped Si (i.e. – absent of any BO-LID effects) confirmed the role of Cu in this degradation, leading to the definition of this mechanism as Cu-LID.

Cu-LID has been shown to rely on the presence of Cu_i^+ in the bulk prior to illumination, with TID measurements demonstrating a subsequent reduction in Cu_i during illumination [134]. In B-doped FZ-Si, P-doped FZ-Si and Ga-doped Cz-Si, Cu-LID is observed as a single exponential decay that can similarly be fitted according to Equation 2.4 [42, 43, 105], which can also be seen in the degradation curves in Figure 2.4. However, in B-doped Cz-Si the degradation consists of a three stage decay – a fast initial decay, followed by a second slow decay and a final much slower decay [135]. The degradation rate of Cu-LID has since been observed to increase with increasing temperature [135], illumination intensity [105, 136], Cu_i concentration [42, 45] and O/BMD concentration [137]. Conversely, the degradation rate decreases with increasing doping concentration for B and Ga-doped Cz-Si [43, 135], most likely due to trapping of Cu_i via donor-acceptor pairing as discussed earlier in Section 2.1.

The activation energy for Cu-LID has also been demonstrated to be dependent on the doping concentration for B-doped Si, with the activation energy for the slow decay in B-doped Cz-Si due to Cu-LID measured as 0.323 ± 0.09 eV in 3.4–3.9 $\Omega\cdot\text{cm}$ and 0.146 ± 0.025 eV in 18–24 $\Omega\cdot\text{cm}$ wafers, respectively [135]. As the doping concentration is decreased, the activation energy approaches the intrinsic energy for Cu_i^+ diffusion in Si (0.18 ± 0.01 eV [66]). Thus, the activation of Cu-LID may be related to the diffusion of Cu_i^+ in Si, thus an increase in donor-acceptor pairing is reflected in the increasing activation energy with doping concentration. Unlike BO-LID, only partial recovery of

Cu-LID has been observed in Cz-Si and FZ-Si after annealing at 200 °C, and only if the concentration of Cu_i^+ is below 10^{14} cm^{-3} [138], whilst no recovery has been observed in Si with higher Cu_i^+ concentrations [see Figure 2.4 (b)]. However, high temperature rapid-thermal annealing (800-900 °C) can result in full defect dissociation [84, 95, 134].

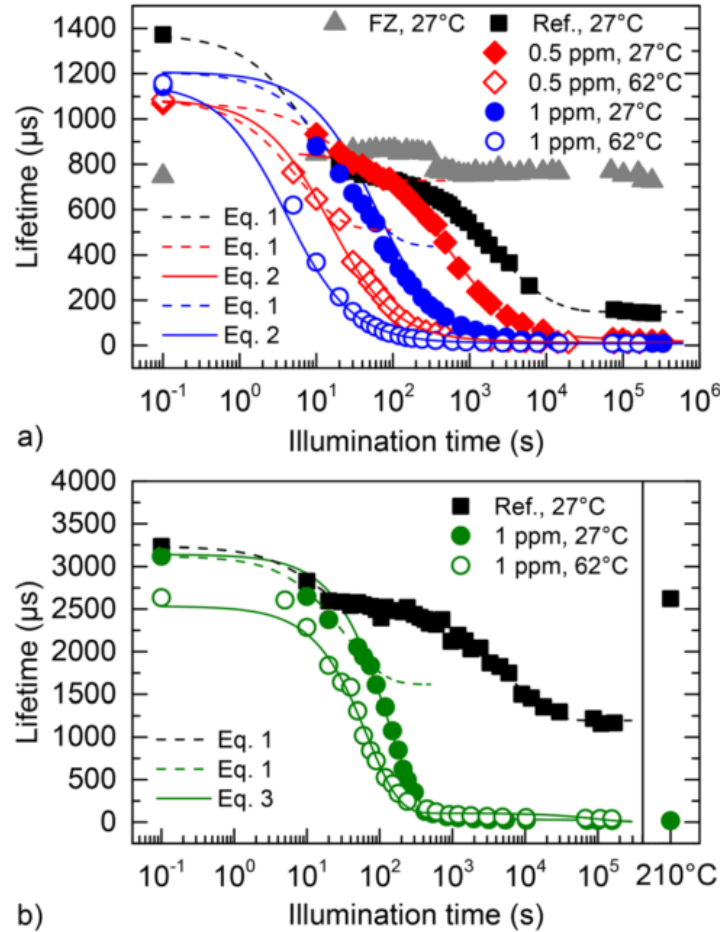


Figure 2.4: Effective minority carrier lifetime as a function of illumination duration and temperature (a) for clean and Cu-contaminated Cz- and FZ-Si, and (b) clean and Cu-contaminated Cz-Si with a final dark anneal at 210 °C to remove BO-LID (from [135]).

Early work attributed Cu-LID to the dissociation of Cu_5Cu_i pairs and subsequent formation of recombination-active Cu_5 in Si [104, 105, 139]. However, this does not adequately explain the observed decrease in Cu_i^+ during Cu-LID defect formation [134]. Moreover, recent analysis of Cu-LID defects in Si by Inglese *et al.* using lifetime spectroscopy (see Chapter 3 for more details) identified two defect levels – one shallow level at $E_C - (0.1-0.2) \text{ eV}$ and a deep level at $E_C - (0.48-0.62) \text{ eV}$ with an associated k value of 1.7-2.6 [95]. These results could not be adequately explained with the acceptor-

like behaviour of Cu_s , which would impose a large majority carrier capture cross-section (i.e. $-k \ll 1$). Instead, the observed recombination activity of the Cu-LID defect more closely aligns with that of Cu precipitates (described previously in Section 2.2.3), with the two identified defect levels in Si experiencing Cu-LID representative of the edges of the band of defect energy states generated by extended Cu precipitates in the Si bulk. The Cu-LID defect recombination parameters identified by Inglese *et al.* also correspond with the recombination parameters determined for thermally-generated Cu precipitates as identified by Macdonald *et al.* [94], thus strengthening the hypothesis of Cu precipitates as the defect responsible for Cu-LID in Si. The exact kinetics of Cu precipitate formation and growth and the associated influence of illumination are discussed further in Section 2.4. The different characteristics of BO-LID and Cu-LID behaviour are summarised in Table 2.1.

Table 2.1: Summary of the behaviours of BO-LID and Cu-LID in Si (adapted from [60]).

| BO-LID | Ref | Cu-LID | Ref |
|----------------------------------|-----------------|---|------------------------|
| Only occurs in B-doped Cz-Si | [128, 129] | Occurs in B/P-doped Cz-Si, FZ-Si and Ga-doped Si | [42, 43] |
| Rate increases with T | [103] | Rate increases with T | [135] |
| Rate increases with Δn | [115] | Rate increases with Δn | [105, 136] |
| Two stage degradation | [113, 114, 140] | Single exponential decay Three-stage degradation | [42, 43, 105] [135] |
| Full recovery at 200 °C | [107] | Minimal recovery at 200 °C | [135, 141] |
| $R_{deg} \propto p_0^2$ or p^2 | [115, 118] | R_{deg} decreases with N_A | [43, 135] |
| E_{def} independent of N_A | [103] | E_{def} increases with N_A | [135] |

2.3.3 Light and elevated temperature induced degradation

Initially identified by Ramspeck *et al.* [106], a firing-activated form of LID has recently been the topic of increasing research, especially since it seems to primarily impact Si cells employing PERC structures such as that examined in this work [142]. Since elevated temperatures of ≥ 75 °C are required to observe such a defect, it has been termed LeTID. The degradation itself occurs at a significantly slower rate compared to BO-LID and Cu-LID, with up to 100 hrs required to observe complete degradation at 75 °C, followed by a subsequent recovery after 700 hrs [143, 144]. Recent studies have

shown that increasing the firing temperature results in an increasing degradation extent, with no degradation observed in unfired samples [145, 146]. Modulation of LeTID by manipulating the H content of $\text{SiN}_x/\text{AlO}_x$ films [147, 148] indicates H introduction during firing as primary possible candidate for the cause of LeTID. Although initially only seen in multicrystalline (mc-Si), similar behaviour has also been observed in passivated p-type Cz-Si (as shown in Figure 2.5 below [149, 150]), as well as passivated n-type Si [151, 152]. Thus, whilst not the focus of the work presented in this thesis, its impact on the degradation analysis performed on p-type PERC and n-type PERT cells in Chapter 6 should not be ignored.

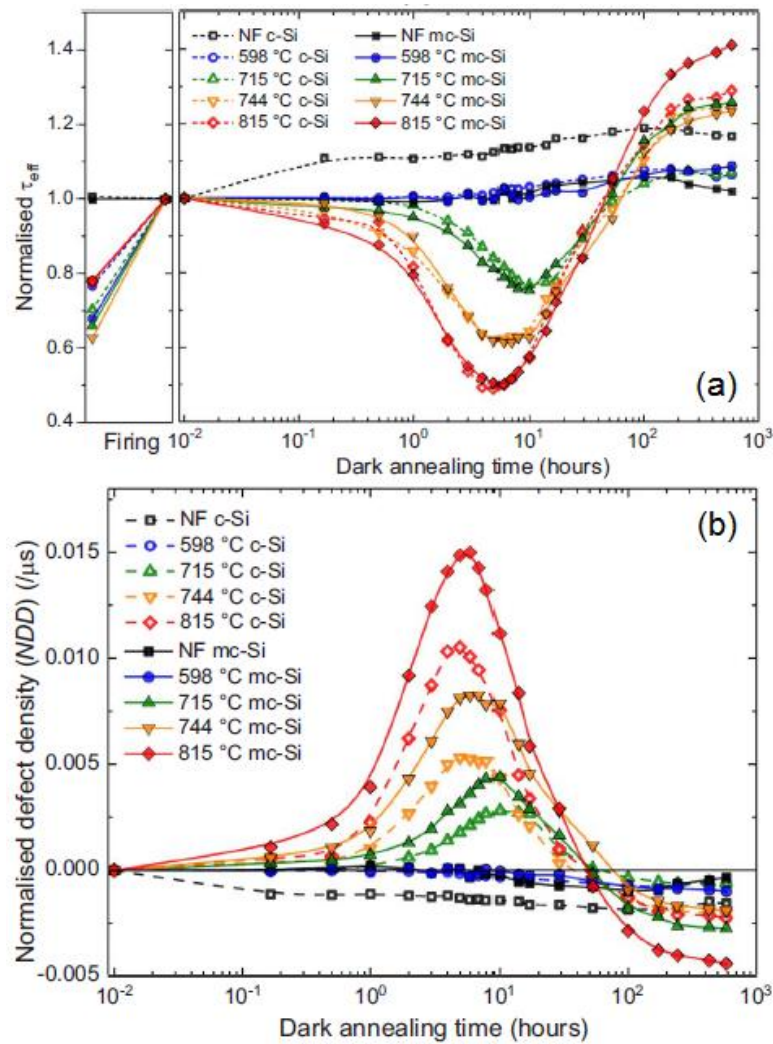


Figure 2.5: (a) Normalised effective lifetime vs. dark annealing duration at 175 °C for fired (598 °C to 815 °C) and not fired (NF) Cz-Si (solid lines) and mc-Si (dashed lines), and (b) Corresponding NDD as a function of dark annealing time (from [149]).

2.4 Copper precipitate formation kinetics

As mentioned in previous sections, Cu precipitates (namely η'' -Cu₃Si) are the most common Cu-related defect, both in the dark and under illumination. The following section provides a more detailed examination of the mechanisms of Cu precipitate nucleation and growth in Si as detailed in previous models of Cu precipitation [37, 153].

2.4.1 Precipitate nucleation

Nucleation of precipitates requires supersaturation of Cu_i⁺ (i.e. – dissolved concentration above the solid solubility) to overcome the nucleation barrier defined by the thermodynamics of phase transformation [28]. Under supersaturation conditions, the chemical driving force for forming a precipitate of n atoms can be defined by a Gibbs free energy change [154, 155]:

$$\Delta G_n = -nk_B T \cdot \ln\left(\frac{C_{Cu_i}}{S_{Cu}}\right) + \Delta G_n^{ex} \quad (2.6)$$

where C_{Cu_i} is the total Cu_i⁺ concentration (taking into account Cu-B pairing), S_{Cu} is the equilibrium Cu solubility and ΔG_n^{ex} is the excess Gibbs free energy change given by:

$$\Delta G_n^{ex} = V_n \Delta G_S + A_n \gamma \quad (2.7)$$

ΔG_n^{ex} takes into account forces opposing precipitate formation, including energy changes related to strain induced by precipitates (ΔG_S), the interfacial energy (γ) between the precipitate surface area (A_n) and silicon matrix and the presence of pre-existing nucleation sites (such as grain boundaries, dislocation loops and O precipitates). As previously discussed in Section 2.2.3, the cooling rate affects the nucleation of Cu precipitates in Si. Quenching of Si results in immediate supersaturation (high C_{Cu_i} + low S_{Cu}) and subsequent homogenous platelet-like precipitate formation in the bulk [36, 97, 100], whereas slow cooling will result in a slower build up to supersaturation and precipitates will initially form at sites with a lower nucleation barrier (i.e. – lattice defects, where ΔG_n^{ex} is low). This nucleation behaviour is also reflected in the impact of doping and BMD concentration on Cu-LID degradation rates (see Section 2.3.2).

Within the classical theory of nucleation, the formation of a precipitate of size n involves a reaction between an existing precipitate cluster and a Cu_i^+ atom, which is considered an $n = 1$ precipitate. The nucleation rate for a precipitate of size n , I_n , is thus given by [153, 156]:

$$I_n = g_n f_n - d_{n+1} f_{n+1} \quad (2.8)$$

where f_n is the density of n -sized precipitates and g_n and d_n are the growth and dissolution rates, respectively. Growth and dissolution are both a product of A_n , Cu_i^+ concentration at the precipitate-Si interface and the diffusion-limited surface reaction rate, k_n :

$$k_n = \frac{D_{\text{Cu}}}{\delta} \exp\left(\frac{\max(\Delta G_{n+1} - \Delta G_n + \Delta G_{act}, \Delta G_{act})}{k_B T}\right) \quad (2.9)$$

where D_{Cu} is the Cu_i^+ diffusion coefficient, δ is the length of a single diffusion step and ΔG_{act} is the activation barrier associated with incorporating a Cu atom into the existing precipitate.

It is important to note that according to classical nucleation theory, only precipitates greater than a critical size, r_{cr} , will grow (since $\Delta G_{n+1} - \Delta G_n < 0$ beyond the critical size), while those smaller than a critical size will tend to reduce in size [156]. The relationship between r_{cr} and ΔG_s is given as [157]:

$$r_{cr} \propto \frac{\gamma}{\Delta G_s} \propto \frac{\gamma}{kT \ln\left(\frac{C_{\text{Cu}_i}}{C_{\text{Cu}_{eq}}}\right)} \quad (2.9)$$

where $C_{\text{Cu}_{eq}}$ is the equilibrium Cu concentration at the precipitate interface. Since ΔG_s is proportional to the supersaturation of Cu_i at the interface, which increases with decreasing temperature, the critical size subsequently decreases with decreasing temperature [156]. This can result in time-dependent nucleation rates, with precipitates changing from postcritical at one temperature to subcritical at higher temperatures. Once a sufficient density of precipitates exists to getter the remaining Cu_i^+ and ΔG_n can no longer overcome the nucleation barrier, the creation of new precipitates will cease [28]. As a result, faster nucleation rates (for example, after quenching as well as under illumination) generally result in a higher density of smaller precipitates, whereas a lower density of larger precipitates is obtained with slower cooling/nucleation rates.

2.4.2 Precipitate growth

The kinetics of Cu precipitation are complicated by electrostatic interactions between growing Cu precipitates and Cu_i^+ within the Si lattice. Whilst Cu_i^+ is known to be positively charged, it has been observed in DLTS measurements that Cu precipitates are also positively charged in p-type Si [36]. However, Cu precipitates were determined to be neutral or negatively-charged in n-type Si, particularly when the Fermi level is above $E_C - 0.2$ eV [36]. This critical energy level coincides with the electroneutrality level for Cu precipitates, which results in their observed amphoteric nature (i.e. - both positive and negative charge states possible depending on the position of the Fermi level). Subsequently, Flink *et al.* demonstrated that precipitation in p-type Si is kinetically favoured over out-diffusion only when the concentration of Cu_i^+ is sufficiently high to raise the Fermi level above the neutrality level ($C_{\text{Cu}_i, \text{crit}} = N_A + 10^{16} \text{ cm}^{-3}$ [37]). Various studies have confirmed that Cu precipitates form in n-type Si with much lower Cu_i^+ concentrations compared to p-type Si [86, 104], which is consistent with the electrostatic model for Cu precipitate growth proposed by Flink *et al.* [37]. Similar behaviour has also been observed in Cu-LID studies, which identified a dependence of the degradation rate on the position of the electron quasi-Fermi level (E_{Fn}) in relation to the neutrality level for Cu precipitates [136].

Vahlman *et al.* recently developed a model for Cu precipitation under illumination with the objective of replicating lifetime degradation observations during Cu-LID [153, 158], employing this notion of a charged precipitate. An example of the impact of illumination on the precipitate-Si interface is illustrated in Figure 2.6.

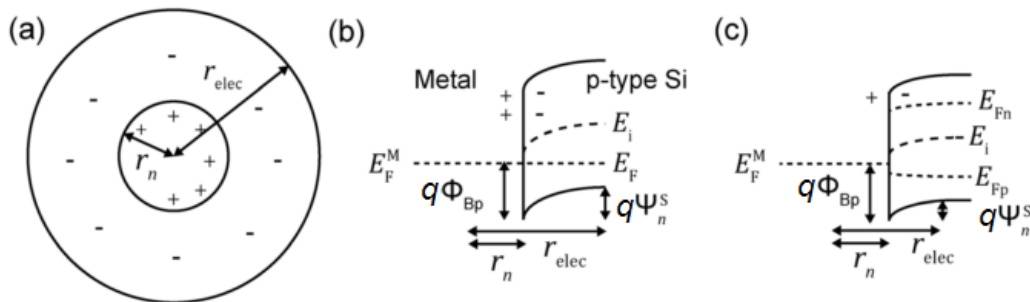


Figure 2.6: (a) Model of a spherical charged precipitate in the Si lattice and the corresponding energy diagram (b) in thermal equilibrium and (c) under illumination (from [153]).

In Figure 2.6, a spherical precipitate of radius r_n forms a Schottky junction at the precipitate-Si interface with a barrier height $q\Phi_{Bp}$ (q is the elementary charge). This generates an electric field (otherwise known as a space charge region, SCR) extending out with a radius of r_{elec} with a corresponding built-in voltage $q\Psi_n^S$ associated with the downward band bending at the interface (due to alignment of the Fermi levels). Thus, an electrostatic barrier for Cu_i^+ is present in the dark at RT [153]. Under illumination, the separation of the Fermi level into E_{Fn} and E_{Fp} leads to a reduction in $q\Psi_n^S$, which increases the interface concentration of Cu_i^+ and thus the precipitation rate. This can be determined quantitatively using a Schottky junction model for spherical charged precipitates developed by Plekhanov and Tan [159].

In terms of the growth rate of precipitates, the growth (g_n) and dissolution (d_n) rates of the precipitates are defined using a kinetic precipitation model coupled with the electrostatic model discussed earlier (see Vahlman *et al.* for a more detailed description of this model [153]). The concentration of Cu_i^+ around a precipitate is determined by considering both diffusion gradients and drift due to the electric field around an existing Cu precipitate. The change in precipitate size with time is subsequently determined by the expression:

$$\frac{\partial n}{\partial t} = g_n - d_{n+1} = A_{elec} k_{eff} [C_{Cu_i}(r_{elec}) - S_n^*] \quad (2.10)$$

where $A_{elec} = 4\pi r_{elec}^2$ is the surface area of the volume affected by the electric field, k_{eff} is the effective reaction rate at the precipitate interface, S_n^* is the effective interface solubility and $C_{Cu_i}(r_{elec})$ is the concentration of Cu_i^+ at the electric field boundary. In this expression, the kinetics of precipitate growth are significantly affected by the illumination conditions due to the exponential relationship between the effective reaction rate and the built-in voltage of the Schottky junction:

$$k_{eff} \propto \exp\left(-\frac{q\Psi_n^S}{k_B T}\right) \quad (2.11)$$

The growth and dissolution rates can also be expressed as functions of the bulk Cu_i^+ concentration ($C_{Cu_i}^\infty$) and S_n^* :

$$g_n = \lambda_{kin} D_{Cu} C_{Cu_i}^\infty \quad d_n = \lambda_{kin} D_{Cu} S_n^* \quad (2.12)$$

In the expressions above, λ_{kin} is the kinetic growth factor, defined as:

$$\lambda_{kin} \equiv \frac{A_{elec}}{r_{elec} + \frac{D_{Cu}}{k_{eff}}} \quad (2.13)$$

The dependence of λ_{kin} on k_{eff} (and thus the built in potential of the Schottky junction) results in a 5 order of magnitude increase in the growth factor under carrier injection with $\Delta n = 5 \times 10^{15} \text{ cm}^{-3}$ (corresponding to approximately ~ 1 Sun [153]).

The Schottky model mentioned earlier can also be used to predict the recombination activity of Cu precipitates in Si, based on the theory of thermionic emission of charge carriers across the Schottky junction formed at the precipitate-Si interface [159, 160]. Thermionic emission currents for electrons and holes are calculated using the following expressions:

$$J_e^S = J_e^{sat} \left(\exp \left(\frac{E_{Fn}^S - E_F^M}{k_B T} \right) - 1 \right) \quad (2.14)$$

$$J_h^S = -J_h^{sat} \left(\exp \left(\frac{E_F^M - E_{Fp}^S}{k_B T} \right) - 1 \right) \quad (2.15)$$

where J_e^S and J_h^S are the saturation current densities for electrons and holes at the interface, respectively. At the precipitate-Si interface, electrons and holes recombine almost instantaneously, resulting in the following boundary condition [153]:

$$J_e^S = -J_h^S \quad (2.16)$$

At a given generation rate, G , and N_A , the recombination rate due to a single precipitate size is determined by:

$$R_{prec}(n, G, N_A, T) = f_n \times \frac{4\pi r_n^2 \times J_e^S(n, G, N_A, T)}{q} \quad (2.17)$$

where f_n is the density of precipitates of size n . A parameterisation introduced by Kwopil *et al.* allows for a quick determination of injection-dependent lifetime by determining the dependence of the precipitate capture-cross section (σ_{prec}) on the doping, injection level and precipitate radius [160]. The corresponding precipitate-related lifetime can thus be calculated with the equation:

$$\tau_{prec} = \frac{1}{N_{prec}(r_{prec})\sigma_{prec}(\Delta n, r_{prec}, N_d)v_{th}} \quad (2.18)$$

Where N_{prec} the density of precipitates with radius r_{prec} and v_{th} is the thermal velocity (10^7 cm/s). Combining the Schottky model with the kinetic precipitation model described above, Vahlman *et al.* were able to adequately simulate the degradation of lifetime as a result of Cu-LID by simulating Cu precipitation under illumination [158]. An example of the agreement between experimental and modelled Cu-LID can be seen in Figure 2.7.

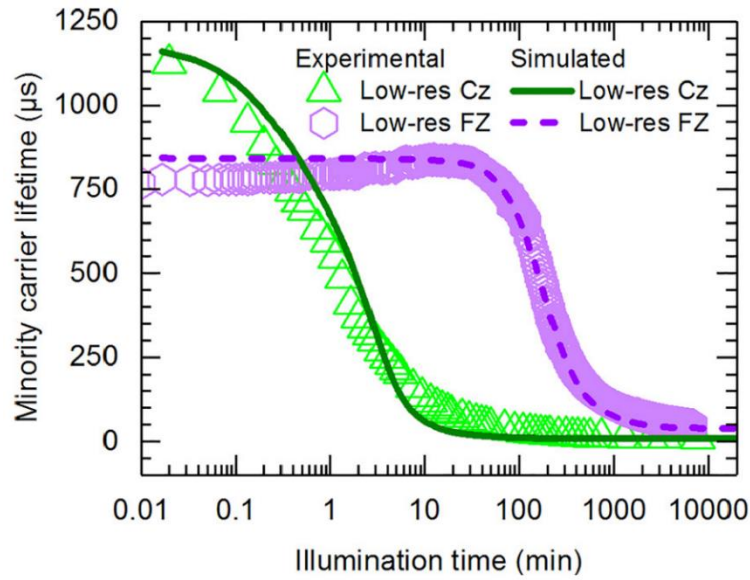


Figure 2.7: Experimental Cu-LID curves in low-res FZ-Si and low-res Cz-Si illuminated under 0.65 Suns at RT (from [158]).

Whilst good agreement was obtained between experimental and simulated results, the assumption of spherical precipitates has been acknowledged as a limitation of this model in its current form, since η'' - Cu_3Si are more likely to form platelet-like precipitates in Si (as discussed in Section 2.2.3). This model limitation is discussed further in Chapter 3, where the above-described model was used to predict precipitate size and density from recombination activity.

2.5 Chapter Summary

The fundamental properties of Cu in Si have been reviewed in this chapter. The diffusivity and solubility of interstitial Cu was discussed, along with the various states

in which Cu can occupy. These include substitutional Cu and associated point defect complexes, and Cu silicide precipitates, which are the most likely Cu-related defect to form due to Cu penetration into Si from plated contacts. Also detailed is the mechanism of Cu-LID, which is known to accelerate the formation of Cu precipitates. The different degradation and recombination behaviours between the main forms of LID (BO-LID, Cu-LID and LeTID) were examined in order to distinguish Cu-LID from other forms of LID that may be encountered during thermal stability testing under illumination. Finally, the kinetics of precipitate nucleation and growth were detailed to better understand the factors that influence the density and size of Cu precipitates that form in Si and the relationship between precipitate size/density and associated recombination activity.

Chapter 3 Lifetime Spectroscopy Analysis of Copper in Silicon

The characterisation of Cu precipitates and their recombination activity in Si has been investigated in numerous studies as previously discussed in Chapter 2. However, there is still uncertainty in literature as to the specific recombination properties of Cu precipitates, since variations in the size and distribution of precipitates can have a large impact on the defect properties. Lifetime spectroscopy (LS) has been employed in recent years to characterise the recombination behaviour of Cu precipitates formed during extended illumination (Cu-LID). In this chapter, advanced lifetime spectroscopy analysis is applied to the characterisation of Cu precipitates in Si. Defect parameters for Cu precipitates (capture cross-section ratio, k , and defect energy level, E_t) in p-type Si under different formation conditions are characterised with TIDLS and standard Shockley-Read-Hall (SRH) model fitting, whilst information about the size and distribution of Cu precipitates are obtained using a recombination model for metallic precipitates.

3.1 Defect Parameterisation using Lifetime Spectroscopy

3.1.1 Recombination mechanisms in silicon

There are three main components of recombination that are relevant to the LS analysis performed in this experimental work – intrinsic recombination (τ_i), which accounts for both radiative (τ_{rad}) and Auger recombination (τ_{Auger}), bulk defect recombination, often referred to as SRH recombination (τ_{SRH}), which forms the basis for LS analysis of bulk defects in Si, and surface recombination (τ_s). Rein provides an extensive overview and discussion of all these mechanisms [123], thus they will not be discussed in depth in this chapter. The following subsections will briefly introduce and explain each of these recombination components that need to be accounted for when extracting defect properties through LS and SRH defect modelling.

3.1.1.1 Radiative recombination

Radiative recombination is defined by the direct extinction of generated electron-hole pairs, whereby a conduction band electron relaxes to the valence band, resulting in the release of a photon with energy approximately equal to that of the band gap of the material (i.e., the reverse process to photogeneration). The net recombination rate for radiative recombination is dependent on the density of free electrons and holes (n and p , respectively), and can be calculated using the expression:

$$U_{rad} = B(np - n_i^2) \quad (3.1)$$

where B is the radiative recombination coefficient ($4.7 \times 10^{-15} \text{ cm}^3 \text{ s}^{-1}$ at 300 K for Si [161]) and n_i is the intrinsic carrier concentration ($9.65 \times 10^9 \text{ cm}^{-3}$ for Si at 300 K [162]). The probability of radiative recombination occurring is reflected in the value of B . In direct semiconductors such as gallium arsenide (GaAs), conservation of energy and momentum is achieved solely with the release of a photon, whilst both a photon and phonon are required for energy and momentum conservation, respectively, in indirect semiconductors like Si. The involvement of an additional particle in the process inherently reduces the probability of radiative recombination occurring in Si.

A general expression for the radiative component of effective lifetime is subsequently provided by [123, 163]:

$$\frac{1}{\tau_{rad}} = B(n_0 + p_0 + \Delta n) \quad (3.2)$$

In this equation, n_0 and p_0 are the equilibrium electron and hole concentrations and Δn is the density of excess carriers. From this expression, it is clear that the radiative lifetime component is dependent on the bulk doping concentration at low injection levels, whilst it is more strongly dependent on Δn at higher injection [123, 163]. However as mentioned earlier, its impact is minimal compared to other recombination mechanisms in Si due to the indirect bandgap nature of the material. Nevertheless, it has been noticed that radiative recombination in Si can increase with temperature [163], consequently it is still accounted for in this work for completeness.

3.1.1.2 Auger Recombination

Auger recombination involves a three-particle interaction whereby energy released during the recombination of an electron-hole pair is transferred to a third carrier, resulting in the release of energy as phonons (known as thermalisation [123]). The third carrier can either be a hole in the valence band (*ehh* process) or an electron in the conduction band (*eeh* process), with the recombination rate proportional to the product of the concentrations of particles involved in the three-particle reaction. The net recombination rate is thus defined by the expression:

$$U_{Aug} = U_{eeh} + U_{ehh} = C_n(n^2p - n_0^2p_0) + C_p(np^2 - n_0p_0^2) \quad (3.3)$$

where C_n and C_p are the Auger coefficients of the *eeh* and *ehh* processes, respectively, and vary depending on the temperature, dopant type and dopant concentration [164, 165]. The most commonly quoted values for these coefficients in Si were determined by Dziewior and Schmidt to be $C_n = 2.8 \times 10^{-31} \text{ cm}^6\text{s}^{-1}$ and $C_p = 9.9 \times 10^{-32} \text{ cm}^6\text{s}^{-1}$ [165]. The Auger-related component of effective lifetime for p-type and n-type Si can subsequently be determined by the following equations:

$$\frac{1}{\tau_{Auger}} = C_p p^2 + C_n p \Delta n \quad \text{for p - type Si} \quad (3.4)$$

$$\frac{1}{\tau_{Auger}} = C_n n^2 + C_p n \Delta n \quad \text{for n - type Si} \quad (3.5)$$

The inverse-quadratic dependence of Auger lifetime on carrier density results in a dominance of Auger recombination over radiative recombination at high injection levels as seen in Figure 3.1 [123].

Although traditionally modelled as interactions between non-interacting quasi-free particles, aside from the case of highly-doped Si ($N_A > 1 \times 10^{18} \text{ cm}^{-3}$) [165], Auger recombination is enhanced by coulombic interactions between electrons and holes [166]. Thus, both the coulombic enhancement and temperature-dependence of intrinsic recombination mechanisms were accounted for in this study. For the analysis presented in this chapter, the general parameterization given by Richter *et al.* was used [167]. The expression for intrinsic recombination at room temperature (25 °C) provided by this model is given by [167]:

$$\tau_{int} = \frac{\Delta n}{(np - n_i^2)(2.5 \times 10^{-31} g_{eeh} n_0 + 8.5 \times 10^{-32} g_{ehh} p_0 + 3 \times 10^{-29} \Delta n^{0.92} + B)} \quad (3.6)$$

where B is the Coulomb-enhanced, temperature-dependent radiative recombination coefficient using the parameterisation provided by Altermatt *et al.* [168]. The terms g_{eeh} and g_{ehh} are carrier density-dependent enhancement factors for the two types of three-carrier interactions involved in Auger recombination, reflecting the increased probability that the carriers involved in recombination will be in the same place [123, 167]. These enhancement factors are given by:

$$g_{eeh}(n_0) = 1 + 13 \left\{ 1 - \tanh \left[\left(\frac{n_0}{N_{0,eeh}} \right)^{0.66} \right] \right\} \quad (3.7)$$

$$g_{ehh}(p_0) = 1 + 7.5 \left\{ 1 - \tanh \left[\left(\frac{p_0}{N_{0,ehh}} \right)^{0.63} \right] \right\} \quad (3.8)$$

where $N_{0,eeh} = 3.3 \times 10^{17} \text{ cm}^{-3}$ and $N_{0,ehh} = 7.0 \times 10^{17} \text{ cm}^{-3}$. Whilst the temperature-dependence of Auger recombination has not been examined in detail, Wang and Macdonald determined a constant Auger coefficient for temperatures up to 200 °C [169], which covers the temperature range examined in this work. Hence, the Richter model was assumed valid across the measured temperature range used for all TIDLs analysis presented in this thesis.

3.1.1.3 Bulk defect (SRH) recombination

First developed by Shockley and Read [170] and Hall [171] in 1952, SRH recombination describes the recombination activity due to defects in Si (such as impurities or crystallographic defects) that introduce electronic states within the Si bandgap that facilitate the relaxation of conduction band electrons, with excess energy released as phonons to the Si lattice [172]. The recombination process itself is described as a two-step process in classical SRH theory, with one of two scenarios occurring:

- 1) A conduction band electron and a valence band hole are captured by the defect level and recombine at the defect level.
- 2) A conduction band electron relaxes to the defect energy level before relaxing to the valence band to recombine with a free hole in the valence band.

The recombination activity of the defect level depends on temperature, location of the Fermi level and defect energy level, as well as the capture cross-sections of the defect and the concentration of the defect [173]. Assuming the states are non-interacting and the defect capture and relaxation times of carriers are non-limiting, the recombination rate of a single defect state is given by [170]:

$$U_{SRH} = \frac{np - n_i^2}{[\tau_{n0}(p + p_1) + \tau_{p0}(n + n_1)]} \quad (3.9)$$

with τ_{n0} and τ_{p0} defined as the electron and hole capture time constants, defined as $\tau_{n0} = (N_t v_{th} \sigma_n)^{-1}$ and $\tau_{p0} = (N_t v_{th} \sigma_p)^{-1}$, respectively, where σ_n and σ_p are the capture cross-sections of electrons and holes and N_t is the defect density. In Equation 3.9, n_1 and p_1 describe the SRH densities of electrons and holes at E_t , and can be calculated using the following expressions:

$$n_1 = N_C \exp\left(-\frac{E_C - E_t}{kT}\right) \quad (3.10)$$

$$p_1 = N_V \exp\left(-\frac{E_t - E_V}{kT}\right) \quad (3.11)$$

where N_C and N_V are the effective density of states in the conduction band and valence band, respectively. Hence, the lifetime component associated with a SRH recombination component with a single trap level is defined by [174]:

$$\tau_{SRH} = \frac{\Delta n}{U_{SRH}} = \frac{[\tau_{n0}(p_0 + p_1 + \Delta n) + \tau_{p0}(n_0 + n_1 + \Delta n)]}{p_0 + n_0 + \Delta n} \quad (3.12)$$

These equations form the basis of the LS analysis and SRH defect parameter extraction from TIDLS measurements presented in this chapter.

3.1.1.4 Surface recombination

Discontinuation of the crystal structure at the surface of a Si substrate results in the presence of large concentrations of partially-bonded Si atoms (also known as dangling bonds). These crystal defects introduce surface recombination states in the Si bandgap. As a result, surface recombination is simply a special case of the previously discussed SRH recombination, with the defects located at the surface instead of the bulk. Thus, the

recombination rate for a single surface defect state can be described according to a specific formulation of the SRH recombination expression in Equation 3.9:

$$U_s = \frac{S_{n0}S_{p0}(n_s p_s - n_i^2)}{S_{n0}(n_s + n_1) + S_{p0}(p_s + p_1)} \quad (3.13)$$

In this equation, n_s and p_s are the electron and hole densities at the surface, whilst S_{n0} and S_{p0} are the surface recombination velocities, which are dependent on the concentration of surface defect states per unit area at a single energy level, D_{it} :

$$S_{n0} = \sigma_n v_{th} D_{it} \quad S_{p0} = \sigma_p v_{th} D_{it} \quad (3.14)$$

However, surface defect states tend to occupy energy levels throughout the bandgap, and thus the true recombination rate must be integrated across all E_t , with the energy-dependent contributions of n_1 , p_1 and D_{it} considered, leading to the expression:

$$U_s = \int_{E_V}^{E_C} \frac{v_{th}(n_s p_s - n_i^2)}{\frac{[n_s + n_1(E_t)]}{\sigma_p(E_t)} + \frac{[p_s + p_1(E_t)]}{\sigma_n(E_t)}} D_{it}(E_t) dE \quad (3.15)$$

Surface recombination is a rate per unit area parameter (instead of a per unit volume area, as in the case of the other recombination parameters discussed previously in this chapter), and thus the surface recombination velocity (SRV), S , is typically used in place of minority carrier lifetime [123]:

$$S \equiv \frac{U_s}{\Delta n_s} \quad (3.16)$$

where Δn_s is the excess carrier concentration at the surface. If n_s and p_s are unknown, then an effective surface recombination velocity is often quoted, S_{eff} , defined as the recombination rate at a plane representing the edge of the surface SCR, with an upper bound of $S=1 \times 10^7$ cm/s imposed by the thermal velocity of carriers [123].

Assuming samples with symmetrically-passivated surfaces, there are two limiting cases that allow for simplified expressions for the surface recombination contribution that was proposed by Sproul [175]. In the case of high S , the effective lifetime is dependent on carrier diffusion towards the surfaces rather than recombination at the surface (since carriers recombine immediately once they reach the surface). Hence, the surface lifetime component reduces to the expression:

$$\frac{1}{\tau_s} = D_n \left(\frac{\pi}{W} \right)^2 \quad \text{for} \quad \frac{SW}{D_n} > 100 \quad (3.17)$$

where W is the Si wafer thickness and D_n is the excess carrier diffusion constant. Conversely, in instances of low S values, carrier diffusion towards the surfaces can be ignored and thus τ_s can be determined by:

$$\frac{1}{\tau_s} = \frac{2S}{W} \quad \text{for} \quad \frac{SW}{D_n} < \frac{1}{4} \quad (3.18)$$

Sproul demonstrated that both these expressions were valid within 4% for the ranges of validity stated above [175]. Grivikas *et al.* proposed a combination of these two limiting expressions to explain the surface contribution across the whole parameter plane, which successfully covered intermediate ranges with a deviation of less than 5% for arbitrary values of S , W and D_n [175, 176]:

$$\frac{1}{\tau_s} = \left(\frac{W}{2S} + \frac{1}{D_n} \left(\frac{W}{\pi} \right)^2 \right)^{-1} \quad (3.19)$$

Recently, McIntosh and Black [177] demonstrated that S_{eff} is dependent on the substrate doping and the stored charge in the dielectric. Thus, depending on the accumulation/inversion conditions at the Si-dielectric interface, passivation quality of undiffused Si may better be defined by a surface saturation current density, J_{0s} .

3.1.1.5 Effective lifetime

The sum of these different recombination contributions above gives rise to the effective minority carrier lifetime for a given sample:

$$\frac{1}{\tau_{eff}} = \frac{1}{\tau_{Aug}} + \frac{1}{\tau_{rad}} + \frac{1}{\tau_{SRH}} + \frac{1}{\tau_s} \quad (3.20)$$

The injection-dependent contributions of intrinsic and bulk defect recombination can be seen in Figure 3.1. Each of these components need to be accounted for to extract accurate information about defect parameters using TIDLS analysis. Of particular importance is the removal of surface recombination effects, which can be achieved through effective passivation techniques or subtraction of different lifetime curves with identical surface conditions. This is discussed further in Section 3.2.3.1.

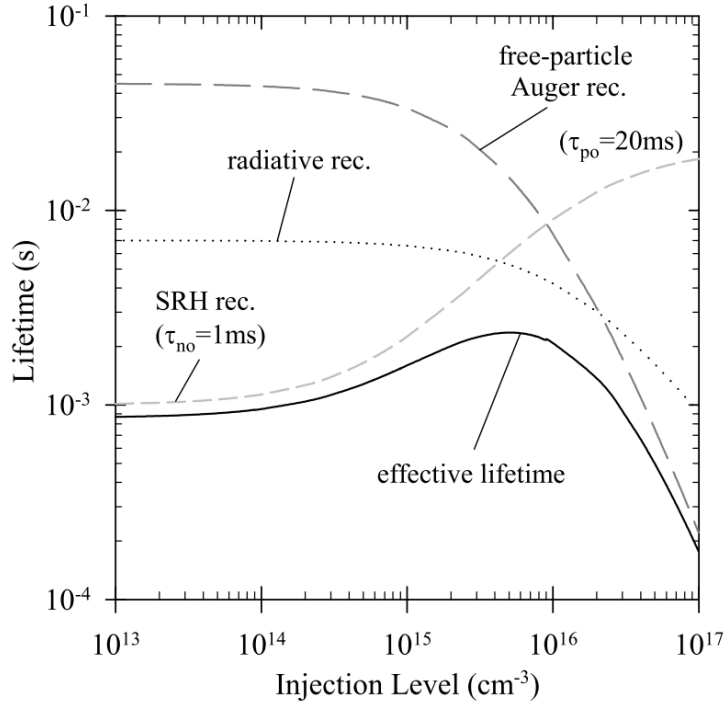


Figure 3.1: Component lifetime curves for a 1 Ω .cm p-type Si wafer, showing impact of intrinsic recombination (Auger and radiative) and SRH recombination via a deep defect on the injection-dependent effective lifetime (from [178]).

3.1.2 SRH fitting and defect parameter extraction

Extracting information about the defect responsible for increased SRH recombination generally involves fitting the SRH equation (Equation 3.12) to experimentally-obtained injection-dependent lifetime curves (known as injection dependent lifetime spectroscopy, IDLS). Since the electron and hole capture cross-sections for a defect state may differ by several orders of magnitude, one of the absolute quantities, τ_{n0} or τ_{p0} , is often replaced with k :

$$k = \frac{\sigma_n}{\sigma_p} = \frac{\tau_{p0}}{\tau_{n0}} \times \frac{v_{th,h}}{v_{th,e}} \quad (3.21)$$

As a result, the SRH equation becomes:

$$\tau_{SRH} = \tau_{n0} \left[\frac{p_0 + p_1 + \Delta n}{p_0 + n_0 + \Delta n} + k \frac{n_0 + n_1 + \Delta n}{p_0 + n_0 + \Delta n} \right] \quad (3.22)$$

Like E_t , k is a relative defect parameter which does not depend on N_t or $\sigma_{n,p}$, which are difficult to determine with LS techniques. Assuming the minority carrier

concentration is negligible compared to the majority carrier concentration at thermal equilibrium, Murphy *et al.* developed a mathematical method to simplify the fitting procedure via linearisation of the injection-dependent lifetime curve for p-type Si [179]:

$$\tau_{SRH} = \left[\tau_{n0} + \frac{\tau_{p0}n_1}{p_0} + \frac{\tau_{n0}p_1}{p_0} + X \left(\tau_{p0} - \frac{\tau_{p0}n_1}{p_0} - \frac{\tau_{n0}p_1}{p_0} \right) \right] \quad (3.23)$$

where X is defined as the ratio between the total electron and hole concentrations, n/p . Through this linearisation, only linear curves are now fitted with the gradient m and intercept b of the fitted line expressed as a function of E_t , σ_n and σ_p :

$$m = \tau_{p0}(\sigma_p) - \frac{\tau_{p0}(\sigma_p) \cdot n_1(E_t)}{p_0} - \frac{\tau_{n0}(\sigma_n) \cdot p_1(E_t)}{p_0} \quad (3.24)$$

$$b = \tau_{n0}(\sigma_n) + \frac{\tau_{p0}(\sigma_p) \cdot n_1(E_t)}{p_0} + \frac{\tau_{n0}(\sigma_n) \cdot p_1(E_t)}{p_0} \quad (3.25)$$

Employing this linearisation, the optimum fitting parameters are presented as a defect parameter solution surface (DPSS), a least-squares minimization methodology introduced by Rein [123]. For each energy level, the optimum k and τ_{n0} are determined. However, the same fitting quality (i.e., least squares fitting error) can be obtained for a wide range of energy levels. Therefore, a single DPSS- k curve will produce a wide range of defect parameter combinations that adequately fit the curve as seen in Figure 3.2. This ambiguity can be removed by performing the same IDLS measurements on samples with: (a) different base doping concentrations (known as N_{dop} -IDLS); or (b) the same sample but at different temperatures (TIDLS). The intersection points of different DPSS- k curves reveal two possible combinations of optimum defect parameters that provide an adequate fit across the whole range of IDLS measurements, narrowing the determination of defect parameters.

Whilst variations on fitting procedures based on the DPSS method have been introduced in recent years by Sun *et al.* [180], Bernardini *et al.* [181] and Zhu *et al.* [182], the original methodology described above is that fitting procedure that was employed in the characterisation of Cu defects in Si as presented in this chapter. It is also assumed in DPSS analysis that k is temperature-independent, however this may not necessarily be the case (since $\sigma_{n,p}$ can vary with temperature, as discussed later in this chapter).

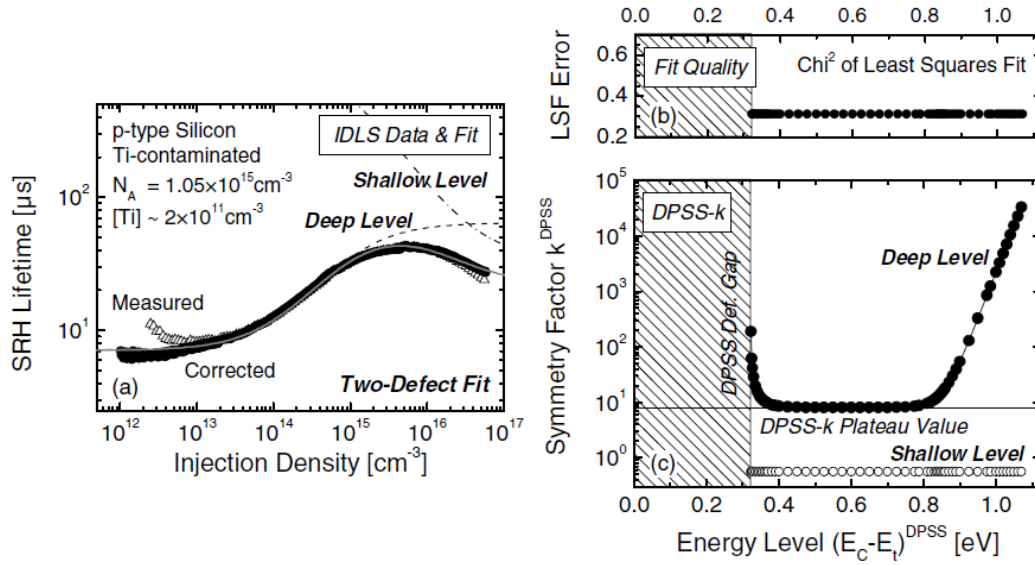


Figure 3.2: SRH defect analysis for a Ti-contaminated Si wafer, including: (a) IDLS curve and 2-level SRH fit; (b) χ^2 of least squares fit; and (c) corresponding DPSS curve, showing the ambiguity in the defect parameter fitting optimisation when performed on a single ILDS curve (from [123]).

3.2 Characterisation of Cu precipitates using TIDLS

3.2.1 Introduction

The characteristics of Cu precipitates in Si (size, density, distribution) have a significant impact on their carrier recombination activity [183]. The nucleation and growth of precipitates is dependent on several factors, including density of nucleation sites, Cu_i concentration and illumination conditions [153, 158]. Since Cu can be introduced at various stages in the cell processing sequence, the impact of precipitate growth conditions on Cu defect recombination activity needs to be more thoroughly assessed - in particular, the differences between Cu precipitate formation due to Cu contamination during ingot formation compared to light-activated Cu precipitation from surface-diffused Cu in the bulk (which is of particular importance when examining Cu diffusion and degradation from plated contacts for Si solar cells). This section reports on advanced lifetime spectroscopy analysis of both light-activated and ingot-grown Cu defects in Si using TIDLS to compare the recombination activity (k and E_t) and relate this to the precipitate formation conditions present in the different contamination methodologies.

3.2.2 Experimental

3.2.2.1 Sample Preparation and processing

In this experiment, two different batches of 100 mm p-type FZ-Si wafers were contaminated with Cu using separate approaches (see Figure 3.3 below for process summaries and Table 3.1 for summary of wafer conditions). For the first approach, a 280 μm thick $\sim 3 \Omega\cdot\text{cm}$ double-side polished FZ-Si wafer was symmetrically-passivated with a $\sim 15 \text{ nm}$ thermal oxide (SiO_2) grown during a 40 min dry oxidation at 900°C followed by a 20 min anneal at the same temperature in nitrogen (N_2) ambient. Following thermal oxidation, surfaces were spin-coated with a 1 ppm copper sulfate (Cu_2SO_4) solution, followed by a 20 min anneal at 800°C to drive Cu into the Si bulk (cooling rate $\sim 4^\circ\text{C/s}$), resulting in an estimated Cu concentration of $1\text{--}2 \times 10^{14} \text{ cm}^{-3}$.

For the second approach, 240 μm thick Si wafers were taken from a 100 mm $3 \Omega\cdot\text{cm}$ FZ ingot in which a surface Cu source was driven into the Si bulk during the FZ crystallization process of a Cz ingot. Details of the cooling rate for the ingot were not provided by the ingot supplier. Wafers were initially saw damage etched to remove 20 μm from the wafer thickness, removing surface saw damage as well as random-pyramid texturing the surface (removal of saw damage confirmed through microscope inspection of surface condition). Wafers were then symmetrically-passivated with a $\sim 80 \text{ nm}$ SiN_x deposited using PECVD with a Meyer Burger MAiA system. Wafers were selected from different heights in the ingot, with the Cu concentration ranging from approximately 3×10^{14} to $5 \times 10^{14} \text{ cm}^{-3}$ (estimation only based on surface concentration).

Table 3.1: Sample conditions for the Cu-contaminated Si wafers in this work.

| | Surface Contaminated | Ingot Contaminated |
|--|------------------------------|----------------------------------|
| Thickness (μm) | 286 | 220 |
| Resistivity ($\Omega\cdot\text{cm}$) | 3 – 3.5 | 3 – 3.5 |
| Surface condition | Polished | Textured |
| Dielectric passivation | SiO_2 | SiN_x |
| J_{0s} (fA/cm^2) | 27 | 27 |
| O Content (cm^{-3}) | $< 5 \times 10^{16}$ | $< 5 \times 10^{16}$ |
| Cu content (cm^{-3}) | $1\text{--}2 \times 10^{14}$ | $3\text{--}5 \times 10^{14}$ (*) |

(*) Variation in concentration between wafers from different heights in the ingot.

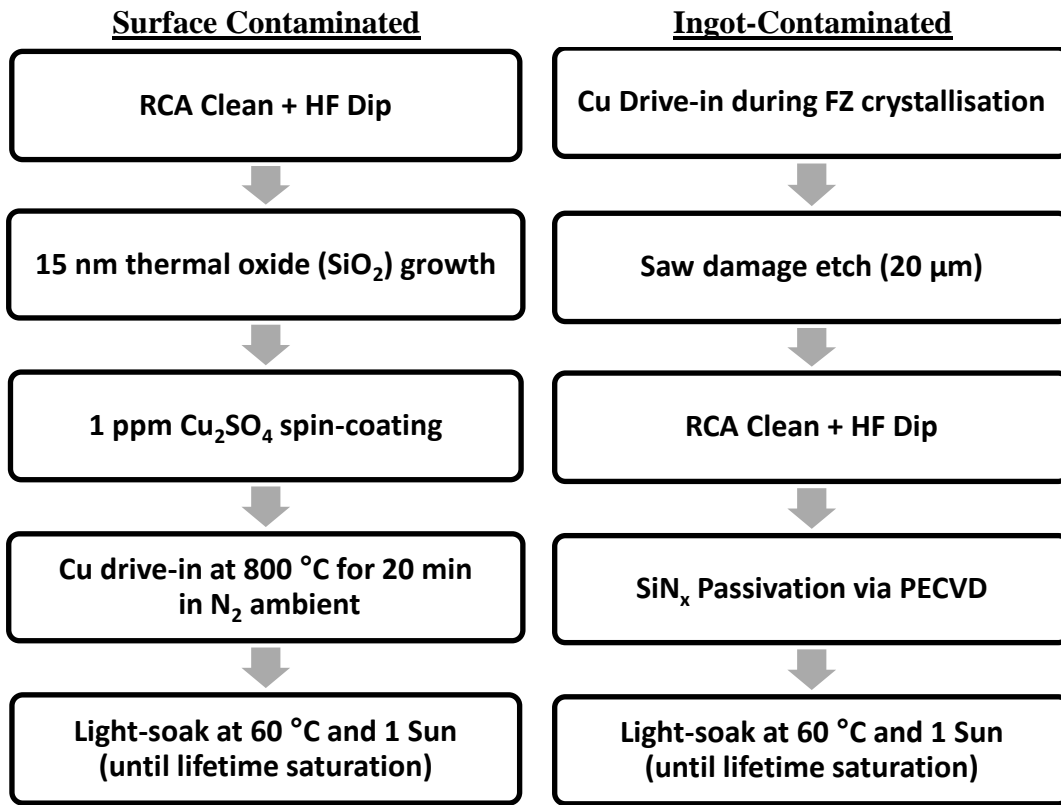


Figure 3.3: Summary of the different processing sequences for Cu defect formation in the different FZ-Si wafers examined in this experimental work.

For the surface-contaminated sample, the wafer was cleaved into quarters as required by the measurement system used for TIDLS measurements (detailed more in the following section). For the ingot-contaminated samples, wafers were cleaved down to $40 \times 40 \text{ mm}^2$ tokens. Due to non-uniform Cu distribution and lifetime across each 100 mm wafer, the central region was selected for analysis as it likely contained the highest concentrations of Cu and minimised the impact of non-uniform lifetime on the extraction of defect parameters via TIDLS.

All wafers examined in this work were exposed to 1 Sun illumination with the use of $4 \times 500 \text{ Watt}$ Halogen floodlights until lifetime saturation was achieved. This was to initiate Cu-LID in the case of the surface-contaminated samples, as well as confirm the pre-existing formation of the defect in the ingot-contaminated samples [44, 134]. The sample temperature was maintained at 60 °C using a calibrated hotplate. Following light-soaking, samples were dark annealed at 210 °C for 10 min to remove any potential BO degradation [122]. An image of the light-soaking setup used in these experiments is shown in Figure 3.4.

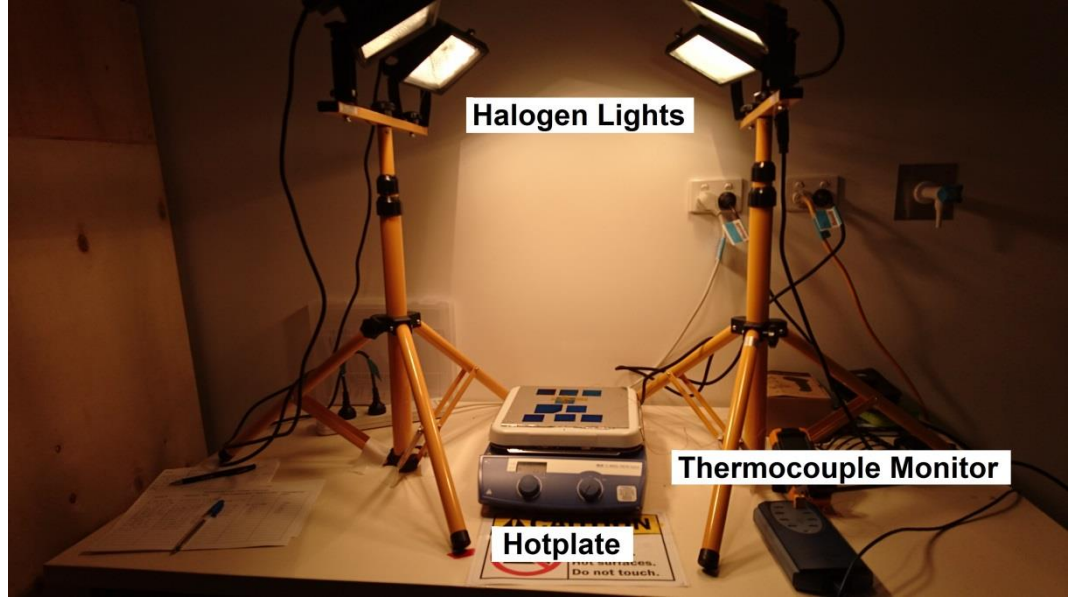


Figure 3.4: Light-soaking setup used in this experiment, including halogen lights and hotplate with thermocouple to maintain a constant temperature during light-soaking.

3.2.2.2 Characterisation and Modelling

Samples were characterised before and after light-soaking using a combination of quasi steady-state photoconductance (QSS-PC) measurements with a Sinton WCT-120 lifetime tester at room temperature (RT) and PL imaging with a BT Imaging LIS-R1 imaging tool. The oxygen content of each sample was measured using Fourier transform infrared spectroscopy (FTIR). The surface passivation quality of both samples was assessed using three different methodologies on uncontaminated Si wafers:

- 1) Application of the Kane-Swanson method for extraction of J_{0s} and thus S_{eff} from the slope of the intrinsic-corrected lifetime curve at high injection [184]:

$$J_{0s} = \frac{qWn_i^2}{2} \frac{d}{d\Delta n} \left(\frac{1}{\tau_{eff}} - \frac{1}{\tau_i} \right) \quad (3.26)$$

$$S_{eff} = J_{0s} \frac{N_A + \Delta n}{qn_i^2} \quad (3.27)$$

- 2) Plotting inverse lifetime vs inverse half thickness for a set of samples with different thicknesses and identical high bulk lifetime [175, 185].
- 3) Determining the injection-dependent upper limit of S_{eff} using the equation below and the Richter model for intrinsic recombination (Equation 3.6):

$$S_{eff_upper\ limit} = \frac{W}{2} \left(\frac{1}{\tau_{eff}} - \frac{1}{\tau_i} \right) \quad (3.28)$$

After light-soaking and dark annealing, TIDLS measurements were performed on a modified Sinton WCT-120 with an 18 mm diameter sensor region (minimising edge recombination effects) and a liquid nitrogen-cooled sample stage, providing a wider temperature range for TIDLS measurements than the commercially-available WCT-120TS (-150 °C → 400 °C). For these experiments, the temperature range selected was -25 °C to 200 °C, with measurements taken at steps of 25 °C. A combination of QSS flash measurements and 810 nm LED measurements were performed to obtain lifetime data across a wide injection range. Calibrations of temperature and photoconductance decay (PCD) measurements were both performed to maximise the accuracy of lifetime data and DPSS analysis (see Appendix A for details on calibration procedure). Lifetime stability during temperature-dependent measurements was monitored with room temperature measurements before and after the TIDLS measurements of representative samples. As the measurements before and after TIDLS were found to be similar, no hysteresis effect was identified for wafers presented in this chapter.

With the data obtained through TIDLS measurements, the defect parameters associated with Cu precipitates were obtained by applying the fitting procedure described in Section 3.1.2. In previous studies [95, 186], the examination of defects in Si was performed by extracting the SRH lifetime from samples with and without the defect in question as given by:

$$\frac{1}{\tau_{Cu}} = \frac{1}{\tau_{deg}} - \frac{1}{\tau_{ref}} \quad (3.29)$$

Since adequate reference samples could not be obtained for all the samples examined in this work, this methodology could not be applied. However, in the case of sufficiently well passivated surfaces and significant bulk recombination (assuming Cu as the only source of recombination), the effective lifetime equation can be simplified to:

$$\frac{1}{\tau_{Cu}} = \frac{1}{\tau_{eff}} - \frac{1}{\tau_i} - \frac{1}{\tau_s} \approx \frac{1}{\tau_{eff}} - \frac{1}{\tau_i} \quad (3.30)$$

Thus, it was assumed that the bulk defects represented the dominant recombination mechanism and the effect of surface/edge recombination could be considered negligible.

This was considered a fair assumption in the case of significant Cu-related degradation as observed in this experiment (discussed further in Section 3.2.3.1). Cu precipitate density and radius was also estimated by fitting RT IDLS curves to a fitting model specific for metallic precipitates (for more details, see Section 2.4 [159, 160]).

3.2.3 Results and discussion

3.2.3.1 Assessment of surface impact on effective lifetime

The impact of surface recombination on the effective lifetime was extracted using control wafers with no Cu contamination, allowing the influence of bulk lifetime to be considered negligible. Using the Kane-Swanson method [184], recombination current densities of $< 30 \text{ fA/cm}^2$ were measured on both the SiO_2 and SiN_x passivated samples, corresponding to an S_{eff} of approximately 25 cm/s at $\Delta n = 1 \times 10^{16} \text{ cm}^{-3}$ according to Equation 3.27, indicating sufficiently good passivation for both the Si wafers examined in this work. Despite sufficient passivation quality implied by the Kane-Swanson method, band-bending at the dielectric-Si interface due to charges at the semiconductor surface leads to an injection-dependent S_{eff} [187]. An upper limit on S_{eff} across the entire injection range was obtained using Equation 3.28 for a set of uncontaminated Si wafers passivated with SiN_x , with the results presented in Figure 3.5 below.

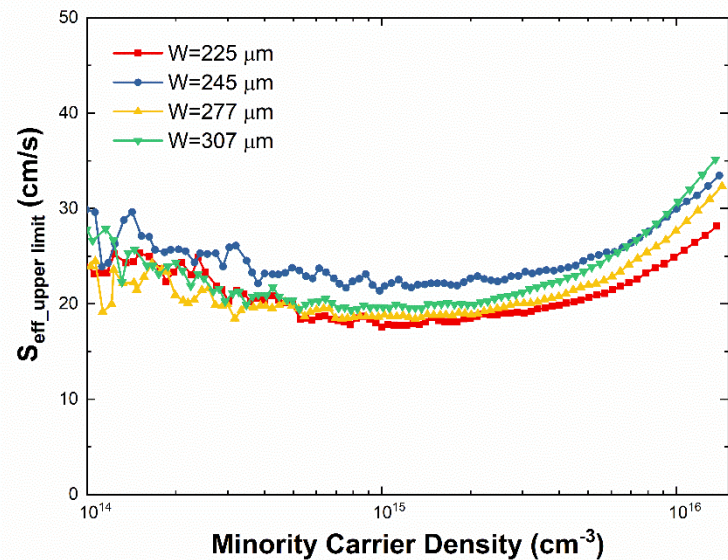


Figure 3.5: Upper limit of S_{eff} as a function of injection level for uncontaminated p-type FZ-Si samples of different thicknesses with an 80 nm SiN_x layer on both sides.

The overall trend between the four samples was very similar, with an upper limit on S_{eff} of 18-35 cm/s across the entire injection range. Since the upper limit of the SRV was highest in the high-injection range, the inverse of effective lifetime was plotted against the inverse of the half-thickness to extract S_{eff} from the slope of the curve at an injection level of $\Delta n = 1 \times 10^{16} \text{ cm}^{-3}$, with the results of this method presented in Figure 3.6 below. Initially, an estimated S_{eff} of $\sim 16 \text{ cm/s}$ was determined with this method. However, it was noticed that the wafer with a thickness of $245 \text{ }\mu\text{m}$ did not follow the same trend as the other thickness wafers examined (this mismatch is also visible in Figure 3.5), which distorted the linear fits obtained by plotting inverse lifetime vs inverse half-thickness. Removing this sample and re-examining the trend provided a much more accurate fit and produced an estimated S_{eff} of $\sim 12 \text{ cm/s}$. In both cases, the estimated S_{eff} was below the upper limit for S_{eff} determined by Equation 3.28.

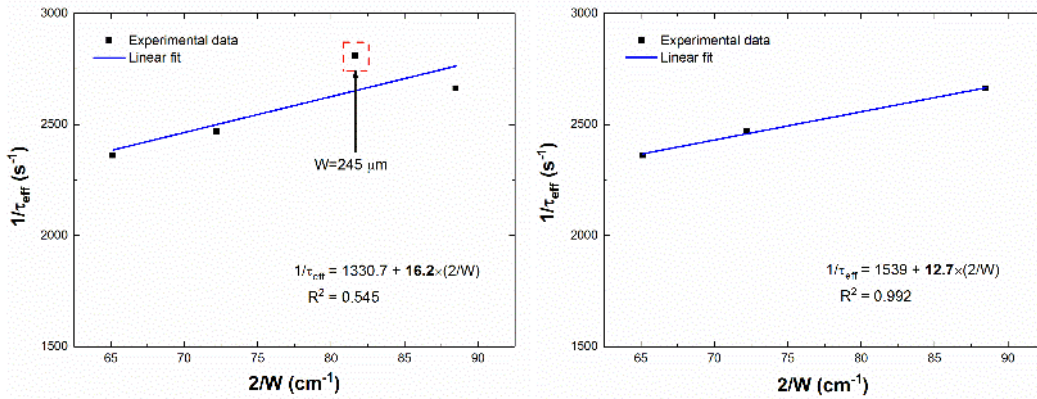


Figure 3.6: Inverse lifetime as a function of the inverse half thickness of the wafer extracted at an injection level of $\Delta n = 1 \times 10^{16} \text{ cm}^{-3}$, (left) with four different samples, or (right) excluding the anomalous wafer with thickness $W = 245 \text{ }\mu\text{m}$.

As mentioned previously, the impact of surface recombination is normally eliminated by subtracting the inverse lifetimes of a control sample from a contaminated sample with an identical passivation layer (Equation 3.29). However, since reference samples with identical conditions were not available for this experiment, the elimination of surface recombination as a factor in impacting the effective lifetime in comparison to the bulk SRH impact of the Cu precipitates had to be assessed. One method to confirm whether the measured effective lifetime was impacted only by bulk SRH lifetime (within 10% experimental error) was proposed by Schmidt and Aberle [188]. Assuming

an inherent systematic error, x , the conditions required by τ_{eff} , W and S_{eff} to ensure the deviation between τ_{Cu} and τ_{eff} is below $x\%$ is given by:

$$\frac{\tau_{eff}}{W} < \frac{x}{200S} \quad (3.31)$$

Thus, the upper-limit on S_{eff} required to eliminate the impact of the surface on effective lifetime was determined for the different wafer thicknesses between the surface-contaminated and ingot-contaminated Si wafers using Equation 3.31. This relationship is shown in Figure 3.7, where the shaded region below the curves represent the regions in which effective lifetime and bulk lifetime could be deemed equivalent within experimental error. The red dashed region highlights the region in which all the Cu-contaminated samples examined in this work can be described, whilst the black dashed line represents an upper limit on S_{eff} for both SiO_2 and SiN_x coated wafers. Since these were undiffused Si wafers, taking into account the conclusions of McIntosh and Black [177], J_{0s} as determined by the Kane-Swanson method (25 cm/s) was chosen as the more accurate measure of surface passivation quality and thus used as the maximum threshold value in the graph below, which determined an upper limit of 60 μs on τ_{eff} below which negligible surface recombination effects can be assumed.

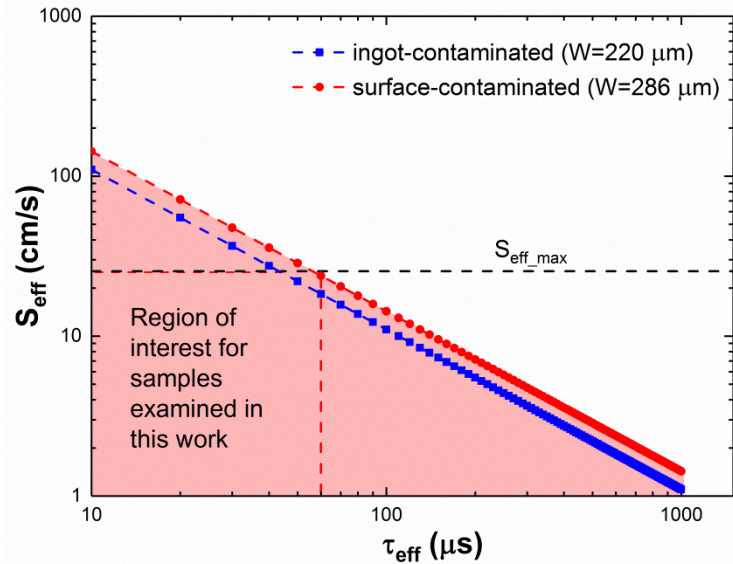


Figure 3.7: Relationship between S_{eff} and τ_{eff} for the sample wafer thicknesses examined in this experimental work.

Whilst the surface recombination of the SiO₂ coated samples were not analysed to the same extent as the SiN_x coated samples, the extremely low lifetime due to more severe bulk recombination observed in these surface-contaminated samples allowed for the assumption of minimal difference between τ_{eff} and τ_{Cu} according to Equation 3.31. Murphy *et al.* made the same assumption when characterising the defect parameters of O precipitates in Si with TIDLS measurements using the methodology described in Section 3.1.2 [179]. This assumption was also made across the entire temperature range examined in TIDLS measurements based on recent studies by Nie *et al.* [189] and Bernardini *et al.* [190] which demonstrated that S_{eff} decreases with increasing temperature for a SiN_x passivation layer equivalent to that employed in this work. As long as the improvement in τ_{Cu} with temperature is less than the improvement in S_{eff} , the assumption of equivalence between τ_{eff} and τ_{Cu} is valid. Since all samples in this work satisfy these requirements, the assumption of negligible surface recombination in comparison to severe bulk recombination is valid within an error range of 10%, which is a tolerable error for advanced lifetime spectroscopy analysis [123].

3.2.3.2 Characterisation of Cu precipitates using TIDLS

Figure 3.8 below presents the monitored lifetime for a surface-contaminated FZ-Si wafer during light-soaking (1 Sun illumination and 60 °C) as well as the uncontaminated wafer used for SRV determination in the previous section. The degradation of lifetime under illumination occurs via a single asymptotic degradation process, with complete lifetime saturation achieved after 24 hr of light-soaking. By comparison, the control sample presented no observable degradation in lifetime, confirming Cu-LID as the sole degradation mechanism activated during light-soaking.

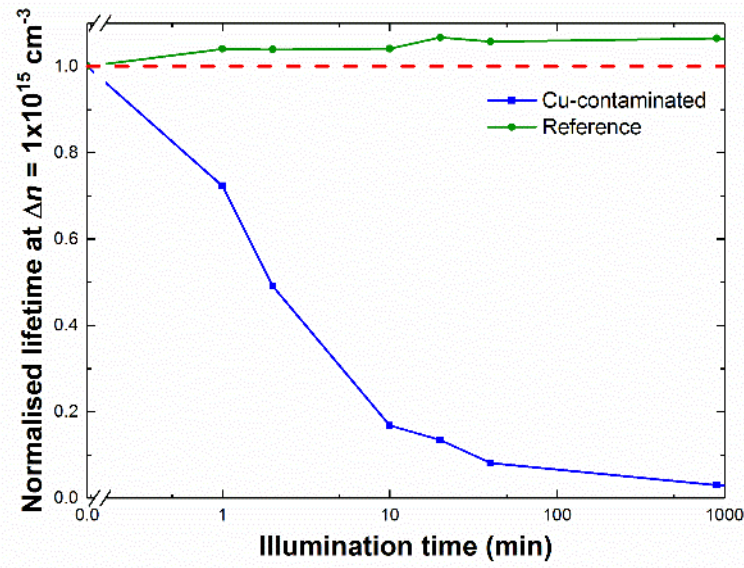


Figure 3.8: (a) Normalised effective lifetime at an excess carrier concentration of $\Delta n = 1 \times 10^{15} \text{ cm}^{-3}$ as a function of light-soaking duration at ~ 1 Sun illumination and 60°C for a Cu-contaminated p-type FZ-Si wafer as well as an uncontaminated reference wafer.

As witnessed in the comparative PL images in Figure 3.9, the lifetime degradation occurred uniformly across the wafer. The brighter region observed along the edge of the degraded PL image could be due to slight non-uniformities in the Cu spin-coating process or potentially an impact of the drive-in process, although the exact cause could not be ascertained in this work. Regardless, the lifetime degradation observed as a result of Cu-LID occurring in the wafer was extensive as seen in Figure 3.9 (a), with nearly two orders of magnitude in lifetime lost as a result of Cu precipitate formation under illumination. In terms of the influence of surface recombination, the good passivation of the thermally-grown SiO_2 ($J_0 = 27 \text{ fA/cm}^2$ as determined from the Kane-Swanson method [184]) combined with the extensive bulk lifetime degradation fell within the margin of error as determined in Figure 3.7. Thus, the effective lifetime and SRH lifetime required for defect parameter characterisation were deemed to be equivalent within a reasonable margin of error.

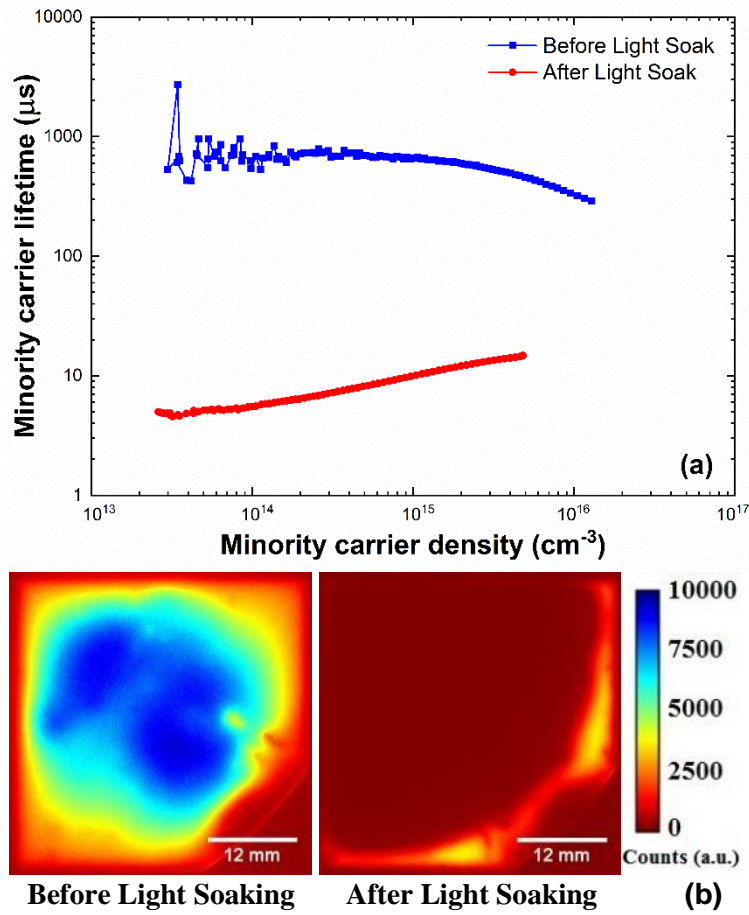


Figure 3.9: (a) Minority carrier lifetime measured on a Cu-contaminated p-type FZ-Si wafer before and after light-soaking at ~ 1 Sun illumination and 60°C , and (b) corresponding PL images (exposure time = 0.5 s, photon flux = $2.72 \times 10^{17} \text{ cm}^{-2}\text{s}^{-1}$).

Based on previous studies [94, 95], an adequate fit of the entire range of lifetime curves requires the assumption of two non-interacting energy levels – a defect level which dominates recombination at low injection levels, and a secondary defect level that primarily affects the lifetime at high injection conditions. These two non-interacting energy levels represent the edges of a band of defect energy states introduced into the upper half of the bandgap [36, 97]. Whilst it is assumed in this work that the levels are non-interacting, this may not be the case and future studies may require more advanced fitting procedures that investigate the possibility of interacting defect levels.

An example of the linearisation of intrinsic-corrected lifetime curves and associated fitting of two defect levels can be seen in Figure 3.10. However, as clear from the set of curves shown in Figure 3.11, the extent of degradation was so severe that high injection conditions could not be obtained with the setup used in this experiment. Hence, the

shallow defect level affecting the high injection region of the lifetime curve could not be fitted in this case. The source of the weak secondary level at very low injection could not be determined at this stage (although trapping is often a cause of anomalous lifetime increase under very low injection conditions $< 1 \times 10^{14} \text{ cm}^{-3}$). However, since significant uncertainty in the secondary level was expected due to the dominance of the other defect level, only the dominant defect energy level was examined in this experiment as it represents the dominant recombination-active defect state for Cu precipitates in Si [95].

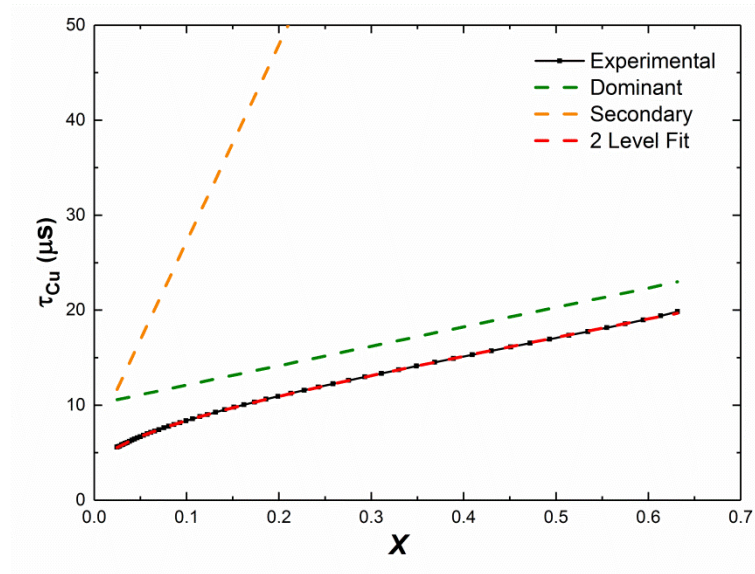


Figure 3.10: Linearisation of intrinsic corrected injection-dependent lifetime curve for a surface-contaminated p-type FZ-Si wafer after light-soaking at ~ 1 Sun illumination and 60°C , showing the optimum fitting of the curve using a two-level defect fit.

The set of temperature and injection-dependent lifetime curves for the Cu-contaminated Si wafer obtained after light-soaking are presented in Figure 3.11.

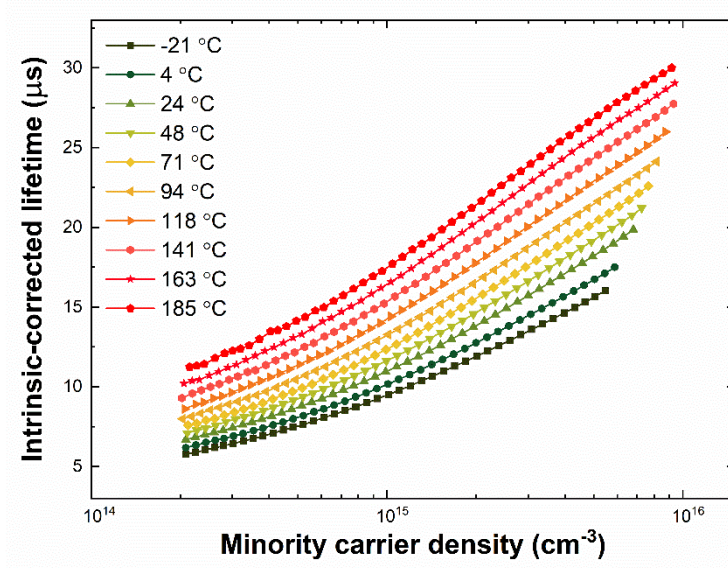


Figure 3.11: Intrinsic-corrected injection-dependent lifetime curves for a surface-contaminated p-type FZ-Si wafer after light-soaking at ~ 1 Sun illumination and 60°C measured at different temperatures (actual wafer temperature given in figure).

Following the fitting methodology defined in Section 3.1.2, The DPSS analysis for a surface-contaminated FZ-Si wafer is presented in Figure 3.12. The convergence of all the DPSS curves revealed two minima in the standard deviation curve [Figure 3.12 (b)] located at $E_t - E_i = -0.14 \pm 0.01$ eV and $E_t - E_i = 0.11 \pm 0.01$ eV. Error margins in E_t and k were determined assuming a 10% tolerance in the width of the minima as used in previous studies [95]. The corresponding capture cross-section ratio determined at these minima was determined to be $k = 1.4 \pm 0.2$. These values are in close agreement (primarily the solution positioned in the upper-half of the bandgap) with recent results obtained by Inglese *et al.* [95], who determined two energy levels at $E_t - E_i = -0.06 \pm 0.01$ eV and $E_t - E_i = 0.08 \pm 0.01$ eV with a corresponding capture cross-section ratio of $k = 1.7 \pm 0.4$ on p-type FZ-Si wafers of similar thickness, resistivity and estimated bulk Cu_i concentration. Inglese *et al.* attributed the defect parameters obtained to Cu precipitates formed during illumination, thus it can be concluded that the same Cu precipitate was formed in the light-soaked samples examined in this work.

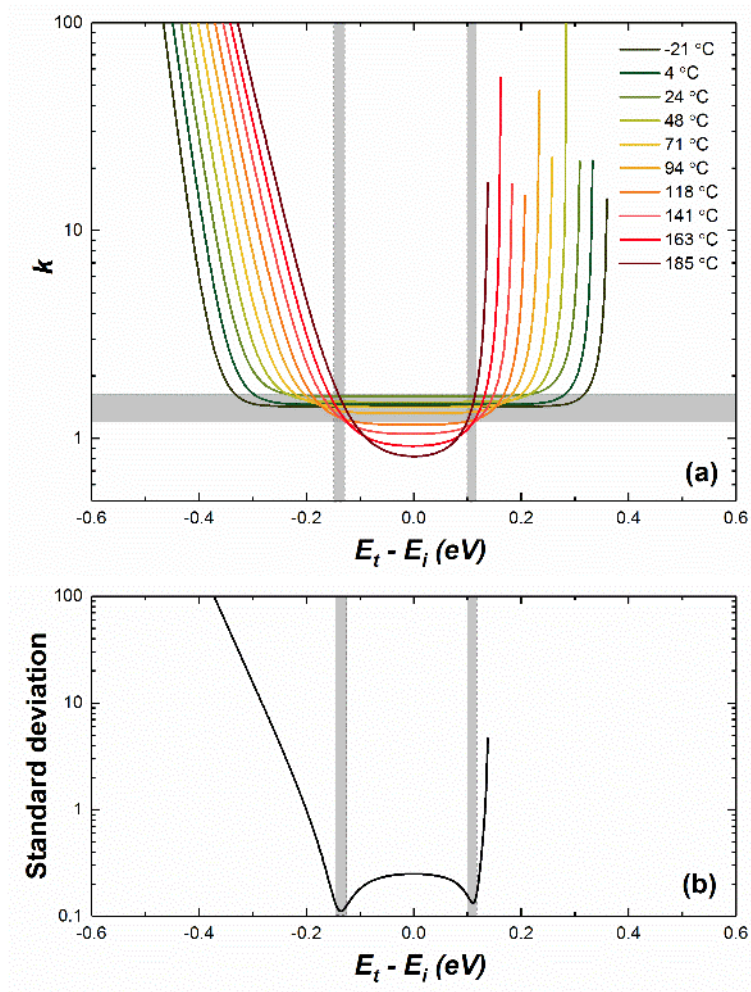
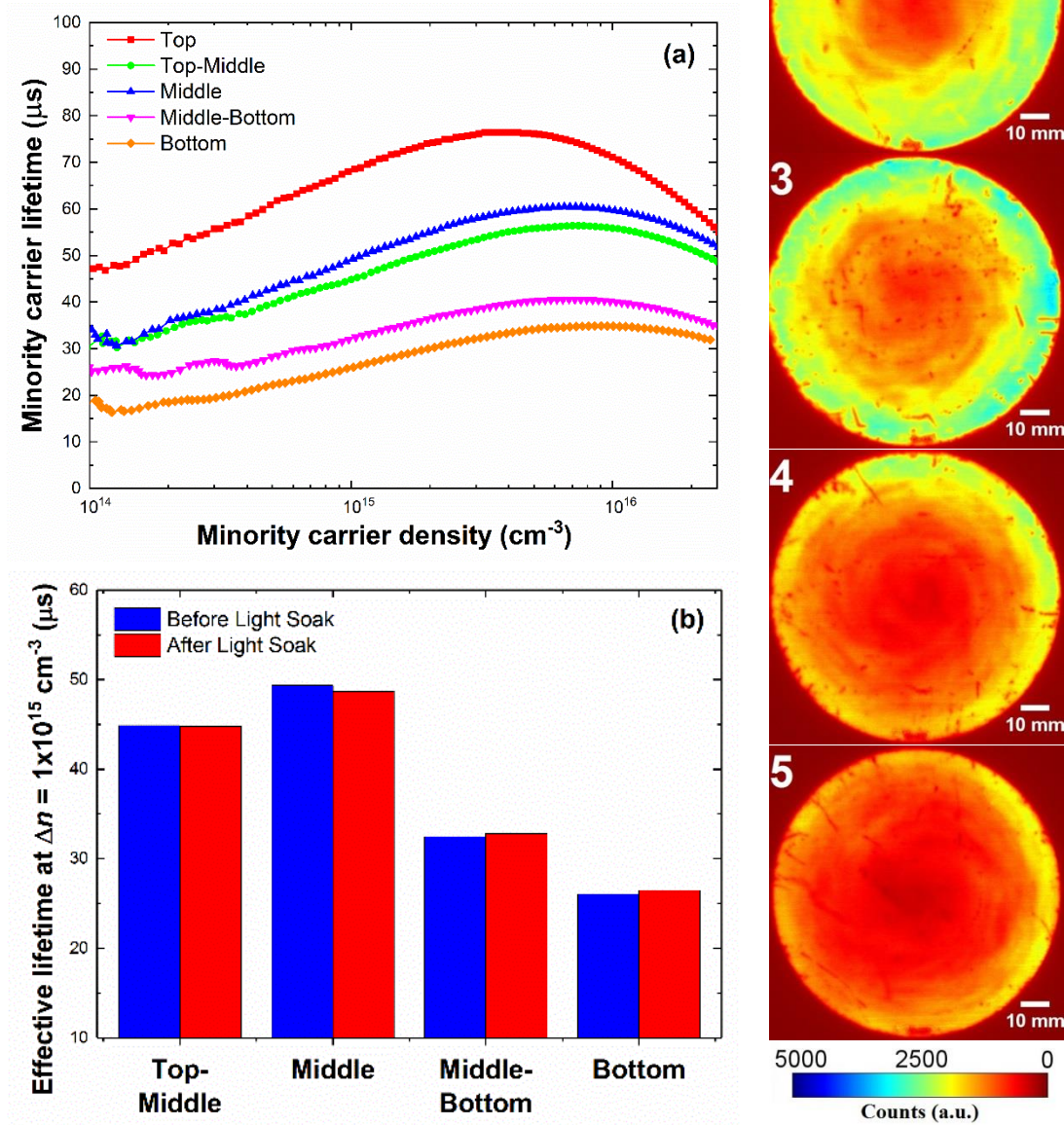


Figure 3.12: Example DPSS analysis of temperature and injection-dependent lifetime curves for a deep level defect in Cu-contaminated p-type FZ-Si wafer after surface Cu contamination, drive-in and light-soaking at ~ 1 Sun illumination and 60 °C. (a) Superposition of DPSS- k curves and (b) associated absolute standard deviations in the DPSS- k curves as a function of defect energy level with respect to the mid-gap level, E_i . The shaded regions define the value ranges within 10% standard deviation of the minima.

Figure 3.13 presents the injection-dependent lifetime curves (measured at the centre of the wafer) and corresponding PL images for the ingot-contaminated set of wafers. There is a clear decrease in carrier lifetime as a function of ingot height, as well as a strong non-uniformity across the 100 mm wafers, with the degradation much more severe in the centre of the wafer. The decrease in lifetime with ingot height and distance from ingot edge can both be attributed to the segregation of interstitial Cu to the molten region during crystallisation of the FZ ingot [191]. Furthermore, the negligible change in effective lifetime after light-soaking at ~ 1 Sun, as shown in Figure 3.13 (b), confirms

that the defect responsible for the observed degradation in these samples was already formed and thus no interstitial Cu remained when light-soaking was performed.

Figure 3.13: (a) Minority carrier lifetimes measured on p-type FZ-Si wafers from different heights in a Cu-contaminated ingot, and (b) measured lifetime at $\Delta n = 1 \times 10^{15} \text{ cm}^{-3}$ before and after light-soaking at ~ 1 Sun illumination and 60°C . PL images showing non-uniform lifetime in ingot-contaminated wafers as a function of ingot height are also shown (exposure time = 0.1 s, photon flux = $2.72 \times 10^{17} \text{ cm}^{-2} \text{ s}^{-1}$) Numbers corresponding to ingot height, 1 = Top, 5 = Bottom.



The temperature and injection-dependent lifetime curves for the most heavily-contaminated Si wafer (bottom of the ingot) are presented in Figure 3.14 below, along with an example of the linearisation and two defect level fitting. As with the previously surface-contaminated and light-degraded sample, these curves could only be adequately fitted assuming contributions from a dominant and secondary defect level. Once again, only the dominant defect level was fitted (with the secondary level only significant under high injection) according to the procedure outlined in Section 3.1.2.

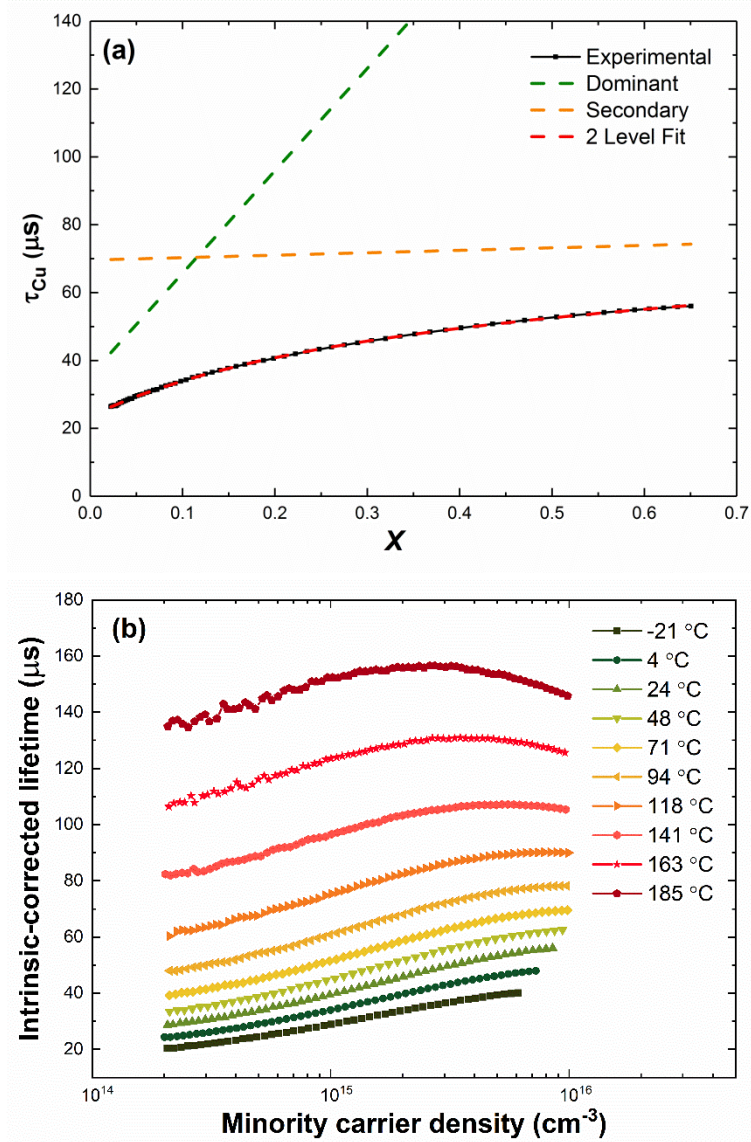


Figure 3.14: (a) Linearisation of intrinsic corrected injection-dependent lifetime curve and the optimum fitting of the curve using a two-level defect fit, and (b) intrinsic-corrected injection-dependent lifetime curves for the most heavily degraded ingot-contaminated p-type FZ-Si wafer (bottom of the ingot) measured at different temperatures (actual wafer temperature provided in figure).

The DPSS analyses for each of the ingot-contaminated FZ-Si wafers are presented in Figure 3.15 below.

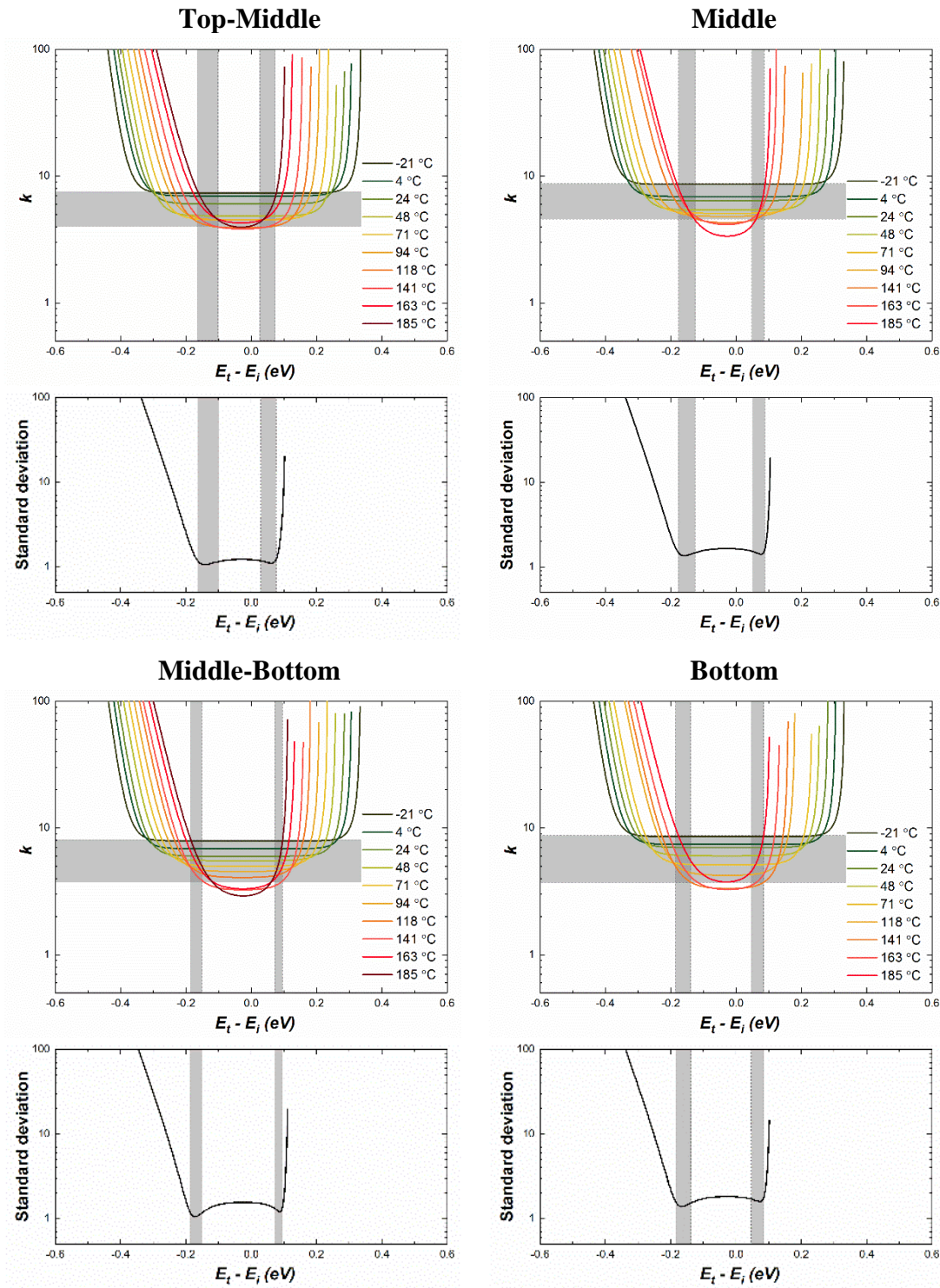


Figure 3.15: DPSS analysis for ingot contaminated p-type FZ-Si wafers from different positions in the ingot, including the superposition of DPSS- k curves and associated absolute standard deviations in the DPSS- k curves as a function of defect energy level with respect to the mid-gap level, E_i (shaded regions identify minima $\pm 10\%$).

Regardless of position in the ingot, DPSS analysis of each sample produced the same two optimum solutions at $E_t - E_i = -0.16 \pm 0.03$ eV and $E_t - E_i = 0.08 \pm 0.03$ eV, as well as a capture cross-section ratio of $k = 5.6 \pm 1.4$, which is significantly higher than that of the light-activated Cu precipitate ($k = 1.4 \pm 0.2$). This k value falls between previous results of Inglese *et al.* [95] ($k = 1.7 \pm 0.4$) and Macdonald *et al.* [94] ($k = 10$), once again indicating the presence of Cu precipitates introducing a band of energy states in the upper half of the bandgap (as discussed in Chapter 2) [36, 97]. The larger standard deviations observed in defect energy levels and k values were due to the poorer convergence of the DPSS- k curves for these samples. Whilst this may have been the result of errors due to assuming negligible surface impact when obtaining TIDLs measurements, potential temperature-dependence of the capture cross-sections could also contribute to the variation of k across the temperature range examined in this work.

To examine this variation between the two sample precipitates and analyse the temperature dependence of the capture cross-sections ($\sigma_{n,p}$), the SRH model was applied to the temperature dependent lifetime of selected wafers from both sample sets at a set injection level ($\Delta n = 2 \times 10^{14} \text{ cm}^{-3}$ so as to examine the impact of the deep defect level only). The TDLS results and SRH fit for both samples can be seen in Figure 3.16.

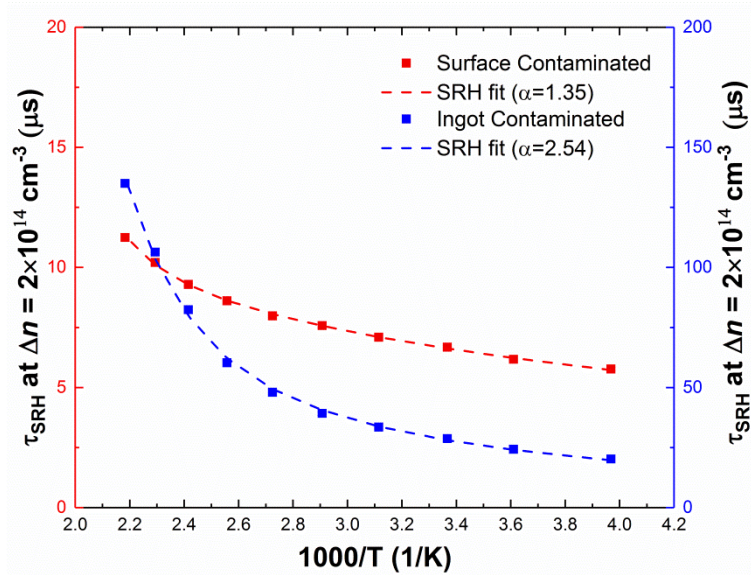


Figure 3.16: Temperature dependence of the Cu precipitate-related SRH lifetime measured at a fixed injection level ($\Delta n = 2 \times 10^{14} \text{ cm}^{-3}$) for a surface-contaminated FZ-Si wafer after light-soaking at ~ 1 Sun illumination and 60°C (red curve, left-hand axis) and a ingot-contaminated FZ-Si wafer (blue curve, right-hand axis).

The optimum fit to the experimental data could only be obtained assuming a defect energy level in accordance with the results of the DPSS analysis and a power-law dependence of σ_n (i.e. $\sigma_T = \sigma_0 \times T^{-\alpha}$), with the corresponding α for each fitted curve given in the graph above. This power-law dependence is also in agreement with the previous temperature dependence identified by Inglese *et al.* [95], where a power-law dependence in the capture cross-section was observed. This power law dependence is often attributed to the excitonic Auger capture process [192], which has been identified as the most efficient mechanism for recombination via deep defect energy levels [123]. From Figure 3.16 it seems that there is stronger temperature dependence for the ingot-contaminated wafers than the surface-contaminated wafers, which has been theorised to be the result of differences in the precipitates formed in the two sample types, and specifically, the temperature dependence of thermionic recombination currents across the Schottky junction formed at the precipitate-semiconductor interface [95, 193].

Although it is acknowledged that the observed temperature dependence is most likely the result of temperature-dependent capture coefficients, it is also possible that due to the extended nature of Cu precipitates, the band of energy states associated with such a defect (as discussed in the previous chapter) impacts the observed temperature dependence. As a result, the temperature dependence can also be due to the secondary, shallow defect level identified using TIDLS (see Figure 3.14 for example). However, the selection of low injection conditions to examine temperature dependence of the deep defect with TDLS should have eliminated the effects of the shallow defect that primarily impacts the SRH lifetime under high injection conditions [194].

A better understanding of the root cause behind the stronger temperature dependence and larger k values for the ingot contaminated samples requires more information to determine if there is any relationship between differences in the temperature dependence of k and the size/density of the precipitates. A summary of the main defect parameters extracted through TIDLS and DPSS analysis are presented in Table 3.2.

Table 3.2: Summary of extracted defect parameters for Cu precipitates formed under different conditions as performed in this experiment.

| SRH Defect parameter | Cu-LID precipitate | Ingot-formed precipitate |
|----------------------------------|---------------------|--------------------------|
| k | 1.4 ± 0.2 | 5.6 ± 1.4 |
| $(E_t - E_i)_{min} \text{ (eV)}$ | -0.14 ± 0.01 | -0.16 ± 0.03 |
| $(E_t - E_i)_{max} \text{ (eV)}$ | 0.11 ± 0.01 | 0.08 ± 0.03 |
| $\sigma(T)$ | $\propto T^{-1.35}$ | $\propto T^{-2.54}$ |

Whilst SRH lifetime fitting using the method developed by Rein is the most established curve-fitting procedure for defect analysis [123], the recombination activity of metal precipitates can also be fitted using an alternative model developed by Kwapil [160] based on a Schottky model for metallic precipitates [159] (as described in Chapter 2), which may help better understand some of the observations made with the results of DPSS analysis on the differently-contaminated Si samples. In Figure 3.17, the precipitate model was fitted using a least squares approach similar to DPSS analysis under the assumption that the entire concentration of Cu_i (as provided in Table 3.1) was converted to precipitates all with some approximated average radius.

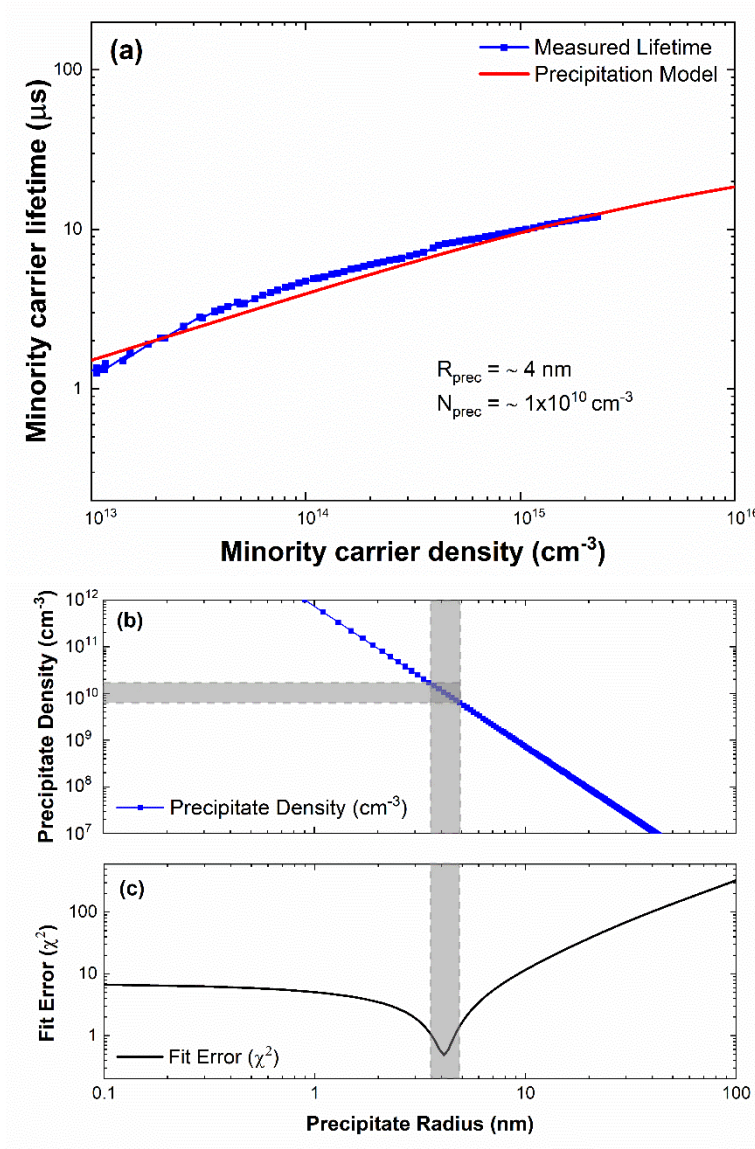


Figure 3.17: (a) Intrinsic-corrected injection-dependent lifetime curve for a Cu-contaminated p-type FZ-Si wafer after light-soaking at ~ 1 Sun illumination and 60°C and the associated best fit with the Schottky precipitation model, including (b) the corresponding precipitate density and (c) the fit error calculated for different precipitate radii. The shaded regions define the value ranges within 10% standard deviation of the minima.

The corresponding best fit for the surface-contaminated FZ-Si wafer was obtained with an estimated precipitate radius of 4 nm and a corresponding precipitate density of $1 \times 10^{10} \text{ cm}^{-3}$, which reflected similar results to a recent study by Inglese *et al.* [183], where the same model was applied to similar samples after formation of Cu precipitates under illumination. Whilst the restriction of the model to spherical precipitates of a

single radius limits the physical interpretation of these results, the good fit between the experimental lifetime curves and the precipitate model indicates that Cu precipitation can adequately describe the defect responsible for Cu-LID in these wafers.

However, performing the same fitting procedure on the ingot-contaminated samples revealed some interesting information. Firstly, using the estimated interstitial Cu concentration as provided in Table 3.1 with the Schottky model could not provide an adequate fit to the SRH lifetime curves. To achieve an adequate fit, the interstitial Cu concentration was left as a floating parameter during the fitting procedure. The optimum precipitate density and radius obtained with this best fit were $2.9 \times 10^{12} \text{ cm}^{-3}$ and 219 nm, respectively. Based on this, the estimated interstitial Cu concentration was determined to be above 10^{21} cm^{-3} using the following relationship [183]:

$$N_{Cu_i} = N_{prec}(r_{prec}) \cdot \rho_{Cu} \cdot V_{prec}(r_{prec}) \quad (3.32)$$

Thus, an adequate fit of the precipitate model was only achieved for the ingot-contaminated samples when assuming an initial Cu_i concentration near the solubility limit for Cu in Si. Whilst at first glance this may seem impossible, the nature of Cu segregation during crystallisation of the FZ ingot may have resulted in significantly high concentrations of interstitial Cu in the centre of the ingot, although this was difficult to determine in this study. Furthermore, like the DPSS results discussed earlier, there is no clear correlation between ingot position and precipitate density/radius as seen in Table 3.3.

Table 3.3: Overview of optimum fit precipitate density and radius for ingot-contaminated p-type FZ-Si wafers from different positions in the ingot as determined with the Schottky precipitate model.

| Ingot Position | Precipitate Density (cm^{-3}) | Precipitate Radius (nm) |
|-----------------------|--|--------------------------------|
| Top-Middle | 1.36×10^{12} | 226 |
| Middle | 1.05×10^{12} | 273 |
| Middle-Bottom | 1.73×10^{12} | 239 |
| Bottom | 2.9×10^{12} | 219 |

Figure 3.18 presents the corresponding fitting results for the Schottky model on the lowest lifetime ingot-contaminated FZ-Si wafer (bottom of the ingot).

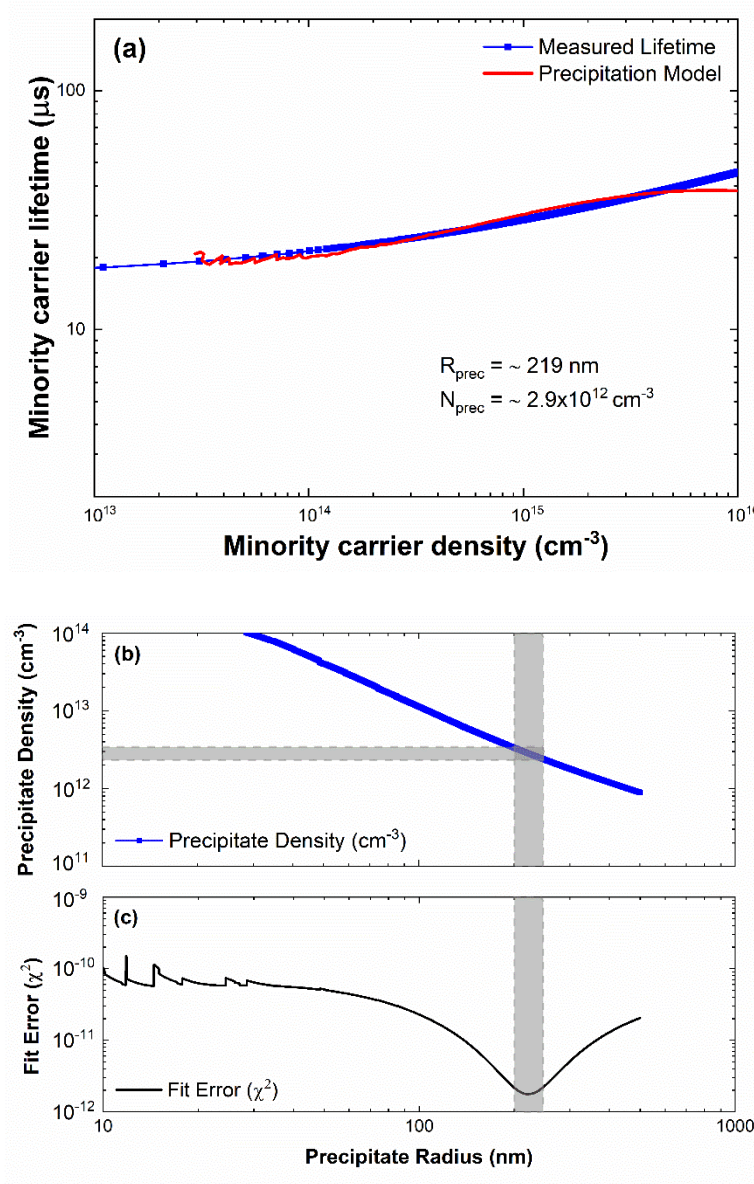


Figure 3.18: (a) Intrinsic-corrected injection-dependent lifetime curve for an ingot-contaminated p-type FZ-Si wafer and the associated best fit with the Schottky precipitation model, including (b) the corresponding precipitate density and (c) the fit error calculated for different precipitate radii. The shaded regions define the value ranges within 10% standard deviation of the minima.

According to the precipitation model described in Section 2.4, Cu precipitation rate is regulated by the solubility of Cu_i atoms in Si, with the supersaturation level representing the primary driving force for Cu precipitation. In the recent study by

Inglese *et al.* [183], it was shown that heavier doping imposed a lower supersaturation level, resulting in a slower degradation rate and subsequently a larger precipitate radius. Thus, the primary driving force between the vastly different recombination behaviours of surface-contaminated/light-activated Cu precipitates and ingot-grown Cu precipitates may be this varying supersaturation condition between the two sample types which in this case was modulated by the differences in Cu_i concentration. The different cooling rates experienced by the two sample types could also have contributed to the different precipitation behaviour due to variations in supersaturation and Cu_i concentration. However, this is difficult to determine due to the different processing sequences used to process the two sample types. The more rapid precipitate formation in the case of the illuminated surface-contaminated Si wafers resulted in precipitates with a small radius. On the other hand, the combination of a potentially high concentration of segregated interstitial Cu in the ingot-grown Si wafers, coupled with the slow defect formation in the absence of extended illumination, resulted in the formation of much larger precipitates. The larger precipitate radius of the ingot-contamination Si samples could also be related to a stronger deviation from the spherical model in these samples. For example, Donolato demonstrated that spherical precipitates of radius r had an equivalent SCR to disc-shaped precipitates with radius $\pi/2r$ [195]. Other factors, such as different concentrations of oxygen precipitates or nucleation sites, may also be responsible, although that could not be determined in this particular study. It was recently shown by Sun *et al.* that Cu intentionally introduced into a Cz ingot during crystal growth formed precipitate colonies along {110} planes, which may have some impact on the precipitate size and distribution, although it was not confirmed in this study [196]. However, the results presented in this chapter have significant implications on the study of Cu precipitate formation due to the diffusion of plated Cu through barrier metals on plated solar cells, as discussed in more detail in Chapter 6.

3.3 Chapter Summary

In this chapter, the recombination activity and properties of Cu precipitates in p-type FZ-Si were characterised using two different methodologies performed on injection-dependent lifetime curves. Two different types of precipitate growth were examined in this work – one set of samples in which Cu was driven into the bulk and then precipitate formation was initiated under illumination at ~ 1 Sun and 60 °C (Cu-LID), and one set

of samples in which the Cu was introduced during the crystallisation of an FZ ingot in the dark, resulting in a build-up of precipitates in the centre of the ingot.

The recombination activity of the different Cu precipitates were first characterised using SRH fitting of temperature and injection dependent lifetime curves. Due to a lack of suitable uncontaminated reference samples, the surface recombination had to be assessed to determine whether it could be deemed negligible in its impact on the effective lifetime curves analysed with TIDLS curve fitting. Both sample types were measured to have surface recombination velocities below 25 cm/s (using the Kane-Swanson method), which was subsequently determined to be insignificant compared to the extensive degradation in the bulk lifetime within an error of 10%. Thus, effective lifetime and bulk SRH lifetime were assumed equivalent for the fitting procedures performed in this work.

The DPSS analysis of the surface-contaminated FZ-Si revealed two possible defect energy levels located at $E_t-E_i = -0.14 \pm 0.01$ eV and $E_t-E_i = 0.11 \pm 0.01$ eV, with a corresponding capture cross-section ratio of $k = 1.4 \pm 0.2$. In comparison, the ingot-contaminated FZ-Si revealed similar defect levels at $E_t-E_i = -0.16 \pm 0.03$ eV and $E_t-E_i = 0.08 \pm 0.03$ eV, as well as a capture cross-section ratio of $k = 5.6 \pm 1.4$, which was significantly higher than that obtained on the surface-contaminated Si samples. Both samples also observed a strong power-law temperature dependence ($\sigma(T) = \sigma_0 T^{-\alpha}$), with $\alpha = 2.54$ for the most-degraded ingot-contaminated samples compared to $\alpha = 1.35$ for the surface-contaminated Si sample. This difference was theorised to be due to the temperature dependence of thermionic emission currents across the Schottky junction formed at the precipitate-Si interface. However, both samples correlate with previous results of Inglese *et al.* ($k = 1.7 \pm 0.4$) and Macdonald *et al.* ($k = 10$), once again indicating the presence of Cu precipitates introducing a band of energy states in the upper half of the bandgap.

Precipitate model fitting was also performed on room temperature injection-dependent lifetime curves from both sample types. The corresponding best fit for the surface-contaminated FZ-Si wafer was obtained with an estimated precipitate radius of 4 nm and a corresponding precipitate density of $1 \times 10^{10} \text{ cm}^{-3}$, whilst the optimum precipitate density and radius determined for the ingot-contaminated FZ-Si samples were $1.3 \times 10^{12} \text{ cm}^{-3}$ and $\sim 219\text{-}280$ nm. For both the DPSS and precipitate model fitting

methods, no significant difference in precipitate recombination activity and size/density were determined for Si wafers from different heights in the ingot. This was theorised to be the result of high concentrations of segregated Cu in the central regions of the ingot overpowering any difference in concentration with ingot height.

In summary the different recombination behaviour of Cu precipitates between the two samples was determined to be due to differences in precipitate size and density as a result of different growth rates between dark and illuminated precipitation conditions. The presence of oxygen precipitates in Cz-Si (such as those used as the substrate in the plated cells analysed in future chapters) has been shown to reduce the nucleation barrier and accelerate the nucleation of Cu precipitates [137, 183]. However, the impact on the capture cross-section ratio in Cz-Si remains unclear. Consequently, it is difficult to relate the findings presented in this chapter directly to Cu-related degradation studies presented in Chapter 6.

Chapter 4 Copper Diffusion through Plated Metals in Solar Cell Contacts

For transition metals such as Cu to impact the performance of Si solar cells as we have seen at a wafer level in Chapter 3, they first need to be introduced into the substrate. In the case of Cu-plated solar cells, one of the key sources of metal contamination is from the plated contacts themselves. This chapter reports on the results of experiments which investigated the diffusion of plated Cu throughout the entire plated contact stack during extended thermal processing and long-term stability testing. Copper diffusion through capping metals on plated contacts is detailed, in terms of its relationship to the properties of the capping layer itself, as well as the impact it has on subsequent electrical degradation analysis with Suns- V_{OC} measurements following extended thermal aging. Observations of plated metal diffusion into the Si substrate are also presented and discussed in terms of Ni barrier quality for Cu-plated solar cells as a precursor to a more detailed electrical degradation analysis of different cell structures which is presented in Chapter 6.

4.1 Diffusion barriers for plated solar cells

4.1.1 Categorisation of diffusion barriers

The implementation of Cu as a replacement for Ag for solar cell contact formation demanded the development of efficient diffusion barriers to protect devices from Cu ingress. Ideally, this barrier layer should be electronically transparent (i.e. - low bulk resistivity and contact resistance), atomically opaque (resistant to inter-diffusion) and thermodynamically stable with adjacent materials [197]. The placement of chemically-different atomic layers in close proximity often leads to elemental migration which can be driven by a number of factors, such as concentration gradients, application of an electric field, availability of thermal energy, or the existence of negative free energy of reaction [198]. The effectiveness of diffusion barriers can be assessed using different approaches based on two primary failure modes: (i) metallurgical mode, whereby the chemical composition of the barrier is altered as a result of increased diffused metal

content within the barrier (several atomic percent), and (ii) electrical mode, in which the electrical properties of the substrate underneath the barrier are altered as a result of metal diffusion through the barrier layer without significant intermixing of the two metals, with the most common diffusion pathways being defects or grain boundaries within the barrier layer [28, 198]. These failure mechanisms indicate that microstructure of the barrier layer, such as the arrangement/density of grain boundaries, plays an important role in determining its performance. The microstructure of thin-film layers can be defined by one of the following categories – single crystal, polycrystalline (with either random or columnar grain structure), nano-crystalline (grain size < 5 nm) and amorphous (no long-range periodicity in lattice structure). These categories are illustrated in Figure 4.1 below.

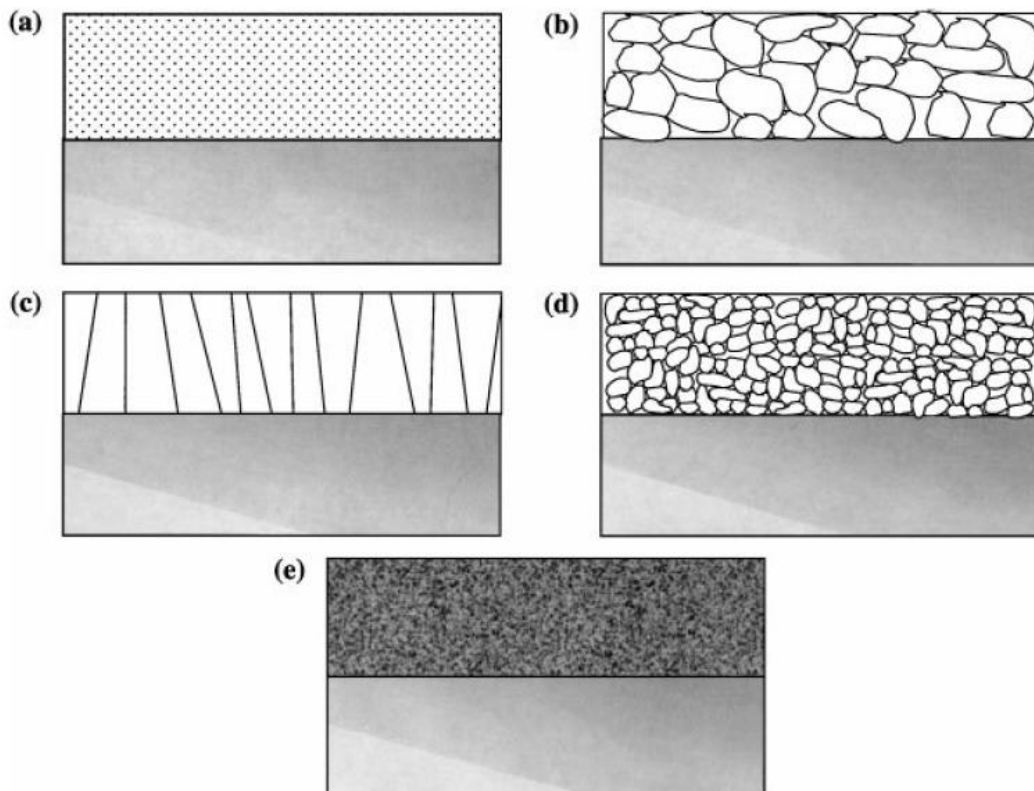


Figure 4.1: Thin film microstructure categories: (a) crystalline; (b) polycrystalline; (c) polycrystalline columnar; (d) nano-crystalline; and (e) amorphous (from [198]).

Metallic refractory alloys have been most extensively investigated as diffusion barriers for IC devices due to their high thermal stability, chemical inertness and high conductivity, ensuring minimal inter-diffusion during subsequent thermal processes involved in device fabrication [199]. Significant efforts were made by several groups in

the 1990s to develop effective thin film diffusion barriers through characterisation of the electrical failure mode of various barrier materials [200–213]. This was achieved by measuring the leakage current of reverse-biased p-n junctions to detect penetration of Cu into the Si substrate [28]. Tungsten (W), tantalum (Ta) and titanium (Ti) were the primary focus of these studies due to their desirable physical, chemical and electrical properties, with several binary and ternary compounds also examined. Through these studies, it was subsequently concluded that amorphous ternary alloys incorporating Si were the most effective diffusion barriers (TaSiN, TiSiN), with pure metals (Ta, W, Ti) having the least effective barrier properties of all the studied materials [214].

The microstructure of a thin film depends significantly on how it is deposited [215]. For films deposited by physical vapour deposition (PVD), a columnar polycrystalline structure is typically obtained, providing a direct fast diffusion path for Cu that traverses the entire film, resulting in the ineffectual diffusion barrier properties of pure metal films deposited by PVD [216]. In general, elemental materials are poor diffusion barriers unless they are completely absent of defects and grain boundaries [217]. To improve this, either the grain size can be increased by annealing after deposition, or the grain boundaries can be ‘stuffed’ with elements such as O, nitrogen (N) and carbon (C) by altering the deposition conditions, such as temperature and gas composition [218–220]. Further additions can be made during deposition (such as the addition of Si) to create nano-crystalline and amorphous films which operate most effectively [205, 221], although it was noted by Istratov *et al.* that Si-containing ternary compounds tend to have the highest resistivity of these barrier materials. Consequently, the Si IC industry tends to use TaN or TiN as a Cu diffusion barrier [28]. The effectiveness of different thin film categories can be ranked according to the flowchart in Figure 4.2.

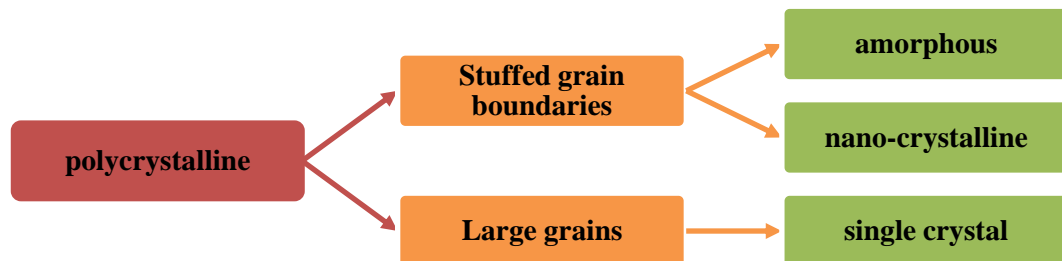


Figure 4.2: Classification of various diffusion barriers according to effectiveness, from worst (left) to best (right) performance (adapted from [219]).

4.1.2 Ni as a diffusion barrier for solar cells

Despite extensive studies on the properties of diffusion barriers for Cu interconnects published by the IC industry, comparative investigations of barrier layers for Si PV applications and their effectiveness are limited. As mentioned previously, the implementation of Ni-Cu plating for solar cell metallisation was developed by Motorola in the 1970s [12, 222], a process which involved electroless plating of a Ni seed layer that was then sintered to form a Ni silicide (NiSi), with the residual Ni stripped and then a contact stack of Ni and Cu deposited using flash plating followed by immersion capping with Ag to prevent corrosion of the Cu. During the same decade, several studies examining the effectiveness of electroless Ni as a diffusion barrier to Cu were also published. In 1974, Turn and Owen investigated the ability of plated Ni and Ni alloys in preventing inter-diffusion of Cu and gold (Au) [46]. Comparing Ni barrier layers of different compositions and thicknesses, an electron microprobe was used to examine the concentration-distance profile of Cu, Ni and Au at temperatures of 400 and 550 °C for 12 to 53 hours. Pinnel and Bennett then extended this analysis to a wider temperature and time range in 1976 [47], obtaining a series of inter-diffusion profiles for the Cu-Ni-Au system. An example of the profiles obtained is shown in Figure 4.3. In both studies, it was demonstrated that while Ni acted as an effective diffusion barrier over the conditions tested, it performed more as a retardant to Cu diffusion, rather than a perfect barrier.

Although Turn and Owen gave minimal description of the mechanisms responsible for the inter-diffusion observed in this early work, they provided early evidence for the improved barrier properties of alloyed and amorphous microstructures [46]. In the hypophosphite-based electroless Ni plating process used by Motorola, P is co-deposited with Ni at concentrations of 3-15% [223, 224]. As the concentration of P in the Ni alloy is increased, Turn and Owen showed that the penetration of Cu through electroless Ni barriers was significantly lower than that of pure electroplated Ni layers [46], a result that was also confirmed in several subsequent studies [49, 225, 226]. It was reported by Bredal *et al.* that once the percentage of incorporated P exceeds 11.6%, the Ni alloy becomes amorphous instead of polycrystalline [226], which explains the improved barrier qualities of impurity-containing Ni alloys (such as Ni-P and Ni-W [220, 227]) due to the elimination of grain boundaries which act as low energy diffusion paths for

Cu. With this early understanding of the barrier properties of electroless Ni layers in mitigating Cu diffusion, Motorola claimed 20 year stability for electroless Ni/Cu systems at $\sim 60^\circ\text{C}$ for 6 hrs/day [13]. Recent analysis of 20 year old BP Solar Saturn modules employing electroless Ni further indicated its effective barrier properties by demonstrating higher PR in the field than comparative screen-printed modules [52].

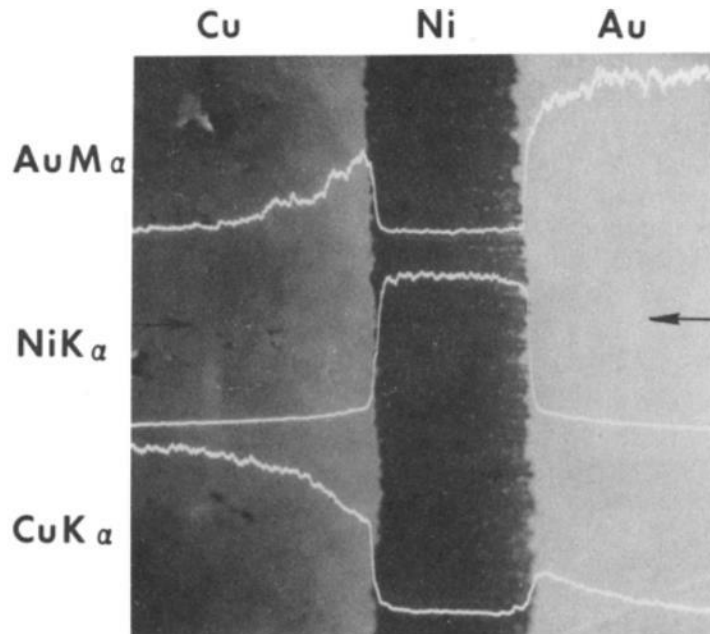


Figure 4.3: Representative inter-diffusion behaviour for Au/Ni/Cu layer stacks at an annealing temperature of 400°C for 80 days (from [47]).

A shift from electroless Ni plating to LIP [14, 23–25] was made when Suntech adopted Cu plating for the metallisation of their Pluto LDSE cells [21, 22, 228], thereby significantly reducing the plating time (3 hr reduced to 10 min for Cu plating) as well as increasing the lifetime of the electrolyte of their inline plating tool. However, the adoption of LIP or pure Ni in place of electroless Ni (doped with P) implied a polycrystalline barrier layer. Despite this, a number of studies have reported success in passing thermal cycling and damp heat tests with Ni/Cu plated modules as required by IEC 61215 quality standard [57, 229–231]. This suggests that, even if Cu is penetrating through the Ni diffusion barrier, it does not appear to be impacting cell performance.

This conclusion is supported by several stability studies tracking pFF of heat-treated Cu-plated solar cells [51, 54, 55]. Using a similar approach to that used by the IC industry (using leakage current to detect Cu precipitate formation at the junction),

Bartsch *et al.* rationalised that Cu penetration would result in an increase in junction recombination due to precipitation of Cu in the n-type region, which could be monitored with Suns- V_{OC} measurements during extended thermal exposure [50]. Using the time taken for the pFF to degrade below 95% of its initial value (similar to the requirements for module power degradation in IEC 61215), it was demonstrated that cell lifetime would not be limited by Cu diffusion with a 20 mg Ni layer (corresponding to ~ 200 nm barrier thickness), and that increasing the thickness of the Ni layer increases the time required to reach this degradation condition [232]. Performing the same test at different temperatures and then assuming an Arrhenius relationship resulted in an estimated activation energy, E_A , of 1.01 eV for 20 mg Ni, which is \sim half the E_A for intrinsic Cu diffusion through pure Ni [232]. Since pFF degradation involves several steps - Cu diffusion through the Ni layer, the Ag seed layer and the Si substrate, as well as Cu precipitation - the estimated E_A is representative of the fastest step associated with the degradation which may in fact be the precipitation reaction rather than the diffusion of Cu through Ni. Thus, the E_A estimated by Kraft for Cu transport through the plated Ni barrier supports previous evidence of the impact of microstructure on enhancing or inhibiting Cu diffusion into Si solar cells.

Despite the apparent electrical stability of Cu-plated cells employing Ni diffusion barriers, material studies present a different story. Flynn and Lennon [233] used cross-sectional transmission electron microscope (TEM) and energy dispersive X-ray spectroscopy (EDS) of heat-treated Cu-plated LDSE solar cells with both electroless and bias-assisted LIP Ni barrier layers, observing Cu precipitates in the underlying Si of both structures if cells were quenched in ethylene glycol (see Figure 4.4). However, if cells were allowed to slow cool (as would be expected in the field), no precipitates were observed. It was presumed that quenching resulted in a local saturation of Cu that was unable to out-diffuse to the surface, instead precipitating in the n-type region of the cell (similar to findings by Istratov *et al.* [36] and Flink *et al.* [37]). As has already been discussed in Chapter 2 and demonstrated in Chapter 3 of this thesis, n-type Si can behave as a very effective gettering site for Cu. Since the modules produced by BP Solar and Suntech both had heavily-doped selective emitter n^+ regions, and the stability tests of Bartsch *et al.* and Kraft *et al.* used cells with moderately heavy diffusions ($50\text{--}90 \text{ } \Omega/\square$) to enable the printing of a screen-printed Ag seed layer, this may have restricted the penetration of Cu to the n^+ regions of the device. In the absence of cooling

rates such as those subjected to plated cells in Flynn and Lennon's work (~ 1000 K/s), Cu typically has sufficient time to out-diffuse to the cell surface, minimising the potential of recombination-active Cu precipitates forming in the bulk of the cell. Although out-diffusion of Cu to the surface may be fortuitous for SE p-type solar cells, the sensitivity of more lightly-doped p-type PERC and n-type PERT Cu-plated cells with direct-plated Ni barriers on laser-ablated openings may be more severe.

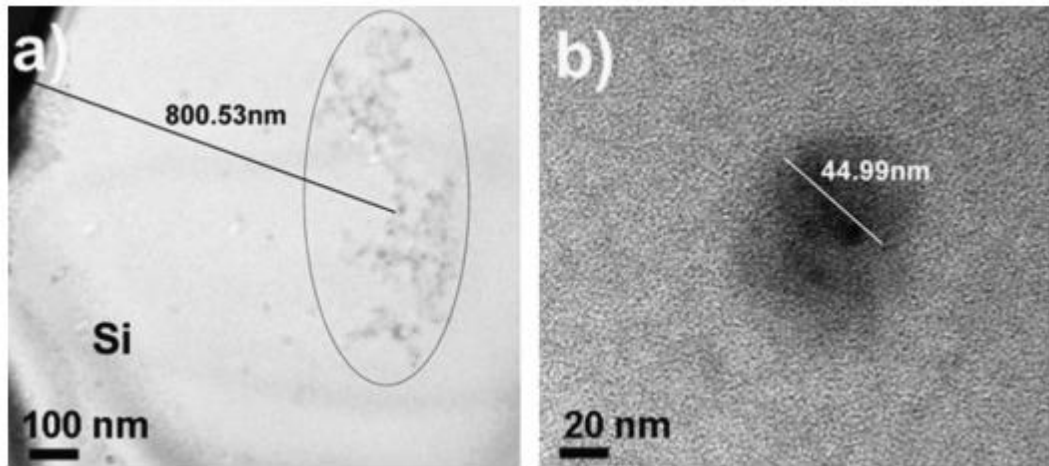


Figure 4.4: (a) closely-packed Cu precipitates (identified using EDS) located under a metal finger in a p-type LDSE cell heated at 400 °C for 5 hrs and then quenched in ethylene glycol; (b) a close-up view of individual Cu precipitates (from [233]).

It should be clear from this discussion that the assumption of direct-plated Ni as an effective diffusion barrier for Cu may be limited. Despite recent examinations of LIP-deposited Ni alloys (namely Nickel-Cobalt, NiCo) [234, 235], the industry has persisted in the application of polycrystalline Ni barrier layers for Cu-plated modules. By incorporating electrical degradation analysis with material characterisation techniques, a more complete picture of the diffusion behaviour of Cu through plated Ni barrier layers may be possible, which is the primary motivation behind the experiments described in the following sections of this chapter.

4.2 Cu diffusion through plated Ag layers

4.2.1 Introduction

Most plated cells employ a Ag capping layer to prevent the plated Cu from oxidising (if cells are not encapsulated) or to prevent Cu from being in contact with, and potentially reacting with, the encapsulant. Whilst BP Solar's Saturn modules were produced using plated Cu capped with immersion Ag, LIP Ag is can also be used [14]. When thermal testing is performed on cells using the methodology introduced by Bartsch *et al.* [50], it is assumed that the Cu remains capped with Ag during the heat treatment in order to prevent Cu oxidation from interfering with the accuracy of the measurements. However, from the discussion on diffusion barriers in Section 4.1, the typically polycrystalline nature of plated metals raises the concern that Cu may penetrate capping layers in experiments designed to test thermal stability and assess Cu diffusion into the Si substrate. Consequently, this section reports on the results of experiments which investigated the contact integrity of plated metal stacks during typical thermal annealing processes that are used to estimate cell lifetime in the field through an Arrhenius analysis [50, 51, 55].

4.2.2 Experimental

4.2.2.1 Plating process

The experimental results obtained from plated solar cells presented throughout this thesis are all obtained using a standard front contact processing sequence which is described in this section (see Figure 4.5 for a summary). Deviations from the standard processing sequence in this and future chapters are specified as required. For this particular group of experiments, cells were fabricated using 156 mm boron-doped 1-3 $\Omega\cdot\text{cm}$ Cz-Si wafers with random-pyramid texturing. A homogeneous phosphorus-doped emitter with a sheet resistivity $\sim 110\text{-}120 \Omega/\square$, surface concentration of $\sim 2 \times 10^{19} \text{ cm}^{-3}$ and junction depth of $\sim 0.4 \mu\text{m}$ was formed using POCl_3 diffusion. After rear etching, a 75 nm SiN_x antireflection coating (ARC) was deposited on the front surface using direct PECVD and a full-area aluminium (Al) rear contact was screen-printed and fired to form a full-area p^+ back surface field (BSF).

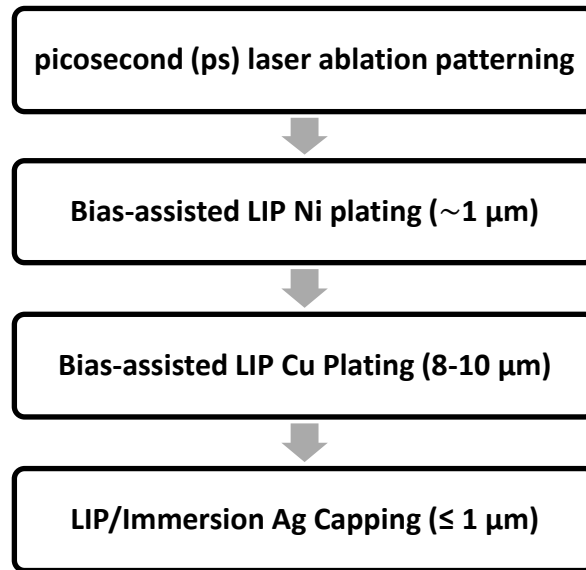


Figure 4.5: Summary of processing sequence common to all cell-based experiments as detailed in this thesis. Steps such as contact sintering and pre-processing before front contact patterning and plating are specified according to individual experiments.

Small cell contact grids (23 mm × 23 mm cell area) were patterned on the front surface using a 266 nm ps Lumera Super Rapid Nd:YAG laser with a BBO crystal for the 4th harmonic, integrated into a galvo/stage micromachining system. The laser system had a nominal aperture width of 15-20 μm and an average laser fluence of 0.44 J/cm² and 37% pulse overlap was used to form both the fingers and busbars (see Appendix B for a description of fluence calculations). The resulting ablated finger width was 13 μm (measured using an optical microscope) and a finger spacing of 1.5 mm (16 fingers in total) was used to form the metal grids via stage scanning. Busbars 1 mm wide were ablated with a 9 μm pitch between adjacent laser scans using stage scanning and each cell grid contained one centrally-located busbar. After removal of the native oxide by immersion of the front surface in 1% (w/v) hydrofluoric acid (HF), front contacts were formed on the exposed Si by plating a stack of Ni (~1 μm) and Cu (8-10 μm) using bias-assisted LIP (described in detail in Ref [236]) with Barrett SN1 Ni sulphamate (MacDermid Inc.) and Helios EP2 Cu (MacDermid Inc.) plating solutions, respectively. Bias currents of 23 mA/cm² and 40 mA/cm² were used for Ni and Cu LIP, respectively. The plating sequence was performed using single-side immersion tools developed in-house, in which electrical contact between the rear electrode and the solar cell is maintained using a vacuum chuck, and the cell front surface in contact with the plating solution is illuminated from underneath, as illustrated in Figure 4.6. To minimise

depletion of metal ions at the Si surface and maintain a constant plating rate, the solution was maintained at a set temperature with a heat bath and refreshing of plating solution was achieved with a recirculation pump. The plated surface was rinsed in DI water between each plating step to prevent cross-contamination, with the surface also kept wet to prevent oxide growth during the deposition of the front contact stack which could impact adhesion.

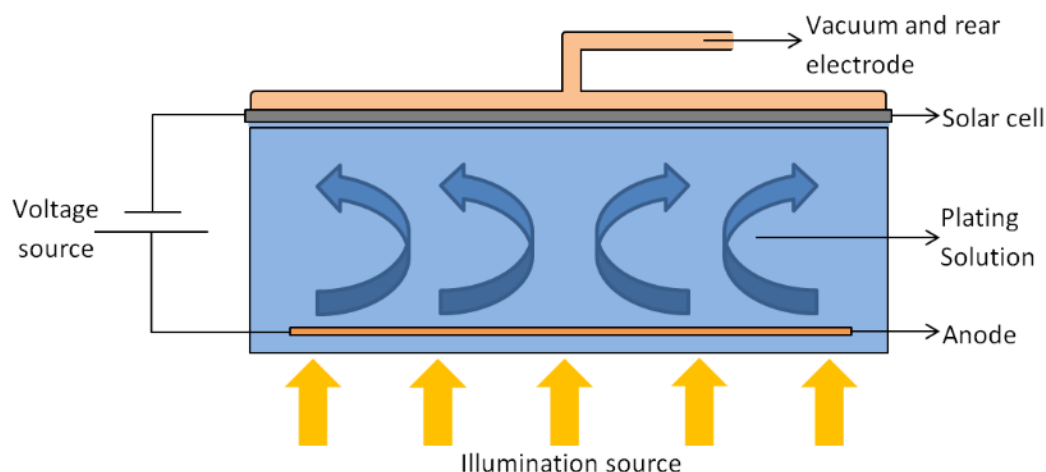


Figure 4.6: Schematic of bias-assisted LIP process employed in this experimental work. The blue arrows represent the re-circulation of plating solution to minimise depletion of the Cu and Ni ions at the Si wafer surface.

Two different capping methods were examined in these experiments: (i) Ag capping deposited using bias-assisted LIP (MacDermid Helios Silver EPF 400); and (ii) capping with a Ag immersion solution (MacDermid Helios Silver IM 452). The average thicknesses of the capping metals were $\sim 1.0 \mu\text{m}$ and $\sim 0.3 \mu\text{m}$ respectively. Each 156 mm cell precursor contained 25 small cells as can be seen in the PL image presented in Figure 4.7, so individual cells were laser-cleaved after plating for edge isolation, characterisation and further processing. The final dimensions of the small plated cells were $25 \times 25 \text{ mm}^2$.

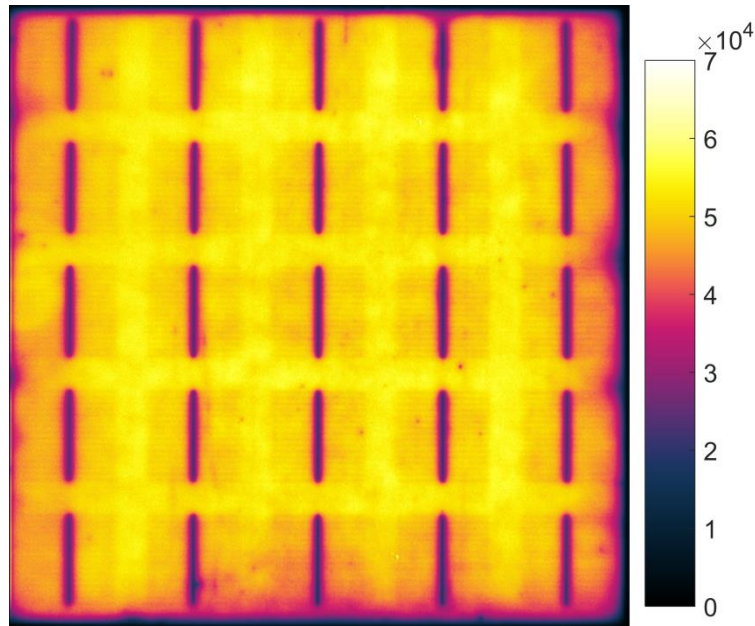


Figure 4.7: Open-circuit PL image of a 156 mm wafer after ps-laser ablation of 25 small cell contact patterns on the SiN_x front surface (photon flux = $2.55 \times 10^{17} \text{ cm}^{-2}\text{s}^{-1}$, exposure time = 0.1 s).

One group was sintered in a rapid thermal processing (RTP) furnace at 350 °C for 1 min in N_2 ambient before characterisation to form a Ni silicide layer, whilst a second group was characterised without sintering. The formation of Ni silicide in cells from the first group was assumed based on previous reports that confirm Ni silicide formation at temperatures of 250-400 °C [237–240]. Cells were exposed to 200 °C in a muffle oven with N_2 ambient for 500 hours to simulate long-term operation at elevated temperatures. Selected samples from each group were used as a control for contact characterisation and did not undergo thermal stability testing. After thermal annealing at 200 °C, some cells were quenched in ethylene glycol (cooling rate $\sim 1000 \text{ K/s}$) immediately after thermal treatment followed by rinsing in DI water while the remaining cells were cooled under ambient conditions (cooling rate $\sim 4 \text{ K/s}$). The different quenching methods were examined to see whether the quenching process contributed to any changes in the contact integrity after thermal annealing, based on the effect of quenching observed by several studies previously mentioned in Section 4.1.2. Individual cell batches will be referred throughout this chapter according to batch IDs based on their processing conditions. A full description of the cell processing conditions examined in this experimental work are summarised in Table 4.1.

Table 4.1: Summary of processing conditions examined in the diffusion barrier analysis experiments detailed in this chapter. Each condition is given an ID which is then combined to describe individual batches of cells.

| Capping Metal | ID | Sintering Condition | ID | Cooling Method | ID |
|---------------|----|---------------------|----|-----------------|----|
| LIP Ag | L | Sintered | S | Quenched | Q |
| Immersion Ag | I | Non-Sintered | NS | Ambient Cooling | A |

4.2.2.2 Characterisation

Cells were electrically characterised before and after thermal exposure using a combination of light and dark I - V measurements using a calibrated in-house constant illumination I - V tester under standard test conditions. Suns- V_{OC} measurements were performed using a Sinton Instruments illumination-voltage tester, with Suns- V_{OC} being measured at three points along the 25 mm long busbar (one at each end of the busbar and one in the centre). Characterisation of the contact structure at regions of interest was performed by obtaining cross-sections using single beam focussed ion beam (FIB) milling (FEI XP200), followed by high-resolution imaging of the contact cross-section using the same tool. A thin layer (1 μm) of platinum (Pt) was deposited on top of the plated contact stack prior to milling to minimise damage of the sample caused by the high current beam during milling. TEM specimens were then prepared using the FEI XP200 and TEM imaging was performed with a Philips CM200 TEM system. EDS measurements were obtained with a Bruker SDD detector.

4.2.3 Results and discussion

During thermal stability testing of the Cu-plated cells, a discolouration of the plated front contacts was observed (see Figure 4.8). This discolouration was visible after only 1-2 days of continuous thermal exposure at 200 °C in the dark. It was often accompanied by anomalous data obtained during Suns- V_{OC} measurements of plated cells after thermal stability testing, and more specifically a reversal in the open-circuit voltage (V_{OC}) that was measured at illumination intensities greater than ~ 2 Suns (see Figure 4.9). This indicated some form of thermally-induced contact damage.

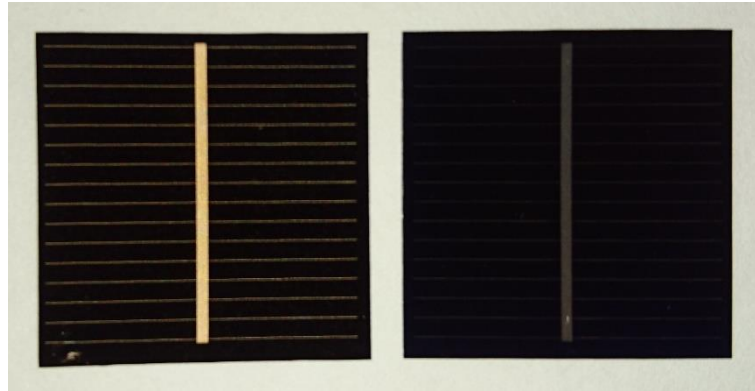


Figure 4.8: Photo of a p-type Al-BSF solar cell with Cu-plated front contacts and LIP Ag capping layer (a) before thermal stability testing (i.e., after plating and sintering), and (b) after 500 hours thermal exposure at 200 °C.

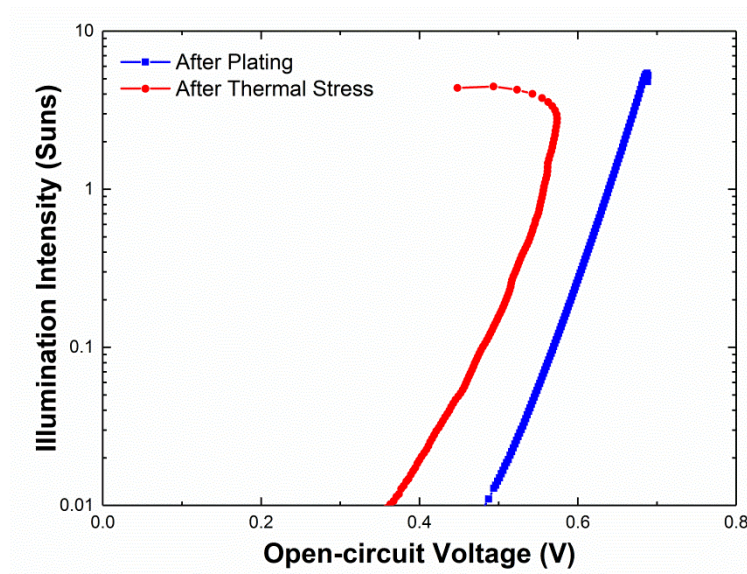


Figure 4.9: Suns- V_{OC} curve measured for a Cu-plated solar cell with a LIP Ag capping layer (sintered) before and after thermal exposure at 200 °C for 500 hours.

For cells exhibiting this voltage reversal at high illumination intensities, there was a significant reduction in the 1-Sun V_{OC} determined using the Suns- V_{OC} measurement compared to the V_{OC} measured on the same cells using an I - V tester. Additionally, the severity of the 1-sun V_{OC} mismatch between the I - V and Suns- V_{OC} measurements varied between different front contact structures and processing sequences. Figure 4.10 graphs V_{OC} values obtained from I - V and Suns- V_{OC} measurements for the different processing groups. The Ag capping method impacted the 1-sun V_{OC} mismatch considerably, with up to 100 mV mismatch recorded for cells capped with a LIP Ag capping layer

compared to ~ 50 mV for cells capped with an immersion Ag layer. Sintering proved to be the next most significant factor, with cells that had undergone sintering prior to thermal stability testing experiencing a larger 1-sun V_{OC} mismatch overall, regardless of the Ag capping method employed. However, no clear correlations were evident between cooling method (i.e., quenching vs ambient cooling) and the severity of the 1-sun V_{OC} mismatch.

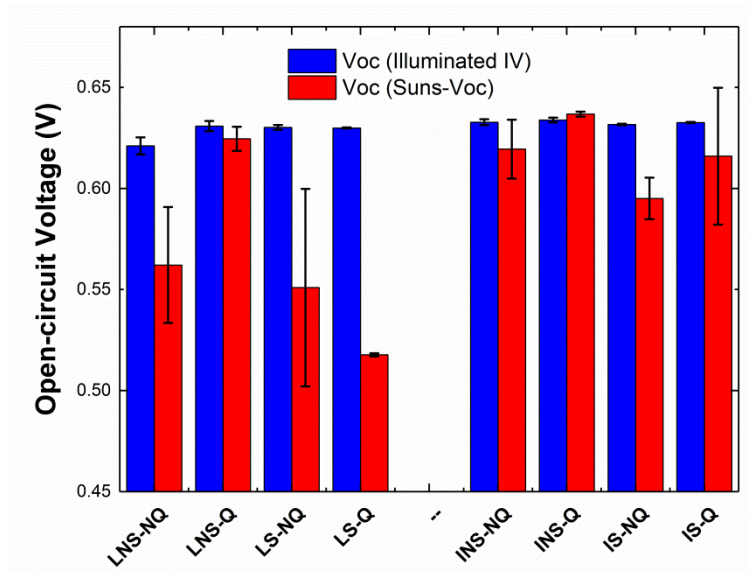


Figure 4.10: Comparison of V_{OC} measurements on cells with different Ni/Cu/Ag plated structures using I - V and Suns- V_{OC} measurements. The x-axis captions are labelled according to the convention outlined in Table 4.1.

Initially, it was suspected that the observed non-ohmic behaviour in Suns- V_{OC} measurements was due to the presence of a Schottky barrier between the measurement probe and the Si, with the Schottky diode building up an opposing voltage to the cell junction voltage at high illumination intensities when the contact resistance between the metal and Si was increased. Although generally observed in relation to rear point contacts [241–243], it has also been reported for plated laser-doped bifacial cells, where insufficient p-type dopants were incorporated during laser doping of the contacts [244]. To understand the underlying cause of this discrepancy between Suns- V_{OC} and I - V measurements, FIB cross-sectional images were obtained from plated cells before and after annealing at 200 °C for 500 hrs in N_2 ambient to examine any deterioration in the plated metal stack. Figure 4.11 shows FIB cross-sections taken before and after extended thermal exposure on plated cells with different contacts stacks.

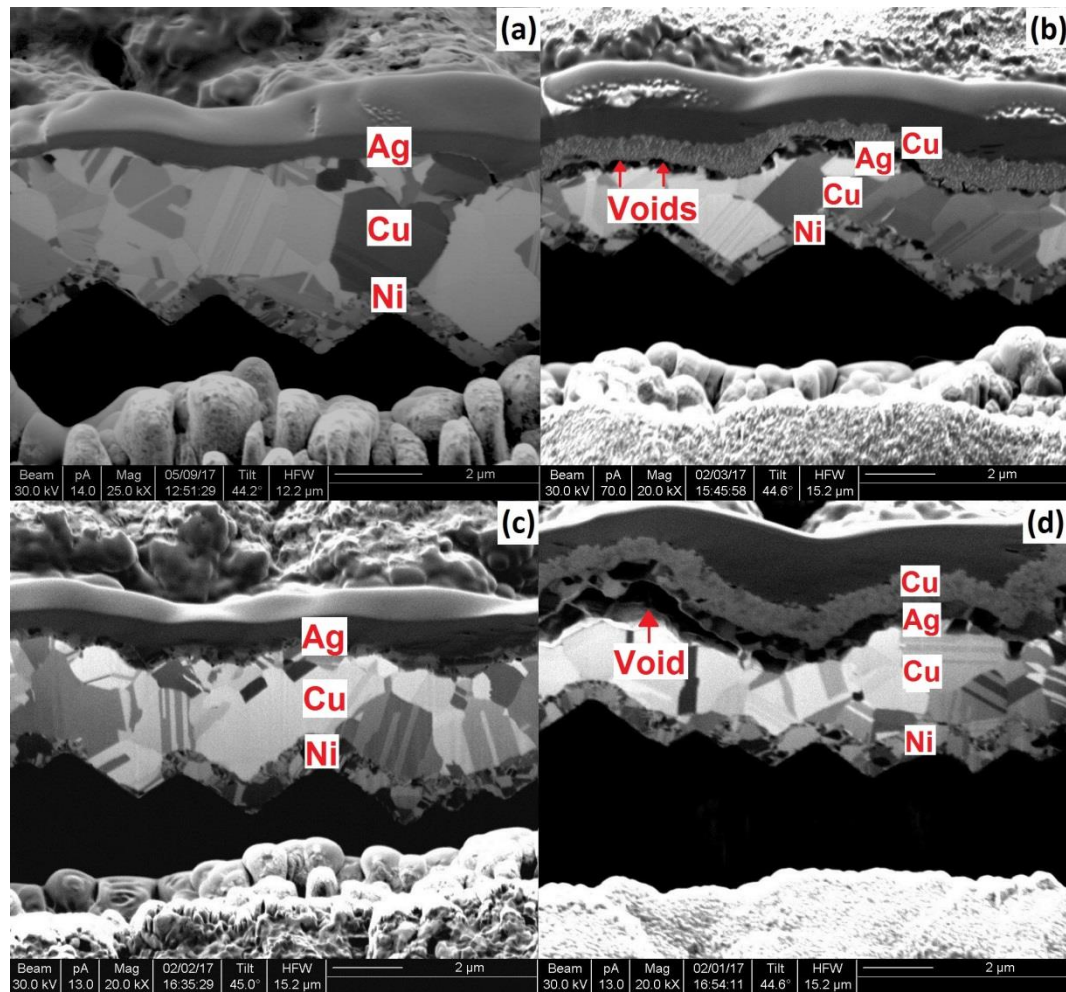


Figure 4.11: Cross-sectional FIB Images of Ni/Cu/Ag plated and sintered contacts with different capping layers before and after thermal testing at 200 °C for 500 hr: (a) immersion Ag before; (b) immersion Ag after; (c) LIP Ag before; and (d) LIP Ag after. The average thickness of the Ag capping layer was 0.3 and 1 μm for the immersion Ag and LIP Ag cells, respectively.

No clear evidence of deterioration in the Ni/Si or Ni/Cu interface was observed in any FIB cross-sections, yet extensive void formation was evident between the Cu and the Ag capping layer. In the LIP Ag capped cells, these voids were several micrometres long as can be seen in Figure 4.11(d), whilst the voids were often smaller and more dispersed in the immersion Ag capped samples, such as that visible in Figure 4.11(c). Furthermore, a completely new layer had developed above the capping Ag in both plated structures (with a thickness of 0.5-1.5 μm). Subsequent TEM/EDS analysis revealed this new layer to comprise of diffused Cu which had formed during thermal stability testing.

In Figure 4.12, EDS line scans of a sintered immersion Ag and sintered LIP Ag plated stack reveal this newly-formed layer to comprise of mostly Cu, but with a small amount of O also being detected. The high-resolution TEM images and EDS line scans also confirm the presence of voids between the plated Cu contact and Ag capping layer.

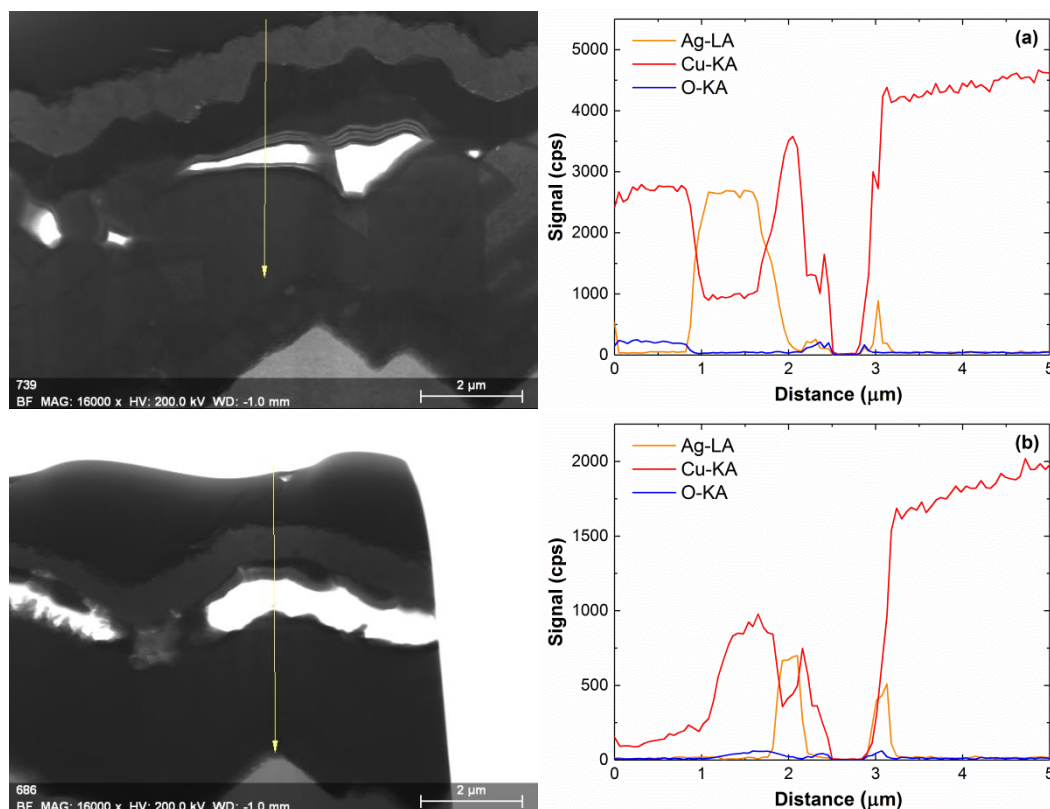


Figure 4.12: High-resolution TEM Image (left) an EDS line scan (right) across a plated Cu contact stack (sintered) capped with: (a) LIP Ag; and (b) immersion Ag capping.

Aside from a recent study by Lee *et al.* that showed evidence of diffused Cu on top of a LIP Ag capping layer after 60s of sintering at 350 °C [240], the presence of such a significant layer of diffused Cu on top of the Ag capping layer for plated solar cells had not been reported in any previous work examining thermal stability of plated contacts, which is surprising as it is not unexpected given the polycrystalline nature of plated metals, especially the LIP Ag capping layer. As discussed in Section 4.1, most barriers act as a retardant to Cu diffusion rather than a complete barrier, especially in the case of polycrystalline barriers formed by most plating techniques since Cu can diffuse rapidly along grain boundaries [205, 245, 246]. Tompkins and Pinnel [247] estimated that at 150 °C the rate of growth of a diffused Cu layer over an electroplated Au capping layer was ~ 45 Å per day (equivalent to ~ 0.1 μm after 500 hrs at 150 °C). At low

temperatures (≤ 250 °C), diffusion along grain boundaries and crystal defects in the plated metal dominate, with an activation energy approximately half that observed for lattice diffusion through an intrinsic metal layer [232, 248]. Thus, the presence of distortion in the Suns- V_{OC} curve after only 1-2 days at 200 °C suggests very low activation energies for Cu diffusion through the Ag capping layer.

Models of grain boundary diffusion typically assume an empty ‘pipe’ (i.e., a grain boundary or dislocation) and an ‘infinite sink’ at the surface. A sink is usually assumed to be a chemical reaction at the surface (e.g., oxidation of Cu), with an ‘infinite sink’ implying that the rate of diffusion is slower than the rate of the surface reaction. Tompkins and Pinnel showed that for Au-capped Cu on printed circuit boards, different ‘surface sinking’ environments could impact the rate at which the Cu penetrated the Au capping layer. Annealing samples in a vacuum resulted in less Cu transport through the capping layer than when samples were annealed in air, where Cu at the surface could be oxidised thereby providing a more effective ‘sink’ reaction. However, even more extensive Cu transport through the Au was observed when the Cu/Au samples were annealed on the printed circuit board. During annealing, chlorine (Cl) was released from the board, and it was proposed that the Cl could react with the Cu as traces of Cl were detected in the surface Cu layer [247].

The surface reaction providing the ‘surface sink’ in this case was not clear given that the cells were annealed in N_2 , which should have minimised surface Cu oxidation. Without such a sink, the diffusion channels through the Ag would have been expected to become saturated and thus reduce the amount of Cu transported through the capping layer. However, a small amount of O was detected in the EDS analysis of the surface Cu layer after thermal annealing. This may have been due to low levels of O being present in the muffle furnace during annealing, or due to impurities that may have been incorporated in the plated stack during deposition. It can be very difficult to completely eliminate O at each of the Si, Ni and Cu surfaces while plating and during sintering/annealing, desorption of such impurities to the surface may offer an appropriate sink [249, 250].

Various models of grain boundary diffusion have been proposed [251–253], although the dependence of diffusive mass transport on the specifics of crystal structure (grain size, impurities at the surface, boundary width and tortuosity), as well as the varying

nature of the surface sink, make it difficult to apply previous measurements of Cu diffusion rates to this particular case. The grain structure of the Ag capping layer depends on the deposition method, with LIP Ag layers being relatively thick (1 μm in this work) and comprising larger grains ($> 500\text{ nm}$) whereas immersion Ag layers are typically thinner ($< 0.5\text{ }\mu\text{m}$) and consist of smaller grains (generally $< 100\text{ nm}$, although difficult to determine from FIB imaging). EDS maps of each type of plated cell as shown in Figure 4.13 show improved layer integrity of LIP Ag compared to immersion Ag capping layers. In certain sections along the TEM, the immersion Ag layer almost disappears entirely, as seen in the extreme case of a sintered immersion Ag capping layer shown in Figure 4.13(b). In the case of immersion Ag capping, this layer may instead perform more as a sacrificial barrier to Cu, with the Ag intermixing with the Cu during thermal processing to produce the more dispersed void formation observed in immersion-capped cells after thermal exposure [205, 209, 222, 254]. Sintering is known to increase grain size [255], and in doing so, may have provided more efficient diffusion paths for Cu to penetrate the Ag capping layer, resulting in the more extensive non-ohmic behaviour observed in sintered cells with both methods of Ag capping. The increased frequency of large void formation in immersion Ag capped cells that had been sintered also suggests that the increased grain size may have influenced the performance of this layer as a sacrificial barrier. Thus, it is possible that there is a relationship between barrier crystallinity and inter-diffusion between two adjacent metals layers.

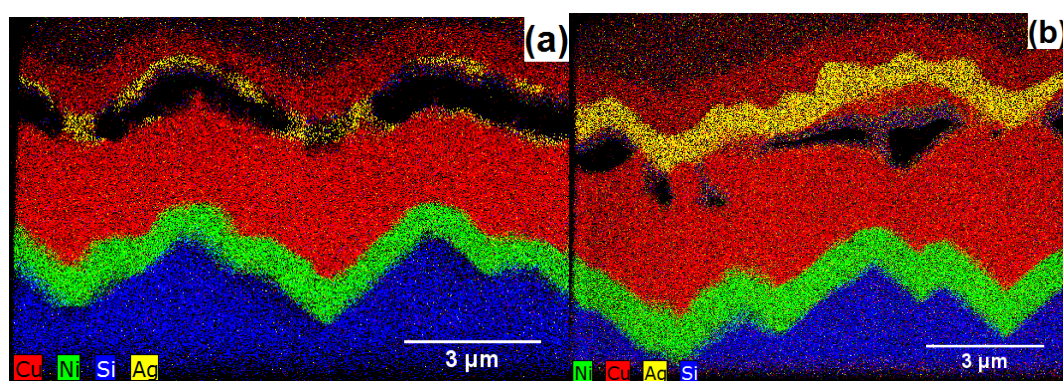


Figure 4.13: EDS maps of a plated contact after sintering and extended thermal exposure at 200 °C for 500 hrs with: (a) immersion Ag; and (b) LIP Ag capping layers.

In an attempt to remove the non-ohmic behaviour, the busbar regions originally probed were ‘scratched’ with the probe tip and then the measurement was repeated. This process removed the voltage reversal effect at high illumination intensities as seen in

Figure 4.14, providing a measured 1-Sun V_{OC} that more closely matched the results obtained with the calibrated I - V tester. A small discrepancy between the two values remained, but these were expected primarily due to differences in the illumination sources used in the Suns- V_{OC} and I - V measurements (flash lamp compared to steady-state halogen lights). Although this improvement after ‘scratching’ could be interpreted as evidence of the presence of a resistive oxide at the surface which is then removed by this process (cuprous oxide is known to act as a semiconductor [256], potentially creating a Schottky barrier between the probe and the metal contact), the FIB cross-sections in Figure 4.15 indicate that collapsing of the voids between the Cu and Ag was responsible for the V_{OC} recovery in Suns- V_{OC} measurements.

The presence of voids in the contact structure at the Cu/Ag interface indicates that high resistance between the probe and the solar cell was responsible for the distorted Suns- V_{OC} curves. The voids reduced the effective contact area between the probe and the underlying cell, thus increasing resistance between the probe and the cell [242]. Although the presence of voids was not reported at the Cu/Au interface, Tompkins and Pinnel similarly reported a large increase in contact resistance after low-temperature annealing ($10\text{ m}\Omega$ to $> 10\text{ }\Omega$ after annealing at $125\text{ }^{\circ}\text{C}$ for 5 days [247]). However, since no resistance effects were observed in the I - V measurements (as highlighted in Table 4.2 below), the increased resistance in this case is not due to any series resistance effects within the cell, but due to the external resistance between the cell and the measurement system used to obtain Suns- V_{OC} data. Thus, collapsing the voids reduced the resistance between the probe and the sample, improving the accuracy of the Suns- V_{OC} data and confirming that the voids due to Cu diffusion were the root cause of the distorted Suns- V_{OC} measurements obtained in these experiments.

Table 4.2: Summary of selected I - V results before and after thermal treatment of Cu-plated solar cells with different Ag capping layers (sintered).

| Ag Capping | Thermal Treatment | I - V V_{OC} (mV) | Sinton V_{OC} (mV) | FF (%) | η (%) | R_s ($\Omega\cdot\text{cm}^2$) |
|------------------|-------------------|----------------------------|-------------------------|-------------|---------------|---------------------------------------|
| Immersion | Before | 639 | 640 | 76.8 | 19.3 | 0.89 |
| | After | 631 | 591 | 75.2 | 18.6 | 0.84 |
| LIP | Before | 636 | 639 | 76.5 | 19.1 | 0.97 |
| | After | 631 | 535 | 75.7 | 18.6 | 0.91 |

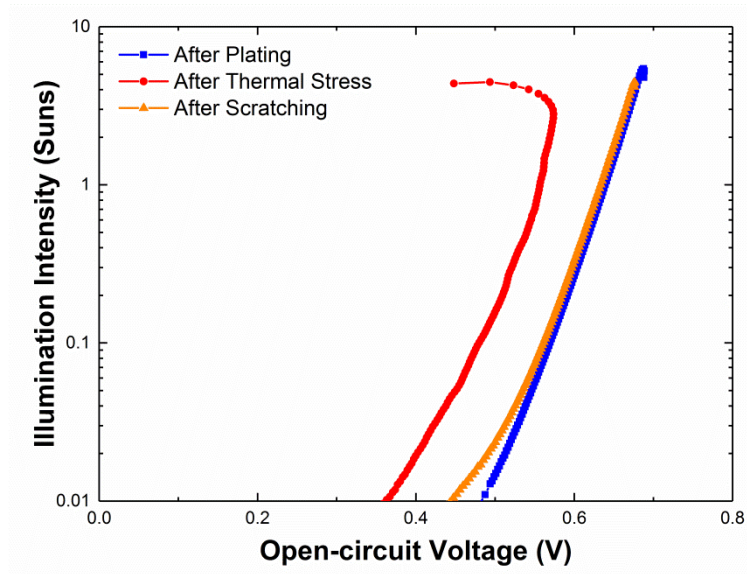


Figure 4.14: Comparison of Suns- V_{OC} curves obtained before and after ‘scratching’ of the busbar region on a plated solar cell with a LIP Ag capping layer (sintered) after 500 hours at 200 °C.

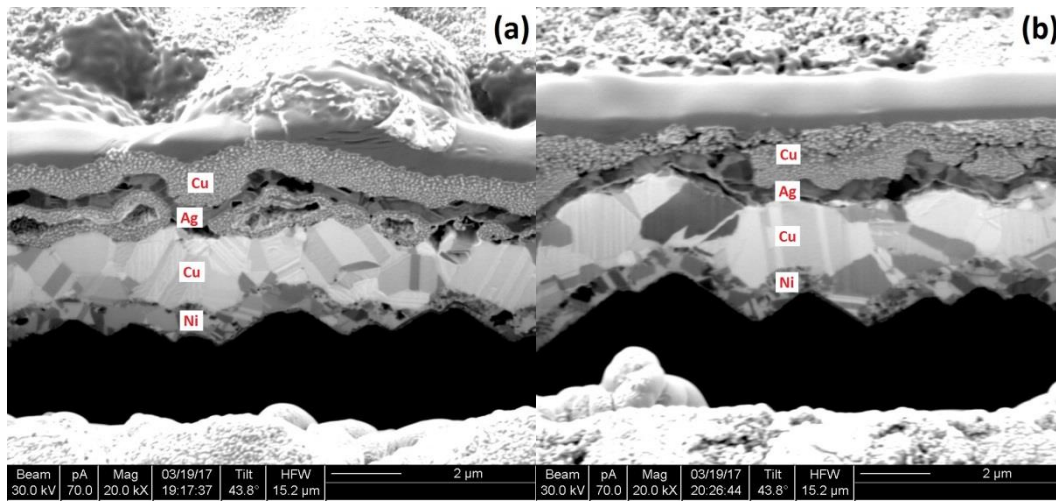


Figure 4.15: Cross-sectional FIB images of plated contact (sintered) with a LIP Ag capping layer: (a) before ‘scratching’ the busbar; and (b) after ‘scratching’ the busbar.

This external resistance effect can be modelled according to the equivalent circuit presented in Figure 4.16, which has been defined previously to model un-metallised cells with high contact resistance [257]. For simplicity, the solar cell is represented by a photodiode acting as a voltage source, with the resistance effects of the solar cell itself assumed to be negligible (a fair assumption based on the corresponding I - V results measured for each sample after thermal treatment as highlighted in Table 4.2).

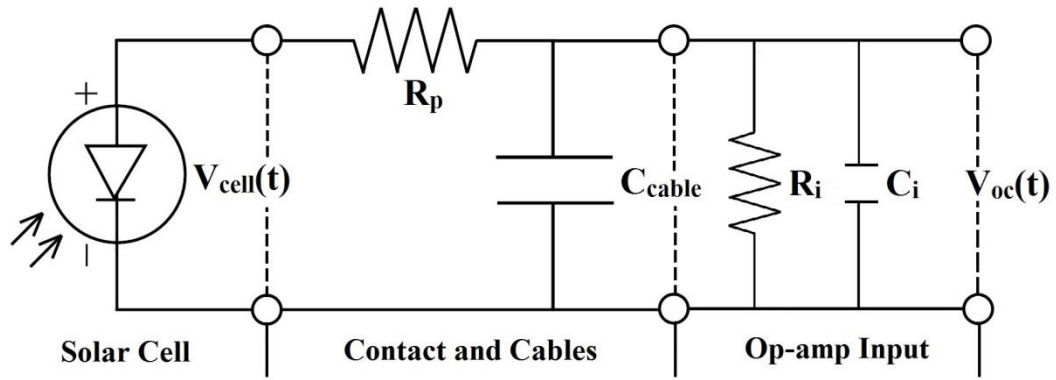


Figure 4.16: Equivalent circuit diagram describing a solar cell coupled with a Suns- V_{OC} measurement system (based on model presented in [257]).

The voltage measured during a Suns- V_{OC} measurement is not the actual V_{OC} of the device, but instead the voltage measured at the amplifier inputs of an A/D data acquisition card used by the tool. The solar cell voltage, V_{cell} , is modified by an RC low-pass filter formed by the capacitance of the tool, C_C (made up of the cable capacitance, C_{cable} and input capacitance of the amplifier, C_i) and the probing resistance between the cell and the probe, R_p . Based on the one-diode model, the open-circuit voltage of the solar cell during a single pulse of the flash lamp can be described by:

$$V_{cell}(t) = \frac{nkT}{q} \left(\frac{J(t)}{J_0} + 1 \right) \quad (4.1)$$

where $J(t)$ is the light-generated current density as a function of time, J_0 is the recombination current density, k is Boltzmann's constant, n is the solar cell ideality factor, q is the elementary charge, and T is the absolute temperature in Kelvin. A single flash pulse (see Figure 4.17) can be separated into two distinct phases – an initial steep rise in light intensity, followed by an exponential decay with a time constant normally on the order of 1-2 ms. In the case of minimal probe resistance, $V_{oc}(t)$ will closely follow the device voltage, $V_{cell}(t)$. However, as demonstrated by Weber and Aberle [257], a high external resistance can result in the observed voltage reversal during the first phase of a flash pulse. During this first phase, the effect of the RC low-pass circuit increases, distorting the high intensity region and creating a rounding of the curve as seen in Figure 4.9. During the second phase of the flash pulse, the exponential decay

only results in a small error from the RC circuit, and thus V_{oc} and V_{cell} follow each other closely.

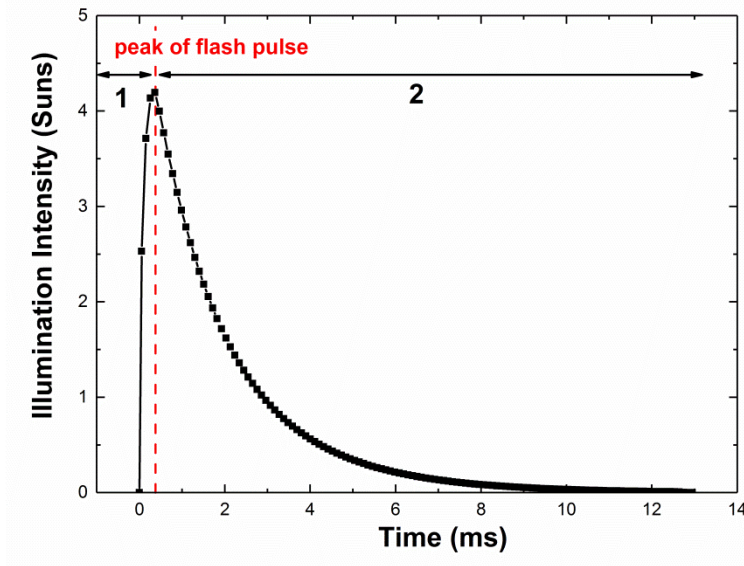


Figure 4.17: Intensity profile for the flash lamp used in the Sinton Suns- V_{oc} tester. The red dash line coincides with the peak intensity, followed by an exponential decay with a time constant, $\tau = \sim 1.7$ ms.

The cell voltage after passing through the RC low-pass circuit is defined according to:

$$V_{RC}(t) = \left(V_{cell}(t) - R_p C_C \frac{dV(t)}{dt} \right) \quad (4.2)$$

However, the description provided by Weber and Aberle was insufficient to explain the voltage shift of the entire curve observed in this experimental work. The cause of this shift was the result of a limitation of the Suns- V_{oc} setup used in these experiments. The input voltage at the amplifier was not just affected by the probe resistance and the capacitance of the tool, but also by the input impedance of the amplifier itself, R_i . Thus, the cell voltage measured at the amplifier input was determined by:

$$V_{oc}(t) = \left(V_{cell}(t) - R_p C_C \frac{dV(t)}{dt} \right) \times \frac{R_i}{R_p \times R_i} \quad (4.3)$$

Depending on the input impedance of the data acquisition card (R_i), the voltage measured by the tool may be shifted significantly. The importance of having a high

input impedance to combat high contact resistance has been stressed previously in relation to Suns- V_{OC} measurements on directly-probed a-Si:H and μ c-Si:H devices [258]. As a result, Weber and Aberle performed their measurements on a system with $R_i=1\times 10^{12} \Omega$, such that even probe resistances of $1 \text{ M}\Omega$ had minimal impact on the Suns- V_{OC} outside of the initial distortion around the peak of the flash pulse [257]. However, Sinton and Cuevas quoted an input impedance of $\sim 1 \text{ M}\Omega$ in their original paper describing the Suns- V_{OC} measurement [241]. Since the distorted curves observed in these experiments were measured on a Sinton tool, the input impedance of the tool had to be verified. To do this, a variable resistor was placed in series between the measurement probe and the input to the amplifier. A control cell with no voids was measured with increasing probe resistance between the cell and A/D card, successfully replicating the observed distortion in the Suns- V_{OC} curve with increasing resistance. The replicated series of Suns- V_{OC} curves are presented in Figure 4.18.

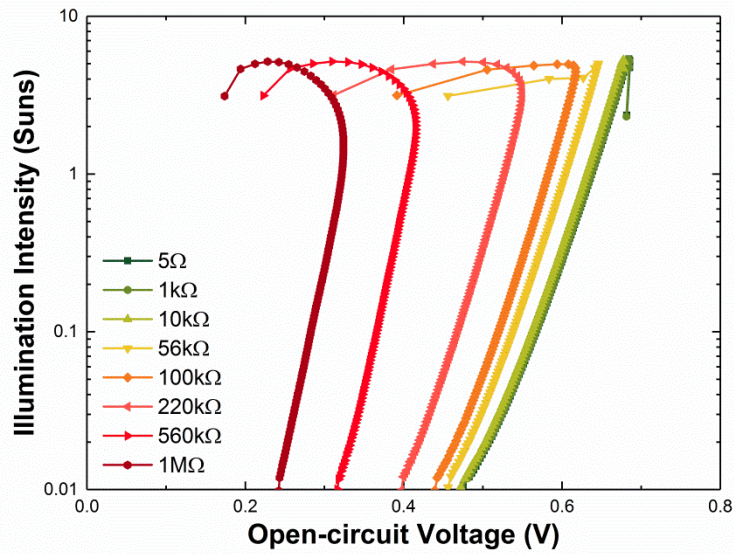


Figure 4.18: Comparison of Suns- V_{OC} measurements on a Cu-plated cell with an external variable resistor connected in series between the probe and the input to the amplifier.

The point at which the 1-Sun V_{OC} , determined from the Suns- V_{OC} curve without any external series resistance effects was halved, represented the input impedance of the amplifier for the tool. From these simulated measurements, the input impedance of the amplifier for the Suns- V_{OC} tool employed in this work was concluded to be approximately $1 \text{ M}\Omega$. Using these simulated measurements, the distortion observed in Figure 4.9 corresponded to a probe resistance of $\sim 140 \text{ k}\Omega$, potentially providing a

useful metric for determining the extent of void formation between plated Cu and Ag capping metals in future studies.

The distortion of the curve around the peak of the flash pulse becomes more rounded as the probe resistance increases due to the increasing RC low-pass effect, and the combination of high probe resistance and low input impedance of the A/D card causes the voltage to shift to a lower range. Fitting of the Suns- V_{OC} curves was also attempted according to Equation 4.3, assuming an amplifier input impedance of 1 M Ω (as determined from the simulated measurements) and a total capacitance of 200 pF (100 pF for a 1 m long RG-58 coaxial cable and 100 pF for a typical A/D card from National Instruments used in Sinton measurement systems [259]). However, the equivalent circuit model alone was insufficient to describe the rounding of the high intensity region of the curve observed due to high probe resistance. Since the calculation of illumination intensity during a flash measurement is dependent on measuring the rate of change in carrier density (which itself relies on measuring the voltage change of the device with time), any distortion in the voltage at the input of the amplifier would not only impact V_{OC} but also the calculation of illumination intensity. Thus, the equivalent circuit model presented in this work should be coupled with a correction of the illumination intensity data based on the distorted voltage measurements.

This distortion of Suns- V_{OC} data suggests that when assessing the stability of plated contacts for solar cells using the pFF technique reported in [50], it is important to consider the effect of contact integrity in the Suns- V_{OC} measurement. Figure 4.19 summarises pFF results obtained before and after ‘scratching’ the busbar. The spread in pFF is significantly greater in the data obtained before ‘scratching’ (blue results in Figure 4.19), with both underestimations and overestimations of pFF measured. The value of pFF determined by Suns- V_{OC} differed by 5 - 10 % compared to that measured after ‘scratching’ the busbar, with the three different Suns- V_{OC} measurements along the busbar of the same cell also varying significantly which indicated non-uniform void formation along the busbar during thermal exposure. After ‘scratching’, all three measurements produced similar outputs for diode parameters and pFF , indicating improved contact uniformity. The spread of the data was greatly reduced after ‘scratching’, with the remaining spread a result of variations between individual cells in

each batch, which was related to potential Cu penetration through the Ni barrier layer, as discussed in more detail in Section 4.3.

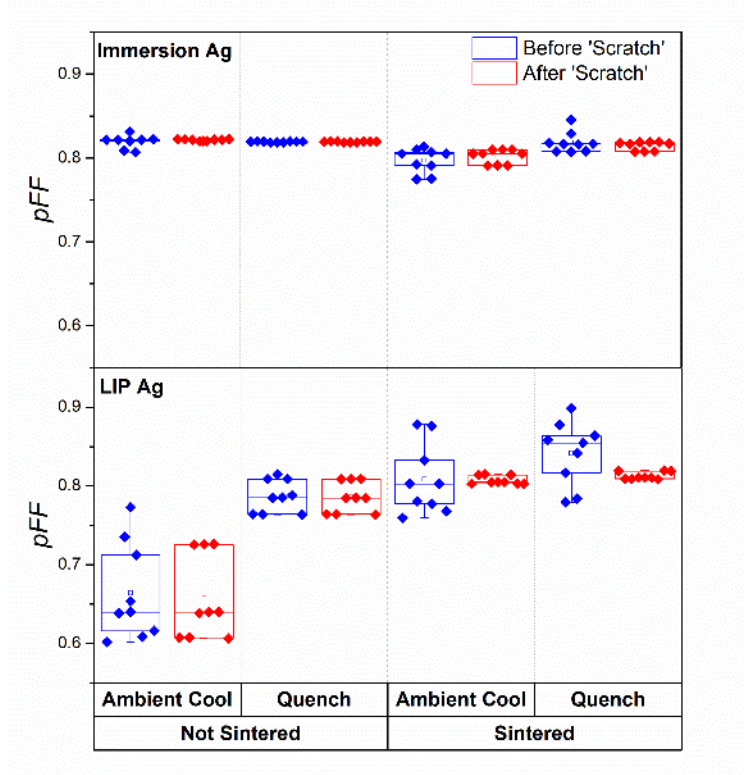


Figure 4.19: Summary of pFF estimates obtained by Suns- V_{OC} measurements on plated solar cells with different processing sequences before and after ‘scratching’ the busbar to address the impact of void formation during thermal treatment.

As mentioned previously in Section 4.1.2, current studies of long-term plating stability based on the method developed by Bartsch *et al.* set a threshold for cell degradation at a 5% relative loss in pFF from its original value [50, 51, 54]. By performing the same measurements at different temperatures, a group of time-temperatures combinations can be plotted into an Arrhenius relationship which can then be extrapolated to estimate the time required to reach the same degradation state under field conditions. Since the diffusion behaviour described by this Arrhenius relationship is exponential, small uncertainties can result in significant differences in estimated lifetime. Thus, a 5-10% variation in pFF could lead to an incorrect determination of threshold degradation time for a certain temperature, which will shift the Arrhenius plot, leading to an incorrect estimation of cell lifetime. The behaviour presented in this chapter may be an extreme case, but it highlights the importance of checking contact

integrity when using pFF values obtained from Suns- V_{OC} measurements to establish long-term stability of Cu-plated cells.

The accuracy of Suns- V_{OC} measurements can be improved in several ways, such as ensuring sufficient input impedance of the Suns- V_{OC} tool, reducing the input capacitance of the A/D card or by increasing the probing contact pressure to collapse the voids before a measurement. However, the distortion observed was instrumental in identifying and characterising Cu diffusion, and by employing a variable input impedance, it may be possible to further characterise Cu diffusion through Ag capping layers by relating it to the probing resistance, R_p . Alternatively, the effects of probing resistance induced by Cu diffusion and void formation can be bypassed entirely in the future by replacing Suns- V_{OC} with Suns-PL [260–262], allowing a more focussed analysis of Cu diffusion through the Ni barrier into the underlying Si.

Another very important question raised by these results is whether Cu diffuses through Ag capping layers in encapsulated modules operating in the field, and if this occurs then what is the impact on module electrical performance. If this was to occur, then Cu would be expected to come into contact with encapsulant and evidence of Cu reaction with encapsulant should be apparent. However, no such behaviour has been reported to date. This could be due to the lack of an efficient sink reaction in encapsulated modules to drive Cu diffusion. The temperature of 200 °C used in this study was also significantly higher than expected field temperatures, and so some cells were exposed to a typical field-operating temperature of 80 °C for 500 hrs. The FIB cross-sections of cells after the heat treatment are shown in Figure 4.20.

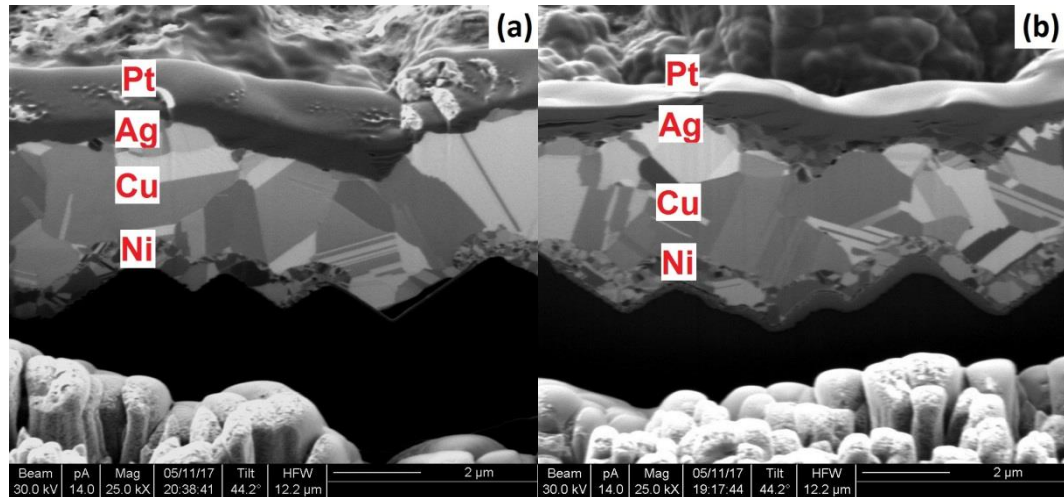


Figure 4.20: Cross-sectional FIB images of a plated contact (sintered) with: (a) an immersion Ag capping layer; and (b) a LIP Ag capping layer, after 500 hrs at 80 °C.

At this annealing temperature, there was no evidence of voids at the Cu/Ag interface or a diffused Cu layer above the Ag in the contacts of cells capped with immersion Ag and LIP Ag, suggesting that Cu diffusion may only be driven at a higher temperature. This also means that the impact of the interdiffusion reported in this section may be limited to higher temperature thermal treatments used, for example, to predict the lifetime of plated modules in the field. Whilst no Cu diffusion was observed, the FIB images did reveal both non-uniform Ni layer formation and an unidentified layer underneath the plated Ni, which will be examined in more detail in the next section.

4.3 Evidence of Cu diffusion through plated Ni barriers

4.3.1 Introduction

Copper diffusion into Si through the plated Ni was also examined using FIB and TEM imaging techniques after thermal treatments of cells. This investigation was motivated by an earlier report by Flynn and Lennon which identified the presence of Cu precipitates in the Si region under the Ni/Cu plated contacts [233]. Correlations between observed Cu diffusion through Ni barrier layers and associated degradation in cell performance can provide useful information in assessing the electrical impact of Cu penetration into Si. This section presents results from the same thermally-processed cells used for the experiments reported in Section 4.2, with the focus now on the Ni/Si

interface and associated electrical degradation of Cu-plated cells in the absence of external resistance effects.

4.3.2 Experimental

The cells discussed in this section were the same batch of cells processed according to the experimental details provided in Section 4.2.2. Electrical performance (I - V and $Suns$ - V_{OC}) was measured before and after extended thermal exposure at 200 °C for 500 hrs, with external resistance effects eliminated from $Suns$ - V_{OC} measurements by applied pressure to the contact probe before measurement. Characterisation of the Ni/Si interface was performed by FIB milling (FEI XP200), followed by high-resolution imaging of the contact cross-section using the same tool. TEM specimens were then prepared using the FEI XP200 and imaging was performed with a Philips CM200 TEM system. EDS measurements were obtained with a Bruker SDD detector.

4.3.3 Results and discussion

Figure 4.21 graphs the V_{OC} , pFF and η of Ni/Cu/Ag plated solar cells before and after thermal exposure at 200 °C for 500 hours. Since the plating sequence was identical for all cells regardless of the Ag capping layer, they have been combined in this case to focus more on the impact of sintering and cooling rate (see Appendix C for detailed cell results). Unlike the examination of Cu diffusion through the Ag capping layer, determining trends for Cu diffusion through the Ni barrier were significantly more complicated. Most cells performed reasonably well after 500 hours of thermal exposure, with 75% of cells experiencing < 5% loss in efficiency. However, some cells degraded by ~ 20% relative efficiency after thermal exposure, suggesting significant penetration of Cu into the underlying material. Contrary to the behaviour observed with the Ag capping layers, the most degradation was observed in cells with non-sintered Ni barrier layers. Also contrary to the discussion in Section 4.1.2, quenching did not result in any enhanced degradation of plated cells due to Cu diffusion through the Ni layer.

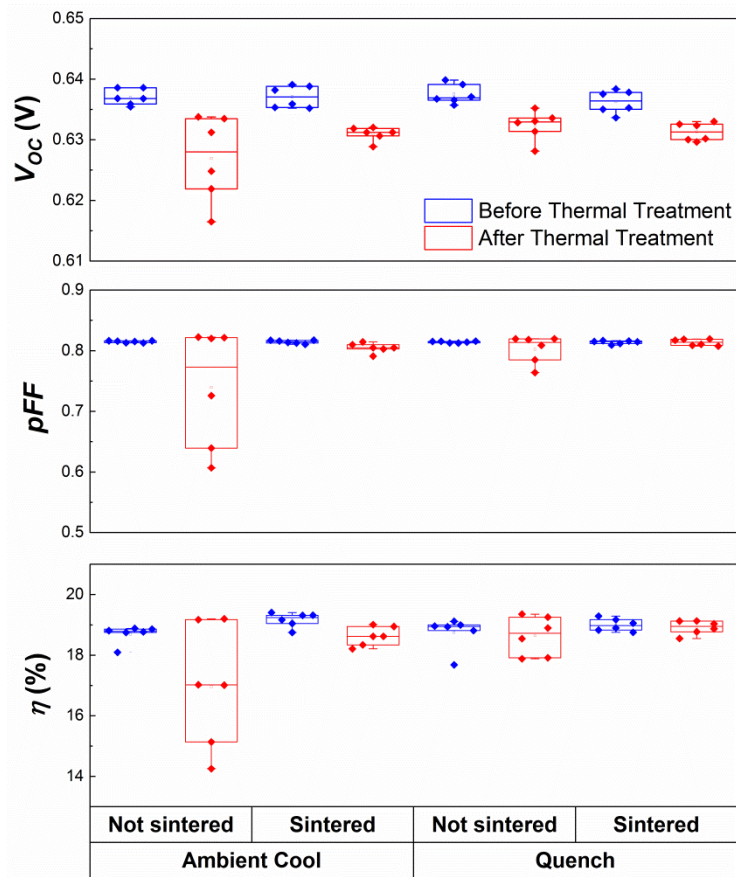


Figure 4.21: Performance summary of plated solar cells with both LIP and immersion Ag capping layers before and after extended thermal exposure at 200 °C for 500 hrs.

Something that is clear from the FIB images presented in the previous section is the polycrystalline nature of the LIP Ni barrier layer plated for these solar cells. Upon closer examination of the Ni layer itself (see Figure 4.22), the evolution in microstructure after sintering the plated contacts is visible. After sintering, the high density of small grains is annealed into an arrangement of larger grains. The purpose of sintering the contacts is primarily to grow a NiSi layer that improves adhesion of the plated metal to Si, although sintering to increase grain size has also been demonstrated to remove tensile stress within the plated metal as a result of self-annealing behaviour within the plated metal [255, 263]. However, the increased grain size should have also resulted in more efficient diffusion paths according to the trend in diffusion barrier effectiveness discussed earlier in this chapter [205], leading to more pronounced Cu-related degradation in the sintered cells.

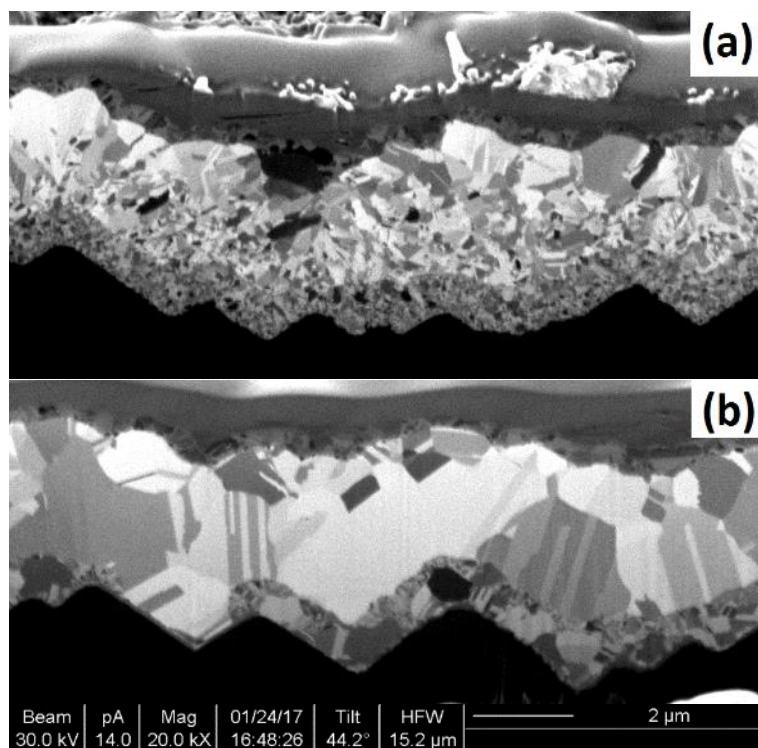


Figure 4.22: Cross-sectional FIB images of a plated contact with a LIP Ag capping layer: (a) before sintering; and (b) after sintering, showing evolution in microstructure.

High resolution TEM and EDS line scans presented in Figure 4.23 revealed the presence of large areas of Cu in the Si underneath the Ni barrier layer in both LIP Ag capped and immersion Ag capped cells that had degraded during thermal stability testing (corresponding relative pFF losses of 3% and 1%, respectively). These large regions of diffused Cu extended as far as $0.4\ \mu\text{m}$ from the Ni/Si interface, and most likely consisted of a cluster of Cu precipitates that had formed at the surface. Although difficult to conclude from the results obtained in these experiments, it was noticed that these Cu clusters appeared deeper in the Si when the Ni barrier was thinner. As seen in the EDS line scan results, the Ni layer in Figure 4.23(a) is approximately $0.8\ \mu\text{m}$ thick, and the Cu is located at the Ni/Si interface. For the LIP Ag capped cell in Figure 4.23(b), the Ni layer is roughly half that ($\sim 0.4\ \mu\text{m}$) with the Cu peak within the Si region appearing further from the Si surface. Whilst both clusters were detected in the near surface region, it is possible that the thicker Ni layer provided a more effective diffusion barrier, resulting in a shallower penetration of Cu into the Si substrate. Furthermore, the observed Cu penetration depth between these samples corresponded with their relative pFF losses (more degradation with deeper penetration depth). This

would concur with previous studies highlighting that thicker Ni layers improve the long-term stability of plated solar cells with Ni as a barrier layer [47, 50, 51].

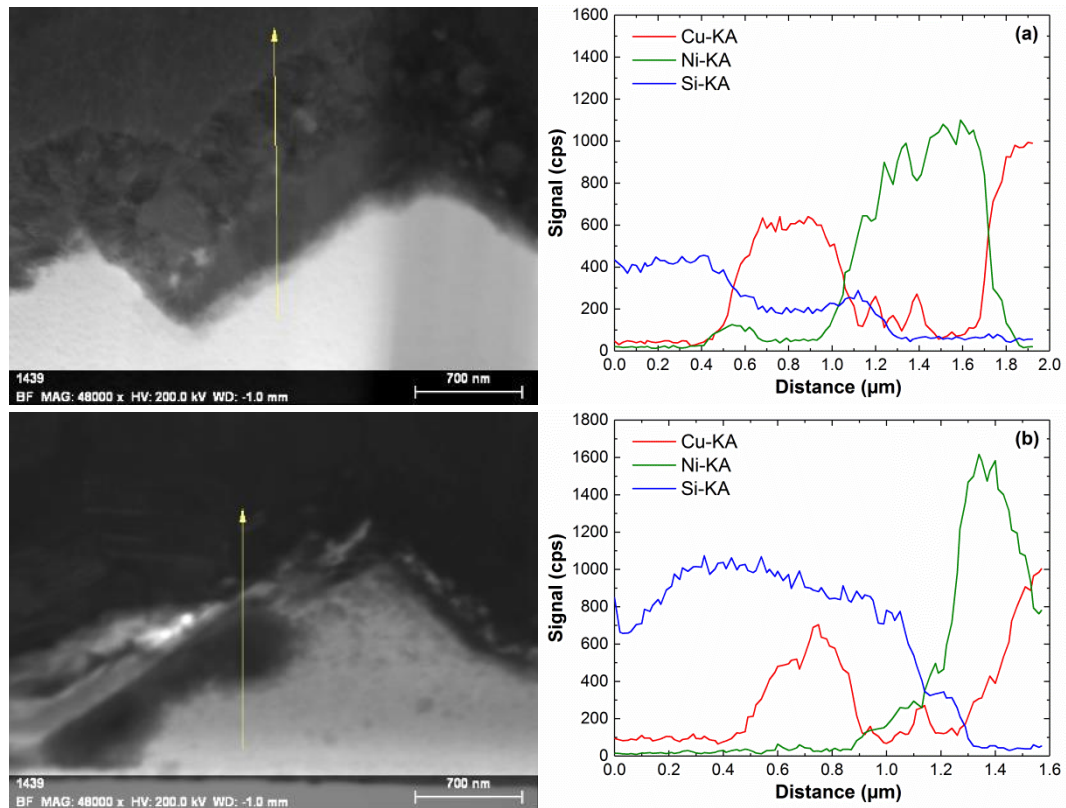


Figure 4.23: High-resolution TEM Image (left) and EDS line scan (right) across the Si/Ni/Cu interface with (a) immersion Ag capping (sintered) and (b) LIP Ag capping (sintered), after 500 hrs at 200 °C.

In Figure 4.24, comparative EDS maps of Cu diffusion through a region with a uniform Ni layer and a region with large gaps in the Ni barrier further highlight the impact of uniformity in the Ni layer on the extent of Cu penetration into the Si substrate. In the presence of a uniform Ni layer, Cu that had penetrated through the barrier appeared to be localised to a surface region near the Ni/Si interface. Similar observations have recently been presented in a study by Dang *et al.*, who also observed surface Cu build-up at the Ni/Si interface after thermal stability testing at 235 °C [264]. However, in the absence of a Ni layer, Cu was detected deeper in the Si and voids between the Cu and Si are evident. This suggests that Cu diffusion behaviour may differ significantly depending on whether it occurs in the presence or absence of a diffusion barrier. In the presence of a barrier layer, grain boundary diffusion is the primary mechanism behind Cu penetration into Si, with defects at the surface possibly providing

a sink reaction for continued Cu penetration and the subsequent build-up of Cu precipitates at the surface. Without a barrier layer, more Cu can reach the Si where it can penetrate further into the Si to find other sink reactions such as oxygen precipitates in the Si or crystal defects, such as dislocations or stacking faults, in the lattice that initiate the nucleation of Cu precipitates [28, 136].

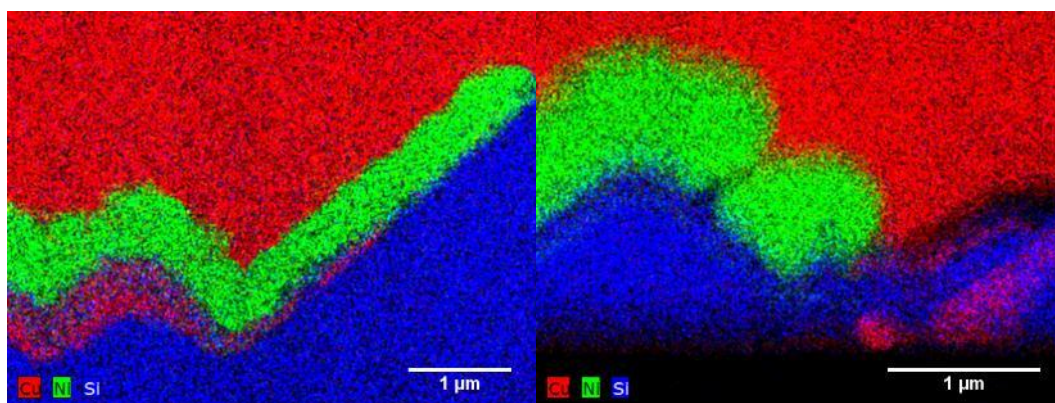


Figure 4.24: EDS maps showing Cu penetration through (a) a uniform Ni barrier layer (sintered), and (b) a non-uniform Ni barrier layer (sintered) after 500 hrs at 200 °C.

It is also important to consider the influence of non-uniform laser ablation and potential laser-induced defects at the surface (e.g., produced during laser ablation of a dielectric ARC) providing an effective sink reaction for Cu to diffuse through Ni and precipitate at the surface [265, 266]. Non-uniform ablation of the front dielectric would impact the ability to form a uniform Ni layer during plating (though remaining dielectric could not be confirmed in this work), and whilst SiN_x has been demonstrated as an effective barrier to Cu diffusion in previous studies [51], partial ablation of the SiN_x may have prevented the plating of Ni which resulted in a weakened barrier, presenting an effective diffusion path for Cu to enter the Si substrate.

It appears the dominating factor impacting Cu diffusion through the Ni layer is not microstructure as in the case of the Ag capping metal, but rather the uniformity of the Ni barrier between the Cu and the Si. In the presence of a uniform Ni layer, it is possible that the crystallinity of the barrier is more important. As mentioned earlier, thicker Ni layers improve the long-term stability of plated solar cells with Ni as a barrier layer [47, 50, 51], thus large non-uniformities in the plated Ni layer thickness potentially due to non-uniformities in the laser ablation of the contact openings can result in several entry points for Cu to pass through the barrier metal entirely and

penetrate deeper into the Si substrate where it can degrade plated cell efficiency. The influence of laser ablation conditions on Cu penetration into Si through plated Ni barrier layers will be discussed in more detail in Chapter 6.

4.4 Chapter Summary

In this chapter, observations of Cu diffusion through plated Ag capping layers and Ni diffusion barrier layers in contact structures for Si solar cells after thermal treatment were presented. Motivated by an approach of combining electrical and material characterisation to determine diffusion barrier effectiveness, the behaviour of Cu diffusion through polycrystalline plated metals was assessed under different processing conditions following extended thermal exposure utilised in long-term stability testing of plated solar cells.

Suns- V_{OC} curves recorded after 500 hours at 200 °C demonstrated a reversal in the V_{OC} at high illumination intensities. Examination of the thermally-aged contacts using a combination of FIB cross-sectional imaging and EDS/TEM imaging revealed the presence of a 0.5-1.5 μm thick layer of diffused Cu on top of the Ag capping layer and significant void formation between the Cu and Ag layers. The presence of these voids was identified as the cause of the V_{OC} reversal at high illumination intensities, with an increased external resistance between the measurement probe of the tool and the solar cell resulting in the voltage reversal artefact due to an RC low-pass effect within the system. Low input impedance to the A/D card also caused the curve to shift to lower voltages, which resulted in a significant mismatch between the 1-Sun V_{OC} determined with Suns- V_{OC} compared with that measured using calibrated I - V measurements.

The extent of void formation was demonstrated to be dependent on the microstructure of the Ag capping layer, with thicker LIP Ag layers experiencing more severe void formation than cells capped with an immersion Ag layer. This was presumably because the more amorphous nature of the immersion Ag layer provided less grain boundary pathways for Cu diffusion. Sintering the cells after plating resulted in greater V_{OC} distortion, and this was theorised to be due to the creation of more efficient grain boundary diffusion paths by grain growth that occurs during sintering.

Collapsing the voids by applying high pressure to the contacts through ‘scratching’ was demonstrated to remove the void artefact from subsequent Suns- V_{OC} measurements. However, it was demonstrated that the distortion caused by degraded metal stack integrity could result in errors of 5-10% in extracted pFF values. This highlights the sensitivity of this technique to contact integrity and the potential for significant errors in the predicted lifetime of Cu-plated solar cells from an Arrhenius analysis.

Examination of the Ni/Si interface of the heat-treated cells also revealed Cu penetration through the plated Ni barrier layer, although any relationship to Ni microstructure was more difficult to determine in this case. The primary factor impacting Cu ingress through the Ni barrier layer was identified to most likely be uniformity of the Ni layer. Thinner regions of Ni were accompanied by deeper penetration of Cu into the Si surface as identified in TEM/EDS line scans and mapping. In some samples, large gaps in the Ni layer resulted in Cu directly in contact with Si, with Cu detected further into the Si than if a uniform Ni layer was present. The lack of uniformity in Ni barrier layers across the plated cells examined in this study made it difficult to conclude whether sintering of Ni improved or weakened its qualities as a barrier to Cu diffusion.

In summary, the experimental work presented in this chapter revealed the propensity of Cu to diffuse through polycrystalline plated metal layers. The diffusion is mediated by grain boundaries in the polycrystalline metal and may only occur if a ‘sink’ reaction exists for the Cu. This new understanding means that it is necessary to consider fully the impact of using Cu as part of the metal contact for Si solar cells, and if Cu is used, then a more complete understanding of the properties required for barrier layers is required. The use of plated Ni as an effective diffusion barrier for Cu has been assumed since the 1970’s when Motorola developed the electroless Ni/Cu system used by BP Solar in the production of their Cu-plated Saturn modules. Although these modules appear to be performing well in the field, the results presented in this chapter highlight the importance of validating the effectiveness of diffusion barriers from a physical, or metallurgical, perspective as well from an electrical perspective, as the next generation of higher efficiency Si solar cells may be more sensitive to metal impurities and Cu ingress (through plated Ni barrier layers) may indeed start to impact module performance in the field.

Chapter 5 Elemental Analysis of Plated Ni Barrier Performance

The importance of Ni barrier uniformity in determining its effectiveness at mitigating Cu ingress into the Si substrate was reported in Chapter 4. However, the techniques employed in the previous chapter required long sample preparation/analysis times and only provided qualitative information about the relationship between Ni barrier uniformity, Cu diffusion into the Si wafer and associated degradation of Cu-plated solar cell performance during thermal stability testing. In this chapter, the application of laser ablation inductively-coupled plasma mass spectrometry (LA-ICP-MS) as a more quantitative technique for the analysis of Cu penetration from plated contacts into Si is described. The applicability of LA-ICP-MS was assessed based on several factors – the minimisation of surface metal interference for accurate analysis of Si substrate contamination, the characteristics of laser ablation efficiency during line-scanning measurements, and the ability of the technique to correlate degradation of cell *I-V* response with an increase in metal content in the Si substrate.

5.1 Elemental analysis techniques for bulk impurities in silicon

For the analysis of plated metal uniformity and penetration of metals into the Si substrate of solar cells, a microanalytical technique with high spatial/depth resolution capable of sampling small areas comparative to the contact dimensions is required. Several analytical techniques have been applied in previous studies to analyse impurity concentrations in Si materials, although these have predominantly focused on the analysis of either surface impurities on Si wafers or near-surface impurities incorporated into Si during ingot formation or subsequent processing. Secondary ion mass spectrometry (SIMS) is one of the most commonly used elemental analytical techniques in the semiconductor industry for both surface and depth profiling of a range of impurities introduced into the Si material during different stages of both wafer and cell production [267, 268]. A schematic of a SIMS measurement setup is presented in Figure 5.1. In a SIMS measurement, the sample material is sputtered with a primary ion source

(such as oxygen, O_2 or caesium, Cs), ejecting secondary ions that are subsequently detected and analysed to determine depth-resolved impurity concentration profiles (nm range resolution) with low limits of detection ($< \text{ppb}$) and high lateral resolution ($< 10 \mu\text{m}$) [268, 269]. As a result, SIMS has been used to characterise near-surface dopant profiles [270–272], quantify surface metal contamination [273, 274] and also measure bulk impurity concentrations in low-cost Si substrates [275]. It has also been previously employed in Cu diffusion barrier analysis by Stavrev *et al.* to determine the effectiveness of rf-magnetron sputtered Ta films with different grain structures, demonstrating the improvement in diffusion barrier quality with amorphous structure as discussed in the previous chapter [219]. However, simultaneous sampling and ionisation leads to SIMS suffering severe matrix effects (related to the interaction between a sputter source and individual sample matrix components), high molecular ion formation as well as relative sensitivity factors (RSF) of several orders of magnitude between different elements due to variations in the sputtering yield of different materials [268, 276]. Segregation of Cu under ion bombardment during SIMS measurements [277] has also been detected, and this further limits the applicability of SIMS for bulk depth profiling of Cu contamination from plated metals on a Si surface.

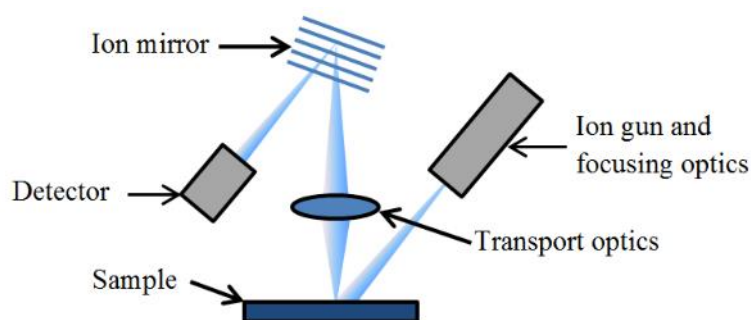


Figure 5.1: Schematic of SIMS measurement setup (adapted from [278]).

Glow discharge mass spectrometry (GD-MS) or glow discharge optical emission spectrometry (GD-OES) [279] improves upon SIMS in several ways. By separating the sputtering from ionisation, interference due to matrix effects is reduced resulting in relatively uniform RSFs for all elements [280]. As illustrated in the measurement schematic shown in Figure 5.2, the sputtering ion source is produced by passing an electrical current through a gas, such as Argon (Ar). This generates a partially-ionised gas (glow discharge) which is sustained in a reduced pressure environment [281].

Ionised Ar particles sputter the sample (which acts as the cathode in the glow discharge setup), and then the sputtered material is ionised in the glow discharge before being carried to the mass spectrometer for elemental analysis [281]. The reduced vacuum requirements of GD-MS compared to SIMS allows for faster depth profiling (a few μm over several minutes) with comparative depth resolution to SIMS (in the nm range) [282]. Detection limits in the sub-ppb range are achievable with GD-MS/GD-OES, which makes it highly suited to the analysis of ultra-trace impurities in Si [283]. As a result, it has been applied to the characterisation of impurities in several photovoltaic applications [279, 284–288], including the aforementioned study by Stavrev *et al.* on Ta diffusion barrier analysis [219]. However, the large sputter area (typically 4–8 mm) of GD-based spectrometry techniques results in poor lateral resolution which is not suited to the analysis of Cu penetration through plated contacts for solar cells (with contact widths of $< 1\text{ mm}$) [280].

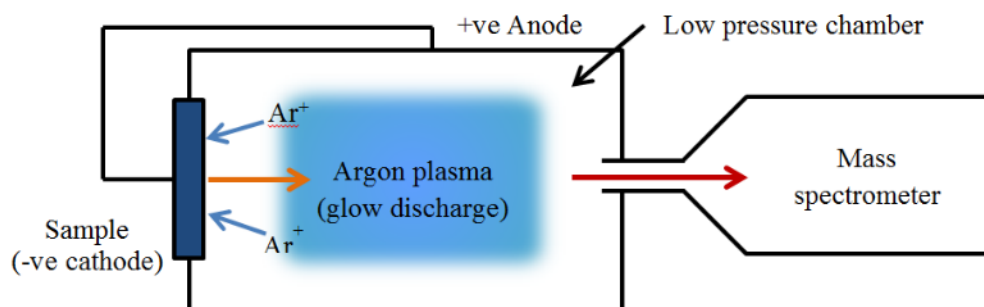


Figure 5.2: Simplified schematic of GD-MS measurement setup (adapted from [283]).

Inductively-coupled plasma mass spectrometry (ICP-MS) is a frequently used inorganic mass spectrometry technique for the characterisation of high purity materials, and solutions due to its simplicity and high sensitivity (ppt to ppb range limit of detection) [268, 289]. As a result, ICP-MS has been used in several previous studies for the analysis of trace impurities both on the Si surface and in the bulk material [290–292]. However, solution-based ICP-MS of Si requires dissolution of the subject material in a mix of HF/HNO₃ which not only increases risk of contamination [293] but also eliminates the possibility of spatially-resolved analysis of the contacted regions of solar cells.

By coupling ICP-MS with laser sampling methods (as illustrated in Figure 5.3), LA-ICP-MS combines the advantages of SIMS and GD-MS to perform spatially-resolved

analysis (spot size $\geq \sim 10 \mu\text{m}$) of ultra-trace impurities in the sub-ppm range, whilst significantly reducing sample preparation requirements [294]. Similar to GD-MS/GD-OES, atomisation and ionisation are separated, minimising the severe matrix effects of SIMS. Depth resolution is primarily determined by the laser conditions (wavelength, pulse length, pulse energy density), with depth resolution in the nm range possible [280]. As a result, LA-ICP-MS has been used in the analysis of the spatial distributions of several metallic impurities in both solar grade and metallurgical-grade Si substrates [295–298]. Thus, LA-ICP-MS demonstrates significant potential as a powerful analytical tool for characterising Cu penetration from plated contacts on solar cells during extended thermal testing. A comparison of different capabilities of available analytical techniques for the quantification of trace impurities in Si is presented in Table 5.1.

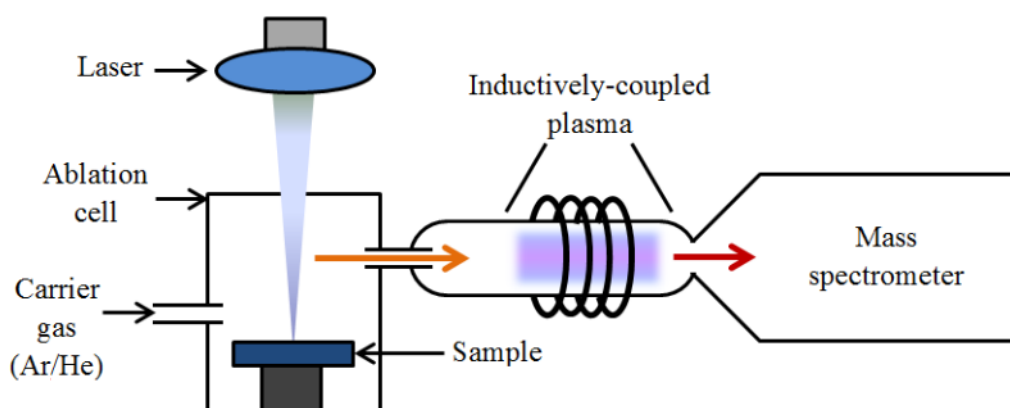


Figure 5.3: Schematic of LA-ICP-MS measurement setup (adapted from [268]).

There are several factors influencing the quantitative capabilities of LA-ICP-MS for the analysis of substrate contamination from plated metal contacts on Si solar cells during extended thermal stability testing, such as laser material interactions, transport efficiency to the ICP and the availability of standard reference materials (SRM) for accurate quantification of metal concentrations in Si [280, 299, 300]. These will be discussed in more detail in the following sections of this chapter.

Table 5.1: Summary of main features between different techniques for the bulk analysis of trace impurities in Si materials (adapted from [268, 280]).

| | SIMS | GD-MS | ICP-MS | LA-ICP-MS |
|---------------------------|--|--|--|---------------------------------|
| Analysis mode/s | Spot | Spot | Solution | Spot, line scan |
| Lateral resolution | < 10 μm | 4-8 mm | — | $\geq 10 \mu\text{m}$ |
| Depth resolution | > 5 nm | > 10 nm | — | 100 nm – 1 μm^* |
| RSF⁺ | 10^3 - 10^6 | 0.2-5 | — | 0.3-3 |
| Limit of Detection | < ppb | ppb – ppm | < ppb | ppb – ppm |
| Calibration | Ion-implanted SRM [^] | SRM | solution | SRM, solution |
| Limitations | Large matrix effects Molecular ion interference High vacuum requirements | Poor lateral resolution Vacuum requirements | Requires dissolution Interferences No spatial resolution | Matrix effects Interferences |

* Depth resolution dependent on laser parameters (wavelength, pulse length, etc).

⁺ RSF = relative sensitivity factor, which relates to the detection ratio between an element and the matrix it is located in.[^] SRM = standard reference material, which is a material with a quantitatively known concentration of elements used for calibration.

5.2 Minimising surface interference during LA-ICP-MS

5.2.1 Introduction

For the experiments reported in this chapter, the region of interest for LA-ICP-MS analysis was the exposed Si directly underneath the plated contacts, as this represents the entry point for any diffused Cu into the substrate. Consequently, an appropriate method for removing the plated metal from the laser-ablated Si surface had to be developed in order to eliminate surface contamination from interfering with LA-ICP-MS measurements of the underlying Si. In previous applications of this analytical technique, a pre-ablation step was used to remove a surface layer prior to measurement [295]. However, the high likelihood of metal contamination within 1-2 μm of the surface necessitated the development of an alternative method of sample surface preparation. This section reports on experimental results aimed at optimising a solution-based etching and cleaning process for the removal of surface contaminants from the laser-ablated Si openings for LA-ICP-MS measurements.

5.2.2 Experimental

Different surface preparation procedures were performed on small-area Ni/Cu/Ag plated cells (25 mm \times 25 mm cell area) fabricated on 156 mm boron-doped 1-3 $\Omega\cdot\text{cm}$ Cz-Si wafers with random-pyramid texturing, a phosphorus-doped emitter (sheet resistivity $\sim 110\text{-}120 \Omega/\square$, surface concentration of $\sim 2 \times 10^{19} \text{ cm}^{-3}$ and junction depth of $\sim 0.4 \mu\text{m}$), a 75 nm SiN_x ARC (deposited on the front surface using direct PECVD) and a full-area Al rear contact. Front contact grids were patterned using 266 nm ps laser ablation with a Lumera Super Rapid Nd:YAG laser with a BBO crystal for the 4th harmonic and plated using bias-assisted LIP according to the processing sequence detailed in Section 4.2.2.1 to form a contact stack of Ni ($\sim 1 \mu\text{m}$) and Cu (8-10 μm), with a thin Ag capping layer (0.3 μm) formed using immersion Ag plating. Samples were not sintered before surface preparation to avoid interference from potential NiSi formation in LA-ICP-MS measurements to assess cleanliness of plated surface after contact removal. After contact formation, small-area cells were laser-cleaved for edge isolation and surface preparation.

Small-area cells were separated into four different batches examining different surface cleaning approaches. Two etching solutions were examined in this work: (i) a

1:1 dilution of 70% (w/v) nitric acid (HNO_3); and (ii) a solution of 5% hydrofluoric acid (HF) and 10% hydrochloric acid (HCl). Nitric acid effectively dissolves metals, including Ni, Cu and Ag [301, 302], although the etch rate is significantly dependent on the temperature of the dilution which decreases over time. Thus, the etching efficiency of HNO_3 was assessed both with and without temperature control (RT = room temperature). For the temperature-controlled HNO_3 solutions, the temperature was maintained at 40 °C with the use of a hot plate. The HF/HCl solution was considered as a method of residual metal removal rather than bulk metal removal due to the etching of SiN_x by HF which was undesirable because it makes alignment to laser-ablated regions difficult during LA-ICP-MS measurements. For each method, samples were immersed in the etching solution for 5 min (10 min total etching for the two-step etching methods), with manual-agitation being used to ensure that the etchant was replenished at the plated surface. For all surface preparation methods, samples were rinsed in DI water for 6 min following plated contact removal. A summary of the different surface preparation methods examined in these experiments is detailed in Figure 5.4.

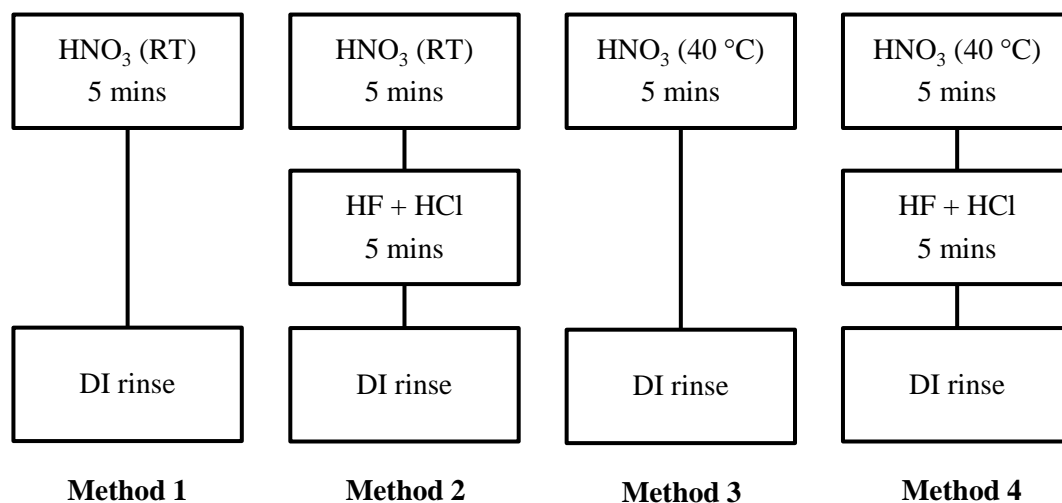


Figure 5.4: Different surface preparation processes for LA-ICP-MS measurements investigated in these experiments.

The quality of surface metal removal was assessed using LA-ICP-MS measurements of the laser-ablated contact regions. Laser ablation ICP-MS measurements were performed using a PerkinElmer Nexion ICP-MS integrated with an ESI-NewWave NWR213 Laser Ablation accessory consisting of a pulsed 213 nm laser. Two separate line scans (4 mm in length) were performed along the busbar region of each sample solar cell, and the transport line was flushed for 30 s between consecutive line scans. A

summary of the measurement conditions used in this study and the experiments discussed in Section 5.4 (unless stated otherwise) are presented in Table 5.2. The isotopes examined for analysis were selected based on their abundance, with the impact of interferences (in particular, $^{40}\text{Ar}^{23}\text{Na}^+$ and ^{63}Cu) assumed to be negligible. Since no Si reference materials were available, silica glass NIST614 (concentration range 0.5 – 50 ppm) was selected as the non-matrix matching external calibration standard for quantitative analysis, whilst ^{29}Si was used as the internal standard element [303]. Individual cells were placed on a glass slide with tape to minimise shifting of the sample during analysis. All ICP-MS data processing, including separation of individual scans, conversion of counts per second (CPS) to concentration, and integration with the laser time log, was performed using the Iolite software provided in Igor Pro [304].

Table 5.2: Operating parameters for LA-ICP-MS measurements on Si solar cells after different sample surface preparation sequences.

| Laser Conditions | |
|---|--|
| Wavelength (nm) | 213 |
| Scan mode | Line scan |
| Laser Fluence (J/cm^2) | 12 ± 2 |
| Scan Speed ($\mu\text{m}/\text{s}$) | 5 |
| Scan length - NIST614 (μm) | 250 |
| Scan length – sample (μm) | 4000 |
| Spot Size (μm) | 20 |
| Repetition Rate (Hz) | 20 |
| ICP-MS Conditions | |
| He Gas Flow (L min^{-1}) | 0.73 |
| Nebulizer (Ar) Gas Flow (L min^{-1}) | 0.62 |
| RF Power (W) | 1150 |
| Dwell time (ms) | 125 |
| Sample Conditions | |
| Elements measured | ^{29}Si , ^{60}Ni , ^{63}Cu , ^{107}Ag |

The effectiveness of different surface preparation methods was also assessed with EDS mapping of the laser-patterned contact regions using a Hitachi S3400 Scanning Electron Microscopy (SEM) Instrument.

5.2.3 Results and discussion

Figure 5.5(a) shows an example EDS map taken on the busbar/finger region of a sample cell after 5 min immersion in HNO_3 at room temperature (Method 1). It is clear from the EDS map that a significant amount of residual surface Ni remains after etching, and this is reflected in the associated LA-ICP-MS measurement results as presented in Table 5.3. Although the corresponding LA-ICP-MS Cu signal is low (see Table 5.3), indicating the effectiveness of room temperature HNO_3 in stripping the bulk of the plated contact, the EDS map of the Cu signal in the inset in Figure 5.5(a) suggests that some residual Cu also remains on the surface after cleaning.

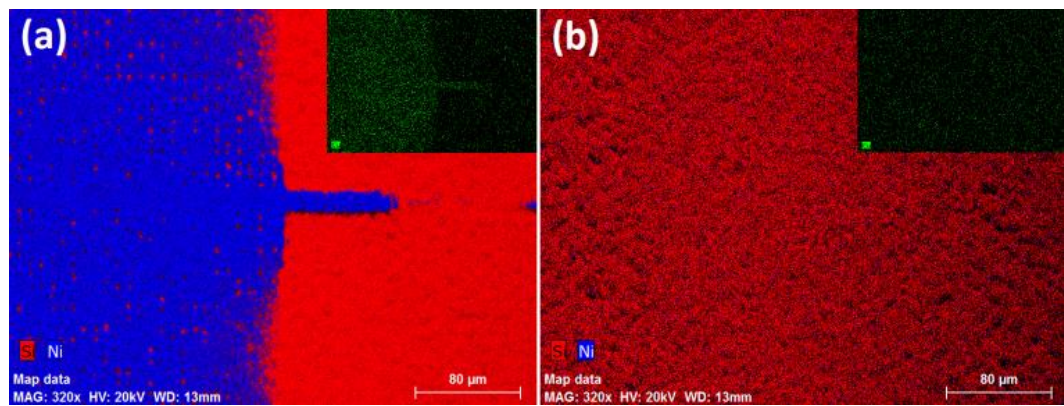


Figure 5.5: EDS maps of Ni and Si signal from the busbar region of a plated solar cell, (a) after room temperature HNO_3 etch; and (b) after HNO_3 etch at 40 °C followed by HF/HCl clean. The insets show the Cu signal from the same region.

Table 5.3: Comparison of measured plated metal concentrations with LA-ICP-MS averaged along a 4 mm line scan for different surface preparation methods, including a control measurement with full plated contacts.

| Surface condition | Ni (ppm) | Cu (ppm) | Ag (ppm) |
|---------------------------------|-------------------|-------------------|-----------------|
| Cell with contacts | 17098 ± 16110 | 28948 ± 26222 | 347 ± 433 |
| HNO_3 only (RT) | 7725 ± 1700 | 0.54 ± 0.02 | 2.26 ± 0.09 |
| HNO_3 (RT) + HF/HCl | 23.4 ± 9.7 | 2.4 ± 2.4 | 3.32 ± 0.01 |
| HNO_3 only (40 °C) | 20.0 ± 2.6 | 0.52 ± 0.08 | 2.52 ± 0.03 |
| HNO_3 (40 °C) + HF/HCl | 76 ± 48 | 0.85 ± 0.09 | 4.28 ± 0.33 |

When the HNO_3 etching temperature was controlled at 40 °C, the bulk of the plated contact as well as surface residual metal was effectively removed. The LA-ICP-MS line scans in Figure 5.6 highlight the significant reduction in surface Ni that was achieved as a result of maintaining the temperature of the HNO_3 solution at 40 °C. Whilst a few spikes of Ni are still evident in the LA-ICP-MS scans from cells where the contact regions were etched in HNO_3 at 40 °C, the average Ni concentration as presented in Table 5.3 was significantly reduced to a negligible concentration. The spikes of Ni remaining after HNO_3 etching could be the result of metal oxide formation at the surface [302].

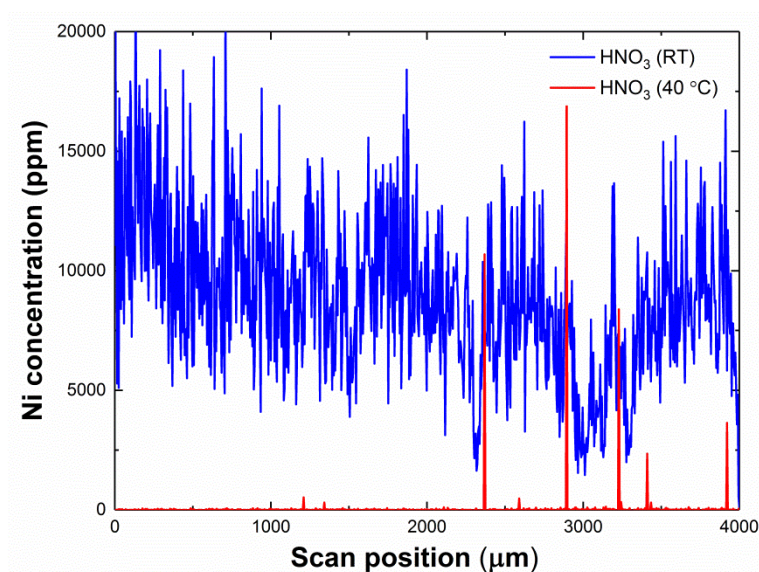


Figure 5.6: LA-ICP-MS line scan profiles measured on a sample after surface preparation with HNO_3 with temperature control (blue curve) and without temperature control (red curve).

The addition of a second metal cleaning step involving HF/HCl was able to more effectively remove all metals from the sample surface when performed after a HNO_3 etch at room temperature, including metal oxides that may have formed during the initial HNO_3 etch. The EDS maps recorded on samples undergoing the full cleaning procedure [see Figure 5.5(b)] show no significant Ni or Cu signal after the two-step cleaning procedure, and the corresponding LA-ICP-MS results in Table 5.3 confirmed that the procedure was effective in minimising the concentration of metals at the surface. However, the average metal concentrations increased slightly with the two-step cleaning procedure in the case of a temperature-controlled HNO_3 etch. This may have

been due to insufficient rinsing of the sample surface during the DI rinse step, or potentially replating of the metal during etching in HF [305], however the metal concentrations are still significantly below that observed in metal-contaminated samples as will be discussed further in Section 5.4. Hence, despite the aforementioned risk of contamination when using solution-based sample preparation methods [293], a suitable level of surface preparation for LA-ICP-MS was obtained using solution-based methods involving acidic etchants.

5.3 Ablation characteristics for Si substrate analysis

5.3.1 Introduction

As mentioned in Section 5.1, the quantitative capability of LA-ICP-MS is reliant on efficient transport of ablated material to the ICP-MS instrument. This is subsequently dependent on the characteristics of laser ablation such as spot size and energy density which determines the ablation depth and ejected mass which is picked up by the carrier gas (Ar/He mix) to be transported to the ICP-MS for analysis. Thus, the ablation of Si needs to be optimised before accurate quantitative data can be extracted from LA-ICP-MS measurements. In this section, the ablation of Si using nanosecond laser ablation, as employed in the LA-ICP-MS measurements, is characterised and discussed in terms of the relationship between laser parameters (spot size, laser fluence and scan speed) and ablation crater morphology and material transport efficiency.

5.3.2 Experimental

Ablation craters were characterised on uncoated planar Si wafers ($40 \times 40 \text{ mm}^2$) to eliminate the effect of surface texturing on the Si ablation. It was assumed in these experiments that differences in the absorption and reflection properties between planar and textured Si was minimal. A series of different laser spot sizes, scan speeds and laser fluence settings were used as detailed in Figure 5.7. Laser spot size was determined with the aid of a variable aperture within the tool. Line scans 2.5 mm in length were performed using different combinations of scan speed and laser fluence. The laser fluence was maintained constant at $12 \pm 2 \text{ J/cm}^2$ when varying scan speed, whilst a $5 \text{ }\mu\text{m/s}$ scan speed was used when varying laser fluence. Since the concentration profiles were not critical for this study, they were not examined. Ablation crater dimensions

(including width and depth) and transport efficiency were assessed using a combination of optical microscope imaging and SEM imaging using a Hitachi S3400.

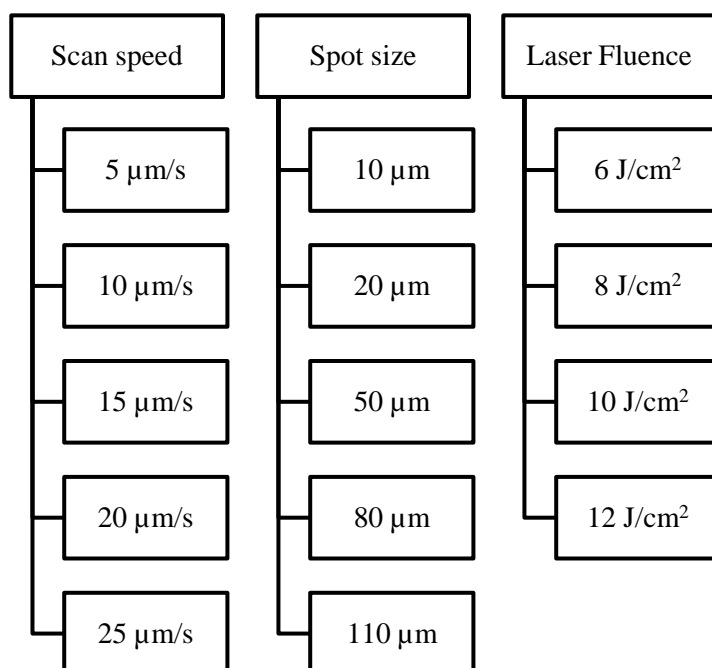


Figure 5.7: Breakdown of laser parameter settings examined for ablation characterisation of Si during ns LA-ICP-MS sampling.

5.3.3 Results and discussion

Crater depth was observed to increase linearly with laser fluence for all spot sizes examined in this experiment (10, 20, 50, 80 and 110 μm) as seen in Figure 5.8(a). This was also mostly the case when varying scan speed whilst maintaining constant laser fluence as can be seen in Figure 5.8(b). However, the crater depth increased by a factor of two for spot sizes greater than 10 μm when the scan speed was reduced to 5 $\mu\text{m/s}$. This dramatic increase in ablated Si at slower scan speeds is related to the interaction between Si and high power density laser pulses during nanosecond (ns) laser ablation. The ablation of Si can occur via non-thermal mechanisms such as direct breaking of the atomic lattice, or thermally through heating, melting and vaporisation, which all depend on the properties of the laser [306]. During ns laser ablation, the occurrence of a molten region is frequently observed and this region can propagate deep into the material. In the case of high intensity ns laser pulses, the material can be heated above the boiling point, resulting in the generation of a metastable liquid phase that leads to an eruption of liquid and vaporised material during ablation, a process which has been described

previously [307]. This explosive change in crater depth during ns laser ablation of Si has also been observed by Yoo *et al.* [308], who similarly demonstrated a significant change in crater volume and depth when the laser intensity was increased above $\sim 2.2 \times 10^{10} \text{ W/cm}^2$ (termed ‘explosive boiling’). Despite slight differences in the ablation laser used in this study compared to previous studies (213 nm compared to 266 nm), this process of explosive boiling is most likely the cause of the observed increase in crater depth at slower scan speeds. The apparent reduction in crater depth for spot sizes above 80 μm at 5 $\mu\text{m/s}$ scan speed is most likely due to a reduction in the energy density across the wider crater, resulting in less explosive boiling and thus a shallower crater depth compared to smaller spot sizes.

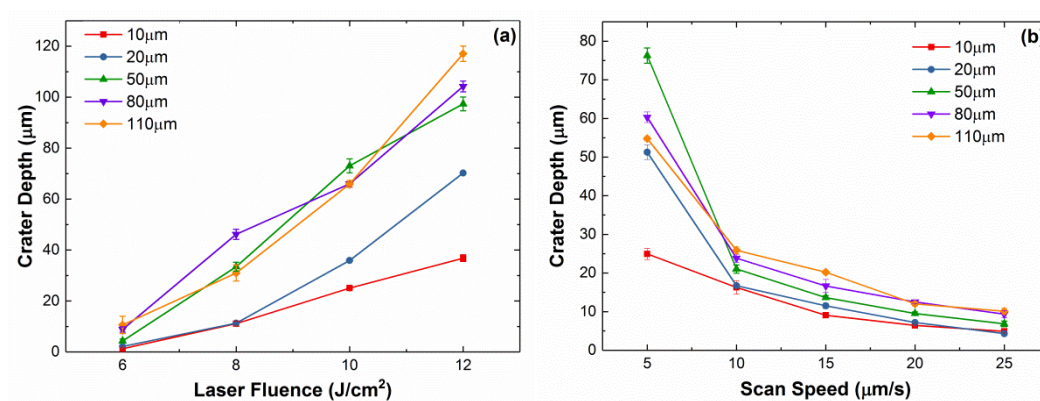


Figure 5.8: Crater depth as a function of: (a) laser fluence; and (b) scan speed for different laser spot sizes.

Another key observation made during the optimisation of the laser ablation process was the variation in transport efficiency with different laser parameters. Figure 5.9 shows an optical microscope image recorded for a Si sample which had several line scans performed using different spot sizes and scan speeds at a constant laser fluence of $12 \pm 2 \text{ J/cm}^2$. A significant amount of ablated material can be seen to accumulate on the surface after LA-ICP-MS measurements, with the total ablated mass remaining on the surface increasing significantly with increasing spot size. The transport of material from the ablated cell to the ICP-MS detector (known as transport efficiency) depends largely on the ablated particle size distribution [309]. The particle size distribution is subsequently dependent on both the laser ablation process as well as the transport gas mixture. It has been demonstrated previously that the use of Helium (He) as a transport gas results in a larger distribution of smaller particles compared to when Argon (Ar) is

used, resulting in improved sensitivity of the ICP-MS due to reduced elemental fractionation effects, which refers to the thermal redistribution of elements during laser ablation [310]. It was suggested that the reduced laser-induced plasma along with the higher heat conductivity of a He environment in the ablation cell helps prevent the condensation and agglomeration of ablated particles which cannot be effectively transported to the ICP-MS instrument. This agglomeration of ablated material, coupled with the explosive boiling effects discussed earlier, most likely explains the significant build-up of re-solidified Si on the wafer surface with increasing spot size. This can be improved with the use of picosecond (ps) and femtosecond (fs) lasers, which can reduce thermal effects and improve transport efficiency of ablated material [311–313].



Figure 5.9: Optical microscope image (5× magnification), showing increasing agglomerated Si build-up on wafer surface with increasing spot size (spot size increasing from bottom to top of image).

Non-uniformities in the ablation crater with larger spot sizes ($> 20 \mu\text{m}$) were also observed, as can be seen in the SEM cross-sections in Figure 5.10. The lack of symmetry in the crater with larger spot sizes indicated some non-uniformity in the laser

beam incident on the sample surface, which may have also contributed to the extensive build-up of ablated material on the Si surface with larger spot sizes. The exact cause of this non-uniformity is unknown, although the Gaussian beam-shape of the laser employed in the tool should have resulted in moderately uniform crater dimensions. It is possible that misalignment of the laser resulted in the non-uniform ablation, which became significantly more noticeable as the spot size increased. Thus, the optimum laser spot size was determined to 10 μm , since it resulted in the least build-up of agglomerated Si on the wafer surface, whilst also providing the highest spatial resolution for analysis of plating uniformity and Cu penetration through the solar cell contacts.

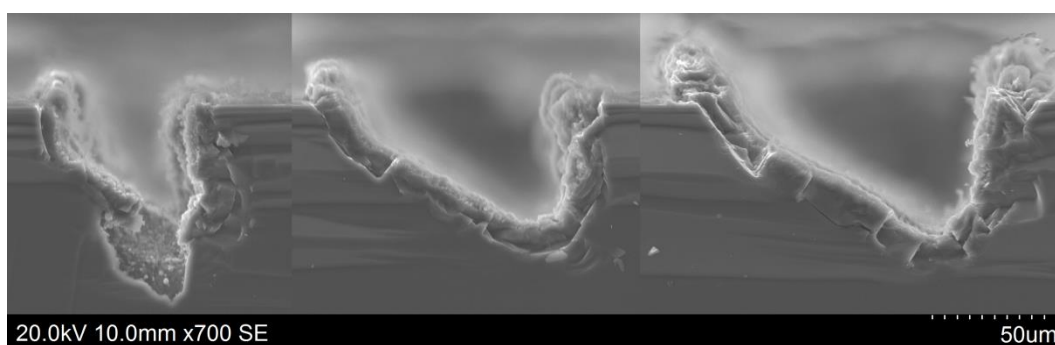


Figure 5.10: SEM cross-sections of non-uniform ablation craters obtained with larger spot sizes (50, 80 and 100 μm) on a planar Si surface with a scan speed of 5 $\mu\text{m/s}$.

The SEM cross-sectional images in Figure 5.11 show the crater dimensions for a series of different scan speeds with a spot size of 10 μm and a laser fluence of 12 ± 2 J/cm^2 , which were the laser parameters selected for the quantitative measurements performed on thermally-treated solar cells with Cu-plated contacts. All the craters show a clear lip along the edges of the line scan due to re-solidification of Si during laser ablation [312]. The crater depth varies from ~ 25 μm to ~ 5 μm with increasing scan speed, whilst the height of the re-solidified Si region follows a similar trend. It is expected that fluctuations of the laser during line-scanning is reflected by non-uniformities in the ablation along the length of the line scan. This is somewhat visible in the 5 $\mu\text{m/s}$ SEM image in Figure 5.11, and may also be reflected in the quantitative LA-ICP-MS results discussed in Section 5.4. Despite certain non-uniformities observed in the ablation crater when using the slowest scan speed (5 $\mu\text{m/s}$), this was the scan speed chosen for the analysis of metal penetration from plated contacts into the underlying Si

since the exact location of Cu within the substrate was unknown and quenching was expected to cause Cu build-up in the bulk of the Si rather than close to the surface. These results are detailed further in the following section of this chapter.

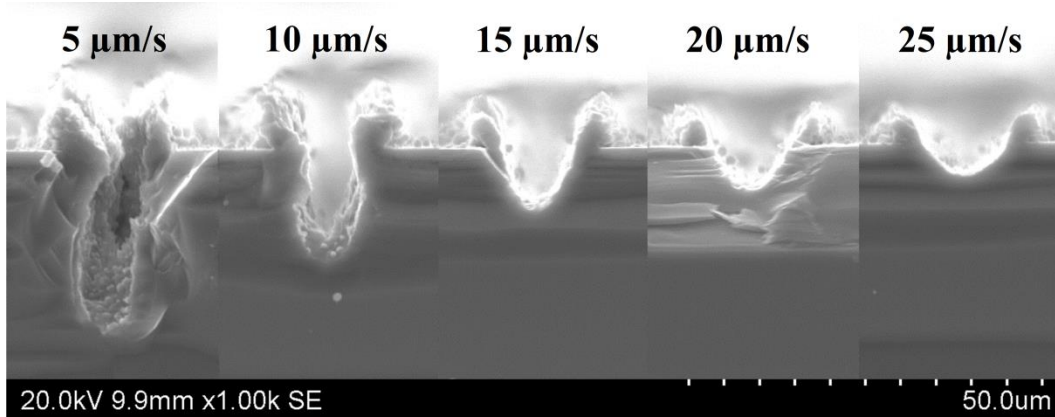


Figure 5.11: SEM cross-sections of LA-ICP-MS line scans at different scan speeds with a 10 μm spot size on a planar Si surface.

5.4 Characterisation of diffusion barrier quality using LA-ICP-MS

5.4.1 Introduction

It is the main assumption of long-term thermal stability studies [50, 54, 55] that the impurity responsible for the observed degradation in plated Si solar cells is Cu. To date, few studies have attempted to confirm the role of Cu in plated cell degradation with elemental analysis techniques and correlate this to weaknesses in the barrier layer. The experiments reported in this section investigated the quantitative capabilities of LA-ICP-MS in detecting Cu penetration from plated contacts into the underlying Si substrate, as well as the relationship between thermal treatment duration, electrical degradation and associated metal impurity signal intensity. The use of LA-ICP-MS as a tool for assessing Ni barrier uniformity is also discussed in order to assess the potential for spatially-resolved analysis of Si wafer contamination from plated metals using line-scanning LA-ICP-MS.

5.4.2 Experimental

Small-area plated PERC cells (25 mm \times 25 mm cell area) were fabricated on 156 mm boron-doped 1-3 $\Omega\cdot\text{cm}$ Cz-Si wafers with random-pyramid texturing, a phosphorus-doped emitter (sheet resistivity \sim 110-120 Ω/\square , surface concentration of $\sim 2 \times 10^{19} \text{ cm}^{-3}$

and junction depth of $\sim 0.4 \mu\text{m}$), a 75 nm direct-PECVD SiN_x ARC and an Al rear PERC structure forming the rear contact. Front contact grids were patterned using ps laser ablation (as described in more detail in Section 4.2.2) and plated with bias-assisted LIP according to the processing sequence detailed in Section 4.2.2.1 to form a contact stack of Ni ($\sim 1 \mu\text{m}$) and Cu (8-10 μm), with a thin Ag capping layer (0.3 μm) formed using immersion Ag plating. Cells were not sintered prior to thermal stress testing as the purpose of this study was to examine metal penetration into the Si and NiSi (which is difficult to remove from the surface by etching) would be expected to interfere with the Ni signal measured during line-scanning LA-ICP-MS.

Cells were exposed to 200 °C in a muffle oven with N_2 ambient for between 5 and 1000 hours to simulate long-term operation at elevated temperatures (5 samples per time step). After thermal annealing, cells were quenched in ethylene glycol (cooling rate $\sim 1000 \text{ K/s}$) within 1-3 seconds after thermal treatment followed by rinsing in DI water. Electrical characterisation before and after thermal exposure included light and dark I - V measurements using a calibrated in-house constant illumination I - V tester under standard test conditions, and Suns- V_{OC} measurements using a Sinton Instruments Illumination-voltage tester. The impact of voids at the Cu/Ag interface was accounted for prior to each measurement by applying pressure to the probe on contacting (see Section 4.2).

Following cell characterisation after thermal treatment, 3 of the 5 test samples were immersed in a 1:1 dilution of 70% (w/v) HNO_3 in DI water maintained at 40 °C for 10 followed by 6 min in 5% HF + 10% HCl to remove residual metals from the surface. Although 5 mins in each solution was shown to provide adequate surface preparation (see Section 5.2), etching steps were extended to account for any reduced etching efficiency as a result of extended thermal exposure.

Line-scanning LA-ICP-MS measurements were performed according to the experimental details provided in Table 5.2, although specific settings employed in the quantitative LA-ICP-MS measurements are also provided in Table 5.4. Similar to the experiments reported in Section 5.2, two separate line scans (4 mm in length) were performed along the busbar region of each sample solar cell, and the transport line was flushed for 30 s between consecutive line scans.

Table 5.4: Operating parameters used for LA-ICP-MS measurements on Si solar cells after extended thermal exposure at 200 °C. Process parameters were as presented in Table 5.2 (in Section 5.2.2).

| Laser Conditions | |
|------------------------------------|---|
| Scan mode | Line scan |
| Laser Fluence (J/cm ²) | 12 ± 2 |
| Scan Speed (µm/s) | 5 |
| Scan length - NIST614 (µm) | 250 |
| Scan length – sample (µm) | 4000 |
| Spot Size (µm) | 10 |
| Sample Conditions | |
| Elements measured | ²⁹ Si, ¹¹ B, ⁶⁰ Ni, ⁶³ Cu, ¹⁰⁷ Ag, ³¹ P, ²⁷ Al |

For comparison, Time-of Flight SIMS (ToF-SIMS) measurements were performed using an ION-TOF TOF.SIMS 5-100 instrument (IONTOF GmbH, Münster, Germany). Samples were sputtered with O₂⁺ primary ions and analysis was performed with Bi⁺ primary ions in interlaced mode within the sputtered crater. A summary of the measurement conditions used in ToF-SIMS measurements is summarised in Table 5.5.

Table 5.5: Operating parameters used for ToF-SIMS measurements on Si solar cells after extended thermal exposure at 200 °C.

| Sputter Conditions | |
|--|-------------------------------------|
| Primary ion source | O ₂ ⁺ |
| Beam energy (keV) | 2 |
| Beam current (nA) | 410 ± 3 |
| Ion dose density (ions/cm ²) | 10 ¹⁸ - 10 ¹⁹ |
| Raster area (µm ²) | 300×300 |
| Analysis Conditions | |
| Primary ion source | Bi ⁺ |
| Beam energy (keV) | 30 |
| Beam current (pA) | 3 ± 0.3 |
| Ion dose density (ions/cm ²) | 10 ¹⁴ - 10 ¹⁵ |
| Raster area (µm ²) | 100×100 |

Samples for ToF-SIMS measurements were selected from a range of different thermal stress testing time-steps, with the measurements performed on busbar regions adjacent to corresponding LA-ICP-MS measurements. Due to a lack of appropriate calibration standards for the elements in question in Si, only qualitative measurements of signal intensity were obtained. Depth profiles were calibrated using a KLA Tencor D-600 stylus profiler.

5.4.3 Results and discussion

Quantitative LA-ICP-MS results for Ni and Cu detected in the Si substrate after different durations of thermal stress testing on plated solar cells are summarised in Figure 5.12. Due to the variability in concentration along the line scan (discussed in more detail further on in this section), the median concentration of Ni and Cu along the line scan was graphed in Figure 5.12(a) and (b) respectively, averaged across all the line scans performed on cells in that time step (6 line scan measurements in total). Since the Ag signal was within the background noise for this LA-ICP-MS setup in the absence of matrix-matched calibration standards, it was not examined in detail. It is apparent that Ni and Cu follow a similar trend in terms of concentration determined by LA-ICP-MS, both showing an overall increase in measured concentration with thermal treatment duration and local peaks observed both at 200 and 750 hours, except the peaks are more distinct for Cu than Ni. The effectiveness of the pre-cleaning process in eliminating surface contamination (as described in Section 5.2) was evident by the fact that no Ni or Cu was detected in the control cells (no thermal treatment).

The noticeable increase in detected Ni after ~ 50 hours of thermal stress at 200 °C may be due to the formation of Ni silicide during thermal stress testing. Typically, Ni/Cu/Ag-plated Si solar cells are sintered at 350 °C after plating to induce silicidation of the Ni layer which acts to improve contact adhesion and resistivity [14, 314]. Several different silicide phases result from annealing at different temperatures [315], and while NiSi is the silicide phase often desired in solar cell manufacturing due to its lower resistivity [316], Ni₂Si is known to form at approximately 200 °C. Since the cells examined in this experiment did not undergo sintering prior to thermal treatment at 200 °C, it was suspected that Ni₂Si is responsible for the high Ni signal observed. This was confirmed by Raman spectroscopy which showed peaks corresponding to Ni₂Si as seen in the example Raman spectra in Figure 5.13. No Raman peaks associated with Cu were

observed on any of these samples, indicating that Cu was not present at the Si surface. The presence of a Ni_2Si layer which would be difficult to remove with the surface etching procedure here may also explain the relatively high Ni concentration (max. 610 ± 261 ppm) compared to Cu (max. 302 ± 164 ppm) measured in the thermally-treated cells with LA-ICP-MS.

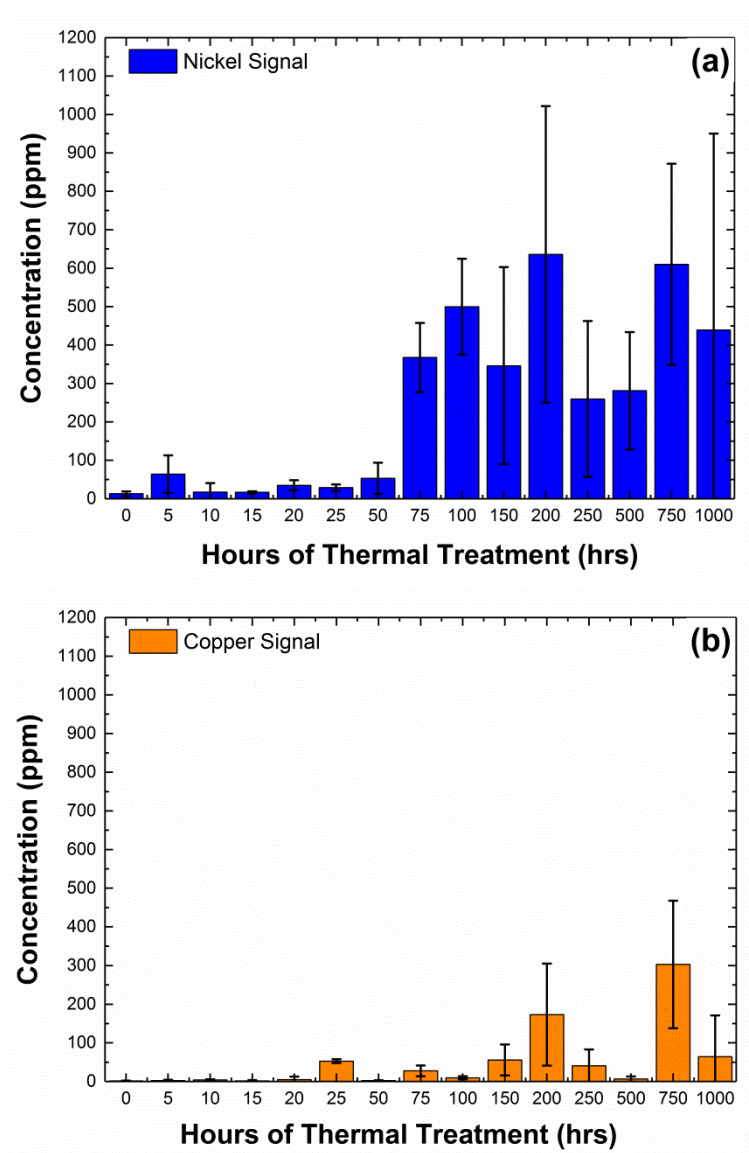


Figure 5.12: (a) Plot of median Ni concentration and (b) plot of median Cu concentration as a function of thermal treatment duration. The values presented here are the average median values across 6 line scans for each time step, and their associated standard deviations.

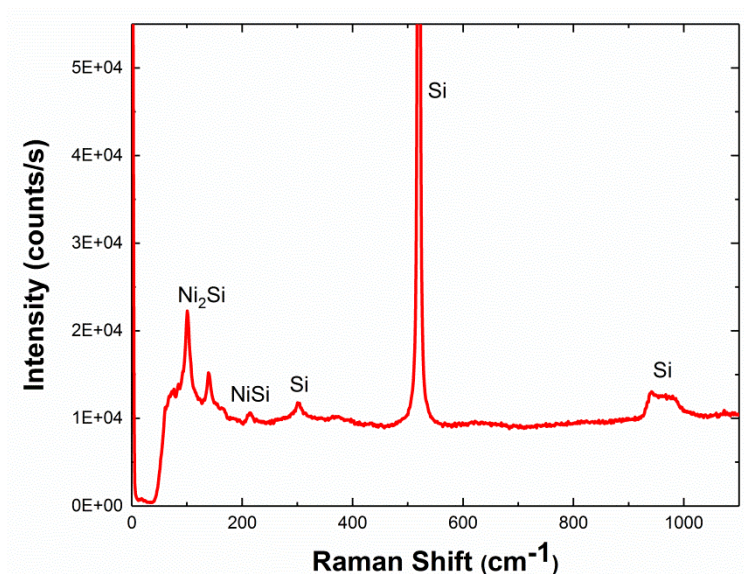


Figure 5.13: Raman spectrum recorded at a busbar region of a non-sintered plated cell after 750 hours at 200 °C.

Not only do the Ni and Cu concentrations measured with LA-ICP-MS follow the same trend in relation to thermal stress duration, but on closer examination of individual line scans, it can be seen that Ni and Cu concentration follow similar trends along each line scan as can be seen in Figure 5.14. This may indicate that Ni and Cu migrate along the same diffusion pathways during thermal treatment, which suggests that the surface morphology may have an impact on the extent of metal ingress. It has been reported that laser ablation patterning for metal contact formation can induce local crystal defects in the Si and these crystal defects may provide diffusion pathways for metal ingress and deep silicide formation [265, 266]. As reported in the previous chapter, Cu is also known to preferentially diffuse along defect pathways, diffusing through both Ni as well as Ag during thermal treatments [47, 247]. Whilst the diffusivity of Ni in Si is comparable to that of Cu [317, 318], it is more likely that Ni and Cu penetrated the Si through other low energy diffusion pathways such as laser-induced defects generated during the formation of contact openings during laser ablation (discussed in more detail in Chapter 6).

Large standard deviations exist in these measurements as seen in Figure 5.12 (sometimes greater than 100%). The deviations may be due to non-uniformities that can influence both the penetration of metal into the Si as well as the LA-ICP-MS measurements themselves. As mentioned previously, non-uniformities in the laser-

patterning (to create openings in the dielectric for metal plating) can result in a localised distribution of crystal defects and diffusion pathways, resulting in localised increased migration of metals into the Si substrate during thermal treatment. Nickel barrier thickness can vary significantly with plating current density and factors such as local variations in emitter resistivity can result in significant differences in plating rate and subsequent Ni thickness [26, 48]. Not only this, but variations in the Ni barrier layer properties (grain structure, impurities, etc.) can also impact Cu diffusion into the Si wafer [205]. Thus, these non-uniformities can result in large standard deviations both within and between cells undergoing the same thermal treatment. In terms of quantitative capabilities, the lack of any existing matrix-matched Si standards limits the quantitative strength of LA-ICP-MS for Si sample analysis. In-house Si standards with a homogeneous distribution of impurities with known concentrations can help improve the quantitative accuracy of LA-ICP-MS [295, 319], although this is difficult to achieve with fast diffusing species such as Cu and Ni, which tend to find sinks to reach thermodynamic stability with the Si lattice. However, the values obtained in this work are comparable to previous quantitative analyses of impurities in Si using LA-ICP-MS [295, 296], and thus demonstrates the usefulness of the technique in understanding and analysing metal penetration from plated contacts on Si solar cells.

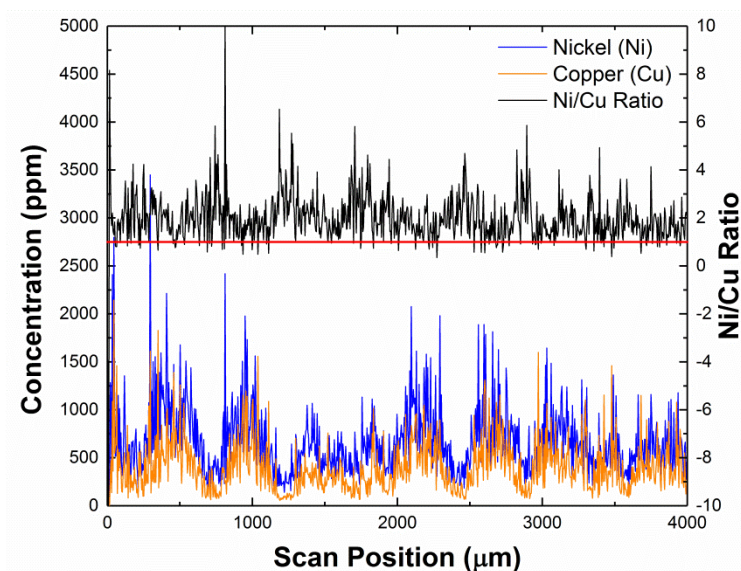


Figure 5.14: Example LA-ICP-MS line scan result for a sample cell after 750 hours of thermal treatment at 200 °C. The black curve denotes the ratio of Ni to Cu along the scan, demonstrating minimal deviation from unity (red line).

Another potential application of LA-ICP-MS for plated solar cells is determination of the plating uniformity of Ni layers before any thermal processing or contact removal. As an example, Figure 5.15 shows LA-ICP-MS line scan results performed perpendicularly across three plated fingers at two locations on a plated cell – close to the busbar and close to the edge of the cell. Close to the busbar, the detected Ni signal across the three fingers is approximately the same, whilst close to the edge of the cell there is a significant difference in measured Ni concentration between the measured fingers. Conversely, the Cu concentration is slightly higher at the edge of the cell compared to the finger regions close to the busbar. Whilst this may be an artefact of non-uniform laser ablation sampling or elemental fractionation during line-scanning LA-ICP-MS [320, 321], it may also be an indicator of non-uniform Ni barrier plating. With further refinement of the technique, LA-ICP-MS may prove a useful analytical tool in plating uniformity analysis for Si solar cells.

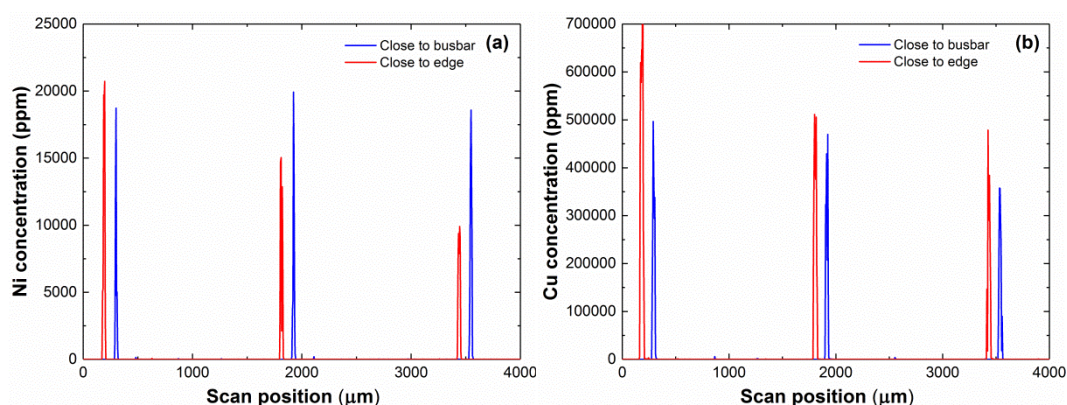


Figure 5.15: (a) Ni concentration and (b) Cu concentration profiles determined from LA-ICP-MS line scans measured perpendicularly across several plated fingers close to the busbar (red line) and near the edge of the plated cell area (blue line).

Comparative SIMS measurements were performed in adjacent regions to the LA-ICP-MS line scans to confirm the measured concentration trend with thermal treatment duration. Figure 5.16 shows SIMS profiles of both Ni and Cu for a range of thermal duration timesteps. However, the use of appropriate calibration standards is significantly more critical in SIMS measurements compared to LA-ICP-MS, so only relative signal intensity between different timesteps were comparable, and no direct correlation between Ni and Cu signal could be ascertained.

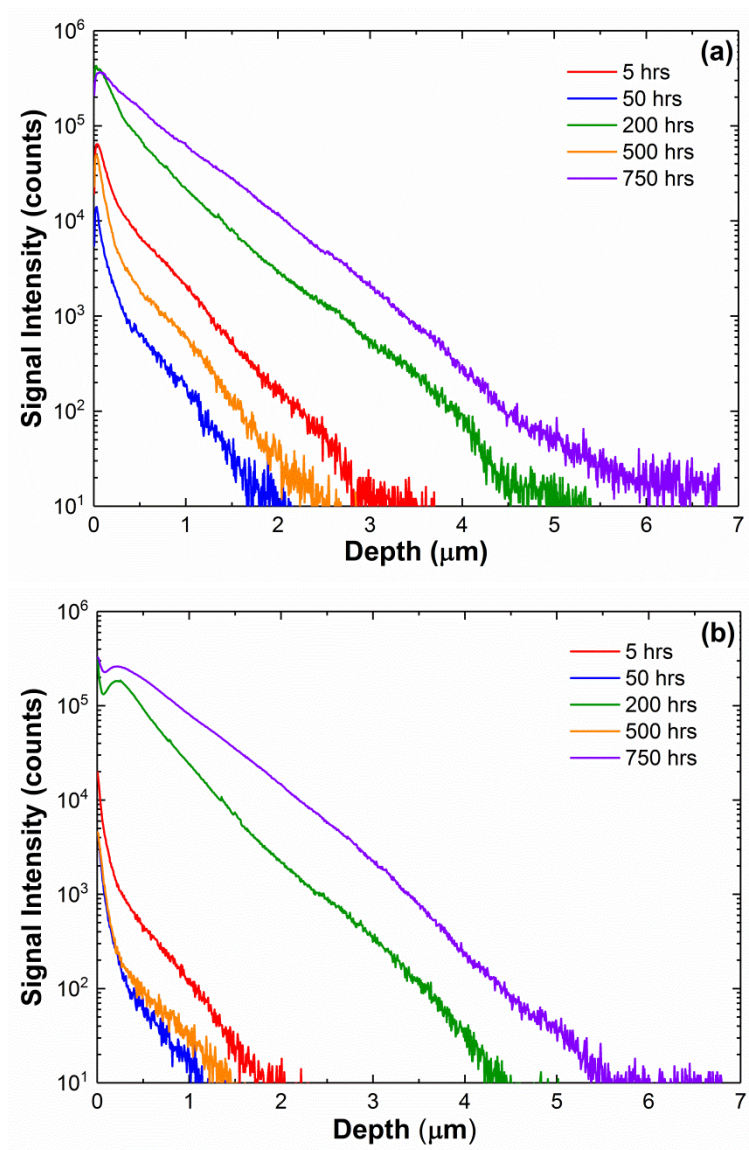


Figure 5.16: SIMS depth profiles for (a) Ni and (b) Cu concentration obtained at adjacent regions to LA-ICP-MS measurements performed on plated solar cells after varying durations of thermal exposure at 200 °C.

The SIMS measurements above confirm the overall trend observed in LA-ICP-MS results (see Figure 5.12), with significantly higher Ni and Cu signals at 200 and 750 hours and a local minimum at 500 hours thermal treatment duration. The penetration depth of Ni and Cu also extends several μm into the Si substrate, well beyond the junction depth for these plated cells ($\sim 0.4 \mu\text{m}$), indicating bulk penetration of plated metals during extended thermal exposure at 200 °C. However, the severe matrix effects observed in SIMS measurements, and the potential segregation of Cu (and perhaps Ni as well) during O_2 ion bombardment in SIMS measurements as noticed by Kilner *et al.*

[277] may distort the depth profile, artificially extending the decay in the Cu/Ni signal. However, these qualitative SIMS profiles were consistent with the concentration trends in Ni and Cu observed in LA-ICP-MS results.

To determine whether metal contamination within the Si correlated with electrical solar cell performance degradation, the open-circuit voltage V_{OC} and pFF of cells were also measured before LA-ICP-MS measurements. While V_{OC} is a strong indicator of substrate contamination [322], pFF has previously been used in the analysis of plated solar cells as a measure of metal penetration close to the solar cell junction [50]. Figure 5.17 shows the correlation between V_{OC} and pFF measurements with detected Ni and Cu concentration.

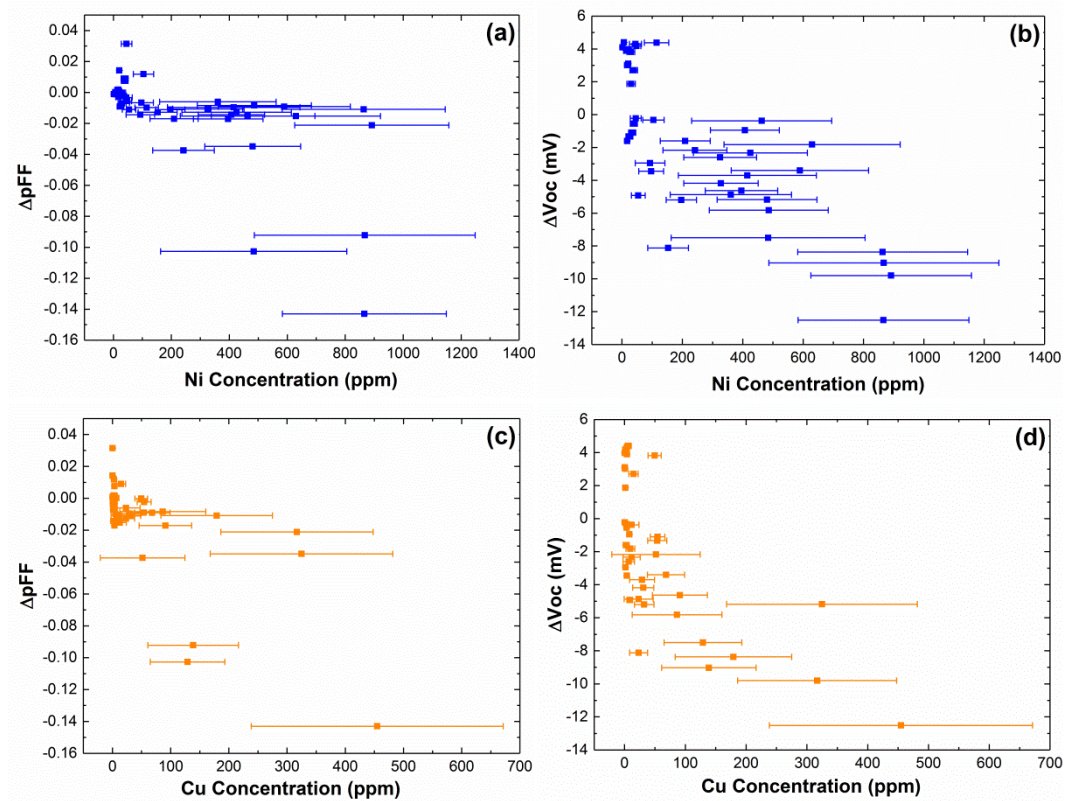


Figure 5.17: Relative reductions in (a) pFF and (b) V_{OC} as a function of median Ni concentration, and (c)-(d) as a function of median Cu concentration. The errors bars on the x-axis represent the interquartile range (IQR) of the dataset obtained in each line scan.

In terms of pFF , no clear linear correlation was evident between both Ni or Cu concentration and pFF reduction as seen in Figure 5.17(a) and (c). This is not unexpected, since previous studies examining pFF during thermal stress testing of Cu-

plated solar cells have shown that pFF will remain stable until a threshold state following which Cu defects (in the form of precipitates) increase in concentration at the junction sufficiently to begin to impact the pFF . Once this threshold is reached then a more rapid decline in pFF tends to follow [50, 51, 54, 57].

Although this study resulted in too few samples with very high Ni and/or very high Cu concentration to be conclusive about the trend of pFF with more extensive metal contamination, the results suggested that pFF was more sensitive to high Cu concentrations than Ni concentrations. The variability of the data for samples with high metal concentrations both along individual line scans and between different samples, as visible from the large error bars in Figure 5.17, suggests that Ni and Cu penetration and indeed the impact of that penetration may be very sensitive to how the metal stacks are plated, although the risk of non-uniform laser ablation of Si during LA-ICP-MS may also impact the observed variability. For example, small differences in laser ablation process parameters or plating parameters may result in significantly different metal penetration effects. From an examination of V_{OC} , it can be seen there is an approximate linear decrease in V_{OC} with increasing Ni concentration [see Figure 5.17(b)], whilst there is an apparent non-linear decrease in V_{OC} with increasing Cu concentration [see Figure 5.17(d)]. This observation is consistent with the theory that Cu, which penetrates into the Si, increases the recombination in the solar cell. It is possible that the ethylene glycol quenching results in the Cu concentration in the Si increasing above its threshold for precipitation in the p-type base where it is more likely to impact the V_{OC} than the pFF . Precipitation of Cu in the Si of the cell was only observed by Flynn *et al.* after heat treatment if cells were quenched in ethylene glycol [233]. They hypothesised that the absence of precipitates when cells were allowed to cool slowly was due to Cu out-diffusing to the solar cell surface where it did not impact the cell's electrical performance. Future LA-ICP-MS studies which compare rapid cooling with ambient cooling of plated solar cells after thermal treatment may be able to confirm this hypothesis, although optimisation of laser parameters for improved depth-resolved analysis would be required, with the use of shorter pulse laser ablation expected to result in improved depth resolution compared with ns laser ablation.

In this particular case, it was difficult to separate the effects of Cu and Ni on V_{OC} . However, the relative concentrations of Cu and Ni as a function of thermal treatment

duration suggest that Cu has a stronger effect on cell degradation than Ni. Whilst Ni has been shown to cause shunting in Cu-plated solar cells, often termed Ni spiking [265, 266, 323], Kraft *et al.* have shown that thermal stability studies on cells with a plated Ni layer observed no thermally-induced degradation in the absence of Cu [51]. However, the presence of a Ag seed layer in these cells may have restricted deep silicide formation in these previous studies.

5.5 Chapter summary

The capabilities of LA-ICP-MS for spatially-resolved analysis of metal penetration from plated contacts on Si solar cells were presented in this chapter, with the primary motivation of correlating electrical degradation observed in plated cells during extended thermal exposure with associated metal contamination in the Si substrate. The analytical technique was developed and optimised for the analysis of substrate contamination in several ways. To improve the quantitative analysis of metal concentration in the Si region underneath plated contacts without the need of a pre-ablation step, a chemical etching procedure was proposed to removal bulk and trace metals from the plated surface before LA-ICP-MS measurements. This consisted of a two-step procedure involving HNO₃ followed by HF/HCl. It was observed that whilst HNO₃ at room temperature was sufficient at removing the bulk of the plated contact, a significant surface layer of Ni remained after etching. By maintaining the temperature of HNO₃ at 40 °C, the etch rate was maintained which significantly improved the efficiency of metal removal from the exposed Si surface. This, combined with the HF/HCl clean to remove trace metals, was demonstrated to be a suitable alternative to pre-ablation steps for LA-ICP-MS sample surface preparation.

The ablation behaviour of Si under ns laser ablation was also assessed to optimise the transport efficiency of ablated material to the ICP for elemental analysis. While a linear relationship between crater depth and laser fluence was observed, a mostly linear increase in crater depth with scan speed was interrupted by a significant increase in crater depth when using the slowest scan speed (5 µm/s). This was theorised to be caused by explosive boiling of the Si during the high power laser ablation, whereby a molten region developing underneath the Si surface resulted in the eruption of Si material and the observed increase in crater depth. Increasing spot size was also

reported to result in significant build-up of agglomerated Si material on the Si surface that was not carried to the ICP for analysis. The aforementioned explosive boiling, coupled with condensation of ablated particles in the Ar environment resulted in the more significant build-up in material with larger volumes of ablated Si produced during ablation with larger spot sizes ($> 50 \mu\text{m}$). Even with the smallest spot size ($10 \mu\text{m}$), re-solidification of ablated Si was observed at the crater edges. In future, replacing ns lasers with shorter pulse laser (ps or fs) would reduce thermal ablation effects and improve transport efficiency and thus accuracy of LA-ICP-MS for the analysis of Si substrate contamination.

Quantitative LA-ICP-MS measurements of plated solar cells exposed to thermal treatments at 200°C for up to 1000 hours showed an increase in both Ni and Cu concentration with increasing thermal treatment duration. Whilst the Ni signal was most likely indicative of silicide formation during thermal processing, the increased Cu signal represented penetration of plated metal into the Si wafer. The similar trends in Ni and Cu concentration along line scans suggest that both metals may follow the same diffusion pathways when migrating into the Si substrate. Large standard deviations both along individual line scans as well as between different cells undergoing the same duration of thermal treatment are theorised to be the result of variability in the patterning and plating quality as well as ablation efficiency along the line scan. Correlating measured Cu and Ni concentration to electrical degradation showed a non-linear decay in V_{OC} with increasing Cu concentration and a more linear decrease with Ni concentration, whilst no clear trend was observed for pFF for either metal.

The experimental work reported on in this chapter highlights the potential for spatially-resolved analysis of plated metal penetration using LA-ICP-MS, demonstrating the possibility of correlating Cu and Ni concentration with associated degradations in pFF and V_{OC} . Although only briefly examined in this work, it is also possible to extend the technique to the analysis of metal layer uniformity directly after plating, providing more information on the uniformity of plated barrier metals. With further refinement of the analytical method, improved standardisation and optimisation of the laser properties and ablation conditions, the technique can prove a powerful tool for the improved understanding of metal diffusion paths at metal-semiconductor interfaces and deconstructing potential failure mechanisms in plated Si solar cells.

Chapter 6 Thermal Stability Testing for Plated Solar Cells

The impact of various processing conditions (temperature, base doping, barrier uniformity, illumination) on the diffusion and recombination activity of Cu in Si has been demonstrated and discussed in previous chapters. This final experimental chapter combines the knowledge obtained from previous experiments to investigate the impact of various parameters on long-term plating stability using the methodology first proposed by Bartsch *et al.* in 2010 [50]. The sensitivity of Cu-related degradation in plated solar cells to base doping polarity is addressed through a comparison of degradation responses between plated n-type PERT and p-type PERC cells. Since the thermal stability test reported first by Bartsch *et al.* was performed in the dark, the acceleration of Cu-related cell degradation with the addition of light during thermal stability testing was also investigated. Finally, the critical role of process control in cell degradation analysis and Arrhenius modelling is also discussed in terms of the impact of laser ablation contact grid patterning and barrier plating uniformity on the variability in thermal stability of Cu-plated cells with identical processing sequences.

6.1 Arrhenius analysis of solar cell degradation

The Arrhenius method for estimating long-term thermal stability of plated solar cells, first introduced by Bartsch *et al.* in 2010, was developed primarily as a way of estimating solar cell lifetime under field conditions [50]. Beginning with well-understood diffusion theory described by Fick's laws [69, 324, 325], the diffusion coefficient that defines the flux of the diffusing species in a material is given by Equation 6.1 [50]:

$$D = D_0 \cdot \exp\left(-\frac{E_A}{k_B T}\right) \quad (6.1)$$

With suitable boundary conditions (infinite diffusion source, constant surface concentration and a semi-infinite diffusion medium), the penetration depth of a diffusing species (L) can be determined according to [50]:

$$L = \sqrt{Dt} \quad (6.2)$$

The critical diffusion length of Cu into the cell is defined as the depth of the SCR associated with the p-n junction, at which point the performance of the cell is expected to be severely impacted. However, before entering the Si, diffusing Cu must first penetrate the Ni barrier layer where its diffusivity is expected to differ from that in Si. This complicates the analysis of Cu diffusion in plated solar cells.

To simplify this analysis, the temperature-dependent diffusion behaviour of Cu can be estimated through Arrhenius modelling. The activation energy, E_A , of the multi-step process of Cu penetrating the Ni barrier and diffusing into the Si of the solar cell for a given time (t) and temperature (T) can be obtained from the slope of a plot of $\ln(t)$ as a function of $1/T$ [50]:

$$\ln(t) = \frac{E_A}{k_B T} + \ln\left(\frac{L^2}{D_0}\right) \quad (6.3)$$

To determine the time-temperature pairs that correspond to a constant diffusion length (assuming also constant D_0), the diode quality of the solar cell can be monitored via tracking pFF with Suns- V_{OC} measurements as a function of time at a set temperature. For each testing temperature, T , the value of t is then defined as the time at which the pFF is reduced by 5% from its initial value before thermal treatment commenced (reflecting degradation thresholds set in test standard IEC 61215 [326]). Suns- V_{OC} measurements are non-destructive and they eliminate series resistance effects, allowing for analysis of the diode quality of the cell without contributions from series resistance which may occur during thermal testing due to contact degradation. This method assumes that a certain loss in pFF (which is highly sensitive to impurities in the SCR) represents a certain degree of Cu diffusion into the cell for equivalent solar cell designs. Thus, a 5% relative loss in pFF (the chosen degradation condition for most studies on plated solar cells [51, 56, 57, 232], including those presented in this chapter) represents a constant diffusion length for different thermal conditions. Subsequently, from

Equation 6.3, an estimation of cell lifetime at assumed outdoor conditions ($\sim 80^\circ\text{C}$) can be obtained.

However, it was acknowledged by Bartsch *et al.* [50] that the Arrhenius modelling employed was highly sensitive to the accuracy of electrical measurements performed on cells during thermal stability testing, with even small errors in the measurement leading to significant inaccuracies in the estimated E_A for Cu diffusion in the cell structure and thus the extrapolated cell lifetime at environmental operating conditions [50]. Subsequently, Kraft also highlighted the sensitivity of the testing methodology to the frequency in which electrical measurements are performed [232]. As seen in Figure 6.1, the degradation rate for solar cells with Cu in direct contact with the Si substrate increased with decreasing measurement frequency during extended thermal exposure at 275°C . This observation was attributed to an increased build-up of Cu in the Si wafer with longer periods of thermal exposure, resulting in a higher supersaturation of diffused Cu in the wafer bulk leading to enhanced degradation due to Cu precipitation [36]. With shorter measurement frequencies, Cu out-diffusion could dominate which resulted in a slower degradation rate [74], further highlighting the need to better understand the sensitivity of Cu-plated cell degradation to the kinetics of Cu diffusion and precipitation.

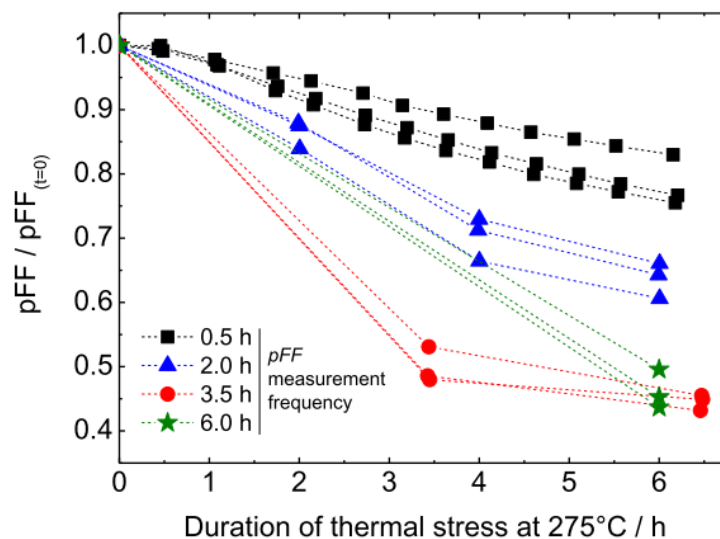


Figure 6.1: Normalised pFF as a function of thermal treatment duration at 275°C for Cu-plated cells without a diffusion barrier tracked with different measurement frequencies (from [232]).

It should also be noted with this Arrhenius analysis, that the pFF degradation involves multiple steps (Cu diffusion through Ni, Cu diffusion in Si and presumably also Cu precipitation close to the junction). Consequently, the estimated E_A is representative of the rate limiting step associated with the degradation. Despite the apparent limitations in the technique, the high sensitivity of the solar cell junction to impurity-related recombination, coupled with the non-destructive nature of the analysis technique make it far more suitable than other forms of characterisation such as SIMS or LA-ICP-MS that have been discussed in the previous chapter. However, there may be beneficial information to be gained from expanding this thermal stability analysis to include parameters in addition to pFF , which will be discussed in this chapter.

6.2 Comparison of n-type and p-type cell degradation

6.2.1 Introduction

In Chapter 2, the greater propensity for Cu defect formation in n-type Si compared to p-type Si was discussed. The amphoteric nature of Cu silicide precipitates results in the precipitate charge state switching from positive to negative as the Fermi level is raised above the neutrality level for Cu precipitates ($E_C - 0.2$ eV) [36]. This implies that changing the base doping of a plated solar cell from p-type to n-type will also change the degradation behaviour due to Cu diffusion from the plated contact into the Si substrate during thermal stability testing, with a higher potential for significant bulk degradation expected in n-type Si. This section reports the results of experiments which examined the degradation responses during thermal stability testing performed on both p-type PERC and n-type PERT solar cells with Cu-plated contacts and compares the associated degradation behaviour of different cell structures during extended thermal exposure.

6.2.2 Experimental

Small-area p-type cells were fabricated on 156 mm B-doped 1-3 $\Omega\cdot\text{cm}$ Cz-Si wafers with random-pyramid texturing, a homogeneous P-doped emitter (sheet resistivity $\sim 110\text{-}120$ Ω/\square , surface concentration of $\sim 2 \times 10^{19}$ cm^{-3} and junction depth of ~ 0.4 μm) and an 80 nm SiN_x ARC (deposited on the front surface using direct PECVD). Cells with a PERC rear contact structure were analysed in these experiments.

Comparative n-type PERT cells were similarly fabricated on 156 mm P-doped 1-5 $\Omega\cdot\text{cm}$ Cz-Si wafers with random-pyramid texturing, a uniform B-doped emitter (sheet resistivity $\sim 80\text{-}90 \Omega/\square$, surface concentration of $\sim 3\times 10^{19} \text{ cm}^{-3}$ and junction depth of $\sim 0.86 \mu\text{m}$), an $\sim 80 \text{ nm}$ $\text{AlO}_x/\text{SiN}_x$ ARC (deposited on the front surface using direct PECVD) and a uniformly P-diffused BSF.

Small cell contact grids (fingers + busbar) were patterned on the front surface via 266 nm ps laser ablation (as detailed in Section 4.2.2) with different optimised laser conditions for the different cell structures to ensure complete removal of the SiN_x layer. The p-type cells were ablated with 0.44 J/cm^2 laser fluence and $9 \mu\text{m}$ pitch between adjacent laser scans, whilst the n-type cells were ablated with 0.3 J/cm^2 and a $9 \mu\text{m}$ pitch between adjacent laser scans. The lower power used on the n-type cells was to compensate for a greater degree of laser damage observed for B-doped emitters compared to the P-doped emitters on the p-type cells.

Cells were metallised using bias-assisted LIP for the p-type cells and field-induced plating (FIP) for the n-type cells [236, 244, 327] to form a Ni ($\sim 1 \mu\text{m}$) and Cu ($8\text{-}10 \mu\text{m}$) contact stack with a $\sim 1 \mu\text{m}$ LIP Ag capping layer. The plating solutions and currents used for both LIP and FIP were identical (according to the methodology described in Section 4.2.2.1). Following plating, 156 mm plated wafers were sintered at 350°C for 1 min to form a NiSi layer. After sintering, small-area cells were laser-cleaved from the 156 mm wafers for edge isolation, characterisation and thermal testing.

To simulate long-term operation at elevated temperatures and replicate the testing conditions used in previous studies [50, 51, 328], the cell temperature was maintained at 200°C on a hotplate in the dark. Cells were characterised before thermal treatment using a combination of PL imaging with a BT Imaging LIS-R1 imaging tool, I - V measurements using a calibrated in-house constant illumination I - V tester under standard test conditions, external quantum efficiency (EQE) measurements with a QEX7 Solar Cell Measurement System from PV Measurements, and $\text{Suns-}V_{\text{OC}}$ measurements using a Sinton Instruments Illumination-voltage tester. Identical characterisation was performed intermittently at intervals of between 24-72 hours to avoid any impact of measurement frequency on observed Cu degradation behaviour [232]. The impact of voids at the Cu/Ag interface was accounted for prior to each measurement by applying pressure to the probe on contacting (see Section 4.2).

6.2.3 Results and discussion

Table 6.1 summarises the average cell output for the n-type and p-type cells tested in this experiment before thermal treatment and after 500 hours on a hotplate at 200 °C. On average, the p-type PERC and n-type PERT cells experienced a similar absolute efficiency loss of 4-5% after 500 hours of thermal exposure. The large standard deviations observed in the degradation cell output parameters were most likely due to significant variability in cell degradation amongst different batches, which will be discussed in more detail in Section 6.4. Whilst both n-type and p-type cells suffered the same average loss in V_{oc} (9.5–10% relative), the p-type cells suffered more severe pFF degradation than the n-type cells, with a relative pFF loss of $\sim 21\%$ for p-type PERC cells compared to only 15% for the n-type PERT cells.

Table 6.1: Comparison of cell I - V parameters for n-type PERT and p-type PERC Cu-plated solar cells before and after 500 hrs at 200 °C on a hotplate in the dark. The number of cells analysed in each batch is given by the value, n .

| | p-type ($n = 6$) | | n-type ($n = 18$) | |
|--|--------------------|----------------|---------------------|---------------|
| | t_0 | t_{500} | t_0 | t_{500} |
| V_{oc} (mV) | 644 ± 4 | 566 ± 110 | 668 ± 1 | 604 ± 93 |
| J_{sc} (mA/cm ²) | 39.4 ± 0.3 | 40.4 ± 0.4 | 40.7 ± 0.3 | 39 ± 5 |
| FF (%) | 74.8 ± 0.9 | 58 ± 14 | 77.1 ± 0.8 | 68 ± 14 |
| pFF (%) | 79.6 ± 0.3 | 62 ± 15 | 80.8 ± 0.4 | 69 ± 14 |
| η (%) | 19.0 ± 0.2 | 14 ± 5 | 21.0 ± 0.3 | 16 ± 5 |
| R_{series} (Ω .cm ²) | 0.8 ± 0.2 | 0.8 ± 0.5 | 0.5 ± 0.1 | 0.7 ± 0.3 |

For all the cells examined in this study, there was minimal observed reduction in short-circuit current, J_{sc} , during thermal stability testing (as confirmed by the example EQE curves presented in Figure 6.2 below, which indicate J_{sc} losses of 0.2 mA/cm² and 0.02 mA/cm² for p-type and n-type cells, respectively). Whilst degradation in the spectral response of thermally-treated cells was only obvious in the case of large reductions in V_{oc} , pFF and J_{sc} , Figure 6.2 (b) shows slight reductions in the broadband EQE for p-type PERC cells (corresponding to a J_{sc} loss of 0.2 mA/cm²), which could be attributed to increased defect density in the substrate or potentially at the surface, which has previously been shown to reduce broadband wavelength response in EQE

measurements in light-soaked solar cells, particularly at shorter wavelengths [329, 330]. It is possible that degradation of the surface passivation was responsible for the observed EQE degradation, however the possibility of metal diffusion in and around the surface, as has already been shown in cross-sectional TEM images in Chapter 4, cannot be eliminated as a cause of the observed EQE response degradation, especially with the inclusion of light, as will be discussed further in the next section.

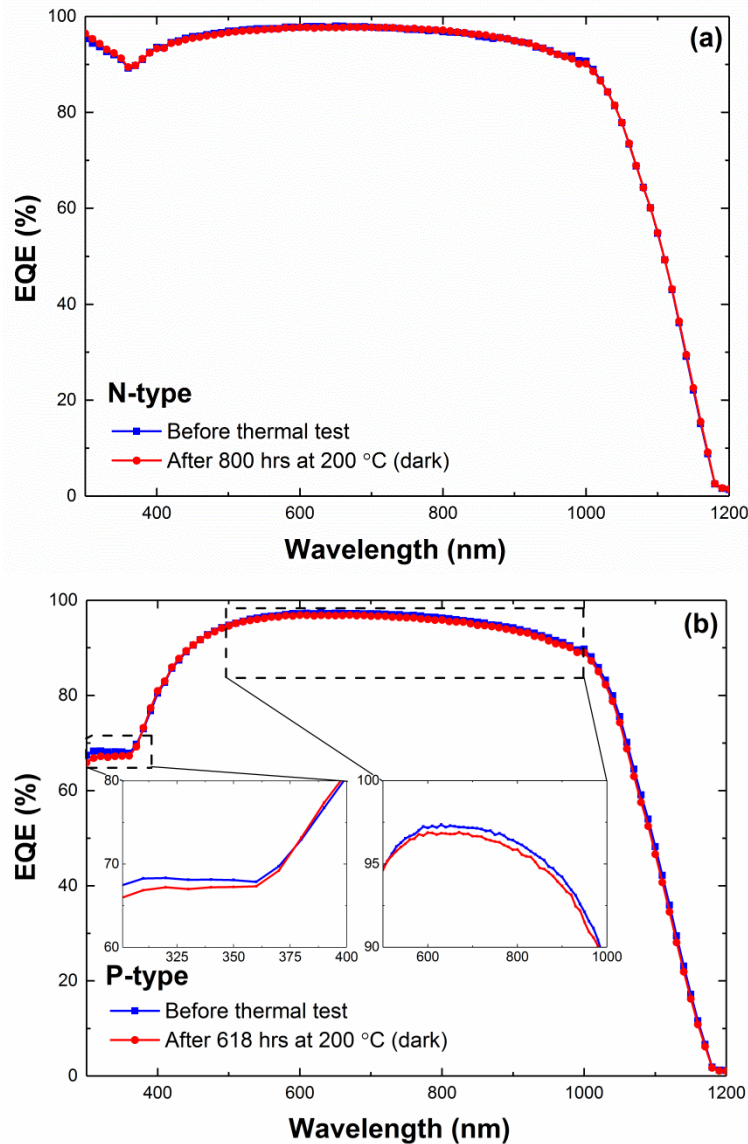


Figure 6.2: (a) EQE curve of a representative Cu-plated n-PERT cell before and after thermal stability testing at 200 °C for 800 hrs in the dark, and (b) EQE curve of a representative Cu-plated p-type PERC cell before and after thermal stability testing at 200 °C for ~ 600 hrs in the dark. The insets in (b) show zoomed in regions of the EQE curve.

To better interpret the different Cu-related degradation responses of the n-type PERT and p-type PERC solar cells, a closer examination of the evolution of degradation with time was required. Figure 6.3 presents a series of pseudo I - V curves obtained with Suns- V_{OC} measurements on example n-type and p-type solar cells, respectively, at different durations of thermal stability testing. Due to the variability in cell degradation within each batch of cell structures, cells with median degrees of degradation were selected for closer examination.

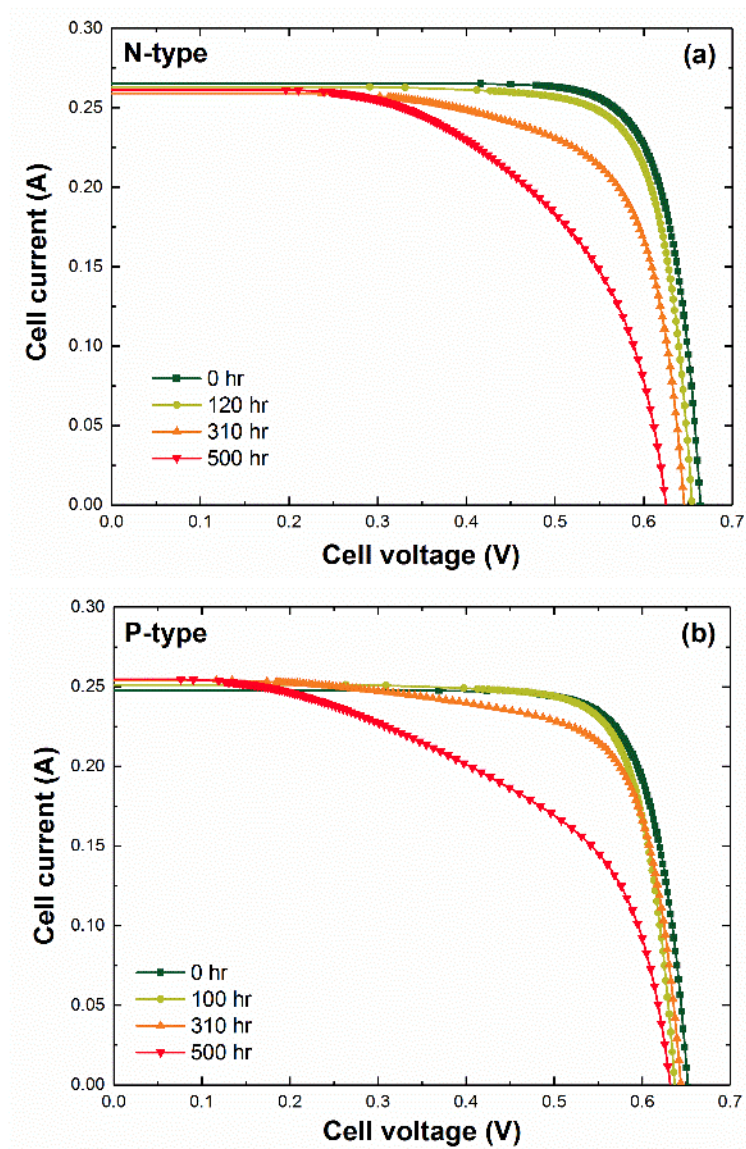


Figure 6.3: Evolution of pseudo I - V response for (a) a representative Cu-plated n-type PERT cell, and (b) a representative Cu-plated p-type PERC cell with increasing duration of thermal treatment at 200 °C in the dark.

Examining the evolution of n-type cell degradation, increased non-ideal recombination effects were observed with increasing duration of thermal exposure, as well as a noticeable shift in the V_{OC} . An increasing shift in the knee of the curve suggested a significant increase in recombination active defects in the SCR of the cell, resulting in the reduced FF and pFF as a result of non-ideal recombination. Comparatively, the p-type cell presented more delayed degradation behaviour, coupled with a less severe reduction in V_{OC} with increased duration of thermal exposure. The different apparent degradation behaviours observed in these two examples suggest different concentrations of Cu defects forming in different regions of the cell. Whilst the pFF reduction is considered an indicator of junction-related recombination according to Bartsch *et al.* [50], V_{OC} is an indicator of bulk recombination within the Si substrate. Thus, the enhanced reduction in V_{OC} in the n-type PERT cell presented in Figure 6.3 (a) compared to the p-type PERC cell presented in Figure 6.3 (b) is consistent with more Cu precipitates forming in the bulk in the n-type cells, most likely due to the reduced barrier to Cu precipitate formation in n-type material [36]. The separation of junction and bulk recombination was further assessed by examining the J_{01} and J_{02} recombination current densities extracted from two-diode model fits on these pseudo I - V curves, with the associated fit parameters from the previously shown pseudo I - V curves presented below in Table 6.2.

Table 6.2: Two-diode model fitted values for J_{01} and J_{02} saturation current densities for a representative n-type PERT and p-type PERC Cu-plated solar cell after different durations of thermal treatment at 200 °C on a hotplate in the dark. The shaded values correspond to measurements in which the 2-diode model did not provide an adequate fit (corresponding R^2 values for each fit are also given).

| Time (hrs) | p-type PERC | | | n-type PERT | | |
|---------------|----------------------------------|----------------------------------|-------|----------------------------------|----------------------------------|-------|
| | J_{01} (A/cm ²) | J_{02} (A/cm ²) | R^2 | J_{01} (A/cm ²) | J_{02} (A/cm ²) | R^2 |
| 0 | 2.8×10^{-13} | 3.7×10^{-8} | 0.999 | 2.4×10^{-13} | 2×10^{-8} | 0.999 |
| 100 | 4.7×10^{-13} | 4.8×10^{-8} | 0.997 | 2.5×10^{-13} | 3.8×10^{-8} | 0.999 |
| 310 | 9×10^{-14} | 1.1×10^{-7} | 0.942 | 7.5×10^{-14} | 1.3×10^{-7} | 0.952 |
| 500 | 1×10^{-14} | 1.8×10^{-7} | 0.921 | 1×10^{-14} | 3.3×10^{-7} | 0.838 |

The unexpected (small) reduction in J_{01} with thermal treatment for both the p-type PERC and n-type PERT cells highlights a problem with two-diode analysis applied to later stages of cell degradation. As the degradation extent increased in both the n-type and p-type cells, the pseudo I - V data was increasingly poorly modelled using a two-diode model as evident in the decreasing R^2 values of the fitted curves, limiting the usefulness of this analysis. Figure 6.4 shows the measured Suns- V_{OC} curve (and an attempted two-diode fit) for a representative p-type PERC cell and n-type PERT cell at different stages of thermal treatment at 200 °C.

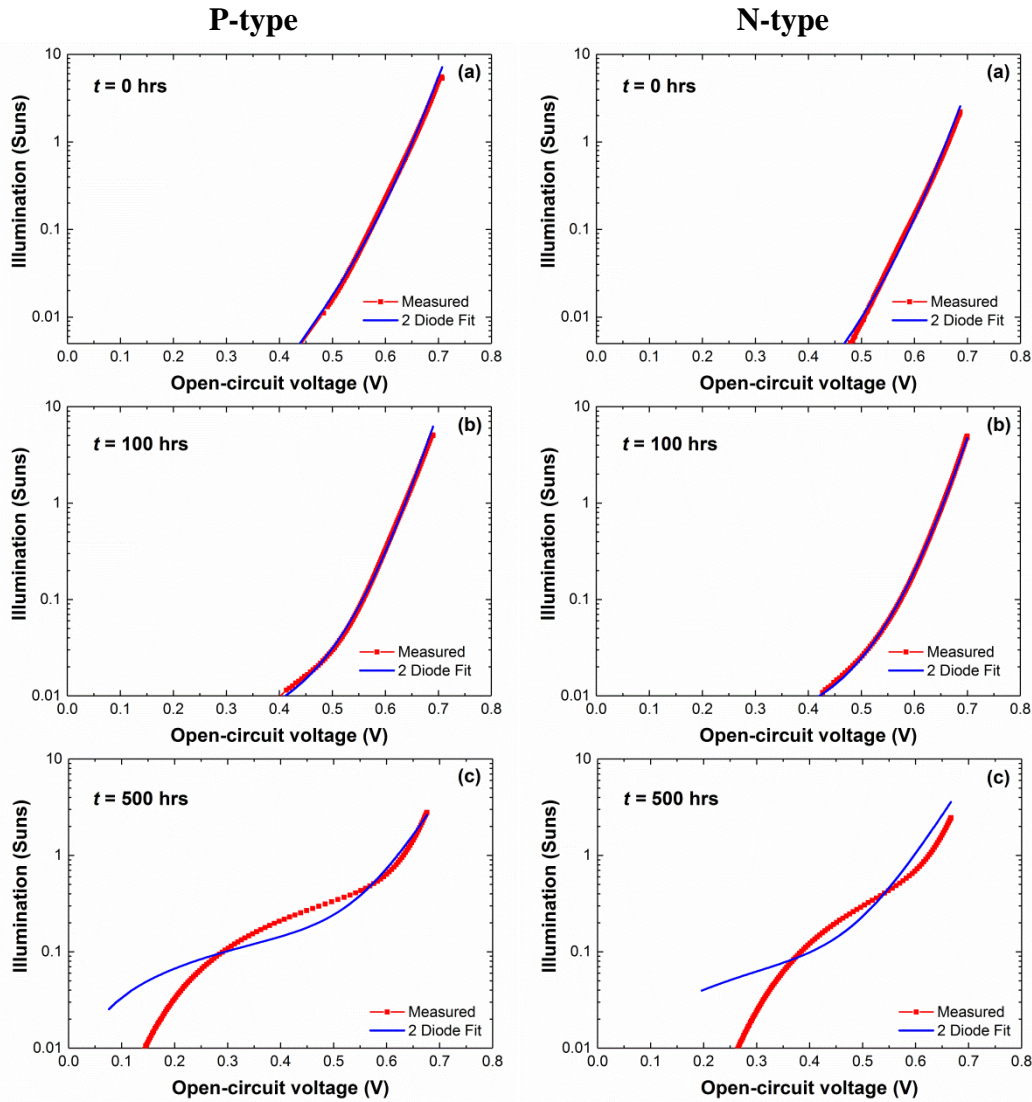


Figure 6.4: Comparison of measured Suns- V_{OC} data and corresponding two-diode model fit for a representative Cu-plated p-type PERC and n-type PERT solar cell after (a) 0 hrs, (b) ~ 100 hrs, and (c) 500 hrs of thermal treatment at 200 °C in the dark.

After ~ 100 hrs of thermal exposure, the two-diode model was still able to adequately fit the measured Suns- V_{OC} curve, and the increasing J_{02} component was visible in the degradation of the curve at low illumination intensities, which is indicative of some degradation at the SCR. However, after 500 hrs of thermal exposure, the distortion of the Suns- V_{OC} curve was so severe such that the two-diode fit and the extracted J_{01} and J_{02} parameters were no longer accurate. Since distortion related to the presence of voids at the Cu/Ag interface had been removed, the degradation of the Suns- V_{OC} curve at this stage of thermal stability testing indicated a high degree of non-ideal recombination occurring in both the n-type and p-type cells. This reflects similar distortion in dark I - V measurements that have been observed in several previous studies [331–333] in which this behaviour was attributed to different recombination centres in Si that result in diode ideality factors much higher than $n = 2$ at low bias voltages. Similar behaviours were also recently observed by Dang *et al.*, who attributed this increased non-ideality to laser-induced dislocations generated during ablation patterning for front contact formation of plated p-type PERC cells, as well as potential Ni/Cu diffusion along laser-induced defects [264, 334]. Whilst dark I - V measurements were not monitored in this work, the similar behaviours of dark I - V curves in previous studies and the Suns- V_{OC} curves in Figure 6.4 highlighted similarities in the degradation behaviours observed. Since the accuracy of fitted parameters for J_{01} and J_{02} using the 2-diode model was poor at later stages of degradation, a two-diode analysis was not used to monitor the cell degradation reported in this chapter.

Corresponding PL images for the representative p-type PERC and n-type PERT cells discussed above were examined to assess the uniformity of cell degradation across the cell, as can be seen in Figure 6.5 below. For the most severely degraded cells, the PL intensity was reduced so much that features of the cell could no longer be resolved at the same PL exposure used to image cells before thermal treatments.

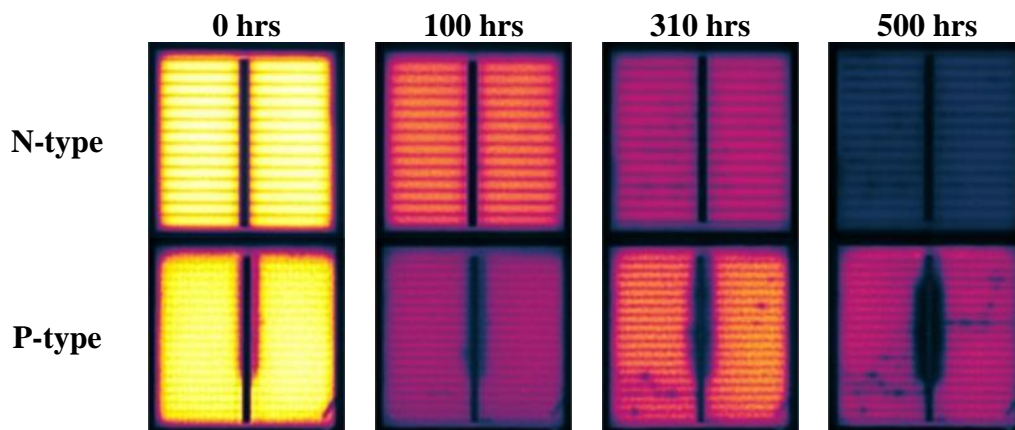


Figure 6.5: PL images of representative n-type PERT and p-type PERC solar cells (used for Figure 6.3) at different stages of thermal stability testing at 200 °C in the dark (exposure time = 0.1 s, photon flux = $2.72 \times 10^{17} \text{ cm}^{-2}\text{s}^{-1}$).

In the PL images shown above, it can be observed that a mostly uniform degradation in PL intensity occurred during thermal stability testing, yet there are also localised regions of decreased PL intensity such as that observed in the p-type PERC cell after 310 hrs of thermal exposure. These localised reductions in PL intensity represented local shunts in the contact structure as well as increased recombination in the cell, potentially as a result of Ni/Cu diffusion into the solar cell junction (as shown previously in Chapter 4, as well as in similar studies [264]), resulting in the observed non-ideal recombination that caused the shift in the knee of the I - V curves seen in Figure 6.3. The increase in PL intensity between 100 and 310 hours for the p-type PERC cell also corresponds with the shift in the V_{OC} in the pseudo I - V response for this particular p-type cell, and may correspond with changes (i.e., reductions) in the p-type bulk recombination occurring during the thermal treatments, although the exact cause could not be confirmed in this study.

Since the two-diode model provided limited information at more advanced stages of degradation during thermal stability testing, the indicators of Cu-related cell degradation selected for subsequent analysis in this study were the V_{OC} and pFF . These parameters were initially selected to monitor changes in bulk and junction-related recombination, respectively. To determine the relative contributions of these parameters to the degradation in cell efficiency during thermal stability testing, the correlations between both V_{OC} and pFF to cell efficiency across all measurements performed in this experiment were graphed in Figure 6.6. Degradation in pFF preceded degradation in

V_{OC} for both the p-type and n-type cells. Cell efficiency appeared to degrade linearly with pFF [see Figure 6.6 (c)], however the relationship between cell efficiency and V_{OC} appeared to be more complex [see Figure 6.6 (a)].

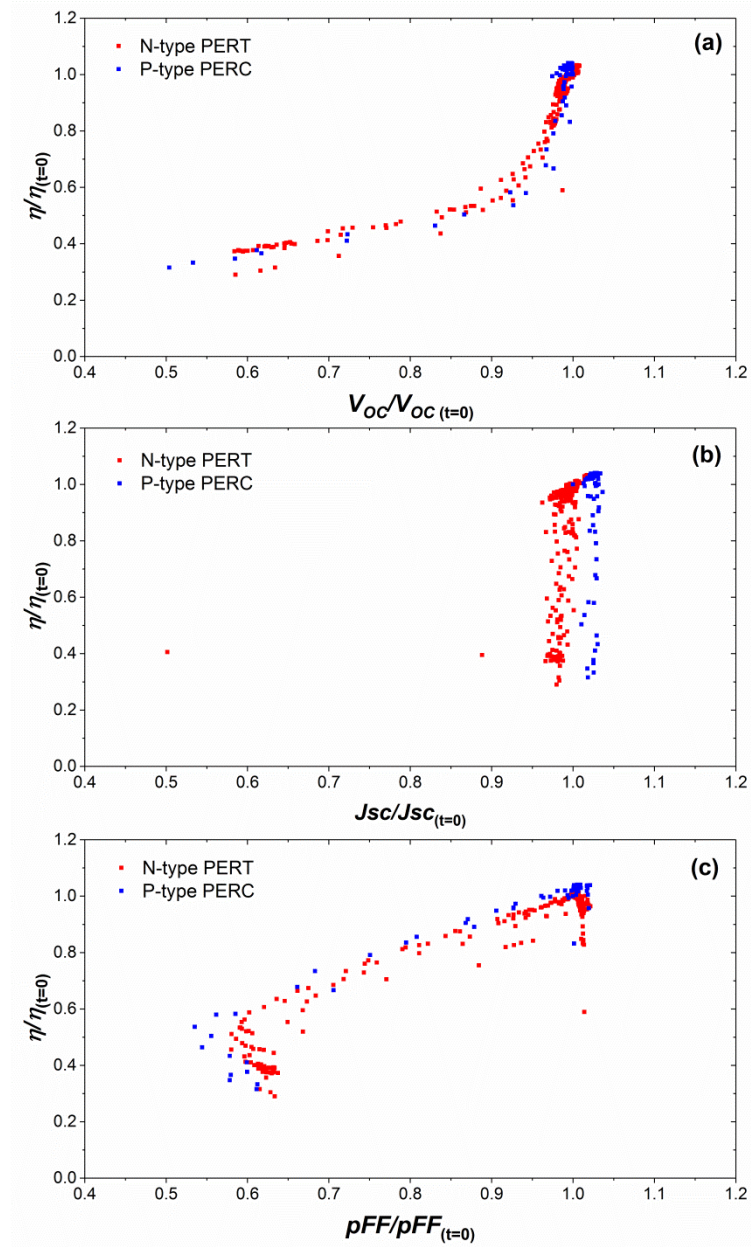


Figure 6.6: Relationship between: (a) normalised V_{OC} and efficiency; (b) normalised J_{sc} and efficiency; and (c) normalised pFF and efficiency (η) for both p-type PERC and n-type PERT solar cells during thermal stability testing at 200 °C in the dark.

This trend of pFF degradation preceding V_{OC} degradation is consistent with the gradual diffusion of Cu from the front contacts into the bulk of the solar cell where J_{01} and V_{OC} were impacted, with the emitter being the region most susceptible to

degradation during thermal stability testing. Another explanation for the observed degradation behaviour is the injection-dependent recombination behaviour of Cu-induced defects or precipitates. The presence of an SRH recombination centre with even a moderate capture asymmetry can lead to strong injection-dependent carrier lifetime in Si [194]. Previous studies by Aberle *et al.* [335] and Macdonald and Cuevas [336] have shown that such injection-dependent SRH recombination at the rear surface and in the bulk can result in reduced FF s in Si solar cells. It was shown in Chapter 3 (see Figure 3.11 and Figure 3.14) that the presence of Cu precipitates also leads to a strong injection-dependent carrier lifetime in Si, with lower lifetimes observed under low injection conditions which correspond more closely with the maximum power point of the I - V curve (the knee of the curve at $\Delta n < 1 \times 10^{15} \text{ cm}^{-3}$) than the V_{OC} . Thus, the presence of injection-dependent recombination can result in the observed sloping knee in the Suns- V_{OC} curves in Figure 6.4 and the concomitant reduced pFF before the defect density could increase sufficiently to impact the V_{OC} of the solar cell. The injection dependence of recombination arising from Cu precipitates may be related to the precipitate size and density, with larger precipitates presenting an apparent stronger injection-dependence. Similar conclusions have also been made in previous studies [158, 183], where an increased density of precipitates resulted in an overall lower bulk lifetime and thus V_{OC} for the resultant cell. Hence, it is possible that as Cu precipitates grow due to increasing Cu concentration in the Si substrate, the severity of pFF degradation increases until the precipitate density increases sufficiently to degrade V_{OC} . However, these studies focussed on iron (Fe), which has a significantly larger capture asymmetry compared to the Cu precipitates examined in this work ($k > 200$ [336] compared to $k = 1.4 - 5.6$ as determined for FZ-Si in Chapter 3). Thus, the impact of SRH defect asymmetry on the I - V characteristics of the solar cells examined in this work would be expected to be much less pronounced. Furthermore, such severe non-ideal recombination would be expected to significantly impact the J_{sc} and J_{01} of the device due to the distribution of precipitates throughout the bulk (rather than localised to the junction), which is not the case as seen in the cell results in Table 6.1 and Table 6.2, as well as the EQE results in Figure 6.2. Shunting of the junction by Cu precipitates more closely coincides with the minimal J_{sc} losses observed, since shunting does not severely impact J_{sc} . Consequently, the observed Cu-related degradation was more consistent with a localised distribution of precipitates close to the junction.

It should also be acknowledged that the duration between consecutive measurements would likely impact the relative trends observed in these experiments as was mentioned earlier in Section 6.1 [232]. Since the average interval between measurements was between 24 and 72 hours, the time available for Cu diffusion into the cell substrate is extended beyond what would be expected during 8 hours of daylight in the field.

The difference between the progressive degradation of the n-type PERT and p-type PERC Cu-plated cells was most clearly resolved when comparing the normalised pFF and V_{OC} as a function of thermal treatment duration. As shown in Figure 6.7 (a), the normalised pFF of both the n-type and p-type cells decreased with increasing thermal treatment duration, however the decrease in pFF was more rapid for the n-type cells than the p-type cells. The large standard deviations observed in this degradation experiment was due to significant variation in cell degradation across the cells tested, which could be the result of process variance between different cell batches, which will be discussed in more detail in Section 6.4. Regardless of base doping, the 95% relative threshold was reached well before 500 hours of thermal treatment, which indicates poorer performance of the plated Ni barrier for the cells in this study compared with previous studies employing the same thermal stability test with optimised uniform Ni barriers on either bare Si or printed Ag seed layers [51, 54, 232].

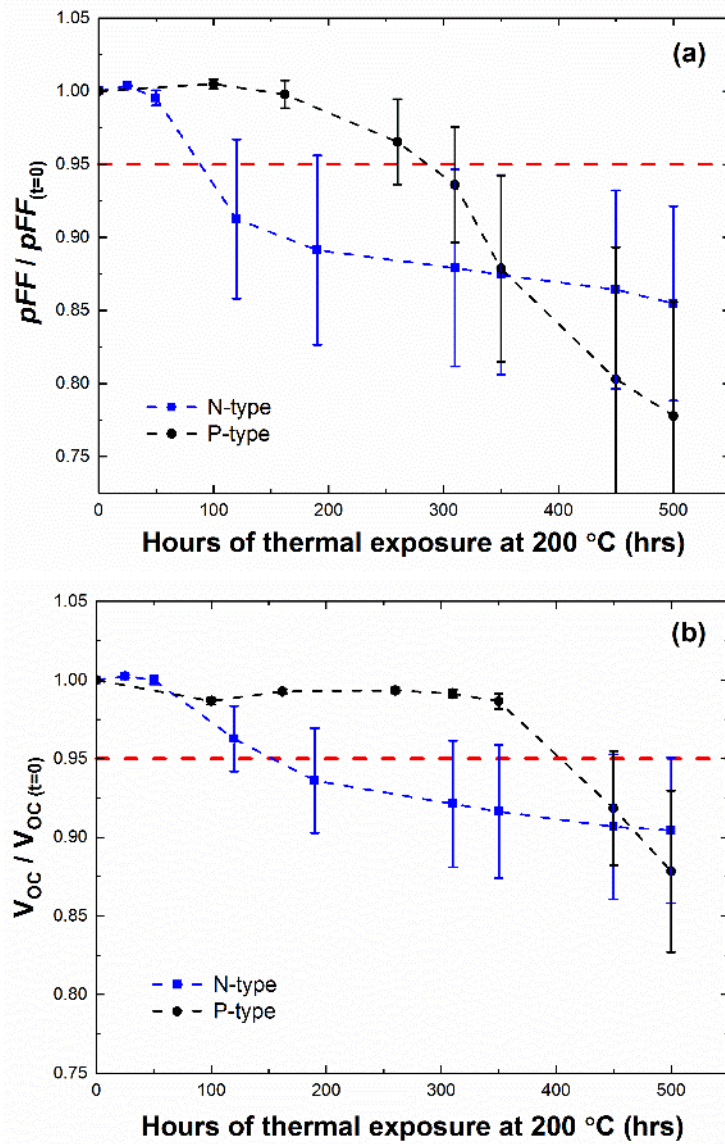


Figure 6.7: (a) Normalised pFF and (b) normalised V_{OC} as a function of thermal treatment duration at 200 °C in the dark for Cu-plated p-type PERC and n-type PERT solar cells. The error bars represent the standard deviation across the batch of cells examined (sample sizes provided in Table 6.1). The red dashed line represents the critical degradation state chosen for Arrhenius analysis (95% relative reduction in pFF).

The trend in V_{OC} degradation with thermal treatment duration is more in keeping with the expected Cu-related degradation responses of n-type and p-type solar cells. For n-type cells, the degradation of the bulk is expected to be more rapid since lower concentrations of Cu are required to trigger Cu precipitation which leads to enhanced bulk recombination and a lower V_{OC} . In the case of p-type solar cells, the Cu concentration needed to overcome the nucleation barrier for Cu precipitation is

generally significantly higher [36, 86], leading to the more delayed degradation in V_{oc} witnessed for p-type cells compared to n-type cells during thermal stability testing.

Regardless of the base doping, the degradation of the plated cells appears to occur initially as a reduction in pFF followed by a reduction in V_{oc} . This behaviour may reflect the diffusion pathways of Cu from the plated contact stack into the Si substrate. Initially, Cu is likely to build up closer to the surface and junction, leading to increased non-ideal recombination at the junction, reducing pFF . As Cu diffusion into the bulk becomes more extensive, there is a more noticeable reduction in V_{oc} .

There are several factors that may have distorted the recombination behaviour observed in each of these cell structures. The preferential formation of Cu precipitates in n-type material may potentially enhance the penetration of Cu in n-type PERT cells by providing a sink for Cu, similar to the way Cu diffusion through the Ag capping layer may have been driven by a sink reaction with the atmosphere as discussed in Chapter 4. Furthermore, variation in ablation patterning conditions for n-type and p-type cells may have introduced different defect densities which vary the available defect pathways for Cu diffusion. It is also possible that non-uniformities in the plated Ni barrier resulted in more enhanced degradation in some cells compared to others. The exact mechanisms behind the degradation behaviour observed could not be confirmed in these experiments. Repeating these experiments with a more consistent batch of p-type PERC and n-type PERT cells would allow for a better comparison of p-type and n-type degradation behaviour due to Cu diffusion. Modelling metal diffusion along defect pathways introduced by the different laser ablation conditions between n-type and p-type cells could also help to shed some light on the different degradation responses observed in this work.

6.3 Influence of illumination on degradation

6.3.1 Introduction

Whilst previous studies based on the methodology introduced by Bartsch *et al.* [50] considered only the diffusion of Cu through the metal barrier layer and subsequent build-up in the Si [51, 57, 264, 328] as the driving mechanism behind the observed degradation, the contribution of illumination to Cu-related degradation (Cu-LID) in

plated cells (which is likely to be experienced in the field) needs to also be understood. As discussed in Chapter 2 and reported in Chapter 3, optical activation of Cu defect formation under even low light intensities can significantly accelerate degradation of the minority carrier lifetime in Cu-contaminated Si due to the nucleation and growth of Cu precipitates [42, 104, 105]. Thus, an examination of the long-term stability of Cu-plated solar cells which are both heated and illuminated may be required to more accurately represent the conditions experienced by cells operating in the field. This section reports on experiments which aimed to investigate the different degradation behaviours of plated p-type PERC and n-type PERT solar cells using thermal treatments with and without illumination.

6.3.2 Experimental

Small-area p-type PERC cells and n-type PERT cells were fabricated according to the experimental description provided in Section 6.2.2. A contact stack of Ni ($\sim 1\ \mu\text{m}$), Cu (8-10 μm) and Ag ($\sim 1\ \mu\text{m}$) was plated and cells were sintered at 350 °C for 1 min in N₂ ambient followed by laser cleaving of the 156 mm wafers for edge isolation, characterisation and thermal testing.

Both the p-type and n-type cells were randomly separated into two different experimental batches – one in which the temperature was maintained at 200 °C on a hotplate in the dark (previously discussed in Section 6.2), and another with cells exposed to ~ 1 Sun illumination provided by 4×500 W halogen flood lights on an identical hotplate calibrated such that cell temperature was maintained at 200 °C (using the setup previously described in Chapter 3). Cells were characterised at different stages of thermal stability testing according to the procedure outlined in Section 6.2.2.

6.3.3 Results and discussion

The I - V response of cells before and after 500 hours of thermal exposure at 200 °C both in the dark (t_{500_Dark}) and under 1-Sun illumination (t_{500_LS}) are summarised in Table 6.3 and compared with the pre-treatment values (t_0). For the n-type PERT cells, there was little observable difference in degradation under illumination compared to thermal treatment in the dark, with only a slightly lower pFF and V_{OC} observed with the inclusion of light in the thermal stability testing procedure. For the p-type cells, there is a significant variation between dark and illuminated samples during thermal stability

testing. With the addition of illumination, V_{OC} decreased by an average of ~ 260 mV after 500 hrs at 200°C under 1-Sun illumination, indicating significantly more advanced bulk degradation under illumination. The pFF of the p-type PERC cells also decreased by 31% for the illuminated cells compared to 22% for cells that underwent thermal stability testing in the dark. This resulted in a two-fold increase in average efficiency loss for illuminated p-type cells compared to that measured on identically-processed samples experiencing the same thermal stability test in the absence of illumination.

Table 6.3: Summary of average cell output parameters for p-type PERC and n-type PERT solar cells before and after thermal stability testing at 200°C for 500 hrs on a hotplate both in the dark and under ~ 1 Sun illumination.

| | p-type ($n = 6$) | | | n-type ($n = 18$) | | |
|-----------------------------------|--------------------|-----------------|----------------|---------------------|-----------------|----------------|
| | t_0 | t_{500_Dark} | t_{500_LS} | t_0 | t_{500_Dark} | t_{500_LS} |
| V_{OC} (mV) | 644 ± 4 | 566 ± 110 | 383 ± 194 | 668 ± 1 | 605 ± 94 | 600 ± 83 |
| J_{sc} (mA/cm ²) | 39.4 ± 0.3 | 40.4 ± 0.4 | 40.1 ± 0.3 | 40.7 ± 0.3 | 39.4 ± 4.7 | 42 ± 0.9 |
| FF (%) | 74.8 ± 0.9 | 58 ± 14 | 49 ± 13 | 77.1 ± 0.8 | 68 ± 14 | 66 ± 13 |
| pFF (%) | 79.6 ± 0.3 | 62 ± 15 | 55 ± 13 | 80.8 ± 0.4 | 69 ± 14 | 69 ± 15 |
| η (%) | 19.0 ± 0.2 | 13.6 ± 4.9 | 8.1 ± 6.2 | 21.0 ± 0.3 | 16.5 ± 5.2 | 16.8 ± 5.2 |

Since the p-type cells were most significantly impacted by the addition of illumination, correlations between both V_{OC} and pFF and cell efficiency across both the dark and illuminated p-type PERC cells that experienced thermal stability testing were re-examined, as presented in Figure 6.8 below. Although the absolute degradation of the cells was greater for the thermally-treated cells under illumination, the relative trends in the pFF and V_{OC} degradation remained unchanged, with pFF decreasing initially (following an apparently linear decrease with efficiency) followed by a decrease in V_{OC} . This remains consistent with the discussion in Section 6.2.3, where an increasing concentration of SRH Cu defects localised in the emitter leads to a more pronounced

degradation in pFF , before increased precipitate density leads to an increase in V_{oc} degradation.

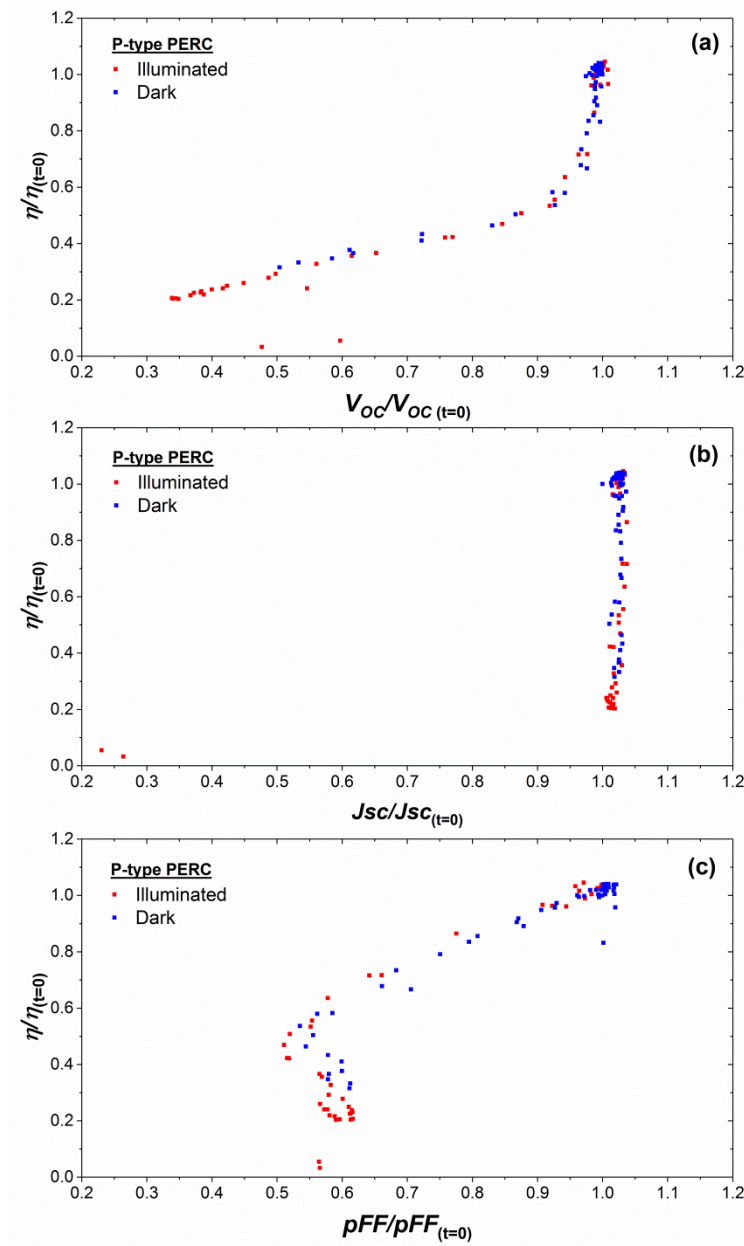


Figure 6.8: Relationship between (a) normalised V_{oc} and efficiency, (b) normalised J_{sc} and efficiency, and (c) normalised pFF and efficiency (η) for p-type PERC solar cells during thermal stability testing in the dark and at ~ 1 Sun illumination at 200°C .

The main impact of illumination on the degradation behaviour of n-type PERT cells was an observed acceleration of the degradation rate of the cells, as witnessed in the normalised pFF and V_{oc} curves in Figure 6.9. Whilst the degradation rate of V_{oc} was only marginally increased, the most significant change was observed in the degradation

rate of pFF , which is consistent with the acceleration of Cu precipitation in Si under illumination [104, 137]. However, after 500 hrs the cells all achieved the same degree of degradation regardless of the presence of illumination.

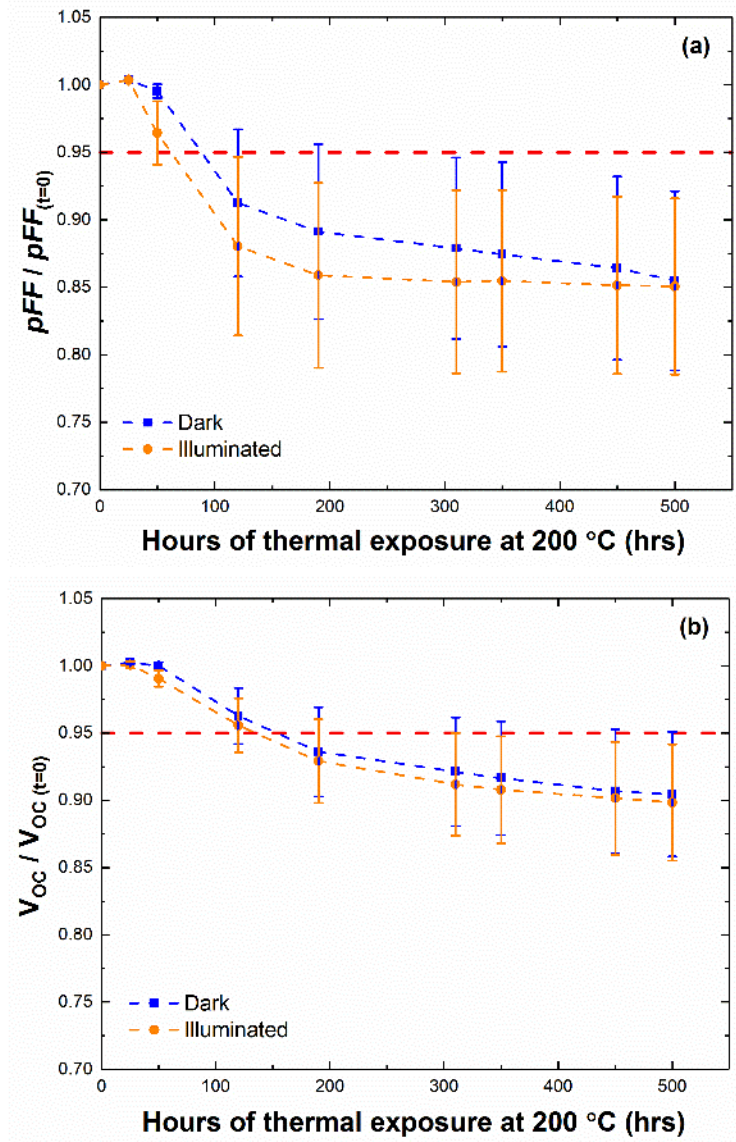


Figure 6.9: Normalised (a) pFF and (b) V_{OC} as a function of thermal treatment duration at 200 °C for n-type PERT solar cells with and without illumination.

As mentioned previously, the threshold for Cu precipitate formation in p-type Si is significantly higher due to the position of the Fermi level in relation to the neutrality level of Cu precipitates ($E_C - 0.2$ eV) that encourages further precipitate nucleation and growth [36, 37]. Whilst this condition may not necessarily be met under 1-Sun illumination ($\Delta n = \sim 1 \times 10^{15} \text{ cm}^{-3}$), the precipitate growth rate would be significantly enhanced by reduction of the built-in voltage around the precipitate-Si interface as

discussed in Section 2.4. Thus, optical activation (i.e. - increased carrier concentration) is most likely to accelerate degradation in the p-type region of a solar cell, which is primarily in the emitter for an n-type solar cell. This may also explain the observed increase in pFF degradation rate for the n-type cells analysed in these experiments under illumination compared to thermal stability testing in the dark.

Whilst the impact of illumination on the thermally-treated n-type PERT cells was minimal, the impact on p-type PERC cells was significantly greater as seen in the normalised V_{OC} and pFF degradation curves presented in Figure 6.10 below.

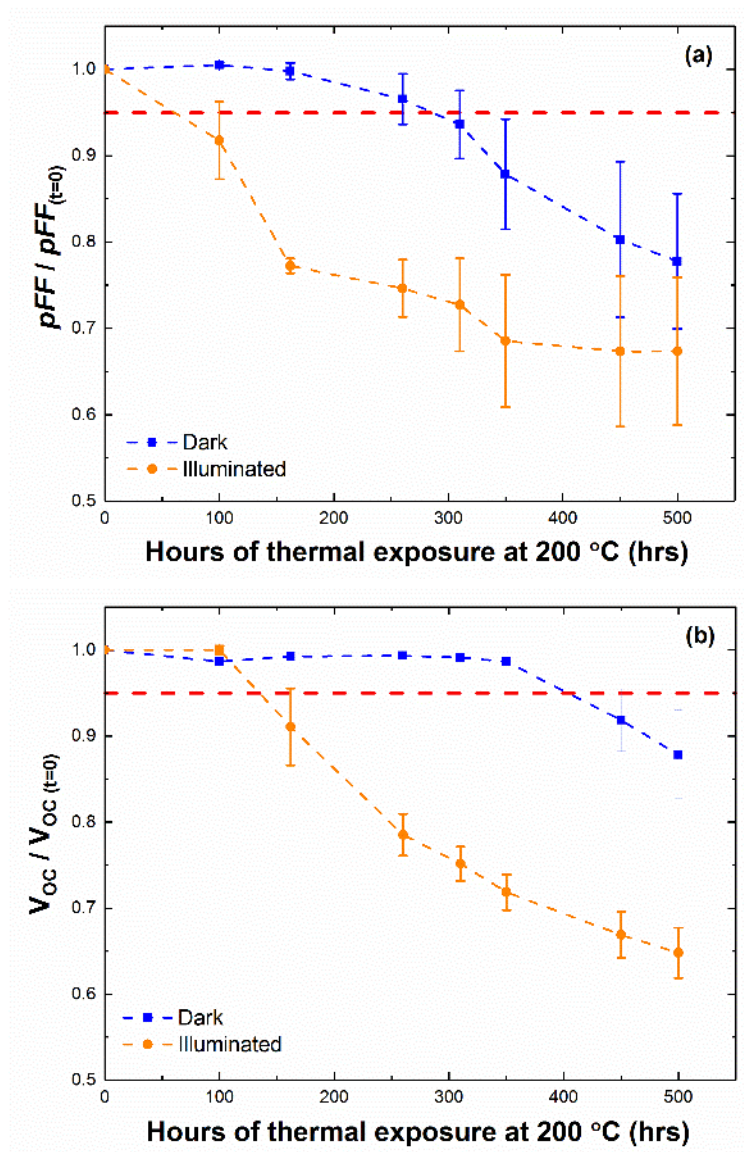


Figure 6.10: Normalised (a) pFF and (b) V_{OC} as a function of thermal treatment duration at 200 °C for p-type PERC solar cells with and without illumination.

Both the V_{OC} and pFF degradation rates are significantly increased under illumination, and as already shown in Table 6.1, the overall extent of degradation after 500 hours of thermal treatment is greater for p-type PERC cells after illumination is included. The enhanced optical activation of Cu precipitate formation in p-type Si compared to n-type Si seen in these results is consistent with previous studies that show Cu degradation in p-type Si requires illumination to push the quasi-Fermi level for electrons above the neutrality level for Cu precipitate formation and reduce the barrier voltage at the precipitate-Si interface [104, 105, 136], increasing the growth rate for Cu precipitates and thus resulting in the observed increased degradation rate of the V_{OC} with illumination during thermal stability testing. However, unlike the n-type cells in which the impact of illumination was primarily evident in the pFF due to the p-type emitter, both pFF and V_{OC} experienced similar increases in degradation rate with illumination during thermal stability testing. The increased rate of pFF degradation in p-type PERC cells with illumination could be due to the Cu precipitation in the bulk occurring predominantly closer to the junction, where recombination in the SCR can also be impacted. Previous studies have demonstrated increased junction leakage currents due to Cu precipitate growth initiated in the n-type region and grown into the p-type region [28, 337]. Additionally, an increased precipitation rate in the p-type bulk can provide a ‘sink’ which increases the amount of Cu that diffuses from the contact region surface from that observed in heat treatments performed in the dark.

Although Cu-LID (i.e. the acceleration of Cu precipitate growth due to illumination) appeared to be occurring in the p-type PERC cells examined in this experiment, there are other forms of LID that can occur in p-type PERC cells, including BO-LID [103] and the more recently reported LeTID [106, 142]. From examination of two identically-processed p-type PERC cells during thermal stability testing at 200 °C under illumination, it is clear that not every cell experienced the same degree of pFF and V_{OC} degradation as evident in the comparative graphs shown in Figure 6.11.

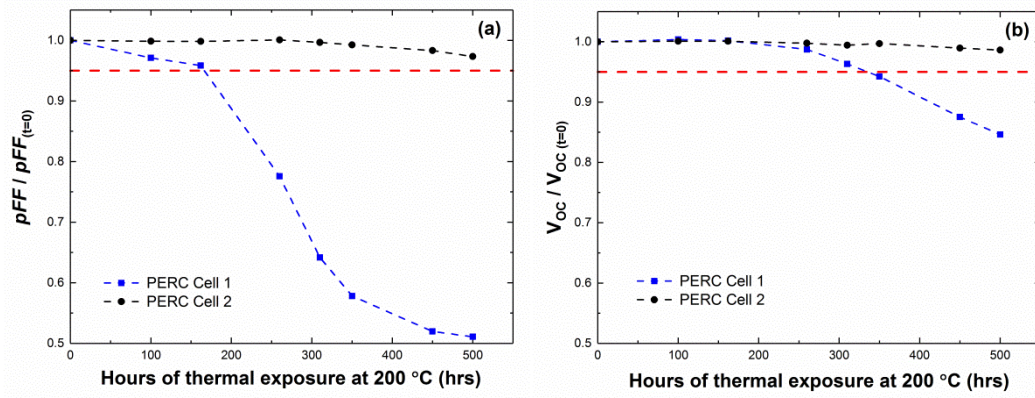


Figure 6.11: Normalised (a) pFF and (b) V_{OC} as a function of thermal treatment duration at 200 °C under ~ 1 Sun illumination for 2 different p-type PERC solar cells with identical cell processing conditions.

Since both cells were processed and cleaved from the same 156 mm precursor cell, it was assumed they would have experienced the same level degradation due to BO-LID and any potential LeTID. Lim *et al.* demonstrated that BO-LID is effectively deactivated under the conditions employed in this experiment (200 °C and ~ 1 Sun illumination [122]). Consequently, it was considered unlikely that the increased degradation was due to BO-LID. Also, whilst LeTID is known to occur in both monocrystalline as well as multi-crystalline PERC cells [149, 150], it would be expected that both cells would have experienced the same extent of LeTID after undergoing identical firing conditions as they were processed up until contact formation and plating on the same 156 mm wafer. Furthermore, Chen *et al.* recently showed that LeTID in Cz-Si solar cells can be fully recovered after ~ 50 hrs of illuminated annealing at 175 °C [149]. Consequently, it is reasonable to assume that the vastly different degradation behaviours between these two selected cells must be LID due to Cu penetration from the plated contacts into the Si, and the differences in degradation due to local non-uniformities introduced during the patterning and/or plating of the Cu-contact structures. This will be discussed more in the next section of this chapter.

The same increase in non-ideal recombination behaviour that was discussed in Section 6.2 can also be seen when comparing the I - V response of a p-type PERC cell tested in the dark [see Figure 6.3 (b)] with the same series of I - V curves for a cell from an identically-processed batch that had undergone thermal stability testing in the presence of ~ 1 Sun illumination as presented in Figure 6.12.

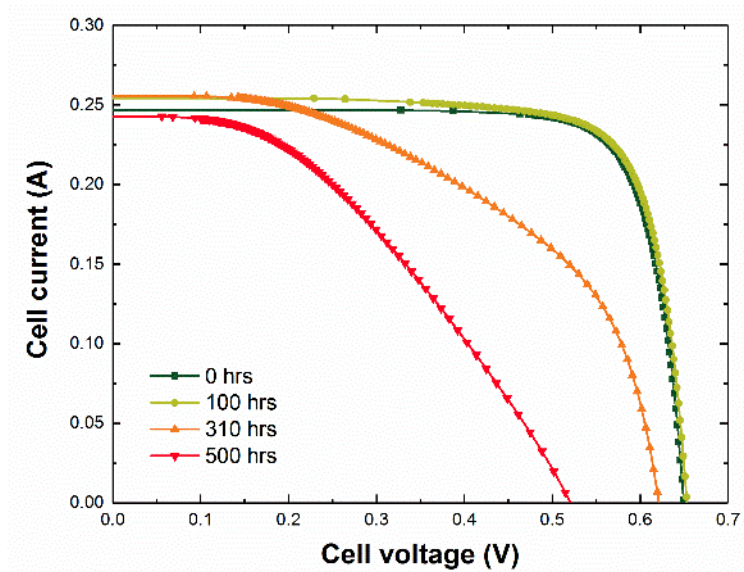


Figure 6.12: Evolution of I - V response for Cu-plated p-type PERC cell with increasing duration of thermal treatment at 200 °C under ~ 1 -Sun illumination.

The severity of the distortion around the maximum power point of the curve is significantly greater for the cell tested under illumination, and the accompanying reduction in V_{OC} is also more severe as seen by the shift in the I - V curve. This suggested accelerated growth of Cu precipitates when the p-type cells were illuminated during thermal treatments resulting in increased non-ideal recombination (i.e., recombination in the SCR of the junction or associated with precipitates in the bulk demonstrating injection-dependent recombination properties) and reduced V_{OC} .

As mentioned previously, the high non-ideality of the severely degraded cells in this experiment rendered the two-diode model highly inaccurate, so information pertaining to changes in diode saturation currents during stability testing (particularly the J_{01} component) could not be resolved in this experiment.

Another interesting effect of illumination on the thermally-treated p-type PERC cells was a significant shift in the spectral response of the p-type cell. Figure 6.13 below compares the EQE curves obtained on selected p-type PERC cells after degradation in the dark and under illumination.

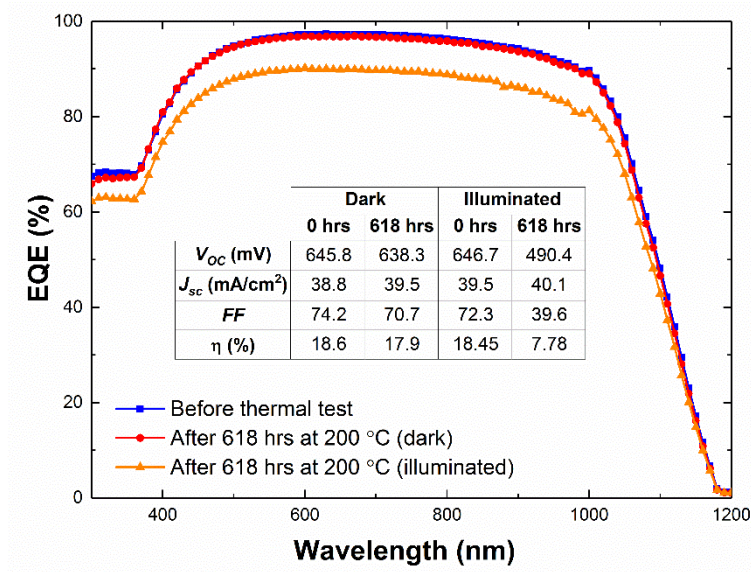


Figure 6.13: Comparison of EQE curves for a representative p-type PERC cell after 618 hrs of thermal stability testing in the dark (minimal bulk degradation) and under 1-Sun illumination (significant bulk degradation). Inset table shows corresponding IV results for both cells.

Whilst the only observable changes for the p-type cell thermally-treated in the dark were small reductions in the short wavelength and broadband EQE response (indicative of increased recombination at the front surface/emitter and bulk, respectively), the carrier collection efficiency was severely degraded over the entire EQE curve for the cell that was illuminated during thermal stability testing, corresponding to a J_{sc} loss of ~ 3 mA/cm². This reduction in EQE across the sample reflects the significant decreases in both pFF and V_{oc} measured for the p-type PERC cells after thermal stability testing under illumination. Similar results were recently observed by Karas *et al.* [330], in which Cu-plated mono BSF and PERC cells experienced degradation in EQE response across all wavelengths that was attributed to an increase in defect density at the SiN_x/Si interface similar to the results of Sopori *et al.* [329]. However, the EQE response observed here contradicts the relatively minimal changes in J_{sc} observed in I - V measurements as presented in the inset table in Figure 6.13. It is possible that a measurement artefact in the tool contributed to this observed discrepancy, although this was not able to be confirmed. The exact cause of the significant EQE degradation with illumination still requires further analysis and understanding, but an increased build-up of Cu defects around the surface/emitter/bulk could all contribute to an overall degradation in the EQE response.

Plated cells and modules in the field are likely to experience elevated temperatures in the presence of illumination, and thus the impact of illumination in accelerating the formation of Cu precipitates should not be ignored in thermal stability testing of plated modules. By short-circuiting the solar cell under illumination, it would be possible to test the proposed role of carrier injection on enhancing precipitation in the p-type cells, however this was not investigated in this work and could be addressed in future studies. The results presented in this section raise implications for the thermal stability of plated cells and modules claimed in previous studies [51, 54, 55], which mostly ignore the influence of illumination in Cu defect formation, focussing mostly on the diffusion of Cu through the Ni layer until the concentration of Cu_i increases above the threshold for precipitate nucleation and growth.

6.4 Impact of process variability on long-term stability testing

6.4.1 Introduction

The integral role of process uniformity on Cu-related cell degradation has been discussed several times throughout this thesis. The results presented in the previous sections of this chapter also highlight significant variations in degradation rate and extent of degradation both between different cell batches and within cell batches with supposedly identical processing conditions. This section more closely examines the degradation behaviour of cells with identical processing sequences to determine factors impacting the variability in thermal stability of Cu-plated solar cells. The influence of laser ablation patterning and Ni plating conditions are discussed in terms of their impact on the surface condition of the contact area, as well as the impact of such factors on both the uniformity of the barrier layer employed as well as the kinetics of Cu diffusion and precipitation during thermal stability testing of Cu-plated cells.

6.4.2 Results and Discussion

To examine the variability in degradation observed throughout the experiments presented in this chapter, the normalised pFF degradation behaviours of different batches were examined individually as seen in the separated curves in Figure 6.14 below.

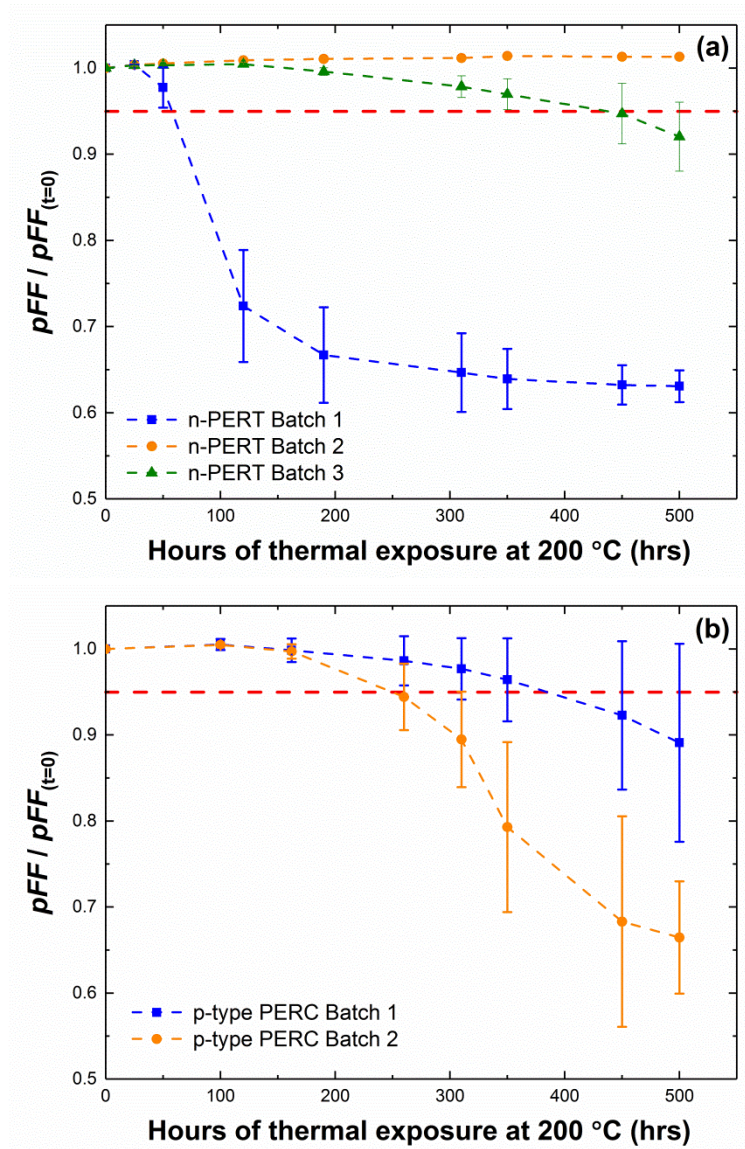


Figure 6.14: Normalised pFF as a function of thermal treatment duration at 200 °C in the dark for (a) n-type PERT solar cells from three different batches with identical processing conditions, and (b) p-type PERC cells from two different batches with identical processing conditions.

For the n-type cells examined in this work, there was a significant difference between the three cell batches processed. Although all three were patterned and plated with the same optimised process (see Section 6.2.2), Batch 1 degraded significantly whilst Batch 3 only marginally degraded and Batch 2 remained relatively stable throughout thermal stability testing. The relative degradation rates of the two p-type PERC batches processed were also noticeably different [see Figure 6.14 (b)]. The standard deviations within each cell batch (evident in the error bars for each data set)

were the result of variations in the degradation rates of different cells within each individually-processed 156 mm wafer used in the production of the small-area Cu-plated solar cells examined in this experiment (a full breakdown of individual cell degradation results from this work can be seen in Appendix D). The use of small cells cleaved from 156 mm precursor wafers permitted increased sample size and minimised variance due to previous processing steps. Consequently, any variance that was evident in the observed results reported in this chapter could be attributed to either the contact formation (laser ablation and/or plating) or the execution of the thermal treatments.

To identify the possible causes of the variation in degradation rates observed between different cell batches, indicative contact stack cross-sections for the three n-type PERT cell batches were examined with FIB and cross-sectional SEM imaging, similar to those performed in the experiments in Chapter 4. Cross-sectional SEM images from a representative cell from each batch of identically-processed n-type plated cells are presented in Figure 6.15. Aside from the layer of diffused Cu above the Ag capping layer and the voids present between the Cu and Ag layers (as discussed in more detail in Chapter 4), there are also significant gaps seen in the Ni barrier layer in all three batches. For the most degraded batch of n-type cells (Batch 1), gaps of 3-4 μm were observed in the Ni layer, whilst breaks in the Ni layer were smaller for the representative cell from the less degraded n-type batches ($< 2 \mu\text{m}$).

Closer examination of the gaps in the Ni barrier layer suggested that these regions may be still covered by the ARC ($\text{AlO}_x/\text{SiN}_x$ in the case of the n-type PERT cells). In other words, ablation of the ARC may not have been complete in these regions. As discussed by Lennon *et al.* [338], Cu diffusion through SiN_x ARCs has not been extensively studied for plated Si solar cells, and there is some evidence to suggest that Cu can diffuse through thin SiN_x layers deposited by PECVD. Added to this concern is the possibility that the absorption of ps laser energy may partially-ablate and hence damage the dielectric, impacting the thickness and barrier properties of any residual SiN_x , resulting in it becoming a possible conduit for diffusing Cu into the underlying cell. This possibility suggests the incomplete ablation of the ARC may not only impact adhesion of the plated fingers and busbars of a grid but also provide a path for Cu to enter the cells. Whilst attempts were made to identify any potential SiN_x remaining on

the surface in regions containing voids, it was extremely difficult to observe such thin layers with the characterisation techniques available.

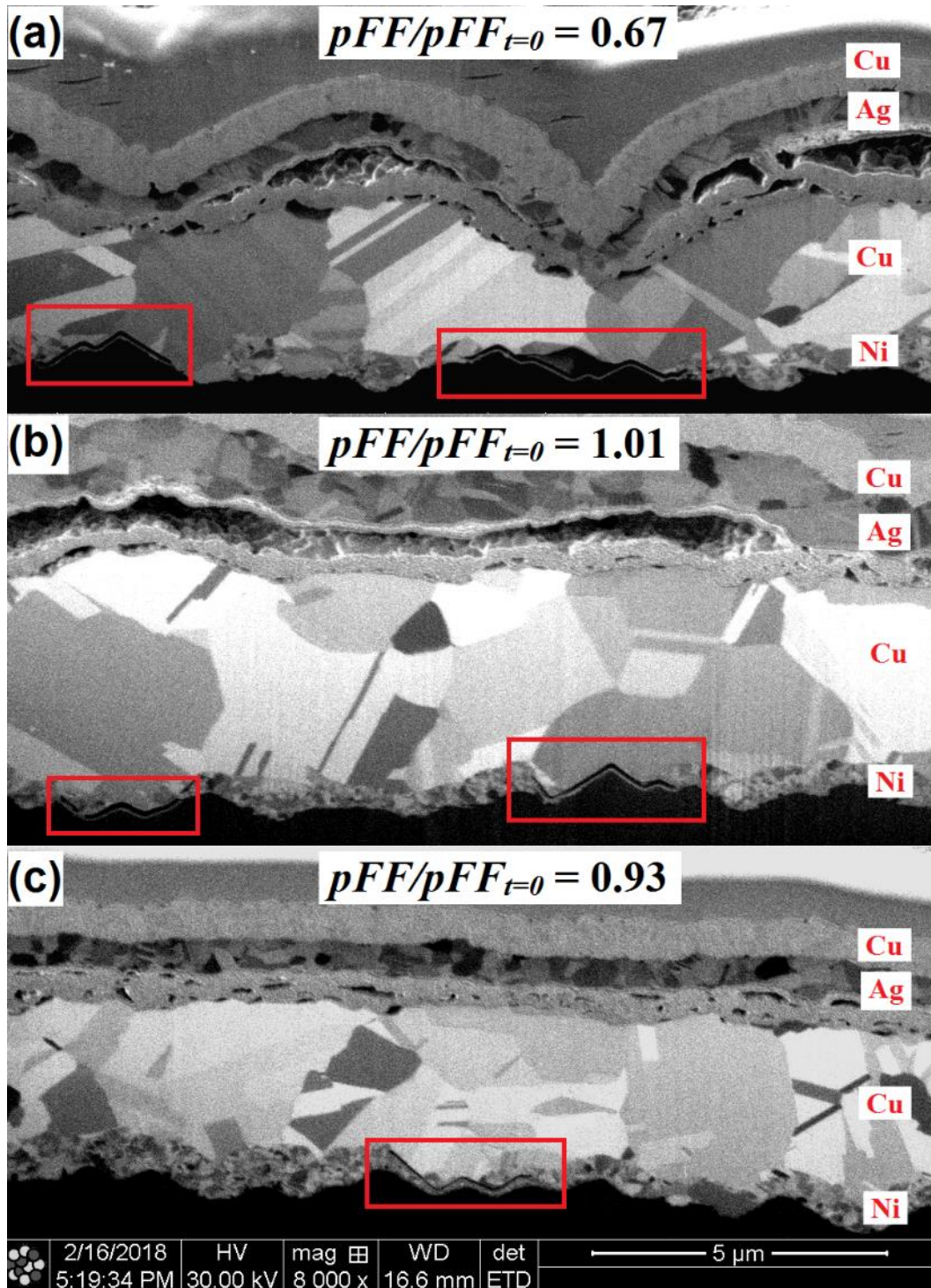


Figure 6.15: Cross-sectional SEM images of plated stack from three different n-type PERT cell batches with identical processing conditions, (a) Batch 1, (b) Batch 2, and (c) Batch 3, showing different degrees of Ni barrier non-uniformity (highlighted by red boxes), along with the corresponding pFF degradation values before imaging.

However, examination of the Ni barrier uniformity via imaging of representative cells is not a practical method by which to assess the frequency of such gaps in the barrier layer. Although the selected regions examined here all presented degrees of barrier non-uniformity, this may not represent the total uniformity of the plated Ni layer across the entire contact structure or indeed across the barrier layer in all the cells in the batch. Interestingly, in Section 4.3 it was shown that diffused Cu was present in the Si under regions that were uniformly plated with Ni, suggesting that non-uniformity in the Ni layer may not be the driving force behind the faster degradation rates observed in some cells and cell batches.

In all batches, at regions where there was a gap in the Ni layer, voids were observed in the Cu/Si interface (with the presence of residual dielectric also possible, yet unconfirmed). It was not determined whether the voids were present before or after thermal stability testing of plated cells, although the presence of a thin interfacial Ni layer in the cross-sectional image from Batch 3 below suggests that this void developed during thermal stability testing similar to the voids forming at the Cu/Ag interface. Extensive Cu diffusion into the Si during thermal stability testing may have resulted in the formation of voids at regions in which the Cu was directly in contact with the Si or partially-ablated dielectric. The samples from Figure 6.15 (a) and (c) were examined using TEM/EDS to try and identify the properties of the Si interface around where these voids had formed (see Figure 6.16 below).

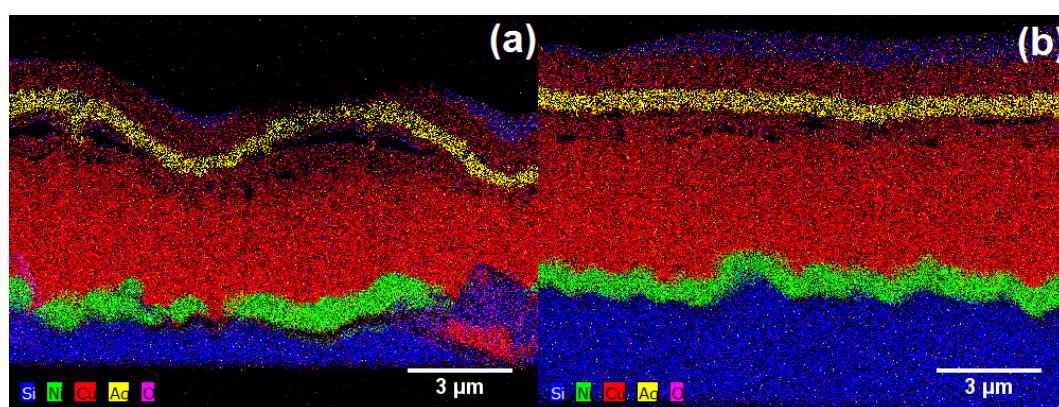


Figure 6.16: EDS maps of a plated contact from (a) Batch 1 and (b) Batch 3 of the n-type PERT cells examined in this work.

The non-uniformity in the plated Ni barrier layer is clear in these EDS maps. One of the primary candidates for the presence of non-uniform Ni plating in these cells was the

patterning method used to form the contact openings in this study. During ps laser ablation, although some energy is absorbed by the SiN_x dielectric layer directly (SiN_x bandgap ~ 3.5 eV [339]), the high incident photon density results in a significant fraction of the laser pulse reaching the Si surface where absorption creates a pressurised liquid-gas layer. The mechanical stress in the dielectric layer, resulting from the increased vapor pressure due to the rapidly formed gaseous Si, increases until the dielectric layer breaks down and is removed in a process known as lift-off ablation [340, 341]. Optimisation of ps laser ablation is required to ensure complete ablation of the SiN_x and minimal Si damage. An example of the ablated Si surface of a p-type PERC cell using the conditions employed in this experimental work can be seen in Figure 6.17 below.

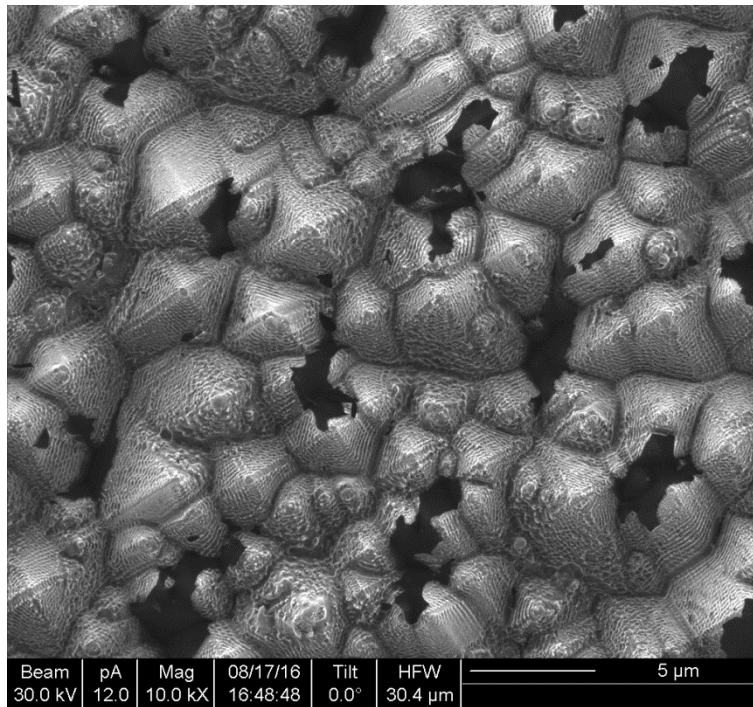


Figure 6.17: An SEM image of the laser-ablated Si surface on a p-type PERC cell after 266 nm ps laser ablation with a laser fluence of 0.44 J/cm^2 .

The ablated surface was roughened by ps laser ablation, with the surface characterized by laser-induced periodic surface structures (LIPSS) [342–345]. The LIPSS form as a consequence of the interaction between the incident laser wave front and the scattered surface optical wave, and are only observed after dielectric ablation using short pulse (ps or fs) lasers but not by nanosecond (ns) lasers [346, 347]. Constructive interference between adjacent pyramids on the textured surface results in

the formation of trenches due to increased absorption and melting of Si. Without optimisation of the laser ablation settings, the dielectric can sometimes remain on the Si surface which can contribute to non-uniform Ni barrier formation during plating. Evidence of remaining dielectric was difficult to observe in the TEM/EDS maps seen in Figure 6.16. However, future studies on the ablated contact interface after plating may be improved by employing different analysis techniques with higher sensitivity such as electron energy loss spectroscopy (EELS). The structure of the LIPSS was also observed to differ between B-doped and P-doped emitters due to the different absorption properties of the different ARC structures. As seen in the SEM image from a laser-ablated Si surface on an n-type cell in Figure 6.18, the LIPSS structure is far less defined in n-type cells due to increased absorption of 266 nm laser wavelengths in the B-doped emitter. This was the motivation behind the use of lower laser fluence for laser patterning of n-type cells (0.3 J/cm^2 instead of 0.44 J/cm^2).

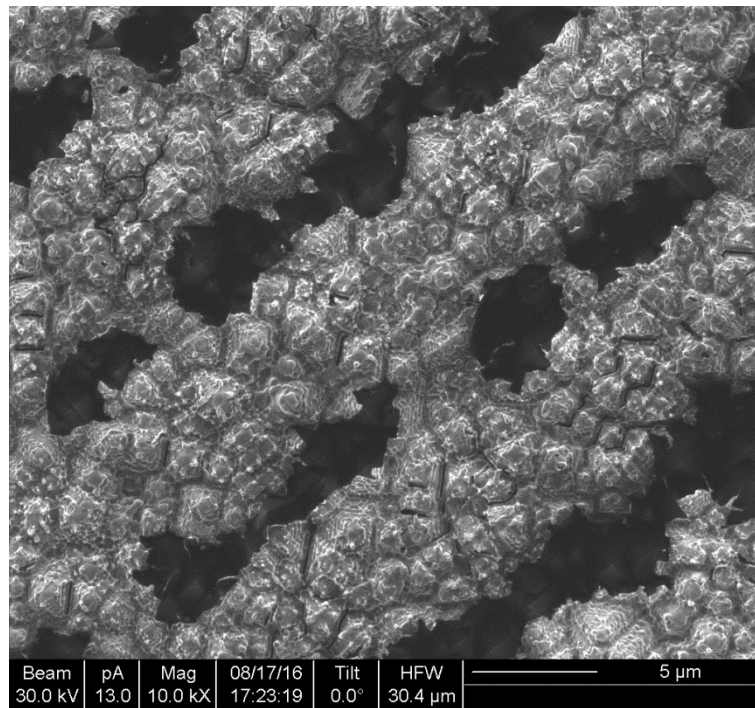


Figure 6.18: SEM image of the laser-ablated Si surface on an n-type PERT cell after 266 nm ps laser ablation with a laser fluence of 0.3 J/cm^2 .

Due to the fast cooling rate (about $10^{13} \text{ }^{\circ}\text{C/s}$ [348]) during resolidification of the molten Si, a layer of amorphous Si (a-Si) is usually formed at the exposed Si surface as seen in Figure 6.19. Figure 6.19(a) shows that an a-Si layer of variable thickness up to 58 nm was formed by 266 nm ps laser ablation. The a-Si was observed where the

ripples were present as seen in Figure 6.17 and Figure 6.18 (identified as the bright regions of the LIPSS structures in the SEM image). The higher resolution image in Figure 6.19(b) shows that there is a distorted Si crystal phase with stacking faults under the a-Si layer that extends 3-4 nm into the crystalline Si. The formation of this a-Si and distorted crystalline Si surface were expected to contribute to additional recombination in the plated cells. Not only this, but the laser-induced a-Si and extended defects induced by ps laser ablation can represent an effective sink reaction for the diffusion of Cu into the Si substrate, particularly in the case where Cu is directly in contact with the laser-ablated Si surface. The validity of this hypothesis was recently supported in recent work by Dang *et al.* [264, 334], which compared the laser-induced damage of different laser fluence conditions. It was shown that cells with ‘hard’ laser ablation (referring to laser fluence $> 0.96 \text{ J/cm}^2$) resulted in more damage and thus faster *pFF* degradation compared to cells that were patterned with ‘soft’ laser ablation (laser fluence $< 0.72 \text{ J/cm}^2$). Thus, fluctuations in the laser fluence during patterning could have resulted in non-uniformities in laser-induced defect density, which may be correlated with metal diffusion into the Si, as observed in the results presented in Section 4.3 as well as the literature.

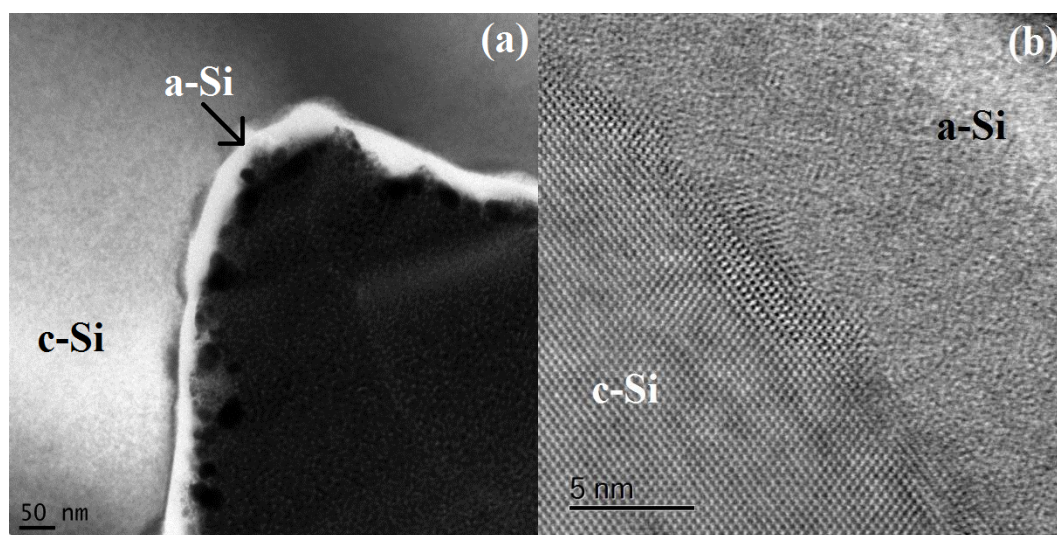


Figure 6.19: (a) A TEM image of an exposed Si surface on a p-type SE PERC precursor after the SiN_x ARC had been ablated using a 266 nm ps laser with a laser fluence of 0.3 J/cm^2 ; (b) a higher resolution image showing the distorted crystalline Si (images obtained by Ning Song, UNSW).

In order to understand the underlying cause of variability observed in the ablation efficiency of SiN_x using 266 nm ps laser ablation and relate this to the variability in Cu-related degradation of Cu-plated solar cells, OPAL2 [349] simulations were used to quantify the difference in the absorption/transmission of the SiN_x ARC at a wavelength of 266 nm. Figure 6.20 shows the simulated percentage of reflection, absorption and transmission of a SiN_x layer with a refractive index of 2.03 as a function of SiN_x thickness for 266 nm laser light. The blue transmission data represents the percentage of laser energy that is transmitted through the SiN_x and penetrates into the Si.

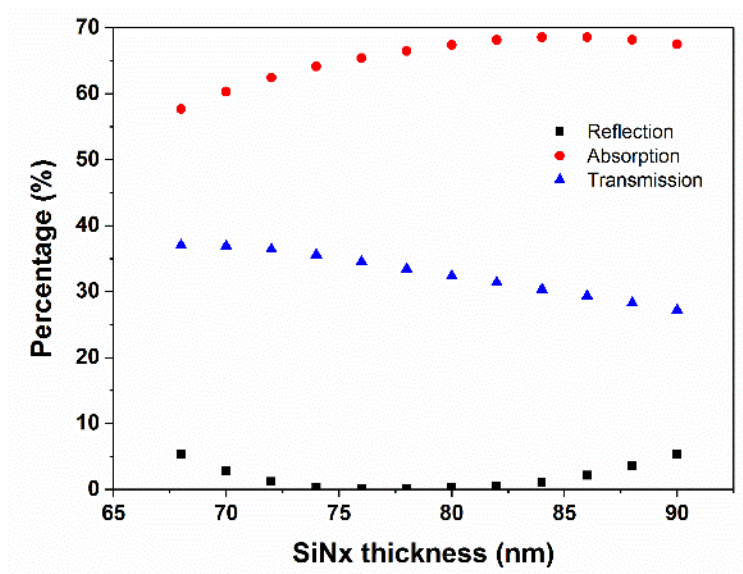


Figure 6.20: Simulated reflection/absorption/transmission of 266 nm laser energy as a function of dielectric layer thickness for SiN_x with a refractive index of 2.03 (provided courtesy of Pei-Chieh Hsiao, UNSW [350]).

The transmission of 266 nm laser energy through the SiN_x ($32.7 \pm 4.9\%$) is sensitive to variations in the SiN_x thickness over the range of 65 to 90 nm. For the cells processed in these experiments, variations of SiN_x layer thickness up to ± 6 nm within cells, ± 5 nm between cells and ± 3 nm between different batches were observed. This can therefore result in non-uniform laser ablation across the surface of 156 mm wafers and hence may have introduced significant variability between different small-area cells as well as different batches, which may have then contributed to the variable degradation rates of plated cells during thermal stability testing. However, there are also other factors that could contribute to potential non-uniform laser ablation, including optical effects due to non-uniformities in the surface texturing (similar to the effect responsible

for LIPSS formation), differences in the SiN_x refractive index, and also non-uniform thermal effects as a result of using high intensity ps laser ablation. Furthermore, few studies have patterned solar cells using 266 nm ps laser ablation, with the 355 wavelength more commonly used for ps laser patterning [229, 231, 339, 346]. Thus, further work is required to better understand the behaviour of dielectrics under 266 nm ps laser ablation.

A continuing theme in this thesis is that the reliability/stability metrics that have been reported for use in the analysis of long-term stability of Cu-plated solar cells is limited in its ability to identify the specific failure mechanisms responsible for the degradation of plated modules under different testing conditions by focussing only on electrical measurements. Accurate assessment of plated cell/module reliability requires an adequate study of all the possible failure mechanisms that may occur in a module in the field. Furthermore, the field environment conditions vary significantly which complicates the list of examinable variables required for accurate reliability analysis. In the IC industry, mean time to failure (MTTF) [351] is a reliability metric often applied for reliability studies of Cu-plated interconnects or other non-repairable failures. Simulations are also used to predict MTTF with the aid of experimental data and failure statistics. The IC industry also has a firm understanding of the physics of failure (PoF) indicators involved, for example, in Cu electromigration, which allows for more targeted technology improvements. However, the PV industry differs in this respect as it relies mostly on electrical measurements and pass/fail statistics. In order to address the large fraction of metallisation and interconnection failures, a greater emphasis may need to be placed on analysing the PoF in Si PV modules, especially to address failures due to metallisation and interconnection. This will be particularly necessary with the introduction of new metallisation and interconnection methods which may have failure mechanisms that are distinctly different from those typically observed for the current technologies.

6.5 Chapter Summary

In this chapter, the thermal stability of Cu-plated n-type PERT and p-type PERC solar cells with ps laser patterned contact structures were studied under different conditions. Employing the thermal stability testing methodology employed by Bartsch

et al. [50], plated cells were exposed to 200 °C on a hotplate and the sensitivity of this technique to thermal treatment duration, doping polarity of the substrate (n-type vs p-type), illumination and variability in laser ablation/plating conditions were investigated.

Comparing p-type and n-type cell degradation in the dark, it was observed that there was an overall decrease in pFF and V_{OC} for both cell structures. Whilst n-type cells experienced significant degradation in both indicators, the p-type cells experienced mostly pFF degradation, followed by a small reduction in V_{OC} . This was accompanied by minimal changes in J_{sc} , which was confirmed by EQE measurements. The relative degradation rates of pFF and V_{OC} reflected the diffusion and precipitation mechanism of Cu as it enters the Si substrate, with expected Cu precipitation around the junction resulting in an initial decrease in pFF , followed by a noticeable decrease in V_{OC} as the Cu concentration in the bulk increased. The introduction of Cu precipitates having injection-dependent recombination behaviour during thermal stability testing was also raised as a potential explanation for the observed initial degradation in pFF and then later reduction in V_{OC} in the thermally-treated cells, however the relatively small capture asymmetry of Cu precipitates suggests this impact may not be as significant as increasing Cu defect concentration around the solar cell junction. This resulted in a significant increase in non-ideal recombination observed in the pseudo I - V curves obtained on degraded cells which precluded the use of a the two-diode model to extract diode recombination currents for both the p-type and n-type Cu plated solar cells.

With illumination, minimal changes were observed in the degradation rates of the pFF and V_{OC} of n-type cells. However, a significant increase in the degradation rate of both the pFF and V_{OC} were evident for p-type plated cells under thermally treated illumination. Increased light-induced Cu precipitation (Cu-LID) in p-type Si was identified as the underlying cause of this degradation. Thermal testing under illumination is more representative of field conditions than stability tests in the dark, the latter tests allowing introspection of diffusion and accumulation of Cu in the cell or parts of the cell without regard to any acceleration of precipitate formation that may be induced by illumination. The results of this study have significant implications for the assumed stability of Cu-plated solar cells made in previous studies which did not include the effects of illumination.

Significant variability in thermal stability both in the dark and under illumination was observed in plated p-type and n-type solar cells. Cross-sectional FIB/SEM imaging identified gaps in the Ni barrier layer and accompanying voids between the Cu and Si in regions with no Ni layer present. It was hypothesised that these voids may have been induced by extensive diffusion of plated Cu into the Si substrate, potentially through a partially ablated dielectric layer which prevented the plating of a uniform Ni barrier layer, leaving behind voids at the interface similar to voids left at the Ag/Cu interface during Cu diffusion through the capping metal. SiN_x ARC ablation with a 266 nm ps laser resulted in the formation of LIPSS on the exposed Si surface as well as an a-Si surface layer and underlying distorted crystalline Si region with stacking faults evident. It was theorised that fluctuations in surface and laser conditions may introduce non-uniformities in laser ablation and laser-induced defect density. Optical simulations indicated that SiN_x thickness can also contribute to non-uniform laser ablation efficiency, with the generation of surface defects that cannot be removed during deglazing prior to plating. This implies that electrical measurements may not be sufficient to assess the long-term stability of Cu-plated solar cells, with further physics of failure studies required.

Chapter 7 Conclusions and Outlook

The aim of this thesis was to investigate the thermal stability of Cu-plated Si solar cells with a particular focus on cells with Ni/Cu grids plated on openings formed by selective-ablation of the antireflection coating using a UV ps laser. The thermal stability and impact of Cu diffusion into and within Si were investigated at both a wafer and a cell level. At the wafer level, Cu precipitates (which are the most common Cu-related defect in Si) were characterised by advanced lifetime spectroscopy analysis, which lead to an improved understanding of the impact of different processing conditions on the formation and recombination activity of Cu precipitates. At a cell level, Cu diffusion in plated solar cells was characterised with a combination of electrical and material techniques. This combined approach enabled a greater understanding of the relationship between cell degradation and Ni/Cu diffusion into Si to be obtained. It also allowed the identification of potential weaknesses in the laser-ablation and Ni/Cu LIP process.

In Chapter 3, TIDLS and DPSS analysis of surface-contaminated FZ-Si and ingot-contaminated FZ-Si containing Cu precipitates identified similar defect energy levels at $E_r-E_i = -(0.14-0.16)$ eV and $E_r-E_i = (0.08-0.11)$ eV, with corresponding $k = 1.4 \pm 0.2$ and $k = 5.6 \pm 1.4$, respectively. A strong power-law dependence in the capture cross section ($\sigma(T) = \sigma_0 T^{-\alpha}$) was also observed. These parameters are consistent with previously-determined recombination properties for Cu precipitates in Si, which introduce a broad band of defect levels in the upper half of the bandgap. Precipitate model fitting of degraded lifetime curves revealed a higher density of larger precipitates in the ingot-contaminated FZ-Si ($1-3 \times 10^{12} \text{ cm}^{-3}$, $r_{prec} = \sim 219-280 \text{ nm}$) compared with that of the surface-contaminated FZ-Si ($1 \times 10^{10} \text{ cm}^{-3}$, $r_{prec} = \sim 4 \text{ nm}$). The differences in precipitate size/density and recombination activity were hypothesised to be the result of different growth rates between the illuminated and ingot-grown precipitation conditions, with faster precipitate growth rates under illumination resulting in a distribution of precipitates with smaller radius.

Chapter 4 focussed on the diffusion of Cu through plated Ni diffusion barriers with a PoF-style approach to characterisation of degradation being applied. Significant Cu

diffusion through plated Ag capping layers during thermal stability testing at 200 °C in the dark were observed. This diffusion was manifest as a distortion in the high illumination intensity region of Suns- V_{OC} measurements. FIB cross-sectional imaging and EDS/TEM imaging revealed the presence of a 0.5-1.5 μm thick layer of diffused Cu on top of the Ag capping layer and significant void formation between the Cu and Ag layers. The extent of void formation was demonstrated to be dependent on the microstructure of the Ag capping layer, with the voids confirmed as the cause of distortion in Suns- V_{OC} measurements (leading to 5-10% error in the estimated pFF). An equivalent circuit model was developed to successfully model this distortion, with the voids represented as a high resistance between the solar cell and measurement probe that could be removed by collapsing the voids in the contact stack prior to measurement. Evidence of Cu penetration through non-uniform Ni plating into the underlying Si was also reported, an observation that highlighted the potential weaknesses of using polycrystalline plated metals as diffusion barriers for Cu.

Demonstration of LA-ICP-MS as a suitable spatially-resolved analytical technique for the detection of metal penetration from plated contacts into the underlying Si was detailed in Chapter 5. A chemical etching procedure consisting of immersion in 40 °C HNO_3 followed by HF/HCl was proposed and shown to successfully expose the underlying Si surface and minimise interference from plated metals on the surface during LA-ICP-MS measurements. The ablation behaviour of Si during ns-LA-ICP-MS experiments identified several limitations when applying this technique to the analysis of near-surface and bulk impurity concentrations. It was shown that laser fluence, scan speed and carrier gas flow/composition can impact the size of ablated particles and the subsequent accuracy of LA-ICP-MS measurements. However, quantitative LA-ICP-MS measurements of plated solar cells after thermal stability testing showed an increase in both Ni and Cu concentration with increasing thermal treatment duration. Thus, the technique was demonstrated as a useful tool for the improved understanding of metal diffusion paths at metal-semiconductor interfaces and deconstructing potential failure mechanisms in plated Si solar cells.

Chapter 6 brought together the observations and learning from the previous chapters and presented a detailed electrical analysis of plated n-type PERT and p-type PERC cells during thermal stability testing. It was observed that both the n-type and p-type

cells experienced pFF degradation initially, followed by a later reduction in V_{OC} during thermal stability testing in the dark, with the rate of degradation being greater for the n-type cells. It was concluded that such behaviour may be indicative of an increasing concentration of Cu SRH recombination centres during thermal stress testing, impacting both pFF and V_{OC} at different rates as the concentration of precipitates increases around the solar cell junction and bulk. With illumination, which is more representative of field conditions than stability tests in the dark, minimal changes were observed in the degradation rates of the pFF and V_{OC} of n-type cells. However, a significant increase in the degradation rate and extent of both the pFF and V_{OC} degradation were evident for p-type plated cells as a result of Cu-LID. Cross-sectional FIB/SEM and TEM/EDS imaging identified gaps in the Ni barrier layer and accompanying voids between the Cu and Si in regions with no Ni layer present. Partial ablation of dielectrics and laser-induced defects which introduce stacking faults at the Si surface were both hypothesised to accelerate penetration of Cu into the Si substrate. Variations in the thickness of the dielectric and laser ablation conditions were assessed to be potential factors affecting the density of laser-induced defects and partially-ablated dielectric regions which may not be removed during pre-treatment before Ni plating, thus impacting the uniformity of the plated layer and subsequent barrier effectiveness.

7.1 Original Contributions

The original contributions arising from the work presented in this thesis are summarised below:

- 1) Characterisation of defect parameters for Cu precipitates formed under illumination compared to during ingot crystallisation in the dark using TIDLS and DPSS analysis.
- 2) Comparison of Cu precipitate size and density formed under different processing conditions with the application of a Schottky-based precipitate model for metallic precipitates in Si.
- 3) Detailed analysis of Cu diffusion through Ag capping metals during thermal stability testing, demonstrating a difference in Cu diffusion behaviour between different Ag capping methodologies based on layer microstructure.

- 4) Equivalent circuit modelling to characterise the distortion in Suns- V_{OC} data due to void formation in plated contact stacks arising from thermal stability testing.
- 5) Use of LA-ICP-MS for analysis of Ni/Cu diffusion in plated solar cells during thermal stability testing, including characterisation of surface preparation methodologies and optimisation of laser ablation conditions.
- 6) Demonstration of relationship between thermal stability testing duration and Ni/Cu concentration in Si substrate underneath plated contacts, as well as correlations between metal concentration and V_{OC} degradation in plated solar cells.
- 7) Detailed comparison of degradation behaviour between n-type PERT and p-type PERC solar cells during thermal stability testing, both in the dark and under illumination, highlighting different Cu-related degradation behaviours between different cells structures.
- 8) Identification of non-uniform laser ablation and Ni barrier plating as the most likely causes for the variable thermal stability of Cu-plated Si solar cells.

7.2 Future Work and Outlook

The work presented in this thesis has not only highlighted several potential weaknesses in the use of laser-ablation patterning and plating for contact formation, but also limitations in previously-reported methods for evaluating the long-term stability of plated contacts for Si solar cells. It highlights the need for further research to evaluate the efficiency potential and durability of Cu plating as an alternative metallisation scheme for future Si PV modules.

Firstly, the characterisation of Cu precipitates in Si is still very much in its infancy. Although several studies of Cu precipitates have been discussed in previous chapters, the variable nature of Cu precipitate formation and growth conditions has significant implications on not only the size and density of such precipitates, but also the recombination activity associated with them. Application of advanced lifetime spectroscopy techniques in future work can assess the impact of precipitation conditions in much more detail. Various factors should be examined, such as the influence of illumination intensity, temperature, base doping and cooling rate on the recombination

activity of Cu precipitates in Si. The use of adequate control samples would also aid to improve the accuracy of extracted parameters. In conjunction with this, confirmation of precipitate parameters with microscopic imaging techniques would strengthen the conclusions drawn from a TIDLS analysis.

This study also highlighted the role of variable Ni barrier uniformity as the underlying cause of the variable thermal stability of Cu-plated cells. It was hypothesised that partially-ablated dielectric layers can result in variable Ni plating and subsequent Cu diffusion into Si through thin residues of dielectric. Although this could not be confirmed in this thesis project, the impact of partial dielectric ablation on Cu diffusion could be more thoroughly investigated with TEM/EDS imaging, as well as other techniques such as EELS and LA-ICP-MS. As already mentioned, the accelerated aging methodology first reported by Bartsch *et al.* [50] does not provide information about the physical and chemical failure mechanisms behind poor thermal-stability of plated solar cells. Thus, a shift to more PoF-style characterisation methodologies incorporating both electrical and material analytical techniques would provide more direction in the development of durable plated contacts for industrial-scale Si solar modules.

The variability in cell degradation with thermal testing observed in this project limits some of the conclusions that can be drawn from the results presented. Comparison of degradation with cells ablated with other lasers (e.g., a 355 nm ps laser) may help clarify the reasons for the variability and strengthen some of the conclusions from this study. It would also allow for improved Arrhenius analysis, with actual cell lifetimes extrapolated to assess the resilience of different plated cell structures to Cu in-diffusion and degradation. However, the variability identified in the thermal degradation experiments also serves to highlight the important contribution of controlled processing conditions (laser ablation and plating) for durable cells with reproducible thermal degradation properties.

Finally, it has been shown that polycrystalline plated metals are not ideal diffusion barriers for Cu in plated solar cells, thus future work should also investigate new diffusion barriers. It may be prudent to shift from using polycrystalline barrier materials to more amorphous materials such as plated alloys. For example, LIP plated alloys such as NiCo have recently been demonstrated as a more effective diffusion barrier than pure Ni [235]. Aforementioned analytical techniques could also be used in future studies to

assess potential metal alloys for suitability as a replacement for pure Ni as a Cu diffusion barrier in the next evolution of Cu-plated solar cells.

List of Publications

Journal papers

J. Colwell, P. Hsiao, X. Shen, W. Zhang, X. Wang, S. Lim and A. Lennon, “Impact of contact integrity during thermal stress testing on degradation analysis of copper-plated silicon solar cells,” *Solar Energy Materials and Solar Cells* 174, pp. 225-232, 2018.

J. Colwell, P. Hsiao, W. Zhang, X. Wang, R. Akter and A. Lennon, “Laser ablation ICP-MS for detection of substrate contamination from plated metal contacts in silicon solar cells,” *Journal of Analytical Atomic Spectrometry*, 33 (3), pp. 422-430, 2018.

A. Lennon, **J. Colwell** and K.P. Rodbell, “Challenges facing copper-plated metallisation for silicon photovoltaics: Insights from integrated circuit technology development”, *Progress in Photovoltaics: Research and Applications*, pp. 1-31, 2018. [Invited review paper]

N. Nampalli, H. Laine, **J. Colwell**, V. Vähänissi, A. Inglese, C. Modanese, H. Vahlman, M. Yli-Koski and H. Savin, “Rapid thermal anneal activates light induced degradation due to copper redistribution,” *Applied Physics Letters*, 113, pp. 32104, 2018.

P. Hsiao, N. Song, X. Shen, B. Phua, **J. Colwell**, U. Römer, B. Johnston, S. Lim, Y. Shengzhao, P. Verlinden and A. Lennon, “266 nm ps laser ablation for copper-plated p-type selective emitter PERC silicon solar cells,” *IEEE Journal of Photovoltaics*, 8 (4), pp. 952–959, 2018.

N. Song, W. Zhang, P. Hsiao, X. Wang, **J. Colwell** and A. Lennon, “Copper microstructure evolution in light-induced plated metal grids for silicon solar cells: Implications for reliable metallization,” *Journal of the Electrochemical Society* 163(14), pp. H1136–H1143, 2016.

N. Song, P. Hsiao, W. Zhang, X. Wang, **J. Colwell**, Z. Li and A. Lennon, “Post-plating annealing of light induced plated copper fingers: implications for reliable metallization,” *Energy Procedia* 98, pp. 136–141, 2016.

Conference papers

J. Colwell, P. Hsiao, X. Shen, S. Lim, O. Kunz, W. Zhang, X. Wang and A. Lennon, “Distortion of Suns- V_{OC} measurements due to plated copper diffusion through silver capping layers on silicon solar cells,” in *7th World Conference on Photovoltaic Energy Conversion (WCPEC-7)*, 2018.

J. Colwell and A. Lennon, “Analysis of copper penetration in selective-emitter silicon solar cells using laser ablation inductively-coupled plasma mass spectrometry,” in *42nd IEEE Photovoltaic Specialist Conference (PVSC)*, pp. 1–5, 2015.

N. Song, P. Hsiao, W. Zhang, X. Wang, **J. Colwell**, Z. Li and A. Lennon, “Self-annealing behavior and rapid thermal processing of light induced plated copper fingers on silicon solar cells,” in *43rd IEEE Photovoltaic Specialists Conference (PVSC)*, pp. 1980–1983, 2016.

P.-C. Hsiao, X. Shen, B. Phua, N. Song, **J. Colwell**, U. Römer, B. Johnston, Y. Shengzhao, P. Verlinden and A. Lennon, “Industrial viability and reliability of plated metallisation for higher efficiency silicon solar cells,” in *Australia Pacific Solar Research Conference*, 2017.

B. Phua, P. Hsiao, X. Shen, N. Song, X. Wang, **J. Colwell**, U. Römer, B. Johnston, Y. Shengzhao, P. Verlinden and A. Lennon, “Cross-sectional analysis of encapsulated solar cells,” in *Australian Pacific Solar Research Conference*, 2017.

Appendix A Calibration Procedure for TIDLS Measurements

In order to obtain accurate temperature-dependent lifetime curves as presented in Chapter 3, raw QSS-PC measurements must be calibrated for temperature and generation rate to obtain an accurate representation of the temperature and injection-dependent lifetime. To calibrate the temperature, a Si sample of equivalent thickness to the measurement Si wafer was placed on the temperature-controlled measurement stage with a thermocouple attached to the wafer surface to monitor sample temperature directly. The correlation between the Si wafer temperature and the set temperature of the measurement stage (for the samples examined in this thesis) can be seen in Figure A.1.

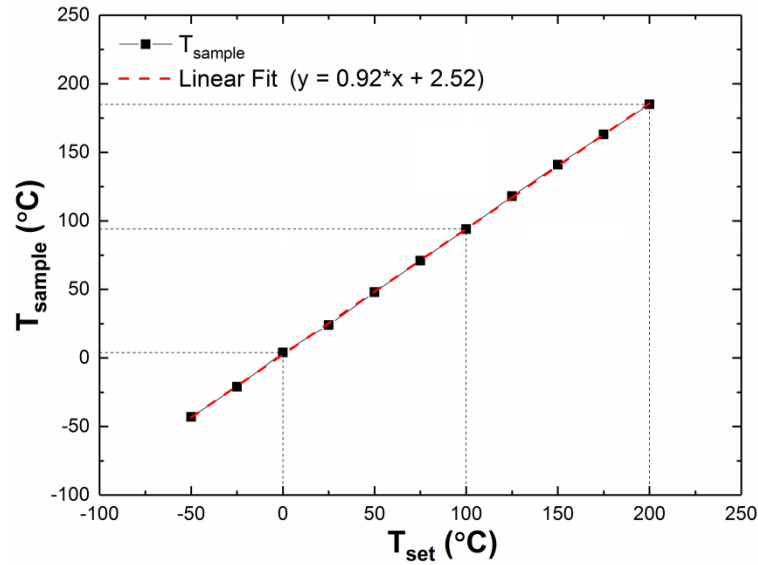


Figure A.1: Relationship between set temperature (T_{set}) and sample temperature (T_{sample}) during TIDLS measurements performed in Chapter 3.

The generation rate and thus lifetime of the Si samples examined in this work was calibrated using a self-consistent calibration procedure as presented in Figure A.2 [352, 353]. Injection-dependent lifetime was obtained using both a Sinton Instruments flash lamp and an 870 nm LED source to obtain as wide injection range as possible. The

reflectance of each sample at the LED wavelength was measured using an integrating sphere in a Lambda 1050 Spectrophotometer from Perkin Elmer. This was used to calibrate the LED/transient measurements. The corresponding QSS flash measurements were subsequently matched to the LED measurements by altering the scaling factor, F_S .

Whilst the procedure described below includes a calibration procedure to match PL and PC measurements, the PL signal was not examined in this work as it provided no extra information that was not obtained with PC measurements.

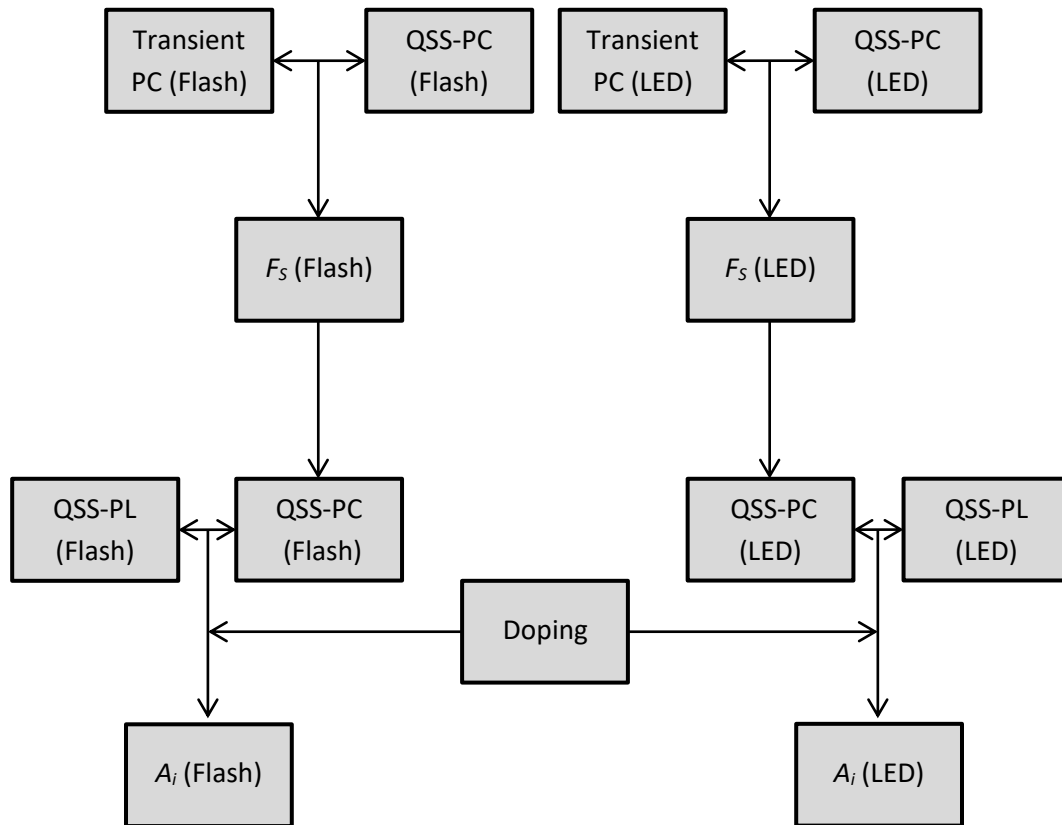


Figure A.2: Self-consistent calibration procedure for QSS-PC measurements as performed in Chapter 3.

Appendix B Calculation of Laser Fluence

In this thesis, laser power delivered to the Si substrate during ablation patterning or sampling is often described in terms of “laser fluence”. Laser fluence is defined as the energy delivered per unit area of a laser pulse. For the lasers utilised in this work (both in laser ablation patterning and LA-ICP-MS measurements), energy is delivered to the surface according to a Gaussian beam-shape (see Figure B.1) which results in a non-uniform energy distribution across the laser spot, which is determined by the aperture employed in the laser system (with power reducing to $1/e^2$ near the edges).

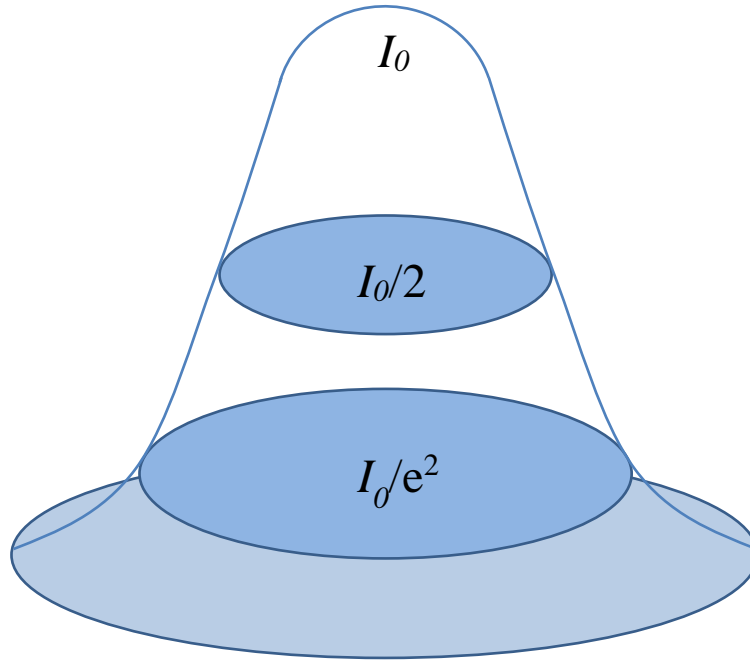


Figure B.1: Example of a Gaussian beam profile.

In general, laser fluence can be determined by the expression:

$$\text{laser fluence (J. cm}^{-2}\text{)} = \frac{I}{A_{spot}} \quad (\text{B.1})$$

where I is the laser power and A_{spot} is the spot size of the laser. Due to the Gaussian profile of the laser, non-uniformity in energy density across the laser spot had to be accounted for during laser ablation patterning and LA-ICP-MS measurements.

Appendix C Cell degradation results for different Ag capping layers

Table C.1: Summary of individual cell results for Cu-plated solar cells with an immersion Ag capping layer before and after 500 hrs of thermal exposure at 200 °C in the dark.

| Thermal Treatment Duration (hrs) | V_{oc} (mV) | | J_{sc} (mA/cm ²) | | FF (%) | | pFF (%) | | η (%) | | R_s (Ω .cm ²) | | |
|----------------------------------|---------------|-----|--------------------------------|------|----------|------|-----------|------|------------|------|-------------------------------------|------|------|
| | 0 | 500 | 0 | 500 | 0 | 500 | 0 | 500 | 0 | 500 | 0 | 500 | |
| Not sintered, ambient cool | Cell 1 | 635 | 631 | 39.3 | 39.2 | 72.5 | 68.9 | 81.6 | 82.0 | 18.1 | 17.0 | 1.69 | 2.40 |
| | Cell 2 | 637 | 633 | 39.3 | 39.2 | 75.2 | 77.3 | 81.6 | 82.2 | 18.9 | 19.2 | 1.19 | 0.96 |
| | Cell 3 | 639 | 634 | 39.3 | 39.2 | 75.0 | 77.2 | 81.6 | 82.2 | 18.8 | 19.2 | 1.27 | 0.97 |
| Not sintered, quench | Cell 1 | 637 | 633 | 39.3 | 39.2 | 70.7 | 72.0 | 81.5 | 81.8 | 17.7 | 17.9 | 2.00 | 1.81 |
| | Cell 2 | 637 | 634 | 39.3 | 39.3 | 75.1 | 77.4 | 81.6 | 82.0 | 18.8 | 19.3 | 1.23 | 0.90 |
| | Cell 3 | 640 | 635 | 39.3 | 39.2 | 75.4 | 77.6 | 81.5 | 81.9 | 19.0 | 19.4 | 1.18 | 0.88 |
| Sintered, ambient cool | Cell 1 | 639 | 631 | 39.3 | 39.2 | 76.8 | 75.2 | 81.6 | 79.1 | 19.3 | 18.6 | 0.90 | 0.84 |
| | Cell 2 | 638 | 632 | 39.3 | 37.2 | 77.3 | 77.4 | 81.7 | 81.0 | 19.4 | 18.2 | 0.84 | 0.75 |
| | Cell 3 | 639 | 632 | 39.2 | 39.1 | 77.1 | 76.6 | 81.7 | 80.5 | 19.3 | 18.9 | 0.91 | 0.81 |
| Sintered, quench | Cell 1 | 638 | 632 | 39.2 | 39.2 | 76.6 | 77.1 | 81.7 | 81.9 | 19.2 | 19.1 | 0.97 | 1.00 |
| | Cell 2 | 638 | 633 | 39.3 | 39.4 | 76.9 | 76.8 | 81.5 | 80.8 | 19.3 | 19.1 | 0.89 | 0.82 |
| | Cell 3 | 638 | 633 | 39.2 | 39.3 | 76.2 | 76.6 | 81.5 | 81.7 | 19.1 | 19.0 | 1.07 | 1.08 |

Table C.2: Summary of individual cell results for Cu-plated solar cells with a LIP Ag capping layer before and after 500 hrs of thermal exposure at 200 °C in the dark.

| Thermal Treatment Duration (hrs) | | V_{oc} (mV) | | J_{sc} (mA/cm ²) | | FF | | pFF | | η (%) | | R_s (Ω .cm ²) | |
|----------------------------------|--------|---------------|-----|--------------------------------|------|------|------|-------|------|------------|------|-------------------------------------|------|
| | | 0 | 500 | 0 | 500 | 0 | 500 | 0 | 500 | 0 | 500 | 0 | 500 |
| Not sintered, ambient cool | Cell 1 | 639 | 622 | 39.0 | 38.7 | 75.8 | 62.9 | 81.5 | 63.9 | 18.9 | 15.1 | 1.13 | 0.36 |
| | Cell 2 | 637 | 616 | 39.2 | 39.0 | 75.2 | 59.3 | 81.3 | 60.7 | 18.7 | 14.3 | 1.16 | 0.95 |
| | Cell 3 | 636 | 625 | 39.2 | 39.1 | 75.3 | 69.7 | 81.3 | 72.6 | 18.8 | 17.0 | 1.17 | 0.81 |
| Not sintered, quench | Cell 1 | 637 | 631 | 39.3 | 39.0 | 75.8 | 76.8 | 81.3 | 80.9 | 19.0 | 18.9 | 1.07 | 0.86 |
| | Cell 2 | 639 | 633 | 39.2 | 39.0 | 76.2 | 75.0 | 81.3 | 78.5 | 19.1 | 18.5 | 1.01 | 0.79 |
| | Cell 3 | 636 | 628 | 39.2 | 39.1 | 75.9 | 72.9 | 81.4 | 76.4 | 18.9 | 17.9 | 1.07 | 0.80 |
| Sintered, ambient cool | Cell 1 | 636 | 631 | 39.2 | 39.0 | 76.5 | 75.7 | 81.3 | 80.5 | 19.0 | 18.6 | 0.97 | 0.91 |
| | Cell 2 | 635 | 631 | 39.2 | 38.9 | 77.0 | 77.4 | 81.4 | 81.4 | 19.2 | 19.0 | 0.90 | 0.86 |
| | Cell 3 | 635 | 629 | 39.1 | 38.8 | 75.5 | 75.1 | 81.0 | 80.3 | 18.7 | 18.3 | 1.11 | 1.06 |
| Sintered, quench | Cell 1 | 635 | 630 | 39.2 | 39.2 | 75.8 | 75.9 | 81.2 | 81.1 | 18.9 | 18.8 | 1.08 | 1.05 |
| | Cell 2 | 635 | 630 | 39.2 | 39.1 | 75.7 | 75.4 | 80.9 | 80.9 | 18.8 | 18.5 | 1.05 | 1.13 |
| | Cell 3 | 634 | 630 | 39.0 | 39.1 | 75.9 | 76.7 | 81.6 | 81.9 | 18.8 | 18.9 | 1.08 | 1.00 |

Appendix D Complete thermal stability results for Cu-plated solar cells

Table D.1: Summary of individual cell results for Cu-plated n-PERT solar cells before and after 500 hrs of thermal exposure at 200 °C in the dark.

| | | V_{oc} (mV) | | J_{sc} (mA/cm ²) | | FF (%) | | pFF (%) | | η (%) | |
|----------------------------------|--------|---------------|-----|--------------------------------|------|----------|------|-----------|------|------------|------|
| Thermal Treatment Duration (hrs) | | 0 | 500 | 0 | 500 | 0 | 500 | 0 | 500 | 0 | 500 |
| Batch 1 | Cell 1 | 669 | 436 | 42.3 | 21.2 | 76.7 | 95.1 | 80.8 | 49.6 | 21.7 | 8.8 |
| | Cell 2 | 667 | 584 | 42.4 | 41.8 | 76.6 | 47.4 | 81.0 | 47.9 | 21.7 | 11.6 |
| | Cell 3 | 670 | 633 | 42.5 | 41.8 | 76.0 | 57.7 | 80.3 | 57.7 | 21.6 | 15.3 |
| | Cell 4 | 670 | 419 | 42.4 | 41.9 | 76.3 | 48.4 | 80.7 | 50.5 | 21.7 | 8.5 |
| | Cell 5 | 668 | 399 | 42.3 | 41.8 | 76.8 | 48.7 | 80.7 | 50.9 | 21.7 | 8.1 |
| | Cell 6 | 669 | 515 | 42.3 | 41.9 | 76.6 | 46.8 | 80.6 | 48.7 | 21.7 | 10.1 |
| Average | | 669 | 498 | 42.4 | 38.4 | 76.5 | 57.4 | 80.7 | 50.9 | 21.7 | 10.4 |
| Standard Deviation | | 1 | 96 | 0.1 | 8.4 | 0.3 | 18.9 | 0.2 | 3.5 | 0.0 | 2.7 |
| Batch 2 | Cell 1 | 670 | 658 | 42.3 | 41.7 | 77.5 | 78.2 | 80.2 | 81.5 | 22.0 | 21.5 |
| | Cell 2 | 669 | 658 | 42.4 | 41.8 | 77.6 | 77.4 | 80.3 | 81.8 | 22.0 | 21.3 |
| | Cell 3 | 670 | 659 | 42.0 | 41.9 | 78.4 | 77.1 | 81.2 | 81.9 | 22.1 | 21.3 |
| | Cell 4 | 670 | 661 | 41.9 | 42.0 | 78.4 | 78.6 | 81.3 | 82.1 | 22.0 | 21.8 |
| | Cell 5 | 670 | 657 | 42.0 | 41.9 | 77.9 | 75.8 | 81.2 | 82.2 | 21.9 | 20.8 |
| | Cell 6 | 670 | 660 | 42.0 | 41.9 | 78.6 | 75.8 | 81.4 | 82.5 | 22.1 | 20.9 |
| Average | | 670 | 659 | 42.1 | 41.9 | 78.1 | 77.2 | 80.9 | 82.0 | 22.0 | 21.3 |
| Standard Deviation | | 0 | 1 | 0.2 | 0.1 | 0.5 | 1.2 | 0.5 | 0.3 | 0.1 | 0.4 |
| Batch 3 | Cell 1 | 666 | 661 | 41.6 | 41.8 | 77.0 | 76.3 | 80.9 | 79.8 | 21.4 | 21.1 |
| | Cell 2 | 667 | 661 | 41.7 | 41.9 | 76.8 | 75.3 | 80.7 | 78.6 | 21.4 | 20.9 |
| | Cell 3 | 667 | 661 | 41.8 | 41.9 | 77.0 | 72.6 | 80.9 | 80.2 | 21.5 | 20.1 |
| | Cell 4 | 667 | 660 | 41.7 | 41.8 | 76.7 | 71.9 | 80.9 | 78.2 | 21.3 | 19.8 |
| | Cell 5 | 666 | 655 | 41.5 | 41.8 | 76.8 | 67.9 | 80.6 | 68.9 | 21.2 | 18.6 |
| | Cell 6 | 665 | 644 | 41.7 | 41.9 | 76.5 | 60.8 | 80.8 | 60.5 | 21.2 | 16.4 |
| Average | | 666 | 657 | 41.7 | 41.9 | 76.8 | 70.8 | 80.8 | 74.4 | 21.3 | 19.5 |
| Standard Deviation | | 1 | 7 | 0.1 | 0.1 | 0.2 | 5.7 | 0.1 | 8.0 | 0.1 | 1.8 |

Table D.2: Summary of individual cell results for Cu-plated n-PERT solar cells before and after 500 hrs of thermal exposure at 200 °C under 1 Sun illumination.

| | | V_{oc} (mV) | | J_{sc} (mA/cm ²) | | FF (%) | | pFF (%) | | η (%) | |
|-------------------------------------|--------|------------------|-----|-----------------------------------|------|----------|------|-----------|------|------------|------|
| Thermal Treatment Duration (hrs) | | 0 | 500 | 0 | 500 | 0 | 500 | 0 | 500 | 0 | 500 |
| Batch 1 | Cell 1 | 669 | 414 | 41.8 | 41.7 | 76.4 | 52.0 | 80.4 | 53.5 | 21.4 | 9.0 |
| | Cell 2 | 669 | 415 | 41.9 | 41.7 | 76.2 | 48.9 | 80.7 | 51.7 | 21.4 | 8.5 |
| | Cell 3 | 671 | 559 | 42.4 | 41.6 | 76.3 | 49.2 | 80.4 | 49.9 | 21.7 | 11.5 |
| | Cell 4 | 669 | 506 | 42.4 | 41.6 | 76.5 | 47.5 | 80.5 | 48.8 | 21.7 | 10.0 |
| | Cell 5 | 670 | 548 | 42.4 | 41.8 | 76.1 | 49.3 | 80.4 | 50.8 | 21.6 | 11.3 |
| | Cell 6 | 668 | 565 | 42.3 | 41.6 | 76.9 | 50.4 | 80.8 | 51.3 | 21.7 | 11.9 |
| Average | | 669 | 501 | 42.2 | 41.7 | 76.4 | 49.6 | 80.5 | 51.0 | 21.6 | 10.4 |
| Standard Deviation | | 1 | 70 | 0.3 | 0.1 | 0.3 | 1.5 | 0.2 | 1.6 | 0.1 | 1.4 |
| Batch 2 | Cell 1 | 669 | 656 | 41.9 | 41.6 | 78.1 | 75.0 | 80.9 | 82.2 | 21.9 | 20.5 |
| | Cell 2 | 671 | 657 | 42.0 | 41.8 | 78.4 | 77.7 | 81.5 | 82.4 | 22.1 | 21.3 |
| | Cell 3 | 669 | 656 | 41.8 | 41.6 | 78.3 | 75.8 | 81.2 | 82.3 | 21.9 | 20.7 |
| | Cell 4 | 670 | 656 | 41.8 | 41.5 | 78.6 | 79.1 | 81.5 | 82.5 | 22.0 | 21.5 |
| | Cell 5 | 670 | 656 | 41.9 | 41.4 | 78.2 | 77.7 | 81.4 | 82.5 | 21.9 | 21.1 |
| | Cell 6 | 669 | 657 | 41.8 | 41.5 | 78.5 | 78.2 | 81.1 | 82.2 | 21.9 | 21.3 |
| Average | | 670 | 656 | 41.9 | 41.6 | 78.4 | 77.3 | 81.3 | 82.4 | 22.0 | 21.1 |
| Standard Deviation | | 1 | 1 | 0.1 | 0.1 | 0.2 | 1.5 | 0.2 | 0.1 | 0.1 | 0.4 |
| Batch 3 | Cell 1 | 666 | 654 | 41.6 | 41.6 | 76.9 | 74.2 | 80.7 | 76.6 | 21.3 | 20.2 |
| | Cell 2 | 666 | 655 | 41.7 | 41.6 | 77.0 | 75.3 | 81.0 | 78.9 | 21.4 | 20.5 |
| | Cell 3 | 665 | 652 | 41.7 | 41.7 | 76.9 | 72.9 | 80.9 | 75.0 | 21.3 | 19.8 |
| | Cell 4 | 666 | 655 | 41.6 | 41.7 | 77.2 | 76.5 | 81.1 | 79.9 | 21.4 | 20.9 |
| | Cell 5 | 666 | 592 | 41.7 | 41.7 | 76.6 | 50.8 | 80.6 | 50.8 | 21.3 | 12.5 |
| | Cell 6 | 666 | 653 | 41.7 | 41.7 | 76.7 | 74.5 | 80.6 | 77.9 | 21.3 | 20.3 |
| Average | | 666 | 644 | 41.7 | 41.7 | 76.9 | 70.7 | 80.8 | 73.2 | 21.3 | 19.0 |
| Standard Deviation | | 0 | 25 | 0.1 | 0.1 | 0.2 | 9.8 | 0.2 | 11.1 | 0.1 | 3.2 |

Table D.3: Summary of individual cell results for Cu-plated p-type PERC solar cells before and after 500 hrs of thermal exposure at 200 °C in the dark.

| | | V_{oc} (mV) | | J_{sc} (mA/cm ²) | | FF (%) | | pFF (%) | | η (%) | |
|----------------------------------|--------|---------------|-----|--------------------------------|------|----------|------|-----------|------|------------|------|
| Thermal Treatment Duration (hrs) | | 0 | 500 | 0 | 500 | 0 | 500 | 0 | 500 | 0 | 500 |
| Batch 1 | Cell 1 | 646 | 641 | 38.8 | 39.9 | 74.2 | 73.1 | 79.7 | 79.2 | 18.6 | 18.7 |
| | Cell 2 | 648 | 648 | 39.7 | 40.8 | 74.0 | 72.4 | 79.1 | 80.6 | 19.0 | 19.1 |
| | Cell 3 | 649 | 627 | 39.7 | 40.8 | 73.9 | 50.5 | 79.8 | 52.7 | 19.0 | 12.9 |
| Average | | 648 | 639 | 39.4 | 40.5 | 74.0 | 65.3 | 79.5 | 70.8 | 18.9 | 16.9 |
| Standard Deviation | | 2 | 11 | 0.5 | 0.5 | 0.2 | 12.9 | 0.4 | 15.7 | 0.2 | 3.5 |
| Batch 2 | Cell 1 | 643 | 464 | 39.5 | 40.6 | 75.8 | 42.0 | 79.8 | 47.8 | 19.2 | 7.9 |
| | Cell 2 | 641 | 392 | 39.3 | 40.3 | 75.9 | 45.7 | 79.7 | 47.8 | 19.1 | 7.2 |
| | Cell 3 | 640 | 626 | 39.5 | 40.3 | 75.3 | 63.0 | 79.3 | 63.0 | 19.0 | 15.9 |
| Average | | 641 | 494 | 39.4 | 40.4 | 75.7 | 50.2 | 79.6 | 52.9 | 19.1 | 10.3 |
| Standard Deviation | | 2 | 120 | 0.1 | 0.2 | 0.3 | 11.2 | 0.3 | 8.8 | 0.1 | 4.8 |

Table D.4: Summary of individual cell results for Cu-plated p-type PERC solar cells before and after 500 hrs of thermal exposure at 200 °C under 1 Sun illumination.

| | | V_{oc} (mV) | | J_{sc} (mA/cm ²) | | FF (%) | | pFF (%) | | η (%) | |
|----------------------------------|--------|---------------|-----|--------------------------------|------|----------|------|-----------|------|------------|------|
| Thermal Treatment Duration (hrs) | | 0 | 500 | 0 | 500 | 0 | 500 | 0 | 500 | 0 | 500 |
| Batch 1 | Cell 1 | 647 | 547 | 39.5 | 40.5 | 72.3 | 39.1 | 79.7 | 77.9 | 18.5 | 8.7 |
| | Cell 2 | 647 | 639 | 39.1 | 40.1 | 74.1 | 72.5 | 80.0 | 49.0 | 18.8 | 18.6 |
| | Cell 3 | 647 | - | 38.9 | - | 74.1 | - | 80.1 | - | 18.7 | - |
| Average | | 647 | 593 | 39.2 | 40.3 | 73.5 | 55.8 | 79.9 | 63.5 | 18.7 | 13.7 |
| Standard Deviation | | 0 | 65 | 0.3 | 0.3 | 1.0 | 23.6 | 0.2 | 20.4 | 0.2 | 7.0 |
| Batch 2 | Cell 1 | 639 | 256 | 39.6 | 39.9 | 75.2 | 44.2 | 79.7 | 47.7 | 19.0 | 4.5 |
| | Cell 2 | 642 | 236 | 39.4 | 39.9 | 76.4 | 44.4 | 80.9 | 49.1 | 19.3 | 4.2 |
| | Cell 3 | 644 | 240 | 39.5 | 40.0 | 75.8 | 45.2 | 80.3 | 49.1 | 19.3 | 4.3 |
| Average | | 642 | 244 | 39.5 | 39.9 | 75.8 | 44.6 | 80.3 | 48.6 | 19.2 | 4.3 |
| Standard Deviation | | 3 | 11 | 0.1 | 0.1 | 0.6 | 0.5 | 0.6 | 0.8 | 0.2 | 0.2 |

References

- [1] W. Steffen, P. J. Crutzen, and J. R. McNeill, “The Anthropocene : Are Humans Now Overwhelming the Great Forces of Nature?,” *Ambio* 36(8), pp. 614–621, 2007.
- [2] E. Dlugokencky and P. Tans, “Global Greenhouse Gas Reference Network - Trends in Atmospheric Carbon Dioxide,” , *NOAA/ESRL*[Online]. Available: www.esrl.noaa.gov/gmd/ccgg/trends/. [Accessed: 03-Jan-2018].
- [3] A. Neftel, E. Moor, H. Oeschger, and B. Stauffer, “Evidence from polar ice cores for the increase in atmospheric CO₂ in the past two centuries,” *Nature* 315, pp. 45–47, 1985.
- [4] CSIRO and Bureau of Meteorology, “State of the Climate 2016,” , 2016.
- [5] H. J. Schellnhuber, S. Rahmstorf, and R. Winkelmann, “Why the right climate target was agreed in Paris,” *Nature Climate Change* 6(7), pp. 649–653, 2016.
- [6] L. Boysen, W. Lucht, H. Schellnhuber, D. Gerten, V. Heck, and T. Lenton, “The limits to global-warming mitigation by terrestrial carbon removal,” *Earth’s Future* 5(5), pp. 463–474, 2017.
- [7] ITRPV, “International Technology Roadmap for Photovoltaic (ITRPV) - Results 2017,” *ITRPV*, pp. 1–37, 2018.
- [8] L. H. Ahrens, “Origin and Distribution of the Elements: International Series of Monographs in Earth Sciences,” 1st ed. Pergamon, 1968.
- [9] InfoMine, “5 Year Copper Prices and Price Charts,” [Online]. Available: <http://www.infomine.com/investment/metal-prices/copper/5-year/>. [Accessed: 29-Dec-2017].
- [10] K. Ralls, T. H. Courtney, and J. Wulff, “Introduction to Materials Science and Engineering,” John Wiley & Sons, Inc., 1976.
- [11] H. Iwasa, M. Yokozawa, and I. Teramoto, “Electroless Nickel Plating on Silicon,” *Journal of The Electrochemical Society* 115(5), p. 485, 1968.
- [12] R. Pryor, “Metallisation of Large Silicon Wafers: Final Report,” , 1978.
- [13] W. Taylor, “Proceedings of the Flat-Plate Solar Array Project Research Forum on Photovoltaic Metallization Systems,” , 1983.
- [14] A. Lennon, Y. Yao, and S. Wenham, “Evolution of metal plating for silicon solar cell metallisation,” *Prog. Photovolt: Res. Appl.* 21(7), pp. 1454–1468, 2013.
- [15] S. Wenham, “Buried-contact Silicon Solar Cells,” *Progress in Photovoltaics: Research and Applications* 1, pp. 3–10, 1993.
- [16] S. R. Wenham, C. B. Honsberg, and M. A. Green, “Buried contact silicon solar cells,”

Solar Energy Materials and Solar Cells 34(1–4), pp. 101–110, 1994.

- [17] T. Bruton, N. Mason, and J. G. Summers, “Towards production of high efficiency terrestrial solar cells,” , in *6th International Photovoltaic Science and Engineering Conference*, 1992, pp. 11–16.
- [18] N. Mason, T. Bruton, and M. A. Balbuena, “Laser grooved buried grid silicon solar cells: From pilot line to 50 Mwp manufacture in ten years,” , in *PV in Europe*, 2002, pp. 227–229.
- [19] T. Bruton *et al.*, “Towards 20% efficient silicon solar cells manufactured at 60 MWp per annum,” , in *3rd World Conference on Photovoltaic Energy Conversion* , 2003, pp. 899–902.
- [20] S. Eager, N. Mason, T. Bruton, J. Sherborne, and R. Russell, “Buried Contact Cell Technology - New Manufacturing Processes with Safety and Environmental Benefits,” *Int. Solar Energy Society UK Conference* 79, pp. 69–72, 2003.
- [21] Z. Shi, S. Wenham, and J. Ji, “Mass production of the innovative PLUTO solar cell technology,” , in *IEEE Photovoltaic Specialists Conference*, 2009.
- [22] Z. Wang, P. Han, H. Lu, H. Qian, L. Chen, Q. Meng, N. Tang, F. Gao, Y. Jiang, J. Wu, W. Wu, H. Zhu, J. Ji, Z. Shi, A. Sugianto, L. Mai, B. Hallam, and S. Wenham, “Advanced PERC and PERL production cells with 20.3% record efficiency for standard commercial p-type silicon wafers,” *Progress in Photovoltaics: Research and Applications* 20(3), pp. 260–268, 2012.
- [23] L. F. Durkee, “Method of plating by means of light,” , US 4144139, Mar-1979.
- [24] W. Späth, “Verfahren zur galvanischen Abscheidung einer Metallschicht auf der Oberfläche eines Halbleiterkörpers,” , 23 48 182, 1979.
- [25] A. Mette, “New concepts for the front side metallization of silicon solar cells,” , 2007.
- [26] A. Lennon, S. Flynn, T. Young, N. Nampalli, M. Edwards, R. Evans, Y. Yao, P. Hsiao, X. Wang, and V. Allen, “Addressing perceived barriers to the adoption of plated metallisation for silicon photovoltaic manufacturing,” , in *Proceedings of the 52nd Annual Conference, Australian Solar Energy Society*, 2014.
- [27] G. Schubert, G. Beaucarne, L. Tous, and J. Hoornstra, “The Future of Metallization and Interconnection – Forecast of Experts of the 6th Metallization Workshop,” *Energy Procedia* 98, pp. 12–22, 2016.
- [28] A. A. Istratov and E. R. Weber, “Physics of copper in silicon,” *Journal of The Electrochemical Society* 149(1), pp. G21–G30, 2002.
- [29] A. A. Istratov and E. R. Weber, “Electrical properties and recombination activity of copper, nickel and cobalt in silicon,” *Applied Physics A: Materials Science & Processing* 66(2), pp. 123–136, 1998.

-
- [30] D. C. Edelstein, G. a. Sai-Halasz, and Y.-J. Mii, "VLSI on-chip interconnection performance simulations and measurements," *IBM Journal of Research and Development* 39(4), pp. 383–401, 1995.
- [31] D. Edelstein, J. Heidenreich, R. Goldblatt, W. Cote, C. Uzoh, N. Lustig, P. Roper, T. McDevitt, W. Motsiff, A. Simon, J. Dukovic, R. Wachnik, H. Rathore, R. Schulz, L. Su, S. Luce, and J. Slattery, "Full Copper Wiring in a Sub-0.25 μm CMOS ULSI Technology," *International Electron Devices Meeting. IEDM Technical Digest* 4, pp. 773–776, 1997.
- [32] P. Gwynne, "Back To The Future: Copper Comes of Age," *IBM Research* 4, pp. 17–21, 1997.
- [33] P. C. Andricacos, "Copper On-Chip Interconnections—A Breakthrough in Electrodeposition to Make Better Chips," *Electrochemical Society Interface* 8, pp. 32–37, 1999.
- [34] R. Rosenberg, D. C. Edelstein, C. Hu, and K. P. Rodbell, "Copper Metallization for High Performance Silicon Technology," *Annual Review of Materials Science* 30(1), pp. 229–262, 2000.
- [35] H. Havemann, J. A. Hutchby, R. H. Havemann, and J. A. Hutchby, "High-performance interconnects: an integration overview," *Proceedings of the IEEE* 89(5), pp. 586–601, 2001.
- [36] A. A. Istratov, H. Hedemann, M. Seibt, O. F. Vyvenko, W. Schröter, T. Heiser, C. Flink, H. Hieslmair, and E. R. Weber, "Electrical and Recombination Properties of Copper-Silicide Precipitates in Silicon," *Journal of The Electrochemical Society* 145(11), pp. 3889–3898, 1998.
- [37] C. Flink, H. Feick, S. A. McHugo, W. Seifert, H. Hieslmair, T. Heiser, A. A. Istratov, and E. R. Weber, "Out-Diffusion and Precipitation of Copper in Silicon: An Electrostatic Model," *Physical Review Letters* 85(23), pp. 4900–4903, 2000.
- [38] A. Goetzberger and W. Shockley, "Metal precipitates in silicon p-n junctions," *Journal of Applied Physics* 31(10), pp. 1821–1824, 1960.
- [39] R. Bohm and H. Klose, "Copper in Silicon n+p Junctions," *physica status solidi (a)* 9(2), pp. 165–168, 1972.
- [40] H. H. Busta and H. A. Waggener, "Precipitation-Induced Currents and Generation-Recombination Currents in Intentionally Contaminated Silicon P+N Junctions," *Journal of The Electrochemical Society* 124(9), p. 1424, 1977.
- [41] M. Miyazaki, M. Sano, S. Sumita, and N. Fujino, "Influence of Metal Impurities on Leakage Current of Si N⁺ P Diode," *Japanese Journal of Applied Physics* 30(Part 2, No. 2B), pp. L295–L297, 1991.
-

-
- [42] H. Savin, M. Yli-Koski, and A. Haarahiltunen, "Role of copper in light induced minority-carrier lifetime degradation of silicon," *Applied Physics Letters* 95(15), 2009.
- [43] J. Lindroos, M. Yli-Koski, A. Haarahiltunen, M. C. Schubert, and H. Savin, "Light-induced degradation in copper-contaminated gallium-doped silicon," *physica status solidi (RRL) – Rapid Research Letters* 7(4), pp. 262–264, 2013.
- [44] M. Yli-Koski, M. Palokangas, A. Haarahiltunen, H. Väinölä, J. Storgårds, H. Holmberg, and J. Sinkkonen, "Detection of low-level copper contamination in p-type silicon by means of microwave photoconductive decay measurements," *Journal of Physics: Condensed Matter* 82–84(48), pp. 510–13125, 2002.
- [45] H. Väinölä, E. Saarnilehto, M. Yli-Koski, A. Haarahiltunen, J. Sinkkonen, G. Berenyi, and T. Pavelka, "Quantitative copper measurement in oxidized p-type silicon wafers using microwave photoconductivity decay," *Applied Physics Letters* 87(3), 2005.
- [46] J. C. Turn and E. L. Owen, "Metallic diffusion barriers for the copper-electrodeposited gold system," *Plating* 61(11), pp. 1015–1018, 1974.
- [47] M. R. Pinnel and J. E. Bennett, "Qualitative observations on the diffusion of copper and gold through a nickel barrier," *Metallurgical Transactions A* 7(5), pp. 629–635, 1976.
- [48] A. Sugianto, O. Breitenstein, B. S. Tjahjono, A. Lennon, L. Mai, and S. R. Wenham, "Impact of localized regions with very high series resistances on cell performance," *Progress in Photovoltaics: Research and Applications* 20(4), pp. 452–462, 2012.
- [49] E. J. O'Sullivan, A. G. Schrott, M. Paunovic, C. J. Sambucetti, J. R. Marino, P. J. Bailey, S. Kaja, and K. W. Semkow, "Electrolessly deposited diffusion barriers for microelectronics," *IBM Journal of Research and Development* 42(5), pp. 607–620, 1998.
- [50] J. Bartsch, A. Mondon, K. Bayer, C. Schetter, M. Hörteis, and S. W. Glunz, "Quick Determination of Copper-Metallization Long-Term Impact on Silicon Solar Cells," *Journal of The Electrochemical Society* 157(10), p. H942, 2010.
- [51] A. Kraft, C. Wolf, J. Bartsch, M. Glatthaar, and S. Glunz, "Long term stability of copper front side contacts for crystalline silicon solar cells," *Solar Energy Materials and Solar Cells* 136, pp. 25–31, 2015.
- [52] M. Alonso-Abella and F. Chenlo, "Toledo PV Plant 1 MWp – 20 Years of Operation," , in *29th European Photovoltaic Solar Energy Conference and Exhibition*, 2014, pp. 2728–2733.
- [53] N. Nampalli, D. Jordan, A. Lennon, R. Evans, S. Wenham, and M. Edwards, "Outdoor Testing Of Field-Aged BP Saturn Modules With Nickel-Copper Plated Contacts," , in *6th World Conference on Photovoltaic Energy Conversion*, 2014, (March 2016).
- [54] A. Mondon, J. Bartsch, B.-J. Godejohann, M. Hörteis, and S. W. Glunz, "Advanced Front Side Metallization for Crystalline Silicon Solar Cells Based on a Nickel-Silicon
-

-
- Contact,” , in *Proceedings of the 2nd Workshop on Metallization*, 2010, pp. 42–47.
- [55] A. Kraft, C. Wolf, A. Lorenz, J. Bartsch, M. Glatthaar, and S. W. Glunz, “Long Term Stability Analysis of Copper Front Side Metallization for Silicon Solar Cells,” *Energy Procedia* 55(Supplement C), pp. 478–485, 2014.
- [56] D. Wood, I. Kuzma-Filipek, R. Russell, F. Duerinckx, N. Powell, A. Zambova, B. Chislea, P. Chevalier, C. Boulord, A. Beucher, N. Zeghers, W. Deng, Z. Feng, P. Verlinden, J. Szlufcik, and G. Beaucarne, “Passivated Busbars from Screen-printed Low-temperature Copper Paste,” *Energy Procedia* 55, pp. 724–732, 2014.
- [57] R. Labie, J. L. Hernandez, J. Govaerts, C. Allebe, L. Tous, A. U. De Castro, R. Russel, I. Gordon, and K. Baert, “Cu Plated I-Perl Cells: Ageing and Humidity Reliability Tests,” *26th European Photovoltaic Solar Energy Conference and Exhibition*, pp. 1195–1198, 2011.
- [58] A. W. Blakers, A. Wang, A. M. Milne, J. Zhao, and M. A. Green, “22.8% Efficient Silicon Solar Cell,” *Applied Physics Letters* 55(13), pp. 1363–1365, 1989.
- [59] A. A. Istratov, C. Flink, H. Hieslmair, S. A. McHugo, and E. R. Weber, “Diffusion, solubility and gettering of copper in silicon,” *Materials Science and Engineering B: Solid-State Materials for Advanced Technology* 72(2), pp. 99–104, 2000.
- [60] J. Lindroos and H. Savin, “Review of light-induced degradation in crystalline silicon solar cells,” *Solar Energy Materials and Solar Cells* 147, pp. 115–126, 2016.
- [61] E. R. Weber, “Transition metals in silicon,” *Applied Physics A Solids and Surfaces* 30(1), pp. 1–22, 1983.
- [62] R. N. Hall and J. H. Racette, “Diffusion and Solubility of Copper in Extrinsic and Intrinsic Germanium, Silicon, and Gallium Arsenide,” *Journal of Applied Physics* 35(2), pp. 379–397, 1964.
- [63] H. Reiss, C. S. Fuller, and F. J. Morin, “Chemical Interactions Among Defects in Germanium and Silicon,” *Bell System Technical Journal* 35(3), pp. 535–636, 1956.
- [64] P. Wagner, H. Hage, H. Prigge, T. Prescha, and J. Weber, “Properties of copper induced complexes in silicon,” , in *Semiconductor Silicon-1990* H. R. Huff, K. G. Barraclough, and J.-I. Chikawa, Eds. Pennington, NJ: Electrochemical Society, 1990, pp. 675–686.
- [65] S. Estreicher, “Rich chemistry of copper in crystalline silicon,” *Physical Review B* 60(8), pp. 5375–5382, 1999.
- [66] A. A. Istratov, C. Flink, H. Hieslmair, E. R. Weber, and T. Heiser, “Intrinsic Diffusion Coefficient of Interstitial Copper in Silicon,” *Physical Review Letters* 81(6), pp. 1243–1246, 1998.
- [67] D. E. Woon, D. S. Marynick, and S. K. Estreicher, “Titanium and copper in Si: Barriers for diffusion and interactions with hydrogen,” *Physical Review B* 45(23), pp. 13383–
-

-
- 13389, 1992.
- [68] J. D. Struthers, "Solubility and Diffusivity of Gold, Iron, and Copper in Silicon," *Journal of Applied Physics* 27, p. 1560, 1956.
- [69] K. Graff, "Metal impurities in silicon-device fabrication," 24Berlin: Springer Science & Business Media, 1995.
- [70] T. Heiser, S. Mchugo, H. Hieslmair, and E. R. Weber, "Transient ion drift detection of low level copper contamination in silicon," *Applied Physics Letters* 70(26), pp. 3576–3578, 1997.
- [71] A. A. Istratov, H. Hieslmair, C. Flink, T. Heiser, and E. R. Weber, "Interstitial copper-related center in n-type silicon," *Applied Physics Letters* 71(16), pp. 2349–2351, 1997.
- [72] T. Heiser, A. Belayachi, and J. P. Schunck, "Copper Behavior in Bulk Silicon and Associated Characterization Techniques," *Journal of The Electrochemical Society* 150(12), p. G831, 2003.
- [73] S. A. McHugo, A. Mohammed, A. C. Thompson, B. Lai, and Z. Cai, "Copper precipitates in silicon: Precipitation, dissolution, and chemical state," *Journal of Applied Physics* 91(10 I), pp. 6396–6405, 2002.
- [74] M. B. Shabani, "Low-Temperature Out-Diffusion of Cu from Silicon Wafers," *Journal of The Electrochemical Society* 143(6), p. 2025, 1996.
- [75] M. B. Shabani, S. Okuuchi, and Y. Shimanuki, "Kinetics of low-temperature out-diffusion of copper from silicon wafers," , in *Analytical and diagnostic techniques for semiconductor materials, devices and processes*, 99th–16th ed. B. O. Kolbesen, C. Claeys, P. Stallhofer, F. Tardif, J. Benton, T. Shaffner, D. Schroder, S. Kishino, and P. Rai-Choudhury, Eds. Pennington, NJ: The Electrochemical Society Proceedings Series, 1999, p. 510.
- [76] Y. Boulfrad, J. Lindroos, M. Wagner, F. Wolny, M. Yli-Koski, and H. Savin, "Experimental evidence on removing copper and light-induced degradation from silicon by negative charge," *Applied Physics Letters* 105(10), pp. 1–3, 2014.
- [77] J. Lindroos, Y. Boulfrad, M. Yli-Koski, and H. Savin, "Preventing light-induced degradation in multicrystalline silicon," *Journal of Applied Physics* 115(101), 2014.
- [78] R. Hoelzl, D. Huber, K.-J. Range, L. Fabry, J. Hage, and R. Wahlich, "Gettering of Copper and Nickel in p/p+ Epitaxial Wafers," *Journal of The Electrochemical Society* 147(7), p. 2704, 2000.
- [79] R. Hoelzl, K.-J. Range, and L. Fabry, "Modeling of Cu gettering in p- and n-type silicon and in poly-silicon," *Applied Physics A: Materials Science & Processing* 75(4), pp. 525–534, 2002.
- [80] M. B. Shabani, T. Yamashita, and E. Morita, "Metallic Impurities in Mono and Multi-
-

- crystalline Silicon and Their Gettering by Phosphorus Diffusion,” in *ECS Transactions*, 2008, 16(6), pp. 179–193.
- [81] D. Macdonald, A. Cuevas, A. Kinomura, and Y. Nakano, “Phosphorus Gettering in Multicrystalline Silicon Studied by Neutron Activation Analysis,” in *29th IEEE Photovoltaic Specialists Conference*, 2002, pp. 285–288.
- [82] A. Bentzen, A. Holt, R. Kopecek, G. Stokkan, J. S. Christensen, and B. G. Svensson, “Gettering of transition metal impurities during phosphorus emitter diffusion in multicrystalline silicon solar cell processing,” *Journal of Applied Physics* 99(9), p. 093509, 2006.
- [83] A. Inglese, H. S. Laine, V. Vähänissi, and H. Savin, “Cu gettering by phosphorus-doped emitters in *p*-type silicon: Effect on light-induced degradation,” *AIP Advances* 8(1), p. 015112, 2018.
- [84] N. Nampalli, H. S. Laine, J. Colwell, V. Vähänissi, A. Inglese, C. Modanese, H. Vahlman, M. Yli-Koski, and H. Savin, “Rapid thermal anneal activates light induced degradation due to copper redistribution,” *Applied Physics Letters* 113(3), p. 032104, 2018.
- [85] A. A. Istratov, C. Flink, H. Hieslmair, T. Heiser, and E. R. Weber, “Influence of interstitial copper on diffusion length and lifetime of minority carriers in *p*-type silicon,” *Applied Physics Letters* 71(15), pp. 2121–2123, 1997.
- [86] R. Sachdeva, A. A. Istratov, and E. R. Weber, “Recombination activity of copper in silicon,” *Applied Physics Letters* 79(18), pp. 2937–2939, 2001.
- [87] A. Sharan, Z. Gui, and A. Janotti, “Hybrid-functional calculations of the copper impurity in silicon,” *Physical Review Applied* 8(2), pp. 1–12, 2017.
- [88] J. Weber, H. Bauch, and R. Sauer, “Optical properties of copper in silicon: Excitons bound to isoelectronic copper pairs,” *Physical Review B* 25(12), pp. 7688–7699, 1982.
- [89] M. Nakamura and H. Iwasaki, “Copper complexes in silicon,” *Journal of Applied Physics* 86(10), pp. 5372–5375, 1999.
- [90] N. Yarykin and J. Weber, “Deep levels of copper-hydrogen complexes in silicon,” *PHYSICAL REVIEW B* 88, 2013.
- [91] S. Kovesnikov, Y. Pan, and H. Mollenkopf, “Investigation of electronic states in copper doped *p*-type silicon,” *Electrochem. Soc. Proc.* 96 473, 1996.
- [92] K. Sufryd, N. Ponweiser, P. Riani, K. W. Richter, and G. Cacciamani, “Experimental investigation of the Cu–Si phase diagram at $x(\text{Cu}) > 0.72$,” *Intermetallics* 19(10), pp. 1479–1488, 2011.
- [93] W. Schröter, V. Kveder, M. Seibt, H. Ewe, H. Hedemann, F. Riedel, and A. Sattler, “Atomic structure and electronic states of nickel and copper silicides in silicon,”

Materials Science and Engineering: B 72(2–3), pp. 80–86, 2000.

- [94] D. Macdonald, A. Cuevas, S. Rein, P. Lichtner, and S. W. Glunz, “Temperature- and injection-dependent lifetime spectroscopy of copper-related defects in silicon,” *Proceedings of 3rd World Conference on Photovoltaic Energy Conversion* 1, pp. 87–90, 2003.
- [95] A. Inglese, J. Lindroos, H. Vahlman, and H. Savin, “Recombination activity of light-activated copper defects in p -type silicon studied by injection- and temperature-dependent lifetime spectroscopy,” *Journal of Applied Physics* 120(12), 2016.
- [96] M. Seibt, R. Khalil, V. Kveder, and W. Schröter, “Electronic states at dislocations and metal silicide precipitates in crystalline silicon and their role in solar cell materials,” *Applied Physics A: Materials Science and Processing* 96(1), pp. 235–253, 2009.
- [97] M. Seibt, M. Griess, A. A. Istratov, H. Hedemann, A. Sattler, and W. Schröter, “Formation and Properties of Copper Silicide Precipitates in Silicon,” *Physica Status Solidi (a)* 166(1), pp. 171–182, 1998.
- [98] M. Seibt, “Homogeneous and heterogeneous precipitation of copper in silicon,” *Proceedings - The Electrochemical Society* 90, pp. 663–674, 1990.
- [99] G. W. Ludwig and H. H. Woodbury, “Electronic Structure of Transition Metal Ions in a Tetrahedral Lattice,” *Physical Review Letters* 5(3), pp. 98–100, 1960.
- [100] M. Seibt, H. Hedemann, A. A. Istratov, F. Riedel, A. Sattler, and W. Schröter, “Structural and Electrical Properties of Metal Silicide Precipitates in Silicon,” *physica status solidi (a)* 171(1), pp. 301–310, 1999.
- [101] S. A. McHugo and C. Flink, “Thermal stability of copper precipitates in silicon,” *Applied Physics Letters* 77(22), p. 3598, 2000.
- [102] S. A. McHugo, “Release of metal impurities from structural defects in polycrystalline silicon,” *Applied Physics Letters* 71(14), p. 1984, 1998.
- [103] K. Bothe and J. Schmidt, “Electronically activated boron-oxygen-related recombination centers in crystalline silicon,” *Journal of Applied Physics* 99(1), p. 13701, 2006.
- [104] W. B. Henley, D. A. Ramappa, and L. Jastrezbski, “Detection of copper contamination in silicon by surface photovoltage diffusion length measurements,” *Applied Physics Letters* 74(2), p. 278, 1999.
- [105] D. A. Ramappa, “Surface photovoltage analysis of phase transformation of copper in p-type silicon,” *Applied Physics Letters* 76(25), p. 3756, 2000.
- [106] K. Ramspeck, S. Zimmermann, H. Nagel, A. Metz, Y. Gassenbauer, B. Birkmann, and A. Seidl, “Light Induced Degradation of Rear Passivated mc-Si Solar Cells,” , in *27th European Photovoltaic Solar Energy Conference and Exhibition*, 2012, pp. 861–865.
- [107] H. Fischer and W. Pschunder, “Investigation of photon and thermal changes in silicon

- solar cells,” , in *Proceedings of the 10th IEEE Photovoltaic Specialists Conference*, 1973, pp. 404–411.
- [108] T. U. Naerland, H. Haug, H. Angelskar, R. Sondena, E. S. Marstein, and L. Arnberg, “Studying Light-Induced Degradation by Lifetime Decay Analysis: Excellent Fit to Solution of Simple Second-Order Rate Equation,” *IEEE Journal of Photovoltaics* 3(4), pp. 1265–1270, 2013.
- [109] B. Hallam, M. Abbott, T. Naerland, and S. Wenham, “Fast and slow lifetime degradation in boron-doped Czochralski silicon described by a single defect,” *physica status solidi (RRL) - Rapid Research Letters* 10(7), pp. 520–524, 2016.
- [110] M. Kim, M. Abbott, N. Nampalli, S. Wenham, B. Stefani, and B. Hallam, “Modulating the extent of fast and slow boron-oxygen related degradation in Czochralski silicon by thermal annealing: Evidence of a single defect,” *Journal of Applied Physics* 121(5), p. 053106, 2017.
- [111] T. U. Naerland, “Characterization of light induced degradation in crystalline silicon,” , 2013.
- [112] J. Knobloch, S. W. Glunz, D. Biro, W. Warta, E. Schaffer, and W. Wettling, “Solar cells with efficiencies above 21% processed from Czochroalski grown silicon,” *Proceedings of the 25th IEEE Photovoltaic Specialists Conference, Washington, DC IEEE*, pp. 405–408, 1996.
- [113] H. Hashigami, Y. Itakura, and T. Saitoh, “Effect of illumination conditions on Czochralski-grown silicon solar cell degradation,” *Journal of Applied Physics* 93(7), pp. 4240–4245, 2003.
- [114] K. Bothe, R. Hezel, and J. Schmidt, “Recombination-enhanced formation of the metastable boron–oxygen complex in crystalline silicon,” *Applied Physics Letters* 83(6), pp. 1125–1127, 2003.
- [115] P. Hamer, B. Hallam, M. Abbott, and S. Wenham, “Accelerated formation of the boron-oxygen complex in p-type Czochralski silicon,” *physica status solidi (RRL) - Rapid Research Letters* 9(5), pp. 297–300, 2015.
- [116] S. W. Glunz, S. Rein, W. Warta, J. Knobloch, and W. Wettling, “Degradation of carrier lifetime in Cz silicon solar cells,” *Solar Energy Materials and Solar Cells* 65(1–4), pp. 219–229, 2001.
- [117] D. W. Palmer, K. Bothe, and J. Schmidt, “Kinetics of the electronically stimulated formation of a boron-oxygen complex in crystalline silicon,” *Physical Review B* 76(3), p. 035210, 2007.
- [118] D. Macdonald, F. Rougieux, A. Cuevas, B. Lim, J. Schmidt, M. Di Sabatino, and L. J. Geerligs, “Light-induced boron-oxygen defect generation in compensated p-type

-
- Czochralski silicon,” *Journal of Applied Physics* 105(9), p. 093704, 2009.
- [119] K. Bothe, R. Hezel, and J. Schmidt, “Understanding and Reducing the Boron-Oxygen-related Performance Degradation in Czochralski Silicon Solar Cells,” *Solid State Phenomena* 95–96, pp. 223–228, 2004.
- [120] R. S. Crandall, “Nature of the metastable boron–oxygen complex formation in crystalline silicon,” *Journal of Applied Physics* 108(10), p. 103713, 2010.
- [121] S. M. Kim, S. Chun, S. Bae, S. Park, M. G. Kang, H. Song, Y. Kang, H. Lee, and D. Kim, “Light-induced degradation and metastable-state recovery with reaction kinetics modeling in boron-doped Czochralski silicon solar cells,” *Applied Physics Letters* 105(8), p. 083509, 2014.
- [122] B. Lim, K. Bothe, and J. Schmidt, “Deactivation of the boron–oxygen recombination center in silicon by illumination at elevated temperature,” *physica status solidi (RRL) – Rapid Research Letters* 2(3), pp. 93–95, 2008.
- [123] S. Rein, “Lifetime spectroscopy : a method of defect characterization in silicon for photovoltaic applications,” Springer, 2005.
- [124] S. Rein and S. W. Glunz, “Electronic properties of the metastable defect in boron-doped Czochralski silicon: Unambiguous determination by advanced lifetime spectroscopy,” *Applied Physics Letters* 82(7), pp. 1054–1056, 2003.
- [125] T. Mchedlidze and J. Weber, “Direct detection of carrier traps in Si solar cells after light-induced degradation,” *physica status solidi (RRL) - Rapid Research Letters* 9(2), pp. 108–110, 2015.
- [126] V. V. Voronkov, R. Falster, K. Bothe, B. Lim, and J. Schmidt, “Lifetime-degrading boron-oxygen centres in p-type and n-type compensated silicon,” *Journal of Applied Physics* 110(6), p. 063515, 2011.
- [127] N. Nampalli, “Characterisation and passivation of boron-oxygen defects in p-type Czochralski silicon,” , 2017.
- [128] S. W. Glunz, S. Rein, J. Knobloch, W. Wettling, and T. Abe, “Comparison of boron- and gallium-doped p-type Czochralski silicon for photovoltaic application,” *Progress in Photovoltaics: Research and Applications* 7(6), pp. 463–469, 1999.
- [129] J. Schmidt, A. G. Aberle, and R. Hezel, “Investigation of carrier lifetime instabilities in Cz-grown silicon,” , in *26th IEEE Photovoltaic Specialists Conference*, 1997, pp. 13–18.
- [130] A. Herguth, G. Schubert, M. Kaes, and G. Hahn, “A New Approach to Prevent the Negative Impact of the Metastable Defect in Boron Doped CZ Silicon Solar Cells,” , in *IEEE 4th World Conference on Photovoltaic Energy Conference*, 2006, pp. 940–943.
- [131] A. Herguth, G. Schubert, M. Kaes, and G. Hahn, “Investigations on the long time behavior of the metastable boron–oxygen complex in crystalline silicon,” *Progress in*
-

- Photovoltaics: Research and Applications* 16(2), pp. 135–140, 2008.
- [132] S. Wilking, A. Herguth, and G. Hahn, “Influence of hydrogen on the regeneration of boron-oxygen related defects in crystalline silicon,” *Journal of Applied Physics* 113(19), p. 194503, 2013.
- [133] I. Tarasov and O. Ostapenko, “Light induced defect reactions in boron-doped silicon: Cu vs Fe,” , in *8th Workshop on Crystalline Silicon Solar Cell Material and Process*, 1998, pp. 207–210.
- [134] A. Belayachi, T. Heiser, J. P. Schunck, and A. Kempf, “Influence of light on interstitial copper in p-type silicon,” *Applied Physics A: Materials Science and Processing* 80(2), pp. 201–204, 2005.
- [135] J. Lindroos and H. Savin, “Formation kinetics of copper-related light-induced degradation in crystalline silicon,” *Journal of Applied Physics* 116(23), 2014.
- [136] H. Väinölä, M. Yli-Koski, a. Haarahiltunen, and J. Sinkkonen, “Sensitive Copper Detection in P-type CZ Silicon using μ PCD,” *Journal of The Electrochemical Society* 150(12), p. G790, 2003.
- [137] M. Yli-koski, “Optical Activation of Copper in Silicon Studied By Carrier Lifetime Measurements,” (September)2004.
- [138] A. Inglese, J. Lindroos, and H. Savin, “Accelerated light-induced degradation for detecting copper contamination in *p* -type silicon,” *Applied Physics Letters* 107(5), p. 052101, 2015.
- [139] D. A. Ramappa, “Quantitative analysis of copper contamination in silicon by surface photovoltage minority carrier lifetime analysis,” *AIP Conference Proceedings* 550, pp. 215–219, 2001.
- [140] J. Schmidt, K. Bothe, and R. Hezel, “Structure and transformation of the metastable centre in CZ-silicon solar cells,” , in *3rd World Conference on Photovoltaic Energy Conversion*, 2003, pp. 2887–2892.
- [141] Y. Boulfrad, J. Lindroos, M. Wagner, F. Wolny, M. Yli-Koski, and H. Savin, “Experimental evidence on removing copper and light-induced degradation from silicon by negative charge,” *Applied Physics Letters* 105(18), p. 182108, 2014.
- [142] F. Fertig, K. Krauß, and S. Rein, “Light-induced degradation of PECVD aluminium oxide passivated silicon solar cells,” *physica status solidi (RRL) - Rapid Research Letters* 9(1), pp. 41–46, 2015.
- [143] F. Kersten, P. Engelhart, H.-C. Ploigt, A. Stekolnikov, T. Lindner, F. Stenzel, M. Bartzsch, A. Szpeth, K. Petter, J. Heitmann, and J. W. Muller, “A new mc-Si degradation effect called LeTID,” , in *2015 IEEE 42nd Photovoltaic Specialist Conference (PVSC)*, 2015, pp. 1–5.

-
- [144] C. Chan, T. H. Fung, M. Abbott, D. Payne, A. Wenham, B. Hallam, R. Chen, and S. Wenham, "Modulation of Carrier-Induced Defect Kinetics in Multi-Crystalline Silicon PERC Cells Through Dark Annealing," *Solar RRL* 1(2), p. 1600028, 2017.
 - [145] C. E. Chan, D. N. R. Payne, B. J. Hallam, M. D. Abbott, T. H. Fung, A. M. Wenham, B. S. Tjahjono, and S. R. Wenham, "Rapid Stabilization of High-Performance Multicrystalline P-type Silicon PERC Cells," *IEEE Journal of Photovoltaics* 6(6), pp. 1473–1479, 2016.
 - [146] D. Bredemeier, D. Walter, S. Herlufsen, and J. Schmidt, "Lifetime degradation and regeneration in multicrystalline silicon under illumination at elevated temperature," *AIP Advances* 6(3), p. 035119, 2016.
 - [147] F. Kersten, J. Heitmann, and J. W. Müller, "Influence of Al₂O₃ and SiN_x Passivation Layers on LeTID," *Energy Procedia* 92, pp. 828–832, 2016.
 - [148] C. Vargas, K. Kim, G. Coletti, D. Payne, C. Chan, S. Wenham, and Z. Hameiri, "Carrier-Induced Degradation in Multicrystalline Silicon: Dependence on the Silicon Nitride Passivation Layer and Hydrogen Released During Firing," *IEEE Journal of Photovoltaics* 8(2), pp. 413–420, 2018.
 - [149] D. Chen, M. Kim, B. V. Stefani, B. J. Hallam, M. D. Abbott, C. E. Chan, R. Chen, D. N. R. Payne, N. Nampalli, A. Ciesla, T. H. Fung, K. Kim, and S. R. Wenham, "Evidence of an identical firing-activated carrier-induced defect in monocrystalline and multicrystalline silicon," *Solar Energy Materials and Solar Cells* 172, pp. 293–300, 2017.
 - [150] F. Fertig *et al.*, "Mass production of p -type Cz silicon solar cells approaching average stable conversion efficiencies of 22 %," *Energy Procedia* 124, pp. 338–345, 2017.
 - [151] C. Renevier, E. Fourmond, M. Forster, S. Parola, M. Le Coz, and E. Picard, "Lifetime Degradation on n-type Wafers with Boron-diffused and SiO₂/SiN-passivated Surface," *Energy Procedia* 55, pp. 280–286, 2014.
 - [152] D. Chen, P. G. Hamer, M. Kim, C. E. Chan, A. Ciesla, R. Chen, M. D. Abbott, B. J. Hallam, and S. R. Wenham, "Hydrogen induced degradation: A possible mechanism for light- and elevated temperature- induced degradation in n-type silicon," *Solar Energy Materials and Solar Cells* 185, pp. 174–182, 2018.
 - [153] H. Vahlman, A. Haarahiltunen, W. Kwapil, J. Schön, A. Inglese, and H. Savin, "Modeling of light-induced degradation due to Cu precipitation in p-type silicon. I. General theory of precipitation under carrier injection," *Journal of Applied Physics* 121(19), 2017.
 - [154] J. W. Christian, "The Classical Theory of Nucleation," , in *The Theory of Transformations in Metals and Alloys* Pergamon Press, 2002, pp. 422–479.
-

-
- [155] W. Schröter, M. Seibt, and D. Gilles, “Electronic Structure and Properties of Semiconductors,” , in *Materials Science and Technology: A Comprehensive Treatment*, 4R. W. Cahn, P. Haasen, and E. J. Kramer, Eds. 1991, p. 576.
- [156] K. F. Kelton, R. Falster, D. Gambaro, M. Olmo, M. Cornara, and P. F. Wei, “Oxygen precipitation in silicon: Experimental studies and theoretical investigations within the classical theory of nucleation,” *Journal of Applied Physics* 85(12), pp. 8097–8111, 1999.
- [157] J. Vanhellemont and C. Claeys, “On the morphology and the critical size of precipitates in crystals with cubic symmetry and application to precipitation in silicon,” , in *Proceedings of the Second Symposium on Defects in Silicon: Defects in Silicon II*, 1991, p. 692.
- [158] H. Vahlman, A. Haarahiltunen, W. Kwapil, J. Schön, A. Inglese, and H. Savin, “Modeling of light-induced degradation due to Cu precipitation in p-type silicon. II. Comparison of simulations and experiments,” *Journal of Applied Physics* 121(19), 2017.
- [159] P. S. Plekhanov and T. Y. Tan, “Schottky effect model of electrical activity of metallic precipitates in silicon,” *Applied Physics Letters* 76(25), pp. 3777–3779, 2000.
- [160] W. Kwapil, J. Schön, W. Warta, and M. C. Schubert, “Carrier Recombination at Metallic Precipitates in p-and n-Type Silicon,” *IEEE Journal of Photovoltaics* 5(5), pp. 1285–1292, 2015.
- [161] T. Trupke, M. A. Green, P. Würfel, P. P. Altermatt, A. Wang, J. Zhao, and R. Corkish, “Temperature dependence of the radiative recombination coefficient of intrinsic crystalline silicon,” *Journal of Applied Physics* 94(8), p. 4930, 2003.
- [162] P. P. Altermatt, A. Schenk, F. Geelhaar, and G. Heiser, “Reassessment of the intrinsic carrier density in crystalline silicon in view of band-gap narrowing,” *Journal of Applied Physics* 93(3), pp. 1598–1604, 2003.
- [163] A. G. Aberle, “Crystalline silicon solar cells : advanced surface passivation and analysis,” Centre for Photovoltaic Engineering, University of New South Wales, 1999.
- [164] J. D. Beck and R. Conradt, “Auger-rekombination in Si,” *Solid State Communications* 13(1), pp. 93–95, 1973.
- [165] J. Dziewior and W. Schmid, “Auger coefficients for highly doped and highly excited silicon,” *Applied Physics Letters* 31(5), pp. 346–348, 1977.
- [166] A. Hangleiter and R. Häcker, “Enhancement of band-to-band Auger recombination by electron-hole correlations,” *Physical Review Letters* 65(2), pp. 215–218, 1990.
- [167] A. Richter, S. W. Glunz, F. Werner, J. Schmidt, and A. Cuevas, “Improved quantitative description of Auger recombination in crystalline silicon,” *Physical Review B - Condensed Matter and Materials Physics* 86(16), pp. 1–14, 2012.
- [168] P. P. Altermatt, F. Geelhaar, T. Trupke, X. Dai, A. Neisser, and E. Daub, “Injection
-

-
- dependence of spontaneous radiative recombination in c-Si: experiment, theoretical analysis, and simulation,” , in *Proceedings of the 5th International Conference on Numerical Simulation of Optoelectronic Devices*, 2005, pp. 47–48.
- [169] S. Wang and D. Macdonald, “Temperature dependence of Auger recombination in highly injected crystalline silicon,” *Journal of Applied Physics* 112(11), p. 113708, 2012.
- [170] W. Shockley and W. T. Read, “Statistics of the Recombinations of Holes and Electrons,” *Physical Review* 87(5), pp. 835–842, 1952.
- [171] R. N. Hall, “Electron-Hole Recombination in Germanium,” *Physical Review* 87(2), pp. 387–387, 1952.
- [172] M. A. Green, “Solar cells : operating principles, technology, and system applications,” Prentice-Hall, 1982.
- [173] D. K. Schroder, “Semiconductor material and device characterization,” IEEE Press, 2006.
- [174] J. S. Blakemore, “Semiconductor statistics,” Dover Publications, 1987.
- [175] A. B. Sproul, “Dimensionless solution of the equation describing the effect of surface recombination on carrier decay in semiconductors,” *Journal of Applied Physics* 76(5), pp. 2851–2854, 1994.
- [176] V. Grivickas, D. Noreika, and J. A. Tellesfen, “Surface and Auger recombination in silicon wafers of high carrier density,” *Lithuanian Physics Journal* 29(5), pp. 48–53, 1989.
- [177] K. R. McIntosh and L. E. Black, “On effective surface recombination parameters,” *Journal of Applied Physics* 116(1), 2014.
- [178] M. J. Kerr, “Surface, Emitter and Bulk Recombination in Silicon and Development of Silicon Nitride Passivated Solar Cells,” , 2002.
- [179] J. D. Murphy, K. Bothe, R. Krain, V. V. Voronkov, and R. J. Falster, “Parameterisation of injection-dependent lifetime measurements in semiconductors in terms of Shockley-Read-Hall statistics: An application to oxide precipitates in silicon,” *Journal of Applied Physics* 111(11), 2012.
- [180] C. Sun, F. E. Rougieux, and D. Macdonald, “Reassessment of the recombination parameters of chromium in n- and p-type crystalline silicon and chromium-boron pairs in p-type crystalline silicon,” *Journal of Applied Physics* 115(21), p. 214907, 2014.
- [181] S. Bernardini, T. U. Naerland, A. L. Blum, G. Coletti, and M. I. Bertoni, “Unraveling bulk defects in high-quality c-Si material via TIDLS,” *Progress in Photovoltaics: Research and Applications* 25(3), pp. 209–217, 2017.
- [182] Y. Zhu, Q. T. Le Gia, M. K. Juhl, G. Coletti, and Z. Hameiri, “Application of the Newton–Raphson Method to Lifetime Spectroscopy for Extraction of Defect
-

- Parameters,” *IEEE Journal of Photovoltaics* 7(4), pp. 1092–1097, 2017.
- [183] A. Inglese, H. Vahlman, W. Kwapil, J. Schön, and H. Savin, “Characterization of light-activated Cu defects in silicon: Comparison with the recombination activity of metallic precipitates,” *physica status solidi c* 14(7), 2017.
- [184] D. E. Kane and R. M. Swanson, “Measurement of the Emitter Saturation Current by a Contactless Photoconductivity Decay Method,” , in *Conference Record of the 18th IEEE Photovoltaic Specialists Conference*, 1985, p. 578.
- [185] E. Yablonovitch, D. L. Allara, C. C. Chang, T. Gmitter, and T. B. Bright, “Unusually Low Surface-Recombination Velocity on Silicon and Germanium Surfaces,” *Physical Review Letters* 57(2), pp. 249–252, 1986.
- [186] C. Vargas, Y. Zhu, G. Coletti, C. Chan, D. Payne, M. Jensen, and Z. Hameiri, “Recombination parameters of lifetime-limiting carrier-induced defects in multicrystalline silicon for solar cells,” *Applied Physics Letters* 110(9), p. 092106, 2017.
- [187] A. G. Aberle, S. Glunz, and W. Warta, “Impact of illumination level and oxide parameters on Shockley–Read–Hall recombination at the Si-SiO₂ interface,” *Journal of Applied Physics* 71(9), pp. 4422–4431, 1992.
- [188] J. Schmidt and A. G. Aberle, “Accurate method for the determination of bulk minority-carrier lifetimes of mono- and multicrystalline silicon wafers,” *Journal of Applied Physics* 81(9), p. 6186, 1998.
- [189] S. Nie, “Advanced Temperature-dependent Characterization of Surface Passivation Materials for Silicon,” , 2017.
- [190] S. Bernardini, Y. Zhu, S. Nie, Z. Hameiri, and M. I. Bertoni, “Analysis of SiN_x SRV Injection- and Temperature-Dependence and Its Degradation via TIDLs Measurements,” , in *7th World Conference on Photovoltaic Energy Conversion*, 2018.
- [191] R. N. Hall, “Segregation of Impurities During the Growth of Germanium and Silicon Crystals,” *The Journal of Physical Chemistry* 57(8), pp. 836–839, 1953.
- [192] A. Hangleiter, “Nonradiative recombination via deep impurity levels in semiconductors: The excitonic Auger mechanism,” *Physical Review B* 37(5), pp. 2594–2604, 1988.
- [193] M. D. Negoita and T. Y. Tan, “Metallic precipitate contribution to generation and recombination currents in p-n junction devices due to the Schottky effect,” *Journal of Applied Physics* 94(8), p. 5064, 2003.
- [194] S. Rein, T. Rehr, W. Warta, and S. W. Glunz, “Lifetime spectroscopy for defect characterization: Systematic analysis of the possibilities and restrictions,” *Journal of Applied Physics* 91(4), pp. 2059–2070, 2002.
- [195] C. Donolato, “The space-charge region around a metallic platelet in a semiconductor,” *Semiconductor Science and Technology* 8(1), pp. 45–49, 1993.

-
- [196] C. Sun, H. T. Nguyen, F. E. Rougieux, and D. Macdonald, "Characterization of Cu and Ni precipitates in n- and p-type Czochralski-grown silicon by photoluminescence imaging," *Journal of Crystal Growth* 460(February 2017), pp. 98–104, 2017.
- [197] M. A. Nicolet, "Ternary amorphous metallic thin films as diffusion barriers for Cu metallization," *Applied Surface Science* 91(1–4), pp. 269–276, 1995.
- [198] A. E. Kaloyeros and E. Eisenbraun, "Ultrathin Diffusion Barriers/Liners For Gigascale Copper Metallization," *Annual Review of Materials Science* 30(1), pp. 363–385, 2000.
- [199] C. Lee and Y.-L. Kuo, "The evolution of diffusion barriers in copper metallization," *JOM* 59(1), pp. 44–49, 2007.
- [200] P. Liu, T. Chang, J. C. Hu, Y. L. Yang, and S. M. Sze, "Reliability of Multistacked Chemical Vapor Deposited Ti / TiN Structure as the Diffusion Barrier in Ultralarge Scale Integrated Metallization," *Journal of The Electrochemical Society* 147(1), pp. 368–372, 2000.
- [201] E. Kolawa, P. J. Pokela, J. S. Reid, J. S. Chen, R. P. Ruiz, and M. A. Nicolet, "Sputtered Ta-Si-N Diffusion Barriers in Cu Metallizations for Si," *IEEE Electron Device Letters* 12(6), pp. 321–323, 1991.
- [202] J. Baumann, M. Markert, T. Werner, A. Ehrlich, M. Rennau, C. Kaufmann, and T. Gessner, "W/TiN double layers as barrier system for use in Cu metallization," *Microelectronic Engineering* 37–38, pp. 229–236, 1997.
- [203] C. Ahrens, D. Depta, F. Schitthelm, and S. Wilhelm, "Electrical characterization of conductive and non-conductive barrier layers for Cu-metallization," *Applied Surface Science* 91(1–4), pp. 285–290, 1995.
- [204] C. Kaufmann, J. Baumann, T. Gessner, T. Raschke, M. Rennau, and N. Zichner, "Electrical characterization of reactively sputtered TiN diffusion barrier layers for copper metallization," *Applied Surface Science* 91(1–4), pp. 291–294, 1995.
- [205] M. A. Nicolet, "Diffusion Barriers in Thin Films," *Thin Solid Films* 52, pp. 415–443, 1978.
- [206] P. J. Pokela, C. K. Kwok, E. Kolawa, S. Raud, and M. A. Nicolet, "Performance of W100-xNx diffusion barriers between Si and Cu," *Applied Surface Science* 53(C), pp. 364–372, 1991.
- [207] E. Kolawa, P. J. Pokela, J. S. Reid, J. S. Chen, and M. A. Nicolet, "Amorphous Ta-Si-N diffusion barriers in Si/Al and Si/Cu metallizations," *Applied Surface Science* 53(C), pp. 373–376, 1991.
- [208] J. Chiou and M. Chen, "Thermal Stability of Cu / CoSi₂ Contacted p + n Shallow Junction with and without TiW Diffusion Barrier," *Journal of The Electrochemical Society* 141(10), pp. 2804–2810, 1994.
-

-
- [209] J. S. Reid, E. Kolawa, R. P. Ruiz, and M. A. Nicolet, "Evaluation of amorphous (Mo, Ta, W)SiN diffusion barriers for $\langle\text{Si}\rangle$ |Cu metallizations," *Thin Solid Films* 236(1–2), pp. 319–324, 1993.
- [210] J. S. Reid, X. Sun, E. Kolawa, and M. A. Nicolet, "Ti-Si-N Diffusion Barriers between Silicon and Copper," *IEEE Electron Device Letters* 15(8), pp. 298–300, 1994.
- [211] T. Chang, W. Wang, L. Wang, J. Hwang, and F. Huang, "Thermal stability study of TiN/TiSi₂ diffusion barrier between Cu and n+Si," *Journal of Applied Physics* 75(12), pp. 7847–7851, 1994.
- [212] S. I. Nakao, M. Numata, and T. Ohmi, "Thin and low-resistivity tantalum nitride diffusion barrier and giant-grain copper interconnects for advanced ULSI metallization," *Japanese Journal of Applied Physics, Part 1: Regular Papers and Short Notes and Review Papers* 38(4 B), pp. 2401–2405, 1999.
- [213] J. Baumann, T. Werner, A. Ehrlich, M. Rennau, C. Kaufmann, and T. Gessner, "TiN diffusion barriers for copper metallization," *Microelectronic Engineering* 37–38, pp. 221–228, 1997.
- [214] A. A. Istratov and E. R. Weber, "The importance of understanding of the physics of copper in silicon for development and characterization of copper diffusion barriers," *Copper interconnects, new contact metallurgies/structures, and low-K interlevel dielectrics*, p. 90, 2001.
- [215] S.-Q. Wang, "Barriers Against Copper Diffusion into Silicon and Drift Through Silicon Dioxide," *MRS Bulletin* 19(08), pp. 30–40, 1994.
- [216] J. O. Olowolafe, C. J. Mogab, R. B. Gregory, and M. Kottke, "Interdiffusions in Cu/reactive-ion-sputtered TiN, Cu/chemical-vapor-deposited TiN, Cu/TaN, and TaN/Cu/TaN thin-film structures: Low temperature diffusion analyses," *Journal of Applied Physics* 72(79), 1992.
- [217] R. A. Levy, "Microelectronic Materials and Processes," Springer Netherlands, 1989.
- [218] A. Kohn, M. Eizenberg, and Y. Shacham-Diamand, "Improved diffusion barriers for copper metallization obtained by passivation of grain boundaries in electroless deposited cobalt-based films," *Journal of Applied Physics* 92(10), 2002.
- [219] M. Stavrev, D. Fischer, F. Praessler, C. Wenzel, and K. Drescher, "Behavior of thin Ta-based films in the Cu/barrier/Si system," *Journal of Vacuum Science & Technology A* 17(3), pp. 993–1001, 1999.
- [220] O. Younes, L. Zhu, Y. Rosenberg, Y. Shacham-Diamand, and E. Gileadi, "Electroplating of Amorphous Thin Films of Tungsten/Nickel Alloys," *Langmuir* 17(26), pp. 8270–8275, 2001.
- [221] D. J. Kim, Y. T. Kim, and J.-W. Park, "Nanostructured Ta-Si-N diffusion barriers for Cu
-

-
- metallization,” *Journal of Applied Physics* 82(10), pp. 4847–4851, 1997.
- [222] B. Gallagher, P. Alexander, and D. Burger, “Electricity from photovoltaic solar cells: Flat-Plate Solar Array Project final report. Volume V: Process development,” , 1986.
- [223] A. Brenner and G. E. Riddle, “Electroless nickel plating,” *Proc. Am. Electropl. Soc* 33, pp. 16–19, 1946.
- [224] A. Brenner, D. E. Couch, and E. K. Williams, “Electrodeposition of Alloys of Phosphorus with Nickel or Cobalt,” *Journal of Research of the National Bureau of Standards* 44, pp. 109–122, 1950.
- [225] J. F. Rohan and G. O’Riordan, “Characterisation of the electroless nickel deposit as a barrier layer/under bump metallurgy on IC metallisation,” *Microelectronic Engineering* 65(1–2), pp. 77–85, 2003.
- [226] E. Bredael, B. Blanpain, J. P. Celis, and J. R. Roos, “On the Amorphous and Crystalline State of Electrodeposited Nickel-Phosphorus Coatings,” *Journal of the electrochemical Society* 141(1), pp. 294–299, 1994.
- [227] Y. Tao, A. Hu, T. Hang, L. Peng, and M. Li, “Effect of W addition on the electroless deposited NiP(W) barrier layer,” *Applied Surface Science* 282, pp. 632–637, 2013.
- [228] B. Tjahjono, J.-H. Guo, Z. Hameiri, L. Mai, A. Sugianto, S. Wang, and S. R. Wenham, “High efficiency solar cell structure through the use of laser doping,” , in *22nd European Photovoltaic Solar Energy Conference*, 2007, pp. 966–969.
- [229] L. Tous, R. Russell, J. Das, R. Labie, M. Ngamo, J. Horzel, H. Philipsen, J. Sniekers, K. Vandermissen, L. van den Brekel, T. Janssens, M. Aleman, D. H. van Dorp, J. Poortmans, and R. Mertens, “Large Area Copper Plated Silicon Solar Cell Exceeding 19.5% Efficiency,” *Energy Procedia* 21(0), pp. 58–65, 2012.
- [230] J. T. Horzel, N. Bay, M. Passig, M. Sieber, J. Burschik, H. Kühnlein, A. A. Brand, A. Letize, B. Lee, D. Weber, and R. Böhme, “Low cost metallisation based on Ni/Cu plating enabling high efficiency industrial solar cells,” , in *29th European Photovoltaic Solar Energy Conference*, 2014, pp. 507–512.
- [231] R. Russell, L. Tous, H. Philipsen, J. Horzel, E. Cornagliotti, M. Ngamo, P. Choulat, R. Labie, J. Beckers, J. Bertens, M. Fujii, J. John, J. Poortmans, and R. Mertens, “A simple copper metallisation process for high cell efficiencies and reliable modules,” , in *27th European Photovoltaic Solar Energy Conference and Exhibition*, 2012, pp. 538–543.
- [232] A. Kraft, “Plated copper front side metallization on printed seed-layers for silicon solar cells,” , 2015.
- [233] S. Flynn and A. Lennon, “Copper penetration in laser-doped selective-emitter silicon solar cells with plated nickel barrier layers,” *Solar Energy Materials and Solar Cells* 130, pp. 309–316, 2014.
-

-
- [234] Q. Huang, "A Study on the Electrodeposition and Silicidation of Nickel-Cobalt Alloys for Silicon Photovoltaic Cell Metallization," *ECS Journal of Solid State Science and Technology* 5(2), pp. P51–P57, 2016.
- [235] Q. Huang, K. B. Reuter, Y. Zhu, and V. R. Deline, "A Study on the Long-Term Degradation of Crystalline Silicon Solar Cells Metallized with Cu Electroplating," *ECS Journal of Solid State Science and Technology* 5(2), pp. Q24–Q34, 2016.
- [236] X. Wang, "Cost-effective and Reliable Copper-plated Metallisation for Silicon Solar Cells: A Development Path," , 2017.
- [237] F. Deng, R. A. Johnson, P. M. Asbeck, S. S. Lau, W. B. Dubbelday, T. Hsiao, and J. Woo, "Salicidation process using NiSi and its device application," *Journal of Applied Physics* 81(12), pp. 8047–8051, 1997.
- [238] J. Foggiato, W. S. Yoo, M. Ouaknine, T. Murakami, and T. Fukada, "Optimizing the formation of nickel silicide," *Materials Science and Engineering B: Solid-State Materials for Advanced Technology* 114–115(SPEC. ISS.), pp. 56–60, 2004.
- [239] S. H. Lee, A. Rehman, E. G. Shin, D. W. Lee, and S. H. Lee, "Analysis of Ni/Cu Metallization to Investigate an Adhesive Front Contact for Crystalline-Silicon Solar Cells," *Journal of the Optical Society of Korea* 19(3), pp. 217–221, 2015.
- [240] S. H. Lee, D. W. Lee, A. ur Rehman, J. W. Baik, and S. H. Lee, "Study of Annealing Temperature for Ni/Cu/Ag Plated Front Contact Single Crystalline Solar Cells," *IEEE Journal of Photovoltaics* 6(5), pp. 1090–1093, 2016.
- [241] R. A. Sinton and A. Cuevas, "A quasi-steady-state open-circuit voltage method for solar cell characterization," , in *Proceedings of the 16th European Photovoltaic Solar Energy Conference*, 2000.
- [242] M. A. Green, A. W. Blakers, J. Zhao, A. M. Milne, A. Wang, and X. Dai, "Characterization of 23-percent efficient silicon solar cells," *IEEE Transactions on Electron Devices* 37(2), pp. 331–336, 1990.
- [243] S. W. Glunz, J. Nekarda, H. Mäkel, and A. Cuevas, "Analyzing Back Contacts of Silicon Solar Cells by Suns-Voc-Measurements at High Illumination Densities," *Proceedings of the 22nd European Photovoltaic Solar Energy Conference, Milan, Italy* (September), pp. 849–853, 2007.
- [244] X. Wang, V. Allen, V. Vais, Y. Zhao, B. Tjahjono, Y. Yao, S. Wenham, and A. Lennon, "Laser-doped metal-plated bifacial silicon solar cells," *Solar Energy Materials and Solar Cells* 131, pp. 37–45, 2014.
- [245] R. S. Barnes, "Diffusion of Copper along the Grain Boundaries of Nickel," *Nature* 166(4233), pp. 1032–1033, 1950.
- [246] N. A. Dolgoplov, A. O. Rodin, A. V Simanov, and I. G. Gontar', "Diffusion of copper
-

-
- along the grain boundaries in aluminum,” *Russian Journal of Non-Ferrous Metals* 50(2), pp. 133–137, 2009.
- [247] H. G. Tompkins and M. R. Pinnel, “Low-temperature diffusion of copper through gold,” *Journal of Applied Physics* 47(9), pp. 3804–3812, 1976.
- [248] M. R. Pinnel and J. E. Bennett, “Mass diffusion in polycrystalline copper/electroplated gold planar couples,” *Metallurgical Transactions* 3(7), pp. 1989–1997, 1972.
- [249] L. Tous, D. H. Van Dorp, R. Russell, J. Das, M. Aleman, H. Bender, J. Meersschant, K. Opsomer, J. Poortmans, and R. Mertens, “Electroless nickel deposition and silicide formation for advanced front side metallization of industrial silicon solar cells,” *Energy Procedia* 21, pp. 39–46, 2012.
- [250] C.-W. Liu, Y.-L. Wang, M.-S. Tsai, H.-P. Feng, S.-C. Chang, and G.-J. Hwang, “Effect of plating current density and annealing on impurities in electroplated Cu film,” *Journal of Vacuum Science & Technology A: Vacuum, Surfaces, and Films* 23(4), p. 658, 2005.
- [251] A. Atkinson, “Grain-boundary diffusion: an historical perspective,” *Journal of the Chemical Society, Faraday Transactions* 86(8), pp. 1307–1310, 1990.
- [252] a. D. Le Claire, “The analysis of grain boundary diffusion measurements,” *Journal of Applied Physics* 14, pp. 351–356, 1963.
- [253] C. Herzig and S. V Divinski, “Grain Boundary Diffusion in Metals: Recent Developments,” *Materials Transactions* 44(1), pp. 14–27, 2003.
- [254] M. Nicolet and M. Bartur, “Diffusion barriers in layered contact structures,” *Journal of Vacuum Science and Technology* 19(3), pp. 786–793, 1981.
- [255] N. Song, W. Zhang, P.-C. Hsiao, X. Wang, J. Colwell, and A. Lennon, “Copper Microstructure Evolution in Light-Induced Plated Metal Grids for Silicon Solar Cells: Implications for Reliable Metallization,” *Journal of the electrochemical Society* 163(14), pp. H1136–H1143, 2016.
- [256] A. E. Rakhshani, “Preparation, characteristics and photovoltaic properties of cuprous oxide-a review,” *Solid State Electronics* 29(1), pp. 7–17, 1986.
- [257] J. W. Weber and A. G. Aberle, “QSS-Voc measurements of unmetallised solar cells: Effect of high contact resistance and parasitic, external capacitance on flash-based measurements,” , in *22nd European Photovoltaic Solar Energy Conference*, 2007.
- [258] N. P. Harder, A. B. Sproul, T. Brammer, and A. G. Aberle, “Effects of sheet resistance and contact shading on the characterization of solar cells by open-circuit voltage measurements,” *Journal of Applied Physics* 94(4), pp. 2473–2479, 2003.
- [259] National Instruments, “Multifunction I/O Device - National Instruments,” [Online]. Available: <http://www.ni.com/en-au/shop/select/multifunction-io-device?modelId=122562>. [Accessed: 26-Jan-2018].
-

-
- [260] T. Trupke, R. A. Bardos, M. D. Abbott, and J. E. Cotter, “Suns-photoluminescence: Contactless determination of current-voltage characteristics of silicon wafers,” *Applied Physics Letters* 87(9), pp. 4–7, 2005.
- [261] R. Dumbrell, M. K. Juhl, T. Trupke, and Z. Hameiri, “Comparison of Terminal and Implied Open-Circuit Voltage Measurements,” *IEEE Journal of Photovoltaics* 7(5), pp. 1376–1383, 2017.
- [262] R. Dumbrell, M. Juhl, M. Li, T. Trupke, and Z. Hameiri, “Metal induced contact recombination measured by quasi-steady-state photoluminescence,” , in *44th IEEE Photovoltaic Specialists Conference*, 2017.
- [263] N. Song, P.-C. Hsiao, W. Zhang, X. Wang, J. Colwell, Z. Li, and A. Lennon, “Post-plating annealing of light induced plated copper fingers: implications for reliable metallization,” *Energy Procedia* 98(May), pp. 136–141, 2016.
- [264] C. Dang, R. Labie, E. Simoen, and J. Poortmans, “Detailed structural and electrical characterization of plated crystalline silicon solar cells,” *Solar Energy Materials and Solar Cells* 184, pp. 57–66, 2018.
- [265] A. Büchler, S. Kluska, M. Kasemann, M. Breitwieser, W. Kwapil, A. Hähnel, H. Blumtritt, S. Hopman, and M. Glatthaar, “Localization and characterization of annealing-induced shunts in Ni-plated monocrystalline silicon solar cells,” *physica status solidi (RRL) – Rapid Research Letters* 8(5), pp. 385–389, 2014.
- [266] S. Kluska, C. Fleischmann, A. Büchler, W. Hördt, C. Geisler, S. Hopman, and M. Glatthaar, “Micro characterization of laser structured solar cells with plated Ni-Ag contacts,” *Solar Energy Materials and Solar Cells* 120(PART A), pp. 323–331, 2014.
- [267] A. B. Tolstogouzov, T. I. Kitaeva, and S. S. Volkov, “SIMS imaging: Apparatus and applications,” *Mikrochimica Acta* 114–115(1), pp. 505–510, 1994.
- [268] J. S. Becker and H. J. Dietze, “State-of-the-art in inorganic mass spectrometry for analysis of high-purity materials,” *International Journal of Mass Spectrometry* 228(2–3), pp. 127–150, 2003.
- [269] A. Benninghoven and K. T. F. Janssen, “Secondary ion mass spectrometry,” Wiley, 1992.
- [270] K. Wittmaack, “High-sensitivity depth profiling of arsenic and phosphorus in silicon by means of SIMS,” *Applied Physics Letters* 29(9), pp. 552–554, 1976.
- [271] S. Fearn and D. S. McPhail, “High resolution quantitative SIMS analysis of shallow boron implants in silicon using a bevel and image approach,” *Applied Surface Science* 252(4), pp. 893–904, 2005.
- [272] T. Fellmeth, A. Born, A. Kimmerle, F. Clement, D. Biro, and R. Preu, “Recombination at metal-emitter interfaces of front contact technologies for highly efficient silicon solar
-

-
- cells,” *Energy Procedia* 8(December), pp. 115–121, 2011.
- [273] M. Van Craen, L. Frisson, and F. C. Adams, “SIMS study of the penetration of metallic secondary impurities in screen-printed silicon solar cells,” *Surface and Interface Analysis* 6(6), pp. 257–260, 1984.
- [274] F. Zanderigo, S. Ferrari, G. Queirolo, C. Pello, and M. Borgini, “Quantitative TOF-SIMS analysis of metal contamination on silicon wafers,” *Materials Science and Engineering: B* 73(1–3), pp. 173–177, 2000.
- [275] D. Macdonald and A. Cuevas, “Metallic Impurities in Multicrystalline Silicon,” in *ISES Solar World Congress*, 2001, pp. 1–5.
- [276] B. Hagenhoff, “High Resolution Surface Analysis by TOF-SIMS,” .
- [277] J. A. Kilner, D. S. McPhail, and S. D. Littlewood, “A quantitative study of copper segregation in silicon under oxygen ion beam bombardment using SIMS,” *Nuclear Instruments and Methods in Physics Research Section B: Beam Interactions with Materials and Atoms* 64(1–4), pp. 632–635, 1992.
- [278] IONTOF, “TOF-SIMS surface analysis: time of flight secondary ion mass spectrometry products by IONTOF,” [Online]. Available: <https://www.iontof.com/tof-sims-5-product-version-100mm-200mm-300mm.html>. [Accessed: 05-Feb-2018].
- [279] M. Di Sabatino, C. Modanese, and L. Arnberg, “Depth profile analysis of solar cell silicon by GD-MS,” *J. Anal. At. Spectrom.* 29(11), pp. 2072–2077, 2014.
- [280] J. Pisonero, B. Fernández, and D. Günther, “Critical revision of GD-MS, LA-ICP-MS and SIMS as inorganic mass spectrometric techniques for direct solid analysis,” *Journal of Analytical Atomic Spectrometry* 24(9), p. 1145, 2009.
- [281] W. W. Harrison, K. R. Hess, R. K. Marcus, and F. L. King, “Glow Discharge Mass Spectrometry,” Springer, Berlin, Heidelberg, 1986, pp. 75–78.
- [282] R. Escobar Galindo, R. Gago, A. Lousa, and J. M. Albella, “Comparative depth-profiling analysis of nanometer-metal multilayers by ion-probing techniques,” *Trends in Analytical Chemistry* 28(4), pp. 494–505, 2009.
- [283] M. Di Sabatino, “Detection limits for glow discharge mass spectrometry (GDMS) analyses of impurities in solar cell silicon,” *Measurement* 50, pp. 135–140, 2014.
- [284] S. W. Schmitt, C. Venzago, B. Hoffmann, V. Sivakov, T. Hofmann, J. Michler, S. Christiansen, and G. Gamez, “Glow discharge techniques in the chemical analysis of photovoltaic materials,” *Progress in Photovoltaics: Research and Applications* 22(3), pp. 371–382, 2014.
- [285] M. Di Sabatino, A. L. Dons, J. Hinrichs, and L. Arnberg, “Determination of relative sensitivity factors for trace element analysis of solar cell silicon by fast-flow glow discharge mass spectrometry,” *Spectrochimica Acta Part B: Atomic Spectroscopy* 66(2),
-

- pp. 144–148, 2011.
- [286] C. Modanese, G. Gaspar, L. Arnberg, and M. Di Sabatino, “On copper diffusion in silicon measured by glow discharge mass spectrometry,” *Analytical and Bioanalytical Chemistry* 406(29), pp. 7455–7462, 2014.
- [287] C. Modanese, L. Arnberg, and M. Di Sabatino, “Analysis of impurities with inhomogeneous distribution in multicrystalline solar cell silicon by glow discharge mass spectrometry,” *Materials Science and Engineering: B* 180, pp. 27–32, 2014.
- [288] A. Menéndez, N. Bordel, R. Pereiro, and A. Sanz-Medel, “Radiofrequency glow discharge-optical emission spectrometry for the analysis of metallurgical-grade silicon,” *J. Anal. At. Spectrom.* 20(3), pp. 233–235, 2005.
- [289] A. Montaser, “Inductively coupled plasma mass spectrometry,” J. Wiley, 1998.
- [290] A. Krushevska, S. Tan, M. Passer, and X. R. Liu, “Advances in trace element analysis of silicon wafer surfaces by VPD and ICP-MS,” *J. Anal. At. Spectrom.* 15, pp. 1211–1216, 2000.
- [291] Kenneth Ong, “Determination of Impurities in Silica Wafers with the NexION 300S ICP-MS,” , 2012.
- [292] M. Balski, H. Kipphardt, A. Berger, S. Meyer, and U. Panne, “Determination of impurities in solar grade silicon by inductively coupled plasma sector field mass spectrometry (ICP-SFMS) subsequent to matrix evaporation,” *Anal. Methods* 6(1), pp. 77–85, 2014.
- [293] J. S. Becker, R. S. Soman, T. Becker, V. K. Panday, and H. J. Dietze, “Trace and ultratrace analysis of gallium arsenide by different mass spectrometric techniques,” *Journal of Analytical Atomic Spectrometry* 13(9), pp. 983–987, 1998.
- [294] J. S. Becker, “Applications of inductively coupled plasma mass spectrometry and laser ablation inductively coupled plasma mass spectrometry in materials science,” *Spectrochimica Acta - Part B Atomic Spectroscopy* 57(12), pp. 1805–1820, 2002.
- [295] P. Luigi Buldini, A. Mevoli, and J. Lal Sharma, “LA-ICP-MS, IC and DPASV-DPCSV determination of metallic impurities in solar-grade silicon,” *Talanta* 47(1), pp. 203–212, 1998.
- [296] J. Pisonero, I. Krosiakova, D. Günther, and C. Latkoczy, “Laser ablation inductively coupled plasma mass spectrometry for direct analysis of the spatial distribution of trace elements in metallurgical-grade silicon,” *Analytical and Bioanalytical Chemistry* 386(1), pp. 12–20, 2006.
- [297] J. S. Lee and H. B. Lim, “Laser ablation ICP-MS to determine Cu on a Si wafer prepared by ion sputtering,” *Journal of Analytical Atomic Spectrometry* 26(7), p. 1534, 2011.
- [298] S. Chakraborty, M. L. Manalo, J. M. Ali, A. G. Aberle, and J. B. Li, “Laser ablation ICP-

-
- MS for impurity analysis in multicrystalline silicon wafers,” *Energy Procedia* 124, pp. 24–30, 2017.
- [299] A. Limbeck, P. Galler, M. Bonta, G. Bauer, W. Nischkauer, and F. Vanhaecke, “Recent advances in quantitative LA-ICP-MS analysis: Challenges and solutions in the life sciences and environmental chemistry,” *Analytical and Bioanalytical Chemistry* 407(22), pp. 6593–6617, 2015.
- [300] D. Pozebon, G. L. Scheffler, and V. L. Dressler, “Recent applications of laser ablation inductively coupled plasma mass spectrometry (LA-ICP-MS) for biological sample analysis: a follow-up review,” *J. Anal. At. Spectrom.* 32(5), pp. 890–919, 2017.
- [301] H. S. Rawdon and M. G. Lorentz, “Metallographic Etching Reagents for Copper,” *Scientific Papers of the Bureau of Standards* 16, pp. 641–668, 2007.
- [302] H. S. Rawdon and M. G. Lorentz, “Metallographic etching reagents: II for copper alloys, nickel and the alpha alloys,” *Scientific Papers of the Bureau of Standards* 17, pp. 636–676, 2007.
- [303] K. Hollocher and J. Ruiz, “Major and Trace Element Determinations on Nist Glass Standard Reference Materials 611, 612, 614 and 1834 By Inductively Coupled Plasma-Mass Spectrometry,” *Geostandards Newsletter* 19(1), pp. 27–34, 1995.
- [304] C. Paton, J. Hellstrom, B. Paul, J. Woodhead, and J. Hergt, “Iolite: Freeware for the visualisation and processing of mass spectrometric data,” *Journal of Analytical Atomic Spectrometry* 26(12), p. 2508, 2011.
- [305] K. R. Williams, K. Gupta, and M. Wasilik, “Etch Rates for Micromachining Processing—Part II,” *Journal of Microelectromechanical Systems* 12(6), pp. 761–778, 2003.
- [306] R. E. Russo, X. Mao, J. J. Gonzalez, V. Zorba, and J. Yoo, “Laser ablation in analytical chemistry,” *Analytical Chemistry* 85(13), pp. 6162–6177, 2013.
- [307] M. M. Martyniuk, “Vaporization and boiling of liquid metal in an exploding wire,” *Soviet Physics Technical Physics* 44, pp. 1262–1270, 1974.
- [308] J. H. Yoo, S. H. Jeong, R. Greif, and R. E. Russo, “Explosive change in crater properties during high power nanosecond laser ablation of silicon,” *Journal of Applied Physics* 88(3), pp. 1638–1649, 2000.
- [309] M. Guillon and D. Günther, “Effect of particle size distribution on ICP-induced elemental fractionation in laser ablation-inductively coupled plasma-mass spectrometry,” *J. Anal. At. Spectrom.* 17(8), pp. 831–837, 2002.
- [310] I. Horn and D. Günther, “The influence of ablation carrier gasses Ar, He and Ne on the particle size distribution and transport efficiencies of laser ablation-induced aerosols: Implications for LA-ICP-MS,” *Applied Surface Science* 207(1–4), pp. 144–157, 2003.
-

-
- [311] B. N. Chichkov, C. Momma, S. Nolte, F. von Alvensleben, and A. Tünnermann, “Femtosecond, picosecond and nanosecond laser ablation of solids,” *Applied Physics A: Materials Science & Processing* 63(2), pp. 109–115, 1996.
- [312] X. Zeng, X. L. Mao, R. Greif, and R. E. Russo, “Experimental investigation of ablation efficiency and plasma expansion during femtosecond and nanosecond laser ablation of silicon,” *Applied Physics A: Materials Science and Processing* 80(2), pp. 237–241, 2005.
- [313] N. L. LaHaye, J. Kurian, P. K. Diwakar, L. Alff, and S. S. Harilal, “Femtosecond laser ablation-based mass spectrometry: An ideal tool for stoichiometric analysis of thin films,” *Scientific Reports* 5(1), p. 13121, 2015.
- [314] A. Mondon, M. N. Jawaideh, J. Bartsch, M. Glatthaar, and S. W. Glunz, “Microstructure analysis of the interface situation and adhesion of thermally formed nickel silicide for plated nickel–copper contacts on silicon solar cells,” *Solar Energy Materials and Solar Cells* 117, pp. 209–213, 2013.
- [315] M. Tinani, a. Mueller, Y. Gao, E. a. Irene, Y. Z. Hu, and S. P. Tay, “In situ real-time studies of nickel silicide phase formation,” *Journal of Vacuum Science & Technology B: Microelectronics and Nanometer Structures* 19(2), p. 376, 2001.
- [316] A. Kale, E. Beese, T. Saenz, E. Warren, W. Nemeth, D. Young, K. Florent, S. K. Kurinec, S. Agarwal, P. Stradins, W. Lafayette, and N. Renewable, “Study of Nickel Silicide as a Copper Diffusion Barrier in Monocrystalline Silicon Solar Cells,” in *Proceedings of the 43rd IEEE Photovoltaic Specialists Conference (PVSC)*, 2016, pp. 2913–2916.
- [317] J. L. Maurice and C. Colliex, “Fast diffusers Cu and Ni as the origin of electrical activity in a silicon grain boundary,” *Applied Physics Letters* 55(3), pp. 241–243, 1989.
- [318] J. Lindroos, D. P. Fenning, D. J. Backlund, E. Verlage, A. Gorgulla, S. K. Estreicher, H. Savin, and T. Buonassisi, “Nickel: A very fast diffuser in silicon,” *Journal of Applied Physics* 113(20), 2013.
- [319] N. Miliszkiewicz, S. Walas, and A. Tobiasz, “Current approaches to calibration of LA-ICP-MS analysis,” *Journal of Analytical Atomic Spectrometry* 30, pp. 327–338, 2015.
- [320] H. P. Longerich, D. Günther, and S. E. Jackson, “Elemental fractionation in laser ablation inductively coupled plasma mass spectrometry,” *Analytical and Bioanalytical Chemistry* 355(5–6), pp. 538–542, 1996.
- [321] J. Lin, Y. Liu, Y. Yang, and Z. Hu, “Calibration and correction of LA-ICP-MS and LA-MC-ICP-MS analyses for element contents and isotopic ratios,” *Solid Earth Sciences* 1(1), pp. 5–27, 2016.
- [322] A. G. Aberle, P. P. Altermatt, G. Heiser, S. J. Robinson, A. Wang, J. Zhao, U.
-

-
- Krumbein, and M. A. Green, "Limiting loss mechanisms in 23% efficient silicon solar cells," *Journal of Applied Physics* 77(7), pp. 3491–3504, 1995.
- [323] A. Büchler, S. Kluska, A. Brand, C. Geisler, S. Hopman, and M. Glatthaar, "Micro Characterization and Imaging of Spikes in Nickel Plated Solar Cells," *Energy Procedia* 55, pp. 624–632, 2014.
- [324] A. Fick, "Ueber Diffusion," *Annalen der Physik und Chemie* 170(1), pp. 59–86, 1855.
- [325] J. Crank, "The mathematics of diffusion," Oxford: Clarendon Press, 1975.
- [326] IEC, "International standard IEC 61215: Crystalline silicon terrestrial photovoltaic (PV) modules – Design qualification and type approval," , 2005.
- [327] J. Bartsch, M. Kamp, D. Hartleb, C. Wittich, A. Mondon, B. Steinhauser, F. Feldmann, A. Richter, J. Benick, M. Glatthaar, M. Hermle, and S. W. Glunz, "21.8% Efficient n-type Solar Cells with Industrially Feasible Plated Metallization," *Energy Procedia* 55, pp. 400–409, 2014.
- [328] A. Kraft, C. Wolf, J. Bartsch, and M. Glatthaar, "Characterization of Copper Diffusion in Silicon Solar Cells," *Energy Procedia* 67, pp. 93–100, 2015.
- [329] B. Sopori, P. Basnyat, S. Devayajanam, S. Shet, V. Mehta, J. Binns, and J. Appel, "Understanding light-induced degradation of c-Si solar cells," , in *2012 38th IEEE Photovoltaic Specialists Conference*, 2012, pp. 001115–001120.
- [330] J. Karas, L. Michaelson, K. Munoz, J. Rand, and S. Bowden, "Degradation Studies Including Light-Induced Degradation of c-Si Solar Cells with Nickel-Copper Plated Contacts," , in *7th World Conference on Photovoltaic Energy Conversion*, 2018.
- [331] O. Breitenstein, J. Bauer, P. P. Altermatt, and K. Ramspeck, "Influence of Defects on Solar Cell Characteristics," *Solid State Phenomena* 156–158(1), pp. 1–10, 2010.
- [332] O. Breitenstein, P. Altermatt, K. Ramspeck, M. A. Green, J. Zhao, and A. Schenk, "Interpretation of the Commonly Observed I-V Characteristics of C-SI Cells Having Ideality Factor Larger Than Two," , in *2006 IEEE 4th World Conference on Photovoltaic Energy Conference*, 2006, pp. 879–884.
- [333] S. J. Robinson, A. G. Aberle, and M. A. Green, "Recombination saturation effects in silicon solar cells," *IEEE Transactions on Electron Devices* 41(9), pp. 1556–1569, 1994.
- [334] C. Dang, R. Labie, E. Simoen, L. Tous, R. Russell, F. Duerinckx, R. Mertens, and J. Poortmans, "Insights into the reliability of Ni/Cu plated p-PERC silicon solar cells," *Energy Procedia* 124, pp. 862–868, 2017.
- [335] A. G. Aberle, S. J. Robinson, A. Wang, J. Zhao, S. R. Wenham, and M. A. Green, "High-efficiency silicon solar cells: Fill factor limitations and non-ideal diode behaviour due to voltage-dependent rear surface recombination velocity," *Progress in Photovoltaics: Research and Applications* 1(2), pp. 133–143, 1993.
-

-
- [336] D. Macdonald and A. Cuevas, “Reduced Fill Factors in Multicrystalline Silicon Solar Cells Due to Injection-level Dependent Bulk Recombination Lifetimes,” *Progress in Photovoltaics: Research and Applications* 8, pp. 363–375, 2000.
- [337] M. Miyazaki, M. Sano, S. Sumita, and N. Fujino, “Influence of Metal Impurities on Leakage Current of Si N + P Diode,” *Japanese Journal of Applied Physics* 30(2B), p. L295, 1991.
- [338] A. Lennon, J. Colwell, and K. P. Rodbell, “Challenges Facing Copper-Plated Metallisation for Silicon Photovoltaics: Insights from Integrated Circuit Technology Development,” *Progress in Photovoltaics: Research and Applications*, 2018.
- [339] A. Knorz, M. Peters, A. Grohe, C. Harmel, and R. Preu, “Selective laser ablation of SiNx layers on textured surfaces for low temperature front side metallizations,” *Progress in Photovoltaics: Research and Applications* 17(2), pp. 127–136, 2009.
- [340] G. Heinrich, M. Bähr, K. Stolberg, T. Wütherich, M. Leonhardt, and A. Lawerenz, “Investigation of ablation mechanisms for selective laser ablation of silicon nitride layers,” *Energy Procedia* 8, pp. 592–597, 2011.
- [341] G. Heinrich and A. Lawerenz, “Non-linear absorption of femtosecond laser pulses in a SiN x layer—influence of silicon doping type,” *Solar Energy Materials and Solar Cells* 120, pp. 317–322, 2014.
- [342] P. M. Fauchet and A. E. Siegman, “Surface ripples on silicon and gallium arsenide under picosecond laser illumination,” *Applied Physics Letters* 40(9), pp. 824–826, 1982.
- [343] J. E. Sipe, J. F. Young, J. S. Preston, and H. M. Van Driel, “Laser-induced periodic surface structure. I. Theory,” *Physical Review B* 27(2), p. 1141, 1983.
- [344] J. F. Young, J. S. Preston, H. M. Van Driel, and J. E. Sipe, “Laser-induced periodic surface structure. II. Experiments on Ge, Si, Al, and brass,” *Physical Review B* 27(2), p. 1155, 1983.
- [345] S. E. Clark and D. C. Emmony, “Ultraviolet-laser-induced periodic surface structures,” *Physical Review B* 40(4), p. 2031, 1989.
- [346] S. Hermann, T. Dezhdar, N.-P. Harder, R. Brendel, M. Seibt, and S. Stroj, “Impact of surface topography and laser pulse duration for laser ablation of solar cell front side passivating SiNx layers,” *Journal of Applied Physics* 108(11), p. 114514, 2010.
- [347] B. Tan and K. Venkatakrishnan, “A femtosecond laser-induced periodical surface structure on crystalline silicon,” *Journal of Micromechanics and Microengineering* 16(5), p. 1080, 2006.
- [348] J. M. Liu, R. Yen, H. Kurz, and N. Bloembergen, “Phase transformation on and charged particle emission from a silicon crystal surface, induced by picosecond laser pulses,” *Applied Physics Letters* 39(9), pp. 755–757, 1981.
-

-
- [349] S. C. Baker-Finch and K. R. McIntosh, "A freeware program for precise optical analysis of the front surface of a solar cell," , in *Photovoltaic Specialists Conference (PVSC), 2010 35th IEEE*, 2010, pp. 2184–2187.
- [350] P.-C. Hsiao, N. Song, X. Wang, X. Shen, B. Phua, J. Colwell, U. Romer, B. Johnston, S. Lim, Y. Shengzhao, P. Verlinden, and A. Lennon, "266-nm ps Laser Ablation for Copper-Plated p-Type Selective Emitter PERC Silicon Solar Cells," *IEEE Journal of Photovoltaics* 8(4), pp. 952–959, 2018.
- [351] L. T. Wang, C. W. Wu, X. Wen, K. S. Abdel-Hafez, S. Bhattacharya, A. Chatterjee, X. Chen, K. T. Cheng, W. Eklow, and M. S. Hsiao, "VLSI Test Principles and Architectures: Design for Testability," Elsevier Science, 2006.
- [352] T. Trupke and R. A. Bardos, "Self-consistent determination of the generation rate from photoconductance measurements," *Applied Physics Letters* 85(16), pp. 3611–3613, 2004.
- [353] T. Trupke, R. A. Bardos, and M. D. Abbott, "Self-consistent calibration of photoluminescence and photoconductance lifetime measurements," *Applied Physics Letters* 87(18), p. 184102, 2005.